Modeling and Analysis of Nonlinear Damping and Mistuning Mechanisms in Rotating Systems

by

Mainak Mitra

A dissertation submitted in partial fulfillment
of the requirements for the degree of
Doctor of Philosophy
(Mechanical Engineering)
in The University of Michigan
2018

Doctoral Committee:

Professor Bogdan I. Epureanu, Chair
Professor Greg M. Hulbert
Associate Professor Kenn R. Oldham
Professor Nickolas Vlahopoulos
Associate Professor Stefano Zucca, Politecnico di Torino

Mainak Mitra

mitram@umich.edu

ORCID iD: 0000-0003-3208-1290

DEDICATION

For my parents

ACKNOWLEDGEMENTS

There are many individuals who have in some part contributed to this academic achievement. Although the space afforded to me here will allow me to mention but a few of them by name, my sincere thanks also goes out to all who have contributed to my graduate success. First, I would like to thank my current PhD. advisor Prof. Bogdan Epureanu for hearing my ideas while guiding and shaping my work, for his unwavering support of my research endeavors over the past four years and facilitating collaborations with researchers at Politecnico di Torino, Italy (Polito). It is through these collaborations that I met my co-advisor Prof. Stefano Zucca, who had the patience to answer my myriad questions and share his expertise with me when I was a novice in this field. I have been since grateful for his help and guidance on many occasions and much of this work would not have been possible without his input. I would also like to thank Prof. Muzio Gola for inviting me to conduct experiments at Polito. I am also grateful to Prof. Daniele Botto for lending his expertise in contact mechanics during the test rig design and Prof. Christian Maria Firrone, who along with Prof. Botto and Prof. Zucca, facilitated my lab orientation and the experimental setup. I am also grateful to my other PhD. committee members Prof. Greg Hulbert, Prof. Kenn Oldham and Prof. Nickolas Vlahopoulos for volunteering their valuable time and knowledge to supervise my work and providing precious feedback which has served to better my research. I would like to thank my first PhD. advisor, Prof. Timothy Gordon whose invaluable lessons in research which have undeniably aided in the success of my present work. I am grateful for the support of all of my peers at Michigan and Italy without whom this work would not have been possible. I would like to express my gratitude to Dr. Andy Madden of Ansys Inc., who was always ready to delve deep to answer the difficult questions regarding the software. I would also like to thank the GUIde 5 Consortium and all its members for funding my research.

TABLE OF CONTENTS

LIST OF FIGURES

Figure

LIST OF TABLES

Table

LIST OF APPENDICES

Appendix

ABSTRACT

Turbine bladed disks (blisks) which constitute critical components of most modern turbomachinery, are known for their complex vibratory behavior. A good blisk design necessitates the knowledge of the dynamic behavior of the component in different regimes of operation. However, small parametric uncertainties and inter-blade structural variations called mistuning are known to affect blisk dynamics drastically under certain conditions. Introduced by manufacturing tolerances, thermal stresses, wear and other causes, these variations make the design process especially challenging. The dynamics of blisks often also involve nonlinearities, such as those arising from friction damping structures such as shrouds or under-platform dampers or from nonlinear damping coatings adhered to the blades. Since it is not possible to eliminate uncertainties due to mistuning, the designer must ensure safe operation within the field of uncertainty of all the design parameters. Presently, the widely accepted method for obtaining a comprehensive understanding of the effects of these uncertainties is to conduct probabilistic analyses with many simulations of different systems generated by applying random mistuning to the nominal tuned system. Finite element modeling techniques when applied in isolation prove too cumbersome and time-intensive to use for this task. To make these simulations computationally feasible, reduced order models which accurately capture the nonlinear mistuned dynamics while being computationally tractable must be developed. This work presents model reduction methods for blisk dynamics involving two specific nonlinear mechanisms. An adaptive microslip projection method is developed to reduce the dynamics of blisks with frictional contacts characterized by complex stick-slip behavior. A reduced order modeling technique developed for blisks with nonlinear coatings using an amplitude dependent mistuning framework to simulate the dynamics is presented also. Both reduced order

models are found to provide significant computational time savings, while retaining high accuracy in comparison to their higher order baseline models. Another practical challenge for accurate non-linear dynamic simulation of blisks, is the identification of physical parameters which represent the physics of the system and are thus employed by both the full and reduced order models. Contact parameters are identified from experimental data using optimization techniques and are used to validate the reduced order model. The specific effects of variations in these contact parameters on the dynamic response of the blisk are also studied by carrying out probabilistic analyses.

CHAPTER I

Introduction

Bladed disks, also alternatively called blisks or rotors which constitute the compressor and turbine stages of all turbomachinery experience high thermal and cyclic structural stresses during their operation which involves extremely high rotational speeds. As a consequence, a significant thrust of research in the field of turbomachinery has been dedicated to understanding, quantifying and modeling the dynamic behavior of bladed disks with the aim of accounting for these inherent harsh conditions and producing reliable and robust designs. Early studies into the subject during the 1960's and 1970's involved quantifying the linear mass, stiffness and damping characteristics of the blisks employing lumped mass representations [1, 2]. With the improvement in modeling techniques and computational capabilities, these simplistic models were replaced by high fidelity finite element (FE) models, which became the standard for industry by the mid 1990's- early 2000's [3]. Although a single linear analysis for even a very large FE model which often contain millions of degrees of freedom (DoFs) can be performed within a reasonable period of time typically on the order of hours or days with current computational speeds, the multiple analyses that need to be carried out during the design procedure makes a design approach based only on such high fidelity simulations impractical. As a result the development of reduced order models (ROMs) of blisks which allow faster simulations for accurate response predictions, emerged as an important research area in the field. The most obvious reduction one may apply to any blisk model is based on

its property of cyclic symmetry. If any cyclic sector of the blisk is considered to be geometrically and materially identical to any another, the DoFs of the blisk dynamic may be reduced by a factor of the number of blades by the application of suitable constraints. However, it was well known that even small differences which exist between different sectors in practice due to manufacturing tolerances and variability in operating conditions, collectively called mistuning, can have significant effects on blisk response amplitudes [3–5]. Mistuning may be small when the variability in parameters between the sectors does not significantly affect the modes of the structure or large when the response of the mistuned blisk in a certain frequency region cannot be captured by a set of nominally cyclic symmetric or tuned modes whose natural frequencies lie in the corresponding region. Thus, the phenomenon of mistuning limits the applicability of a cyclic symmetric model to approximately determining the natural frequencies of a system with small mistuning. The response amplification which occurs due to mistuning also necessitates the use of probabilistic analyses [6, 7] in the design of blisks to account for uncertainties associated with the values of mistuning parameters such as material stiffness and density which cannot be exactly specified in the design as they are subject to the vagaries of manufacturing. ROMs are indispensable for Monte-Carlo (MC) type probabilistic analyses which require multiple runs of different mistuning patterns applied to the same underlying tuned system. The effects of mistuning were studied widely and a number of different ROMs were proposed for linear mistuned blisks. These include modifications of general linear reduction methods such as Craig-Bampton component mode synthesis (CB-CMS) [8–13], as well as more specialized techniques developed especially for blisks such as subset of normal modes (SNM) [14], fundamental model of mistuning (FMM) [15], component mode mistuning (CMM) [16–18] and asymptotic model of mistuning (AMM) [19–21].

However, not all blisks are designed to behave linearly. In fact, nonlinearities are often introduced into blisk design to lower resonant responses and stresses. Traditionally, friction interfaces on shrouds, under-platform dampers (UPDs) or ring dampers have been employed to provide additional damping. Nonlinearities can also occur unintentionally such as cracks or defects in

blades. Modeling these nonlinear effects is paramount to achieve accurate estimates of responses and stresses in the blisks. The earliest attempts at modeling nonlinear contacts in blisks involved approximating the nonlinear forces using lumped parameters [22, 23] at every sector. The research focus then shifted to modeling complex localized behavior of frictional forces [24, 25]. Iwan models which were initially developed for modeling hysteretic behavior under constant unidirectional normal load have been employed extensively to model certain types of interfaces [26–29]. Later, models which predict the local frictional forces under different regimes of stick, slip and separation under varying periodic normal loads were proposed [30–33]. To model nonlinear Coulomb friction accurately, a number of these models must be used at every contact interface to calculate the local values of normal and tangential frictional forces from the local relative displacements. Moreover, to find steady state solutions, the friction forces over the entire period must be calculated iteratively till convergence is achieved. These additional calculations greatly increase the computational effort required to predict forced responses for blisks with frictional interfaces. The computational cost associated also increases sharply with the number of nonlinear degrees of freedom. Practically, simulation times for calculation of the steady state forced response of a high fidelity blisk model with nonlinearities at single frequency using time-marching or transient dynamic analysis (TDA) are in the order of days or weeks, even with modern computational hardware. Hence, reduction in the dynamic simulation times was essential to make computational predictions feasible for nonlinear blisks.

Reductions in calculations were initially obtained in the time-domain by using well-known general approaches to nonlinear differential equation solving such as the harmonic balance method (HBM) [34, 35]. HBM converts the nonlinear differential equations in the time-domain associated with the blisk dynamics into algebraic equations in the frequency domain associated with periodic harmonics of the response. Reductions in calculations are obtained by retaining a finite number of harmonics for calculating the solution. The conversion to the frequency domain entails a complication due to the nonlinear forcing functions in the time-domain equations which appear as functions

of displacements at the interfaces. In general, it is not possible to find a closed form expressions for the equivalent harmonic nonlinear forcing functions which must appear in the frequency domain HBM equations. To address this issue, an alternating frequency-time technique (AFT) [36, 37] was proposed, to numerically obtain the harmonic nonlinear forces by calculating them in the time domain as functions of displacements and converting them back into the frequency domain by using Fourier and inverse-Fourier transforms. Calculation of the forced frequency responses for nonlinear blisk using HBM and AFT has become standard practice in the field [38–48].

Due to the local nature of the forces which act only at contact interfaces, it is possible to obtain further reductions. Researchers have used previously developed linear reduction techniques to obtain spatial reductions at the non-contact linear DoFs only [35, 40, 49, 50]. However, these techniques retain all the nonlinear DoFs from the original models and must perform associated HBM and AFT simulations, which contribute to the majority of the calculation costs. Another perspective on understanding the response of nonlinear systems is the formulation of nonlinear normal modes (NNMs) [51–54] which are nonlinear synchronous motions of the system where the motion of a single DoF of a system can describe the motion along all other DoFs. Unlike linear modes of a system, these modes are energy dependent and change with the level of activation and consequently with response frequency [55, 56]. The calculation of these modes is no easier than calculating the nonlinear response itself. In fact, HBM is commonly used to calculate these modes for large and complex systems such as nonlinear blisks [55, 56]. Since the concepts of superposition and orthogonality do not generally apply for NNMs [55, 57], model reduction by using a reduced order basis is not an option. Instead, researchers have sought to find invariant manifold descriptions [54, 57–60] of these NNMs to reduce the nonlinear dynamics. In the past, such methods have been applied to simple models with relatively few DoFs [57]. Reduction of the dynamics of large models such as blisks with complex friction nonlinearities using NNMs is quite challenging due to high computational costs and remains a field of active research [61].

More commonly for such nonlinear systems, researchers have used other methods to calculate

a linear basis which approximately spans the nonlinear motion space and projected both the linear and nonlinear dynamics onto the basis to obtain ROMs. Many popular methods use proper orthogonal modes (POMs) [62] to estimate the span of the nonlinear response. The main drawback of such POM based methods [63–67] and their derivatives is the computational power required to calculate the nonlinear response. Even with the associated computational cost, they may be feasible for creating models of well-understood systems which are not expected to change their behavior with time. However, they remain a poor choice for systems like blisks where fundamental uncertainties of mistuning and associated probabilistic calculations would require that nonlinear calculations be performed every time the model is changed slightly. Other projection based reduction methods seek to devise specific reduction bases which serve well in the specific circumstances of application they are designed for, but cannot be broadly generalized to all types of nonlinearities. One such reduction method, which is pertinent to blisks with intermittent contact or cracks, is based on ideas of bilinear modes (BLMs) representing the dynamics of localized piece-wise linear systems [68–70]. BLMs are linear normal modes for the system with special boundary conditions at the surface where the intermittent contact takes place. In [69] it was shown that BLMs are able to capture the nonlinear dynamics of a cracked plate with intermittent contact by approximating the dominant POMs calculated from the nonlinear response. The concept of BLMs was extended in [71] to directly calculate approximations for the periodic steady-state response at resonant frequencies using modes similar to BLMs. This method, referred to as bilinear amplitude approximation (BAA) and was considerably faster than the BLM ROMs used in [69] and was also used to construct ROMs for blisks in [72]. More recently, in [70], BLMs were used to reduce a cracked plate where the effects of tangential frictional forces were also considered in addition to the normal reaction forces. Another important operational regime for nonlinear blisks, especially with friction damping mechanisms is microslip [24]. A structure in microslip is dominated by frictional effects and exhibits complex stick-slip behavior at contact interfaces both spatially and temporally. [50] presents ROMs for blisks with ring dampers by using reduction basis comprised of linear modes

of the damper in full stick and gross slip. [73] uses the same reduction basis and achieves further simplification of the dynamics by approximating equivalent linear modal damping and stiffness parameters for the nonlinear forces using an energy equivalence calculation.

In chapter II of this work, ROMs are developed for calculating steady-state dynamics of nonlinear shrouded blisk with frictional contacts. The dynamics of a shrouded blisk is significantly different from the afore-mentioned structures with cracks or blisks with ring dampers. Unlike in cracked structures, friction plays a more dominant role in shrouded blisks. Moreover, due to the contacts at the shrouds being in the proximity of the blade tip, there is a significant effect of the frictional forces on the blisk response to such an extent, that the nonlinear displacements no longer lie on the subspace spanned by the linear modes corresponding to stick and slip. Ideas from previous works are synthesized, modified and amalgamated, to develop a basis called the adaptive microslip projection (AMP) basis which can span the required subspace by approximating the spatial correlations exhibited by the system. The AMPs are obtained from modes of intermediate linear systems corresponding to special boundary conditions (BCs) at the contact interfaces. These BCs are obtained by approximating the blisk's movement with linear modes at different levels of amplitude and predicting its effect on the contact state at the interfaces. Forced frequency responses of ROMs for shrouded blisks with and without small stiffness mistuning in the blades are calculated using HBM and AFT and validated against full order model responses. The subspaces spanned by the AMP modes and the dominant POMs of the nonlinear responses are also compared.

In chapter III, the AMP reduction procedure is validated experimentally. To do so, experimental apparatus and techniques were developed which would allow the detection of spatial coherences in the response of an elastic system subject to contact nonlinearities. The experimental rig consists of a blade-like cantilevered beam, constrained by a contact at its non-fixed end. The contact is relatively large compared to those used in traditional contact experiments [74] to allow complex microslip phenomenon of interest. One of the challenge was the prediction of the actual behavior with simulations, which required accurately identifying model parameters. Frequency responses

and linear modes of this structure were measured experimentally. FE models of the structure were adjusted to match the linear modes and obtain the mass and initial stiffness matrices. These were used in conjunction with node-to-node contact models to simulate nonlinear responses with HBM. All contact parameters were then identified using an optimization process whose objective was to minimize the error between the experimental and simulated frequency responses at multiple excitation levels. The identified nonlinear model was then used to validate the AMPs by comparing ROMs with the non-reduced model frequency responses in simulations. Additionally, POMs were obtained from experimentally observed responses and were compared against AMP modes calculated by assuming stick-slip conditions along the contact interface based on observed displacements near contact.

An important aspect of contact dynamics in blisks, which is not often considered in literature, is the variability in the contacts across a blisk. It is well known that variability in the material properties of the blades plays a significant role in the dynamics and there is a bulk of existing literature on the effects of blade mistuning [5, 7, 19, 75–78]. However, there is a dearth of research regarding the effects of mistuning in the properties of the contacts themselves. Some studies which considered such mistuning in the parameters of the contact interfaces of a blisk [22, 40, 49] used only simple lumped or single-node contact models for modeling friction interfaces. Also, most existing studies focus on the mistuning of damping characteristics in UPDs. Thus, a study is conducted in chapter IV to glean greater insight into the effects of contact mistuning in shrouded blisks analyses. The effect of mistuning in the stiffness parameters of localized contacts at the shrouds of an otherwise tuned blisk is studied, separating the effect of contact mistuning from that of mistuning due to inter-blade variability. The contact stiffness parameters are varied randomly both across and within sectors. The effect of the parameter variations on maximum response amplitude and frequency are analyzed. Probabilistic analyses are carried out by fitting a Weibull function to probabilistic distributions of amplification factors (AFs) obtained from Monte Carlo (MC) simulations of linear and nonlinear forced responses.

Another nonlinear mechanism, which has gained interest from the industry and academia recently, is the use of damping coatings adhered to the blades of the blisk [79–83]. In existing literature, the nonlinear effects of the coating applied to a single blade or beam have been analyzed [81, 83]. In chapter V of this work, the effects of amplitude dependent behavior of the coating are analyzed for an entire blisk with coated blades and a ROM is developed to reduce its dynamics. Studies have shown that at the sector or individual blade level, these coatings behave nonlinearly, providing increasing damping with increase in amplitude. In some cases, the stiffness (and hence the resonant frequencies) are also affected differently by the different excitation levels due to coatings [81, 83]. However, the response amplitude which dictates the level of activation of this nonlinearity does not affect the blade modes significantly [81]. In addition, nonlinear forces due to the coating act everywhere on the face of the blades. These factors distinguish the coating nonlinearity from the more localized friction nonlinearities in terms of its behavior and effects. Consequently a different tactic is motivated for designing ROMs for coated blisks. The level of local response differs substantially from sector to sector in mistuned systems. This implies that the nonlinear effects are different in magnitude from sector to sector. Hence, there are mistuning effects due to the coatings which are dependent on both the nonlinearity and the linear mistuning in coated blades. Hence, a suitable ROM for the nonlinear coated blisk is constructed by modifying the mistuning parameters in a linear blisk ROM to be amplitude dependent. ROM responses are compared with TDA responses of FE models augmented with coating nonlinearities. Probabilistic analyses are also conducted by varying underlying linear mistuning pattern in the blades which affects the nonlinear dynamic response due to the inherent amplitude dependency. MC simulation results for blisks with both linear and nonlinear coatings are compared to show the effect of nonlinearity in coatings and prove the necessity of nonlinear analyses.

This work also expounds on the mathematical formulation of cyclic symmetric matrices for blisks in appendix A and the corresponding CB-CMS reduction for such a blisk in appendix B. CB-CMS is used in chapter II as a pre-reduction step to reduce linear DoFs before the AMPs are

applied for further reductions.

CHAPTER II

Adaptive Microslip Projection

Turbine bladed disks (blisks) which constitute critical components of most modern turbomachinery, are known for their complex vibratory behavior [1, 2, 4]. A good blisk design necessitates the knowledge of the dynamic behavior of the component in different regimes of operation. However, small parametric uncertainties and inter-blade structural variations called mistuning are known to affect blisk dynamics drastically under certain conditions. Introduced by manufacturing tolerances, thermal stresses, wear and other causes, these variations make the design process especially challenging. Since it is not possible to reduce or eliminate these uncertainties beyond a certain point, the designer must ensure safe operation within the field of uncertainty of all the design parameters [2, 4]. To achieve this, probabilistic analyses are often used to study behaviors of various blisk designs with random deviations in certain parameters such as blade stiffness [4]. Finite element (FE) modeling is a powerful technique which may be used to accurately capture the dynamic characteristics of a physical blisk in the computational domain. However, a single time domain analysis of a blisk FE model with millions of DoFs may take days or weeks to simulate. Hence, it is too cumbersome and time-intensive to use FE models with probabilistic analyses, which require a large number of runs to generate meaningful results. Instead, reduced order models (ROMs) derived from the FE models are employed. ROMs aim to reduce the DoFs of the original FE model to facilitate faster simulation, while retaining their accuracy by reducing redundancies

and capturing coherent behaviors between multiple DoFs [4, 6].

Hence, generation of blisk ROMs is an important and well-established field of research. Various techniques have been developed to reduce mistuned blisk models without nonlinearities [10, 11, 13–16, 18–21, 84]. Blisks with friction damping structures such as shrouds or under-platform dampers introduce additional complexity due to localized nonlinearities at the contact interfaces which can lead to complex stick-slip behavior [30–32]. General approaches to nonlinear differential equation solving such as the harmonic balance method (HBM) are often employed to reduce temporal complexity of such problems [34, 35, 38, 42, 43]. In addition, the linear DoFs of the model which do not directly experience the contact forces may be reduced by techniques such as Craig-Bampton component mode synthesis (CB-CMS) [8–10, 12]. However, this still leaves a large number of nonlinear equations at the interface DoFs which must be solved in full. Since, the solution of the nonlinearities is the aspect which requires the most computational effort; it is of significant interest and the primary object of this work to reduce the number of nonlinear equations by reducing the corresponding DoFs.

The case of a blisk with friction interfaces at contacting surfaces on its shrouds is analyzed. The tuned case is analyzed first where all the blades are identical. Later a small-stiffness mistuning is also introduced in the blades. A baseline model considered as a full order model is used to compute the nonlinear forced response using HBM. The baseline response is spatially correlated for various levels of microslip. Also, a relatively low number of these correlations are dominant in the blisk dynamics compared to the number of DoFs in the model and this offers the possibility of model reduction. A novel method is proposed to obtain a set of reduction basis functions for the contact interface DoFs and the remaining DoFs called adaptive microslip projection (AMP). It is postulated that the microslip regime which involves nonlinear friction dynamics can be captured by a set of intermediate linear systems generated by imposing specifically chosen boundary conditions at the contact interfaces. These boundary conditions are generated by comparison of estimated normal and tangential forces as a function of amplitudes of the modes of the fully stuck

system. The modes of these intermediate systems which lie in the frequency range under consideration collectively form the AMP reduction basis which is then used to construct the ROM. The AMP procedure used to develop ROMs involves the solution of linear systems in addition to mathematical operations such as vector multiplication and comparators. No nonlinear equations are solved during the calculation of reduction modes as is the case with other reduction methods such as proper orthogonal decomposition (POD). Simulated responses of full models and ROMs are studied at various engine orders, with single and multiple harmonics included and under varying-conditions of stick and slip. It is seen that the AMP procedure is successful in creating ROMs which predict the response amplitudes with nearly the same accuracy as the baseline model, while reducing computational effort significantly.

2.1 Methodology

2.1.1 Craig-Bampton component mode synthesis

The methodology used to reduce the blisk system is detailed in Fig. 2.1. The system matrices of the full wheel free finite element (FE) model ($\mathbf{M}_F$ and $\mathbf{K}_F$) correspond to the physical degrees of freedom (DoFs) $\mathbf{q}_F$. Here the moniker free refers to the fact that no contact conditions are enforced. i.e. no boundary conditions are enforced at nodes on contact interfaces. The DoFs $\mathbf{q}_F$ may be divided into master DoFs $\mathbf{q}_M$ and slave DoFs $\mathbf{q}_S$ belonging to master and slave nodes respectively. Master nodes include the nodes on contact interfaces, the nodes where static or dynamic forces are applied and nodes where response is calculated. The nodes in the FE model which are not master nodes, are termed as slave nodes. A Craig-Bampton component mode synthesis (CB-CMS) substructuring procedure [8] is then used to reduce the slave DoFs $\mathbf{q}_S$ to a reduced set of modal DoFs η_S. The modes employed for this reduction, also called the slave modes or the normal modes, are modes of the structure with all the master DoFs constrained to zero displacement. The master DoFs $\mathbf{q}_M$ which include the DoFs where nonlinear contact forces act, are retained without any

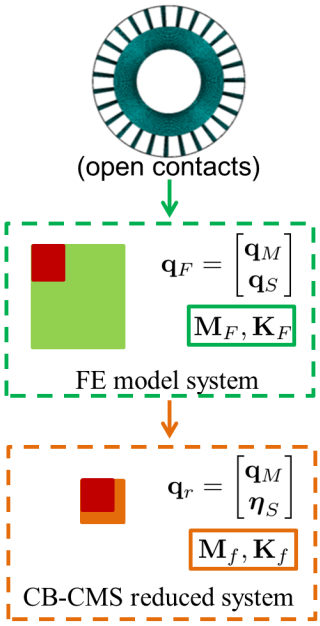

Figure 2.1. Craig-Bampton component mode synthesis

reductions by this procedure. The CB-CMS reduced system DoF vector is represented $\mathbf{q}_r$ and the corresponding system matrices are $\mathbf{M}_f$ and $\mathbf{K}_f$ representing mass and stiffness respectively.

2.1.2 Relative co-ordinates

The dynamic equations describing the shrouded blisk system may be represented in the time domain as:

$$\mathbf{M}_f\ddot{\mathbf{q}}_r + \mathbf{C}_f\dot{\mathbf{q}}_r + \mathbf{K}_f\mathbf{q}_r = \mathbf{f}_E + \mathbf{f}_C(\mathbf{q}_r) \tag{2.1}$$

where $\mathbf{M}_f$ and $\mathbf{K}_f$ are the free mass and stiffness matrices of the blisk with no contact conditions enforced. i.e. the contacting nodes are free and not constrained in any manner when developing these matrices. $\mathbf{C}_f$ is the linear damping matrix of the free system. $\mathbf{f}_E$ is the vector of excitation forces applied to the model. The contact conditions are enforced through the vector of contact forces $\mathbf{f}_C$ which arise due to Coulomb friction nonlinearities and are determined as a function of the displacements using a suitable contact model. The displacements $\mathbf{q}_r$ in Eqn. (2.2) are expressed

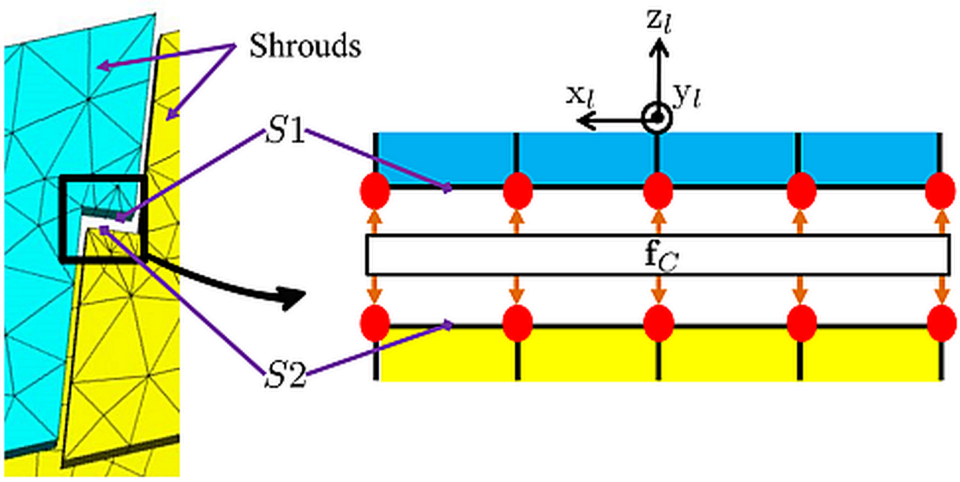

Figure 2.2. Contact surfaces $S1$ and $S2$

in the relative co-ordinates such that:

$$\mathbf{q}_r = \begin{bmatrix} \mathbf{q}_{S2,l} - \mathbf{q}_{S1,l} \\ \mathbf{q}_{S1,l} \\ \mathbf{q}_O \end{bmatrix} = \begin{bmatrix} \mathbf{q}_N \\ \mathbf{q}_L \end{bmatrix} \tag{2.2}$$

where

$$\mathbf{q}_N = [\mathbf{q}_{S2,l} - \mathbf{q}_{S1,l}] \; ; \; \mathbf{q}_L = \begin{bmatrix} \mathbf{q}_{S1,l} \\ \mathbf{q}_O \end{bmatrix} \tag{2.3}$$

$\mathbf{q}_{S1,l}$ and $\mathbf{q}_{S2,l}$ represent the corresponding DoFs of matching node-pairs on contacting surfaces $S1$ and $S2$ in the local co-ordinate system l shown in Fig. 2.2. $\mathbf{q}_O$ represents all other DoFs including any reduced co-ordinates. $\mathbf{q}_N$ is the vector of nonlinear co-ordinates which contains the relative displacements of the contact nodes. The rest of the co-ordinates form the vector of linear co-ordinates $\mathbf{q}_L$. This partition into nonlinear and linear DoFs has been used before in [85] and [86]. It leverages the fact that the nonlinear contact forces, when expressed in these relative co-ordinates

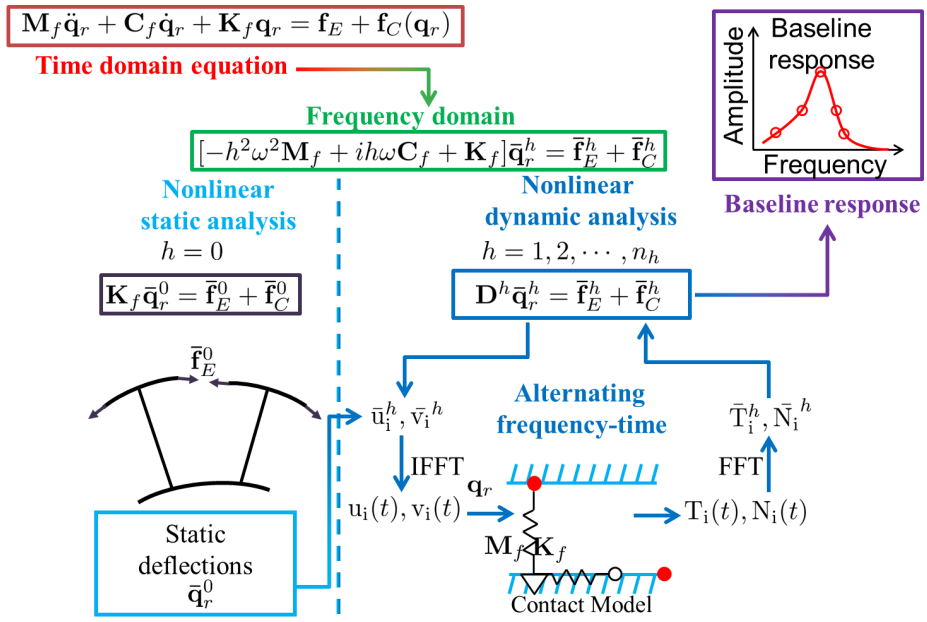

Figure 2.3. Harmonic balance and response calculation

act only along the DoFs of the relative local displacements. Thus, $\mathbf{f}_C$ may be expressed as:

$$\mathbf{f}_C = \begin{bmatrix} \mathbf{f}_{C,N} \\ \mathbf{0} \end{bmatrix} \tag{2.4}$$

The linear DoFs do not directly experience the nonlinear contact forces. Since $\mathbf{f}_C$ is the variable introducing nonlinearity in Eqn. (2.2) the formulation using relative co-ordinates is particularly beneficial as the number of nonlinear equations it involves is proportional to the number of contact node-pairs. If expressed in other co-ordinate systems which do not include the local relative displacements, Eqn. (2.2) will in general, have twice the number of nonlinear equations i.e. proportional to the number of contact nodes. There are other advantages to choosing the relative co-ordinates which will become apparent in section 2.2.2.

2.1.3 Harmonic balance

The steady state solution of the dynamic Eqn. (2.1) can be obtained using a harmonic balance method (HBM) [34, 35, 38]. In HBM, the steady state displacements and nonlinear forces are assumed to be periodic. Hence, they are expressed as a sum of harmonic terms. As the harmonic functions are linearly independent, equating their coefficients yields a set of algebraic balance equations in the frequency domain for harmonic-indices $h = 0$ to $h = n_h$ at a frequency ω as follows:

$$\mathbf{D}^h \bar{\mathbf{q}}_r^h = \bar{\mathbf{f}}_E^h + \bar{\mathbf{f}}_C^h \tag{2.5}$$

where

$$\mathbf{D}^h \coloneqq \left[-(h.\omega)^2 \mathbf{M}_f + (ih\omega)\mathbf{C}_f + \mathbf{K}_f\right] \tag{2.6}$$

Eqn. (5.4) may be solved using a nonlinear algebraic equation solver which tries to optimize $\bar{\mathbf{q}}_r^h$ to obtain a zero residual. The iterative solver uses the alternating frequency time (AFT) procedure [34, 36, 37] in conjunction with a contact model. At each step of the solver, the Fourier coefficients of local relative displacements in the tangential ($\bar{\mathrm{u}}_{\mathrm{x,i}}^h$, $\bar{\mathrm{u}}_{\mathrm{y,i}}^h$) and normal ($\bar{\mathrm{v}}_{\mathrm{i}}^h$) directions are extracted for every node-pair i from the appropriate DoFs of $\bar{\mathbf{q}}^{\mathrm{h}}$. An Inverse Fast Fourier transform (IFFT) is employed to expand these coefficients into periodic functions in the time domain. These time displacements are then used in contact models to determine the local contact forces ($\bar{\mathrm{T}}_{\mathrm{x,i}}^h$, $\bar{\mathrm{T}}_{\mathrm{y,i}}^h$ and $\bar{\mathrm{N}}_{\mathrm{i}}^h$) which are converted back to the frequency domain using a Fast Fourier transform (FFT) . Once the procedure is carried out for every node-pair i, it is used to determine $\bar{\mathbf{f}}_C^h$ which is then used in Eqn. (5.4) to obtain $\bar{\mathbf{q}}_r^h$. Although this information is sufficient for the solver to converge to the solution, convergence rates may be greatly improved by adding the Jacobian of the residual of Eqn (5.4) as an input to the solver. This requires the contact model to also output the derivatives of the Fourier coefficients of the contact forces with respect to the Fourier coefficients of the relative displacements. Though the calculation of these derivatives has been implemented in this study, their calculation procedure is not shown here. The intricacies of such derivations may be found in

[38] and [87].

An arc-length continuation method [35] which uses a predictor-corrector approach, is used to determine the evaluation frequencies during the simulation run-time. This is more robust in tracking the actual response curve than pre-specifying frequency calculation points before simulation. A minimum frequency resolution is specified which limits how far apart two consecutive solution frequency points might be. In this analysis, it is assumed that the dynamics due to higher harmonics do not affect the 0^{th} harmonic static solution [38]. The displacement at static equilibrium $\bar{\mathbf{q}}_r^0$ represents the steady state static solution at ω i.e. the mean displacement over a period. It is the time-independent state about which the higher harmonics which represent the dynamics of the system may be solved. As shown in Fig. 2.3, this static solution may be calculated separately. $\bar{\mathbf{f}}_E^0$ is the vector of static forces applied to the system and in this analysis corresponds to nodal forces applied to the contact nodes normal to the contact surface to enforce the contact. These are balanced by static contact forces $\bar{\mathbf{f}}_C^0$ generated by the contact and the forces exerted due to the stiffness $\mathbf{K}_f$ of the system. $\bar{\mathbf{q}}_r^0$ is determined by solving the set of static nonlinear equations in Eqn. (5.6) which are obtained by substituting $h = 0$ in Eqns. (5.4) and (5.5).

2.1.4 Contact model

The contact conditions are enforced at the contacting surfaces by means of 2 independent nonlinear 1D contact models which capture the dynamics in mutually orthogonal directions at each contact node-pair. The models employed here were first developed in [88] and later used in [35, 89]. They are found to perform suitably well when compared to 2D contact models (which simultaneously model 2 directions of motion [35, 90–92]), while reducing the computational cost significantly. Tangential contact stiffnesses $\mathrm{k_{x,i}}$ and $\mathrm{k_{y,i}}$ and normal contact stiffnesses $\mathrm{k_{z,i}}$ are represented as 1D spring elements. w is the magnitude of slip. The normal contact forces $\mathrm{N_i}$ at node-pair i may be obtained as a function of their normal relative displacement $\mathrm{v_i}$ as shown in

Eqn. (2.7).

$$\mathrm{N_i}(t) = max\left(\mathrm{k_{z,i}}.\mathrm{v_i}(t), 0\right) \tag{2.7}$$

When the surfaces penetrate each other $\mathrm{v_i}$ is positive and $\mathrm{N_i}$ is non-zero [35]. Unlike in the sources cited for the contact model, the normal contact pre-stress is not included explicitly in Eqn. (2.7) because $\mathrm{v_i}(t)$ includes the static solution and indirectly accounts for the pre-stress. The tangential contact forces depend on the contact condition of the system as shown in Eqn. (2.8). Separation occurs at node-pair i when $\mathrm{N_i}(t) = 0$. If $\mathrm{N_i}(t)$ is positive the nodes are in contact and might be in stick or slip. The nodes are said to be in stick in the x-direction if $\mathrm{w_{x,i}}(t)$ remains constant i.e. $\dot{\mathrm{w}}_{\mathrm{x,i}}(t) = 0$ and similarly for the y-direction. If the nodes are not in separation or in stick, they are said to be in slip.

$$\mathrm{T_{x,i}}(t) = \begin{cases} \mathrm{k_{x,i}}\left(\mathrm{u_{x,i}}(t) - \mathrm{w_{x,i}}(t)\right) & \text{stick} \\ sign(\dot{\mathrm{w}}_{\mathrm{x,i}})\mu.\mathrm{N_i}(t) & \text{slip} \\ 0 & \text{separation} \end{cases} \tag{2.8}$$

The y-direction tangential forces may be obtained similarly. It is not possible to pre-determine the contact condition at each instant of time. Instead the model starts off with the assumption that the nodes are sticking at time $t = 0$ and eventually converges to the correct conditions over a period. Switching between the contact conditions involve several transition criteria which may be found in [35].

2.2 Model order reduction

2.2.1 Reduction methods

Figure 2.4 shows an outline of the reduction strategy employed in this study. As described in previous sections, HBM is used to generate the frequency response of the baseline blisk model. The objective is to obtain a reduction basis $\mathbf{\Phi}$, which might be employed to reduce the baseline model. The AMP procedure is employed to obtain this reduction, the details of which are explained

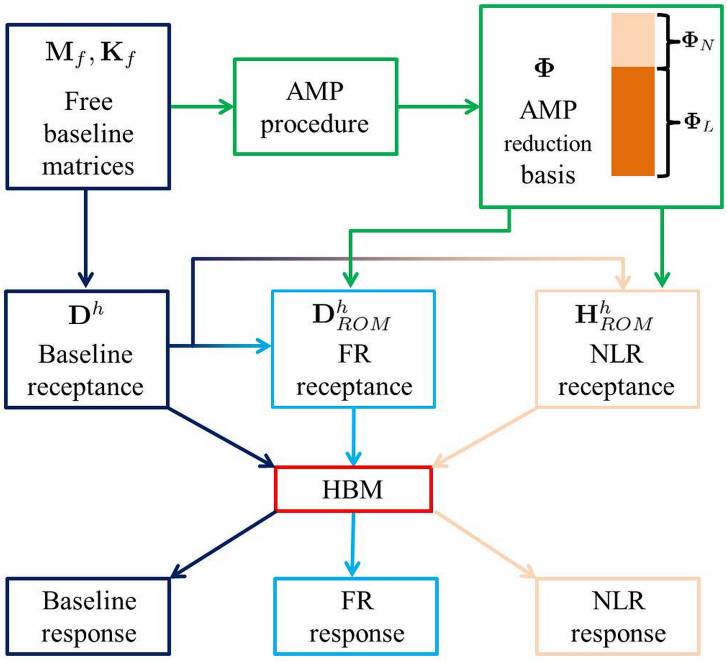

Figure 2.4. Reduction strategy

in section 2.2.2. As shown in Fig. 2.4, depending on whether, all the DoFs of the reduction basis are employed for reduction or only the nonlinear DoFs, different types of reduced order models (ROMs) are obtained. The formulation of and the difference between the two reduction techniques is now explained. It is possible to completely reduce all the DoFs of Eqn. (5.4) to a set of reduced co-ordinates $\mathbf{p}$ if one is able to obtain a reduction basis $\mathbf{\Phi}$ such that:

$$\mathbf{q} \approx \mathbf{q}_0 + \mathbf{\Phi}\mathbf{p} \tag{2.9}$$

Applying the reduction in Eqn. (2.9) to only the dynamics in Eqn. (5.4), one may obtain:

$$\mathbf{D}^h_{ROM}\bar{\mathbf{p}}^h = \bar{\mathbf{g}}^h_E + \bar{\mathbf{g}}^h_C \quad ; \quad (h \geq 1) \tag{2.10}$$

where

$$\mathbf{D}^h_{ROM} := \mathbf{\Phi}^{\mathrm{T}}\mathbf{D}^h\mathbf{\Phi} \tag{2.11}$$

$$\bar{\mathbf{g}}_E^h \coloneqq \mathbf{\Phi}^{\mathrm{T}} \bar{\mathbf{f}}_E^h \tag{2.12}$$

$$\bar{\mathbf{g}}_C^h \coloneqq \mathbf{\Phi}^{\mathrm{T}} \bar{\mathbf{f}}_C^h \tag{2.13}$$

This reduction is henceforth referred to as the full DoF reduction abbreviated as FR. The matrix equation in Eqn. (5.4) may be separated into two sets of equations, corresponding to the linear and nonlinear DoFs of $\mathbf{q}_r$ in Eqn. (2.2) as follows :

$$\begin{bmatrix} \mathbf{D}_{N,N}^h & \mathbf{D}_{N,L}^h \\ \mathbf{D}_{L,N}^h & \mathbf{D}_{L,L}^h \end{bmatrix} \begin{bmatrix} \bar{\mathbf{q}}_N^h \\ \bar{\mathbf{q}}_L^h \end{bmatrix} = \begin{bmatrix} \bar{\mathbf{f}}_{E,N}^h \\ \bar{\mathbf{f}}_{E,L}^h \end{bmatrix} + \begin{bmatrix} \bar{\mathbf{f}}_{C,N}^h \\ \mathbf{0} \end{bmatrix} \tag{2.14}$$

It may be seen from Eqn. (5.6) that the linear DoFs are completely determined by the nonlinear DoFs by the relationship:

$$\bar{\mathbf{q}}_L^h = \left(\mathbf{D}_{L,L}^h\right)^{-1} \left(-\mathbf{D}_{L,N}^h \bar{\mathbf{q}}_N^h + \bar{\mathbf{f}}_{E,L}^h\right) \tag{2.15}$$

Using Eqns. (5.6) and (2.15) one might describe the dynamics of the system only in terms of the nonlinear DoFs:

$$\mathbf{H}^h \bar{\mathbf{q}}_N^h = -\mathbf{D}_{N,L}^h \left(\mathbf{D}_{L,L}^h\right)^{-1} \bar{\mathbf{f}}_{E,L}^h + \bar{\mathbf{f}}_{E,N}^h + \bar{\mathbf{f}}_{C,N}^h \tag{2.16}$$

where

$$\mathbf{H}^h \coloneqq \left(\mathbf{D}_{N,N}^h - \mathbf{D}_{N,L}^h \left(\mathbf{D}_{L,L}^h\right)^{-1} \mathbf{D}_{L,N}^h\right) \tag{2.17}$$

The reduction basis may also be split into its linear and nonlinear DoFs:

$$\mathbf{\Phi} = \begin{bmatrix} \mathbf{\Phi}_N \\ \mathbf{\Phi}_L \end{bmatrix} \tag{2.18}$$

A reduction may be applied to only the nonlinear DoFs for the dynamics as follows:

$$\mathbf{q}_N \approx \mathbf{q}_{0,N} + \mathbf{\Phi}_N \mathbf{s} \tag{2.19}$$

Eqn. (2.19) may be substituted into Eqn. (2.16) to yield the reduced equations:

$$\mathbf{H}_{ROM}^{h}\bar{\mathbf{s}}^{h} = \bar{\mathbf{l}}_{E,L}^{h} + \bar{\mathbf{l}}_{E,N}^{h} + \bar{\mathbf{l}}_{C,N}^{h} \quad ; \quad (h \geq 1) \tag{2.20}$$

where

$$\mathbf{H}_{ROM}^{h} \coloneqq \mathbf{\Phi}_{N}^{\mathrm{T}}\mathbf{H}^{h}\mathbf{\Phi}_{N} \tag{2.21}$$

$$\bar{\mathbf{l}}_{E,L}^{h} \coloneqq -\mathbf{\Phi}_{N}^{\mathrm{T}}\mathbf{D}_{N,L}^{h}\left(\mathbf{D}_{L,L}^{h}\right)^{-1}\bar{\mathbf{f}}_{E,L}^{h} \tag{2.22}$$

$$\bar{\mathbf{l}}_{E,N}^{h} \coloneqq \mathbf{\Phi}_{N}^{\mathrm{T}}\bar{\mathbf{f}}_{E,N}^{h} \tag{2.23}$$

$$\bar{\mathbf{l}}_{C,N}^{h} \coloneqq \mathbf{\Phi}_{N}^{\mathrm{T}}\bar{\mathbf{f}}_{C,N}^{h} \tag{2.24}$$

This is referred to here as the nonlinear DoF reduction and abbreviated as NLR. As mentioned, the static solution is separately evaluated before and is not reduced in either FR or NLR. When nonlinear DoFs are captured by the reduction basis accurately, the NLR reduction is accurate while the FR reduction might not be accurate. This is because the FR reduction reduces the linear DoFs in addition to the nonlinear DoFs. In other words, the approximation made in Eqn. (2.9) is a stronger condition than the approximation made in Eqn. (2.19). However, NLR is also comparatively slower than FR per iteration as it involves the inversion of a full matrix $\mathbf{D}_{L,L}^{h}$ in Eqns. (2.16), (2.17) and (2.22). This comparison does not consider the convergence rates of the two procedures and it is possible for NLR to be faster over a range of frequencies under certain circumstances. This trade-off is analyzed in detail later.

Another important point to note is that in both cases, the reduced co-ordinates must be expanded back to obtain the local displacements during the AFT procedure. However, the nonlinear solver handles only the reduced co-ordinates which accounts for the bulk of the computational effort saved. Although, it might be possible to reduce the contact model itself to some set of reduced co-ordinates, this is beyond the scope of this study. It is possible that such a reduction can lead to significant improvement in simulation time over a large number of iterations. However, since

most of the operations involved in the contact model are comparators and linear operators, which are much faster than the rest of the HBM procedure, the time savings offered by them will be proportionally smaller to those offered by DoF reduction for a fixed number of iterations.

2.2.2 Calculation of AMP modes

Microslip is a nonlinear phenomenon which is a result of the spatial variation of contact conditions across the contacting surfaces. One may imagine an extreme case in which the conditions are such that all the nodes at the interfaces are stuck at all times. In this case, none of the nonlinearities of Eqns. (2.7) and (2.8) are activated at any time. The slip is always zero in all tangential directions and contact is never lost. In effect, the nonlinear blisk system behaves in the same manner as that of a linear system with the contact nodes permanently joined by stiffness elements. Such a stuck system will have the stiffness matrix:

$$\mathbf{K}_{st} = \mathbf{K}_f + \Delta\mathbf{K}_{st} \tag{2.25}$$

In the relative co-ordinate system, $\Delta\mathbf{K}_{st}$ is a diagonal matrix with entries equaling contact stiffnesses at the corresponding nonlinear contact DoFs and zeros everywhere else:

$$\Delta\mathbf{K}_{st} \coloneqq \begin{bmatrix} \ddots & \ddots & \ddots & \cdots & \cdots & \cdots & \cdots & \cdots & \cdots & \vdots \\ \vdots & 0 & \mathrm{k_{x,i}} & 0 & \cdots & \cdots & \cdots & \cdots & \cdots & \vdots \\ \vdots & \vdots & 0 & \mathrm{k_{y,i}} & 0 & \cdots & \cdots & \cdots & \cdots & \vdots \\ \vdots & \vdots & \vdots & 0 & \mathrm{k_{z,i}} & 0 & \cdots & \cdots & \cdots & \vdots \\ \vdots & \vdots & \vdots & \vdots & \ddots & \ddots & \ddots & \cdots & \cdots & \vdots \\ \vdots & \vdots & \vdots & \vdots & \vdots & \ddots & \mathrm{k_{z,n_N}} & \ddots & \cdots & \vdots \\ \vdots & \vdots & \vdots & \vdots & \vdots & \vdots & \ddots & 0 & \ddots & \vdots \\ \vdots & \vdots & \vdots & \vdots & \vdots & \vdots & \vdots & \ddots & \ddots & \vdots \\ 0 & \cdots & \cdots & \cdots & \cdots & \cdots & \cdots & \cdots & \cdots & 0 \end{bmatrix} \tag{2.26}$$

This diagonal form of $\Delta\mathbf{K}_{st}$ is another advantage of choosing the relative co-ordinates and plays an important role in keeping the calculation simple and reducing computational redundancy. The contact condition does not affect the mass of the system and hence the mass matrix remains the same as that of the free system for the stuck system.

$$\mathbf{M}_{st} = \mathbf{M}_f \tag{2.27}$$

One may envision several intermediate linear systems between the free and the stuck systems which correspond to different contact boundary conditions at different nodes. A stuck node-pair has all three contact stiffnesses present. Slipping in a particular tangential direction may be thought of as removing the tangential stiffness element between the nodes in that direction altogether. Separation at a node-pair may be represented by removing all three stiffnesses between the nodes. Thus, a simple masking process may be carried out on $\Delta\mathbf{K}_{st}$ by either retaining a particular stiffness along the diagonal or zeroing it based on the boundary condition. Every masking operation will correspond to a linear system in the microslip regime with unique spatial contact conditions where nodes are in stick, slip or separation for all time. It is postulated that the modes of these intermediate linear systems with constant boundary conditions will, in unison, be able to capture the complex nonlinear dynamics wherein the contact conditions keep changing constantly. However, there are exponentially many possible boundary conditions and choosing them randomly might not yield the required basis. Instead, a method to predict boundary conditions which are representative of the contact behavior is proposed . To do so, the stuck system analyzed first as follows:

$$\mathbf{K}_{st}\mathbf{\Psi}_{st} = \mathbf{M}_{st}\mathbf{\Psi}_{st}\mathbf{\Lambda}_{st} \tag{2.28}$$

The modes of the stuck system in the frequency range of interest can be obtained by solving the generalized eigenvalue problem posed in Eqn. (2.28) where $\mathbf{\Psi}_{st} = [\psi_{st,1} \ \ldots \psi_{st,\alpha}]$ is the matrix consisting of the α mass normalized modes of the system which are expected to respond to the

excitation the system is subjected to. $\mathbf{\Lambda}_{st} = diag\left([\lambda_{st,1} \dots \lambda_{st,\alpha}]\right)$ is the diagonal matrix of the corresponding eigenvalues. Next, normal and tangential force estimate vectors $(\hat{\mathbf{N}}, \hat{\mathbf{T}})$ at the contact interfaces are calculated by considering an artificial modal displacement $\hat{\mathrm{p}}$ along a stuck mode in the frequency range of interest $\psi_{st,\mathrm{j}}$, where $\mathrm{j} \in \{1, 2, \dots, \alpha\}$ as follows:

$$\hat{\mathbf{N}}(\hat{\mathrm{p}}, \mathrm{j}) = \mathbf{N}_0 + \mathbf{k}_{\mathrm{z}} \circ (\psi_{st,\mathrm{j,z}}\, \hat{\mathrm{p}}) \tag{2.29}$$

$$\hat{\mathbf{T}}_{\mathrm{x}}(\hat{\mathrm{p}}, \mathrm{j}) = \mathbf{k}_{\mathrm{x}} \circ (\psi_{st,\mathrm{j,x}}\, \hat{\mathrm{p}}) \tag{2.30}$$

where $\mathbf{N}_0 = \overline{\mathbf{f}}^0_{C,N,\mathrm{z}}(\mathbf{q}_0)$ is a vector of static normal contact forces which may be extracted from the converged static solution. $\mathbf{k}_{\mathrm{z}} = [\mathrm{k}_{\mathrm{z},1}\mathrm{k}_{\mathrm{z},2} \dots \mathrm{k}_{\mathrm{z,i}} \dots]^{\mathrm{T}}$ and $\mathbf{k}_{\mathrm{x}} = [\mathrm{k}_{\mathrm{x},1}\mathrm{k}_{\mathrm{x},2} \dots \mathrm{k}_{\mathrm{x,i}} \dots]^{\mathrm{T}}$, i being the node-pair or DoF index, represent contact stiffness vectors. The symbol $\circ$ represents the entry-wise Hadamard or Schur product of vectors. The stiffness matrix of the linear system corresponding to the predicted microslip boundary condition which itself is a function of $\hat{\mathrm{p}}$ and stuck mode-index j is given by:

$$\mathbf{K}_{ms}(\hat{\mathrm{p}}, \mathrm{j}) = \mathbf{K}_f + \Delta\mathbf{K}_{ms}(\hat{\mathrm{p}}, \mathrm{j}) \tag{2.31}$$

where $\Delta\mathbf{K}_{ms}(\hat{\mathrm{p}}, \mathrm{j})$ is obtained by a simple masking procedure carried out node-wise on the diagonal elements of $\Delta\mathbf{K}_{st}$ as follows:

$$(\Delta\mathbf{K}_{ms})_{3\mathrm{i}-2,3\mathrm{i}-2} \coloneqq \begin{cases} \mathrm{k}_{\mathrm{x,i}} & \text{if} \quad (\hat{\mathbf{T}}_{\mathrm{x}})_{\mathrm{i}} \leq \mu(\hat{\mathbf{N}})_{\mathrm{i}} \quad \text{i.e. stick at DoF i} \\ 0 & \text{if} \quad (\hat{\mathbf{T}}_{\mathrm{x}})_{\mathrm{i}} > \mu(\hat{\mathbf{N}})_{\mathrm{i}} \quad \text{i.e. slip at DoF i} \end{cases} \tag{2.32}$$

$$(\Delta\mathbf{K}_{ms})_{3\mathrm{i},3\mathrm{i}} \coloneqq \begin{cases} \mathrm{k}_{\mathrm{z,i}} & \text{if} \quad (\hat{\mathbf{N}})_{\mathrm{i}} \geq 0 \quad \text{i.e. contact at DoF i} \\ 0 & \text{if} \quad (\hat{\mathbf{N}})_{\mathrm{i}} < 0 \quad \text{i.e. separation at DoF i} \end{cases} \tag{2.33}$$

For a general mistuned blisk the boundary conditions are evaluated at every node-pair i on all the contact-surfaces of the blisk. Tuned cyclically symmetric systems in general, may exhibit localized responses due to nonlinearity. However, no such intrinsically localized modes (ILMs) were found

in the cases used for the study, at least in the regime of microslip under investigation. Hence, for a tuned blisk, the boundary conditions are assumed to be cyclically symmetric for all the cases studied here. i.e. the boundary conditions evaluated for the first sector are enforced at all the sectors. If localized response is expected from a tuned baseline case, then that localized response may be captured by including reduction modes with multiple nodal diameters as opposed to a single nodal diameter by choosing the appropriate stuck modes for the AMP generation process. Alternatively, the symmetric boundary condition requirement may be relaxed and the AMP modes may be evaluated in a procedure similar to the one employed for a mistuned system. The linear system corresponding to the microslip boundary condition specified by $\hat{\mathrm{p}}$ and j may be represented as:

$$\mathbf{K}_{ms}\boldsymbol{X}_{ms} = \mathbf{M}_{st}\boldsymbol{X}_{ms}\boldsymbol{\Lambda}_{ms} \tag{2.34}$$

The corresponding matrix of mass normalized modes may be expanded as:

$$\boldsymbol{X}_{ms} = \boldsymbol{X}_{ms}(\hat{\mathrm{p}},\mathrm{j}) = [\chi_1(\hat{\mathrm{p}},\mathrm{j})\ldots\chi_\alpha(\hat{\mathrm{p}},\mathrm{j})] \tag{2.35}$$

The equations for the local y-direction are similar to those for the local x-direction and may be obtained by replacing subscript 'x' with 'y' in Eqns. (2.30) and (2.32) and changing the masking index on the diagonal of $\Delta\mathbf{K}_{ms}$ from $3\mathrm{i}-2$ to $3\mathrm{i}-1$ in Eqn. (2.32). In the interest of brevity the function arguments $\hat{\mathrm{p}}$ and j have been dropped in Eqns. (2.32) to (2.34). Eqn. (2.34) is solved and the appropriate modes $\boldsymbol{X}_{ms}$ are included in the reduction basis. The procedure is repeated for other stuck-modes of interest $\psi_{st,\mathrm{j}}$ and a range of values for the modal amplitude $\hat{\mathrm{p}} = \hat{\mathrm{p}}_\mathrm{k}$ where $\mathrm{k} \in \{1,2,\ldots,\beta\}$. $\hat{\mathrm{p}}$ can take both positive and negative values. These values of $\hat{\mathrm{p}}$ are a user-supplied input to the AMP generation process. $\hat{\mathrm{p}} = 0$ corresponds to the static condition of the system ($h = 0$ solution) which is usually the same as the stuck system when $\mathbf{N}_0 > 0$ at all DoFs. Increasing the magnitude of $\hat{\mathrm{p}}$ in either the positive or negative direction eventually correspond to boundary conditions which represent slip and ultimately separation when $\hat{\mathrm{p}}$ becomes high enough.

The AMP reduction basis consists of the columns of matrices $\boldsymbol{X}_{ms}(\hat{\mathrm{p}}, \mathrm{j})$ which are referred to as the AMP modes:

$$\begin{aligned}\boldsymbol{\Phi} \coloneqq [\boldsymbol{X}_{ms}(\hat{\mathrm{p}}_1, 1) \dots \boldsymbol{X}_{ms}(\hat{\mathrm{p}}_1, \alpha) \boldsymbol{X}_{ms}(\hat{\mathrm{p}}_2, 1) \dots \boldsymbol{X}_{ms}(\hat{\mathrm{p}}_2, \alpha) \dots \\ \dots \boldsymbol{X}_{ms}(\hat{\mathrm{p}}_{\beta-1}, \alpha) \boldsymbol{X}_{ms}(\hat{\mathrm{p}}_\beta, 1) \dots \boldsymbol{X}_{ms}(\hat{\mathrm{p}}_\beta, \alpha)]\end{aligned} \tag{2.36}$$

To choose practical values of $\hat{\mathrm{p}}$, a maximum value of $|\hat{\mathrm{p}}| = |\hat{\mathrm{p}}|_{max}$ is choosen first to reflect the expected response of the blisk. This is a value the user can estimate from a variety of sources such as conservative linear estimations which depend on material damping (amongst other factors such as contact stiffness) and forcing level. Then the range of values between $-|\hat{\mathrm{p}}|_{max}$ and $|\hat{\mathrm{p}}|_{max}$ is sampled (either uniformly or in some other manner, e.g., with more samples near 0 than near $\pm|\hat{\mathrm{p}}|_{max}$) to create the vector of chosen $\hat{\mathrm{p}}$ values. Then, boundary conditions are generated corresponding to the chosen values of $\hat{\mathrm{p}}$. It may be observed that for some particular stuck mode $\psi_{st,\mathrm{j}}$ the boundary conditions arising out of two different values of $\hat{\mathrm{p}}$ might be the same. Non-unique boundary conditions may also arise from applying different values of $\hat{\mathrm{p}}$ to different stuck modes in the AMP procedure. Since the boundary conditions are applied to the full system, care must be taken to eliminate such duplicate conditions and retain only those values of $\hat{\mathrm{p}}$ which generate unique boundary conditions; otherwise the AMP basis may be rank deficient. The boundary conditions can be generated and checked for uniqueness very fast. Hence, it is computationally easy and inexpensive to initially choose a large number of potential $\hat{\mathrm{p}}$ values (i.e., oversampling $\hat{\mathrm{p}}$) first and then selecting only those values of $\hat{\mathrm{p}}$ which correspond to unique boundary conditions. Those fewer values of $\hat{\mathrm{p}}$ are used for the actual AMP mode generation.

If several chosen values of $\hat{\mathrm{p}}$ (for the same stuck mode) are too close to each other, the boundary conditions generated from them might be unique but still lead to a $\boldsymbol{\Phi}$ which is nearly rank deficient. Such a situation might also arise from boundary conditions generated from different stuck modes which are very similar to each other (e.g. they differ in the contact state at only a few nodes). That is, even when care is taken to exclude non-unique boundary conditions, it is possible to obtain

very similar boundary conditions from the AMP procedure which differ in the contact status at only a few nodes. Such a situation might lend to an ill conditioned $\mathbf{\Phi}$. This is especially true for mistuned cases where boundary conditions might change in the $\hat{\mathrm{p}}$-space node-wise as opposed to a tuned case where boundary conditions at each sector change identically with $\hat{\mathrm{p}}$. Poor conditioning often leads to convergence problems and must be avoided whenever possible. In such a case the AMP basis may be further conditioned by obtaining a singular value decomposition of all the AMP modes as follows [93–95]:

$$\mathbf{U}_{\mathbf{\Phi}}\mathbf{S}_{\mathbf{\Phi}}\mathbf{V}_{\mathbf{\Phi}}^{\mathrm{T}} = \mathbf{\Phi} \tag{2.37}$$

$$\mathbf{\Phi}_{cond} \coloneqq \mathbf{U}_{\mathbf{\Phi},\gamma} \tag{2.38}$$

Instead of eliminating individual vectors in the basis $\mathbf{\Phi}$ to improve conditioning, vectors are selected from the left singular vector matrix $\mathbf{U}_{\mathbf{\Phi}}$. These vectors span the same space as $\mathbf{\Phi}$, but are ordered according to the magnitude of their corresponding singular values (in the diagonal matrix $\mathbf{S}_{\Phi}$). The conditioning of the matrix refers to the ratio of the maximum singular value in $\mathbf{S}_{\mathbf{\Phi}}$ and the minimum singular value retained. To ensure good conditioning this ratio is chosen such that it lies below a user defined threshold. As this ratio decreases the number of conditioned basis vectors retained γ also decreases. The conditioned AMP reduction basis $\mathbf{\Phi}_{cond}$ may be substituted for $\mathbf{\Phi}$ in the equations of FR and NLR reductions.

2.3 Results

2.3.1 Baseline model

For the purposes of this study, a sector model of the blisk containing an individual blade attached to a disk sector was developed first in ANSYS® as shown in Fig. 2.5. The sector model is comprised of 6052 nodes and 14134 elements. A full blisk model, also shown in Fig. 2.5, was

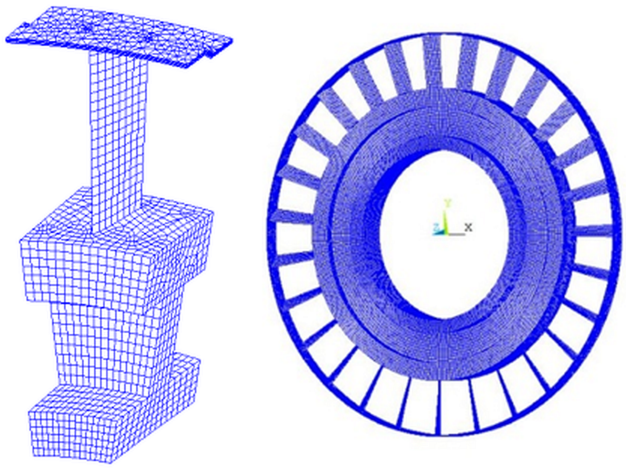

Figure 2.5. FE models of sector and full blisk

developed from the sector model by arranging 27 sector models contiguously around the blisk's central axis and merging the coincident nodes on the adjacent faces of the disk portions of the sector models. Unlike the disk surfaces in the full model, there are other surfaces at the shrouds shown in detail in Fig. 2.6, which also touch, but are designed to be in contact rather than be contiguous. The contacting nodes on these surfaces are not merged but instead form a set of co-incident nodes in contact as in Fig. 2.2. There are 25 pairs of these nodes at each contacting surface pair and 27 such surface pairs across the model. It must be noted that no contact elements are introduced in this FE model. This is a free model where gross penetration or separation of the contacting surfaces is permitted. The blades of all the sectors are modeled with the same elastic material stiffness for the tuned blisk. For the generation of the mistuned blisk, the blade material stiffnesses at the sectors are varied with a standard deviation of 4% around an average stiffness which is the same as that of the tuned case. A rotational velocity about the axial direction is applied to the blisk. Then, a pre-stressed linear static analysis is carried out to obtain the equilibrium position of the free structure. Contact pre-stresses cannot be included at this stage of the analysis with the free model. They are applied later with contact models in MATLAB®. After recording the equilibrium position, the co-ordinates of the structural model are updated. To facilitate analysis and model development the

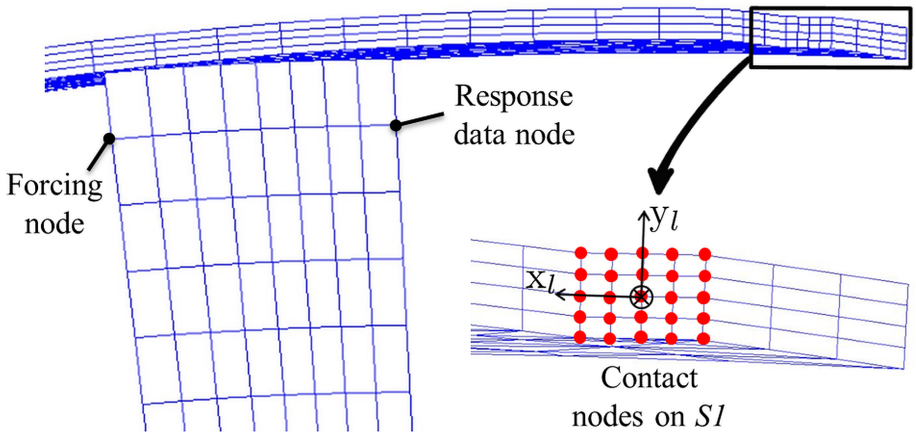

Figure 2.6. Shroud and contact patch

size of the linear model is reduced by conducting CB-CMS sub-structuring analysis of the updated structure in ANSYS® . Well established in the literature, CB-CMS and was originally developed in [8] and [9] and has been subsequently used extensively for modeling of blisks [10, 35, 38, 84]. It involves retaining a certain number of interface DoFs corresponding to specifically chosen master nodes of the full model, while reducing the dynamics rest of the DoFs into a reduced set of orthogonal slave modes. The master nodes selected for this analysis include the ones on the contacting surfaces, in addition to certain nodes near the blade tip where the structure is to be forced externally and the response is to be calculated. The locations of these nodes are shown for a single sector in Fig. 2.6. The master DoFs are chosen in a circularly symmetric fashion around the model i.e. if a node in a certain sector is a master node; the corresponding nodes in all other sectors are also master nodes. After CB-CMS analysis, the mass $\mathbf{M}_f$ and stiffness $\mathbf{K}_f$ matrices of the free system are extracted in the basis of the relative co-ordinates $\mathbf{q}_r$ shown in Eqn. (2.2). These are exported to MATLAB® where the rest of the analysis is carried out. For this study, it is assumed that $\mathbf{C}_f$ is proportional to $\mathbf{K}_f$.

The 1D contact models discussed earlier are applied at each node-pair and the set of nonlinear equations obtained are considered the full order baseline CB-CMS nonlinear system. Although

this baseline contains reduced linear DoFs, it retains all the nonlinear DoFs of contact from the FE model. To simulate the contact pre-stresses due to thermal effects, design interferences and other factors, a vector of constant normal forces $\bar{\mathbf{f}}_E^0 = \mathbf{f}_\mathrm{p}$ is applied on the contact nodes. The static displacement $\mathbf{q}_0$ due to this pre-stress and the ensuing normal contact forces $\mathbf{N}_0$ are calculated. A representative normal contact force magnitude due to the pre-stress $|\mathbf{F0}|$ may be defined as the sum of all entries of $\mathbf{N}_0$ i.e. $|\mathbf{F0}| = \sum_i \mathrm{N}_{0,\mathrm{i}}$, where i is the node-pair index. The dynamic excitation force vector determines the first harmonic of external forcing $\bar{\mathbf{f}}_E^1$. The higher harmonics of $\bar{\mathbf{f}}_E^h$ are zero vectors. In this work, an engine order (EO) excitation is used. A traveling wave excitation is applied axially at preselected nodes near the blade tip which are selected in a circularly symmetric manner. The EO represents the number of peaks of forcing that pass across each blade per revolution. Alternatively, it is the number of peaks the spatial forcing function has at any instant of time. The forcing amplitude is represented by $|\mathbf{F}|$. The baseline model is solved with HBM. A trust region algorithm is used for solving the algebraic balance equations. The amplitude of the periodic response at any excitation frequency along the axial direction of the blisk obtained after the HBM solution at each response data node is denoted by $|\mathbf{X}|$.

The system is then reduced by generating AMP modes and using the reduction basis to either employ FR or NLR reduction. The SVD filtering is carried out wherever necessary. The normalized response $|\mathbf{X}|/|\mathbf{F}|$ of systems with friction damping, is dependent on the level of microslip in the system. The dimensionless parameter $\mu|\mathbf{F0}|/|\mathbf{F}|$ is one of the metrics which has been used to study the dynamic response at various levels of microslip [30, 35, 88]. For a sufficiently high value of this parameter, the nonlinear system is fully stuck at all times and its response is the same as the corresponding stuck linear system. As the value of the parameter decreases, more nodes tend to enter slip. Hence, normalized blisk responses are analyzed for different values of this dimensional parameter to study the response of the system at different levels of microslip. The values of the input parameters such as μ, $\mathbf{f}_\mathrm{p}$ and $|\mathbf{F}|$ are adjusted based on the desired level of microslip and the corresponding magnitude of $\mu|\mathbf{F0}|/|\mathbf{F}|$.

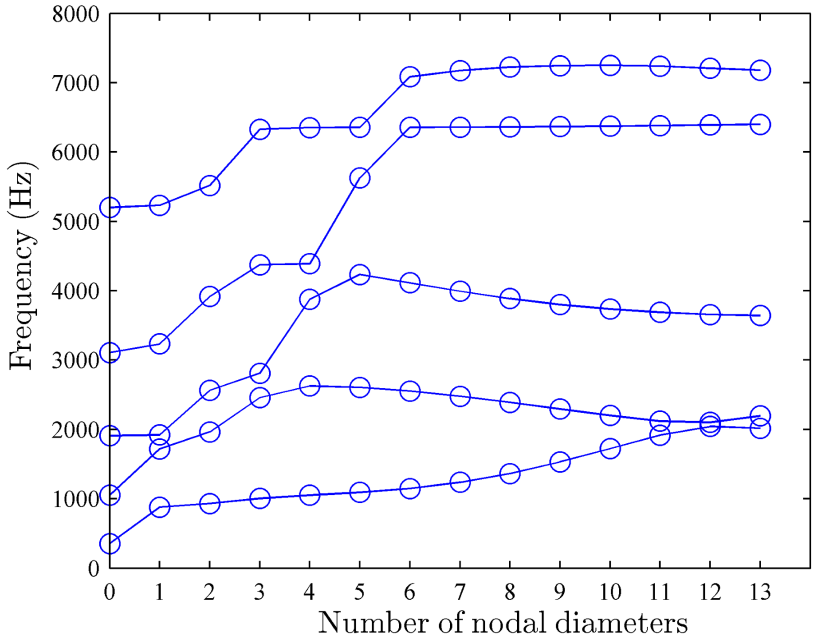

Figure 2.7. Frequency vs number of nodal diameters plot for stuck tuned blisk

2.3.2 ROMs for tuned blisk model

This section involves the comparison between the ROMs generated by using the AMP procedure and the baseline model. The natural frequencies of the linear stuck system are plotted versus the number of nodal diameters (ND) exhibited by their corresponding modes $\psi_{st,\mathrm{j}}$'s in Fig. 2.7. For the tuned system the natural frequencies are repeated (except for ND 0 modes) and thus each frequency has two modes (called a mode-pair) with the same ND associated with it. A mode-pair is excited by a forcing with the same EO as its ND and by higher EO= jn_s±ND where j is any integer and n_s is the number of sectors. Thus, for this system with $n_s = 27$ a ND 1 mode-pair may be excited by forcing with EO 1, EO 26, EO 28 and so on. Each line in Fig. 2.7 passing through frequencies of mode-pairs of all NDs is said to correspond to a family of modes. It may be observed that the second and third families in Fig. 2.7 exhibit a softening behavior as the number of ND increases. This softening behavior in the second and third families (for the stuck tuned blisk) arises out of the interaction between adjacent parts of the shrouds. Although, higher harmonics

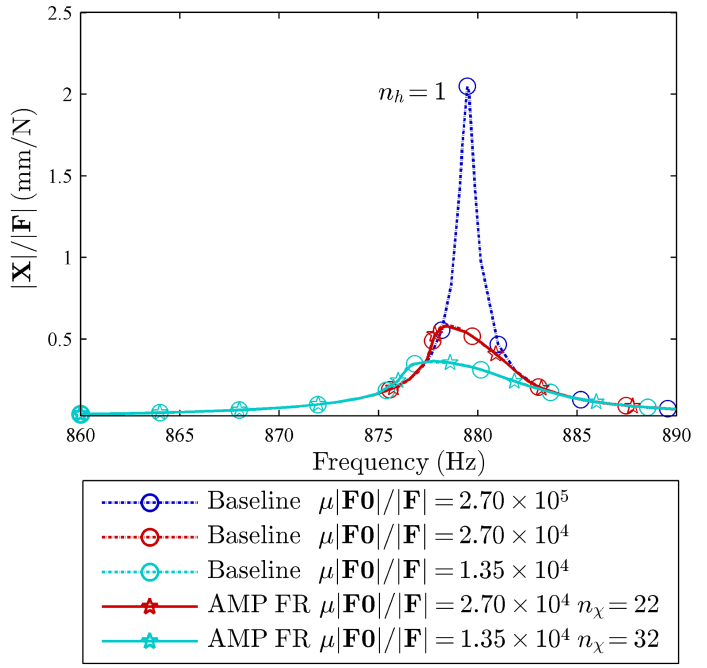

Figure 2.8. Engine order 1 AMP ROM responses

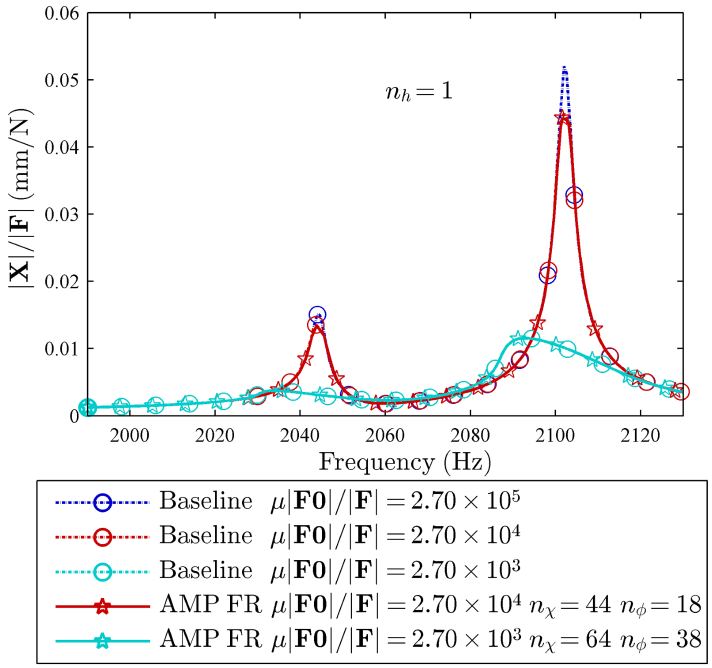

Figure 2.9. Engine order 12 AMP ROM responses

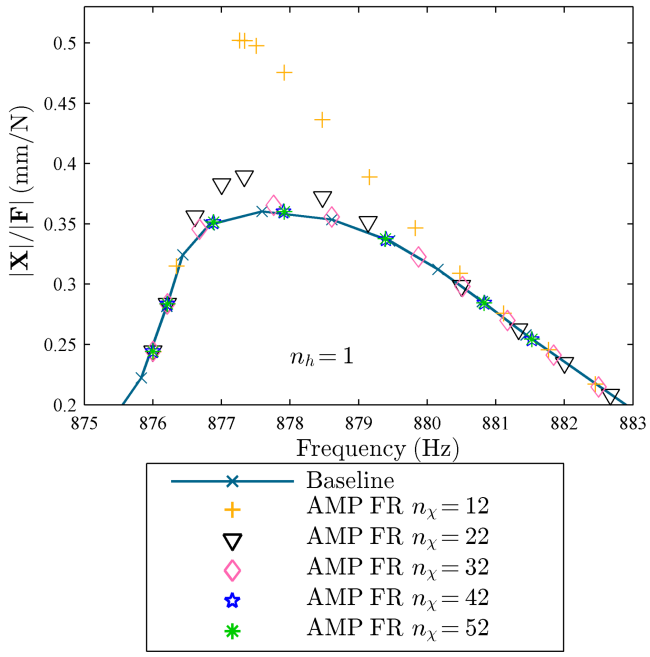

Figure 2.10. ROM (based on full reduction AMP) responses for different AMP basis sizes, EO 1 response, $\mu|\mathbf{F0}|/|\mathbf{F}| = 1.35 \times 10^4$

do also contribute to the response, the contribution of the first harmonic to the response dominates in systems with weak nonlinearities such as friction damping [96]. Thus, the accuracy with which the AMPs capture the first harmonic response is quite significant. In the tuned case, two unconditioned AMP modes are generated from a single boundary condition. Each boundary condition is determined from either one of the two tuned stuck modes which are clocked versions of each other. The same estimated amplitude levels (i.e., $\hat{\mathrm{p}}$ values) are applied to a pair of stuck modes and only the unique boundary conditions arising from the AMP procedure applied to both tuned stuck modes are retained. No discrimination is made between the boundary conditions arising from one stuck mode of the pair or the other. The boundary conditions for several $\hat{\mathrm{p}}$ values applied to a mode can yield the same boundary conditions (e.g., due to mesh resolution and other factors). The highest such $\hat{\mathrm{p}}$ value which corresponds to each boundary condition are retained. The unconditioned AMP modes correspond to the AMP modes generated from these boundary conditions arranged in ascending order of the value of (maximum) $\hat{\mathrm{p}}$ at which the boundary condition was observed for a

particular generating mode. Hence, the number of unconditioned modes generated from a family of stuck modes is referred to as n_χ. If SVD conditioning is applied to the basis, the number of conditioned modes is referred to as n_ϕ.

The normalized responses for both the baseline model and the ROMs using FR reduction for a single harmonic HBM ($n_h = 1$) are shown in Figs. 2.8 and 2.9. The markers on the figures are provided as a visual aid to differentiate between the lines and do not represent all the calculated frequency points. The response of the baseline model for $\mu|\mathbf{F0}|/|\mathbf{F}| = 2.70 \times 10^5$ for both EO 1 and 12 excitation corresponds to a fully stuck linear case. Developing ROMs for the stuck cases would be trivial and the baseline stuck responses are shown here only for purposes of comparison. The stuck frequency response peak at 880 Hz for EO 1 excitation matches the natural frequency of the first family at ND 1 in Fig. 2.7. Similarly, the peaks at 2044 Hz and 2102 Hz for the EO 12 case match the frequencies of the first two families for ND 12. The response amplitudes at all 27 response data nodes (in every blisk sector) are always identical in the tuned case due to circular symmetry. Hence, only responses from the first sector are plotted. The corresponding stuck mode-pairs are used to generate the AMPs using the procedures detailed before. Responses for the ROMs as well as the baseline are plotted for 2 different levels of microslip for every EO excitation case. For EO 1, 22 and 32 unconditioned AMP reduction modes are employed in the ROMs for $\mu|\mathbf{F0}|/|\mathbf{F}| = 2.70 \times 10^4$ and 1.35×10^4 respectively. For the EO 12 case where 2 mode-pairs from different families are excited in the frequency range under consideration, the response is more complex. This necessitates SVD filtering and more AMPs are used for reduction in the higher slip case. For the $\mu|\mathbf{F0}|/|\mathbf{F}| = 2.70 \times 10^4$ case, 18 AMPs were obtained by conditioning a basis of 44 unconditioned modes, 22 unconditioned modes generated from each of the 2 stuck mode pairs. For the $\mu|\mathbf{F0}|/|\mathbf{F}| = 2.70 \times 10^3$ case, 32 unconditioned AMPs were generated from stuck modes of each family to obtain an unconditioned basis of 64 modes which were conditioned to obtain the final basis of 38 AMPs. The ratio of largest and smallest singular values used for conditioning in both cases was 10^4. The number of AMPs used for reduction are determined here on an empirical

basis. Hence, it is possible that fewer number of AMPs than used here might be able to capture the response with the desired accuracy. Empirically choosing the number of AMPs used for reduction is feasible because adding a few more AMPs to the reduction basis than those strictly required for a particular microslip case is generally not prohibitive in terms of computational cost as will be shown later.

However, a more systematic method of determining the required number of AMPs is to conduct a convergence study as shown in Figs. 2.10 - 2.12. Figure 2.10 shows responses of both the baseline and ROMs to EO 1 excitation at $\mu|\mathbf{F0}|/|\mathbf{F}| = 1.35 \times 10^4$ near the peak frequency. No SVD conditioning is employed to calculate the AMPs here. The percentage absolute error in response for the ROMs at peak amplitude (resonance) when compared to the full order baseline is plotted versus the number of AMP modes employed for FR reduction in Fig. 2.11. It is seen that the error decreases monotonically as the number of reduction AMP modes increase upto 42 AMPs, at which point the solution has converged. This behavior is convenient for the determination of a suitable ROM using an iterative procedure where the number of AMPs might be increased at each iteration until the difference in error between subsequent iterations falls below a certain threshold. One may wish to trade-off accuracy with speed in their choice of the number of modes to include in the AMP basis. The responses for different NLR ROMs are not shown here to keep the discussion brief. However, Fig. 2.12 shows the absolute response error for NLR ROMs versus the baseline with different number of AMPs in the reduction bases, for the same conditions as those in Fig. 2.11. It is seen that when 12 AMPs are used, the NLR reduction is nearly 4% more accurate than FR reduction. With 22 AMPs and above, the error is essentially the same for both reduction methods.

The convergence in displacement at the response node with number of AMPs for EO 12 excitation at $\mu|\mathbf{F0}|/|\mathbf{F}| = 2.70 \times 10^3$ is shown in Fig. 2.13. The number of unconditioned modes n_χ from which the conditioned basis was generated is shown as the sum of AMP modes generated from boundary conditions predicted by the 1^{st} and 2^{nd} family ND 12 stuck modes. The conditioning criterion of singular value ratio was maintained at 10^4 for all cases. It is seen that if AMP modes

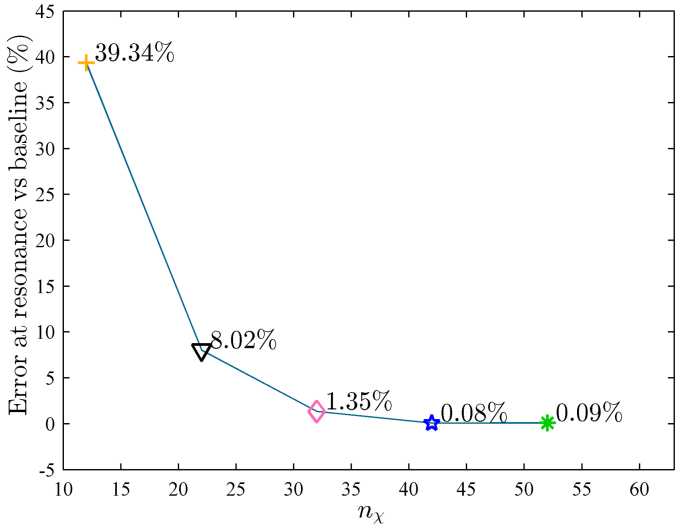

Figure 2.11. FR ROM error vs no. of amps, EO 1 response, $\mu|\mathbf{F0}|/|\mathbf{F}| = 1.35 \times 10^4$

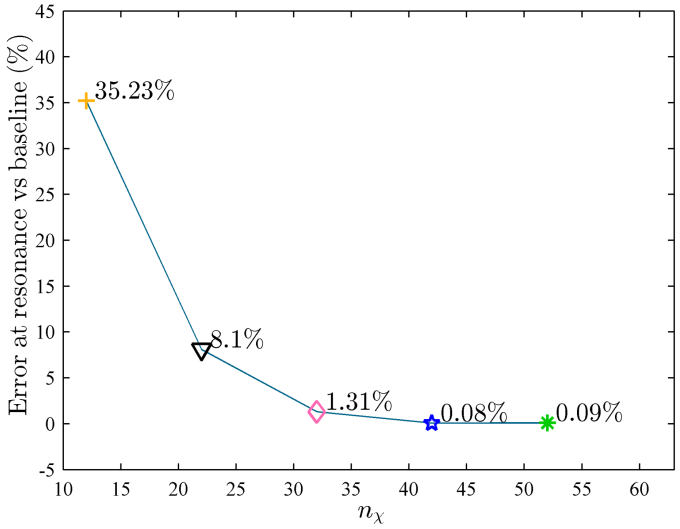

Figure 2.12. NLR ROM error vs no. of amps, EO 1 response, $\mu|\mathbf{F0}|/|\mathbf{F}| = 1.35 \times 10^4$

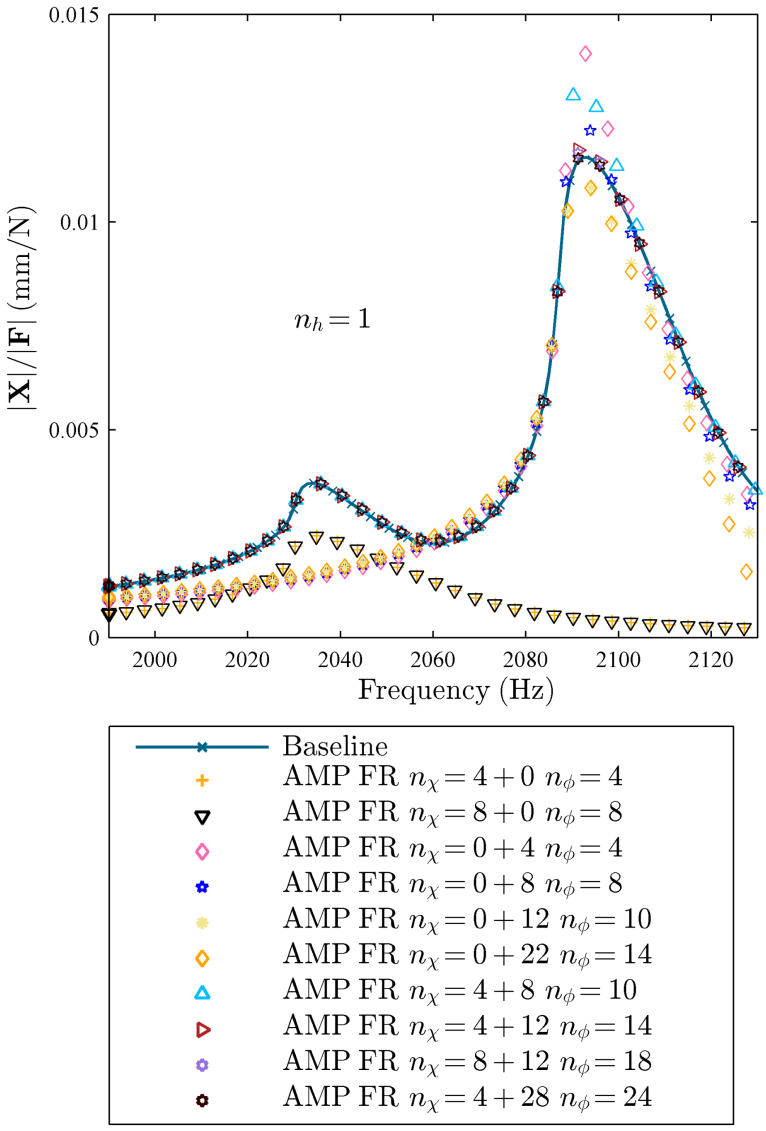

Figure 2.13. FR ROM responses for different AMP basis sizes, EO 12 response, $\mu|\mathbf{F0}|/|\mathbf{F}| = 2.70 \times 10^3$

generated exclusively from either the 1^{st} and 2^{nd} families are used, the ROMs display resonance near only the frequency of the corresponding family and the amplitude converges to incorrect values with increase in the number of modes. Inclusion of AMPs generated from stuck modes of both families in the ROMs causes them to capture both resonances and converge to the correct amplitude levels. The errors in the ROMs versus the baseline response at both resonances are listed in Table 2.1. Figure 2.14 shows the applicability of AMP modes to higher harmonics. It considers

Table 2.1. Errors at resonances ROM (based on full reduction AMP) vs. baseline, EO 12 excitation, $\mu|\mathbf{F0}|/|\mathbf{F}| = 2.70 \times 10^3$

n_χ from 1^{st} fam.	n_χ from 2^{nd} fam.	n_ϕ	error at 1^{st} resonance (2034.2 Hz)(%)	error at 2^{nd} resonance (2093.2 Hz)(%)
4	0	4	33.73	96.18
8	0	8	34.33	96.22
0	4	4	61.05	21.59
0	8	8	59.92	7.03
0	12	10	58.84	5.41
0	22	14	58.55	5.58
4	8	10	0.64	14.98
4	12	14	0.52	1.64
8	12	18	0.32	1.31
4	28	24	0.54	0.28

a case with the same parameters as in Fig. 2.10. The baseline $n_h = 1$ simulation has an amplitude difference of 7.84% versus $n_h = 3$ at resonance. It is seen that despite including more harmonics in the simulation, ROMs with 42 and 52 AMPs still only converge to the $n_h = 1$ baseline case. This occurs because the modes required to reduce the dynamics of the higher harmonics are different from the reduction modes required for the first harmonic. In general no harmonics can be ruled out a priori. Nevertheless, it is known that in case of negligible variation of the normal relative displacements, as in the case under analysis, even harmonics do not contribute significantly to the response [96]. Thus, only the third harmonic is expected to contribute significantly in addition to the first. Due to the nature of how higher harmonics contribute to the response, it is expected that

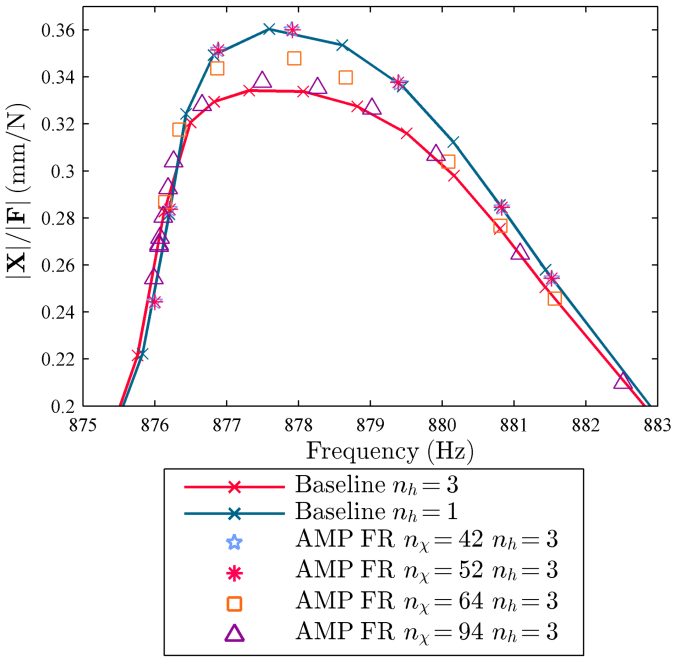

Figure 2.14. ROM (based on full reduction AMP) responses for higher harmonics, EO 1 response, $\mu|\mathbf{F0}|/|\mathbf{F}| = 1.35 \times 10^4$

modes of the structure lying near a frequency region thrice as high (near 2640 Hz) as the one under consideration (near 880 Hz) will contribute to the response. Moreover, due to the cyclic symmetric nature of the structure, it is expected that a ND 3 mode will respond to the third harmonic of an EO 1 excitation (which corresponds to an EO 3 excitation). AMPs are generated from stuck ND 3 modes of the third family, whose modal frequencies (at 2810 Hz) lie near the expected frequency range and append them to the AMP basis used for $n_h = 1$ reductions. The resulting ROM responses begin to converge towards the baseline $n_h = 3$ response. In Fig. 2.14 the ROMs with 64 and 94 AMPs contain 22 and 42 AMPs generated from the third family ND 3 stuck modes, in addition to the same AMPs as those used in the ROM with 52 AMPs (generated from first family ND 1 stuck mode). The errors for the 64 and 94 AMP ROMs at resonance versus the $n_h = 3$ response are 4.11% and 1.13% respectively. In the analysis for the EO 1 response convergence for $n_h = 1$ and for the reduction of the higher harmonics, only unconditioned AMP bases were used.

It must be noted that the actual number of nonlinear equations used in HBM is proportional to the product of the number of DoFs of the model and the number of harmonics retained. Although the number of HBM equations per harmonic for the ROM increases from $n_h = 1$ to $n_h = 3$ due to inclusion of more AMPs, the corresponding increase for the baseline model is much higher. Thus, the time savings versus the baseline for the ROMs is more with $n_h = 3$ than $n_h = 1$ despite the increase in number of reduction modes. Ideally, it might be possible to save even more computational effort by reducing the equations corresponding to each harmonic of the baseline separately using different AMP bases for different harmonics as opposed to a concatenated basis for all the harmonics as is done here. In general, for a tuned blisk, for some harmonic n_h, modes of the stuck system which are expected to respond to an $n_h\times$EO excitation near n_h times the frequency range of evaluation must be retained for use in the AMP procedure [41]. For a mistuned blisk, only the frequency based selection rule will apply as cyclic symmetry will be broken. However, the application of such separate reduction bases for each harmonic and the reduction of a mistuned blisk system with higher harmonics are beyond the scope of the current study. To evaluate the speed

Table 2.2. Simulation times

Reduction method	No. of AMPs	Frequency resolution (Hz)	AMP calculation time (min)	HBM solution time (min)
Baseline	–	0.1	0.00	711.62
NLR	32	0.1	17.75	238.26
FR	32	0.1	17.28	88.22
NLR	12	0.1	6.61	216.57
FR	12	0.1	6.71	80.37
NLR	32	0.5	18.49	51.54
FR	32	0.5	17.24	19.68
NLR	12	0.5	6.54	45.69
FR	12	0.5	6.48	15.85

of the ROMs an evaluation range between 860 and 890 Hz is considered for an EO 1 excitation, $\mu|\mathbf{F0}|/|\mathbf{F}| = 1.35 \times 10^4$ and $n_h = 1$ for simulations on a machine with 8 GB RAM and an Intel®

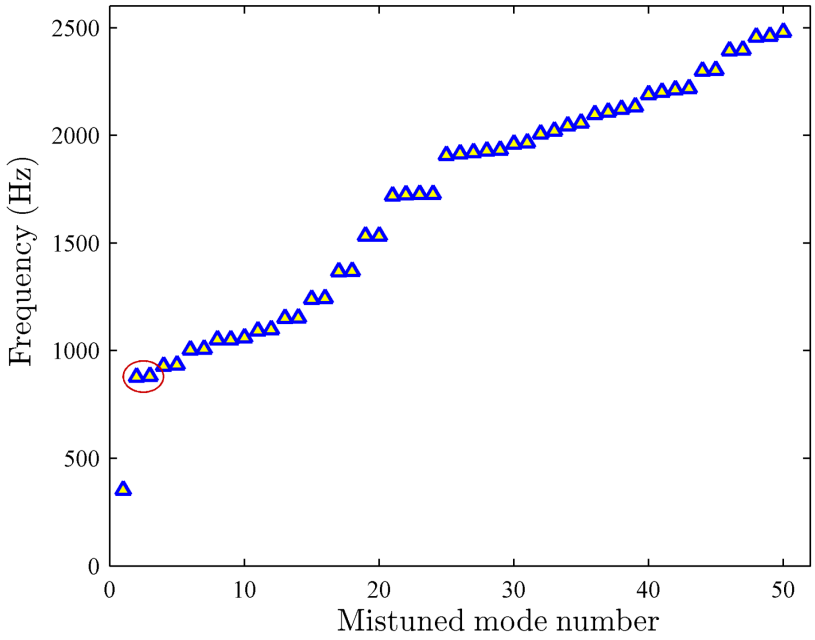

Figure 2.15. Natural frequencies of stuck mistuned blisk

Core™ 2 Quad Q9450 @ 2.66 GHz processor. The results may be seen in Table 2.2. The time required for the solution of the nonlinear HBM equations are shown. The overhead time required to calculate the AMP contact conditions and generate the AMP modes for ROMs of different sizes are displayed as well. It is seen that the total time required for the baseline simulation is much higher than for the ROMs. It is found that every additional AMP mode calculated adds an overhead of 30-40 seconds to the simulation. The FR ROMs simulate much faster than NLR ROMs. It may also be observed that an increase in the number of AMPs for the same ROM type and frequency resolution only leads to small increases in the actual simulation time, especially when compared in proportion to the simulation time of the baseline model.

2.3.3 ROMs for mistuned blisk model

Figure 2.15 exhibits the natural frequencies of the stuck linear model corresponding to the mistuned blisk with small stiffness mistuning in its blades. As opposed to the tuned case, the frequencies are not repeated and the mode shapes which emerge from the solution of the stuck

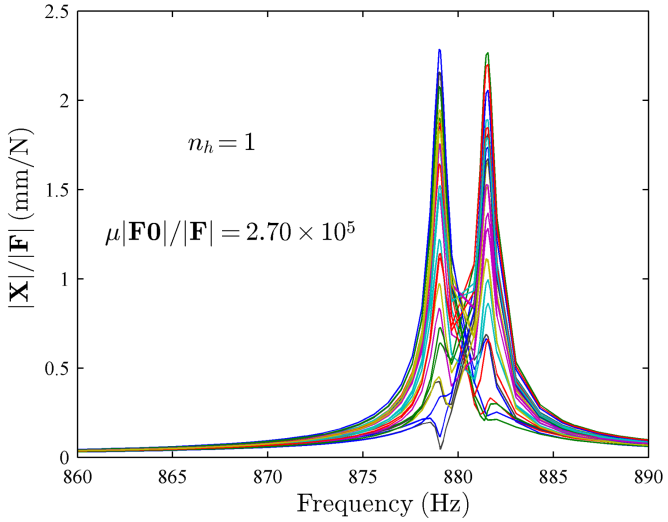

Figure 2.16. Stuck response of mistuned blisk

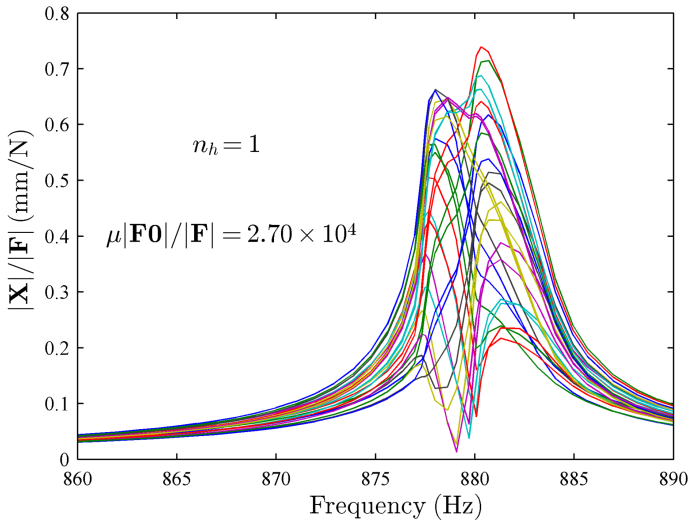

Figure 2.17. Response of mistuned blisk in microslip

mistuned system do not have distinct nodal diameters. Depending on the mode, although a particular nodal diameter pattern might dominate the mode shape, it is not the only component of that mode shape. A nodal diameter pattern may still be noticeable. However, if one conducts a spatial FFT of the mode shape choosing cyclically symmetric DoFs, one observes not only a dominant harmonic, but also non-zero coefficients of other harmonics as well. A frequency range is chosen near the natural frequencies in the circled area in Fig. 2.15, which is close to the first family ND 1 mode-pair of the tuned case. Figure 2.16 shows the baseline mistuned model response to an EO 1 excitation for the stuck case at $\mu|\mathbf{F0}|/|\mathbf{F}| = 2.7 \times 10^5$ in the chosen frequency range. In the mistuned case, the response amplitude at every data node (blisk sector) is different. The 27 distinct response curves corresponding to different sectors are plotted on the same axes. Two resonant peaks corresponding to the stuck modal frequencies are observed. Figure 2.17 shows the baseline mistuned model response to an EO 1 excitation at $\mu|\mathbf{F0}|/|\mathbf{F}| = 2.7 \times 10^4$ when the system is in microslip. The effect of friction damping on the peak response is apparent. The dynamics of the mistuned blisk are more complex than the tuned case. ROM formulation for this case is generally more challenging. Proper sampling must be carried out in the $\hat{\mathrm{p}}$ domain to obtain suitable AMP modes and then SVD filtering must be employed to ensure convergence. An unconditioned basis of 62 modes generated from the mistuned stuck modes was conditioned to a obtain a basis of 22 AMPs. The ratio of largest and smallest singular values used in the conditioning SVD procedure was 3×10^3. Responses for sectors 8 and 19 of a FR and NLR model with 22 AMPs each are plotted in Fig. 2.18 alongside the response of the baseline model to the same excitation conditions as those used in Fig. 2.17. The accuracy of the ROM responses compared to the baseline in these sectors is representative of the accuracy in other sectors. Both the ROMs capture the response very well. The maximum of absolute error in peak response across all sectors is found to be 1.39% for the NLR ROM and 2.48% for the FR ROM.

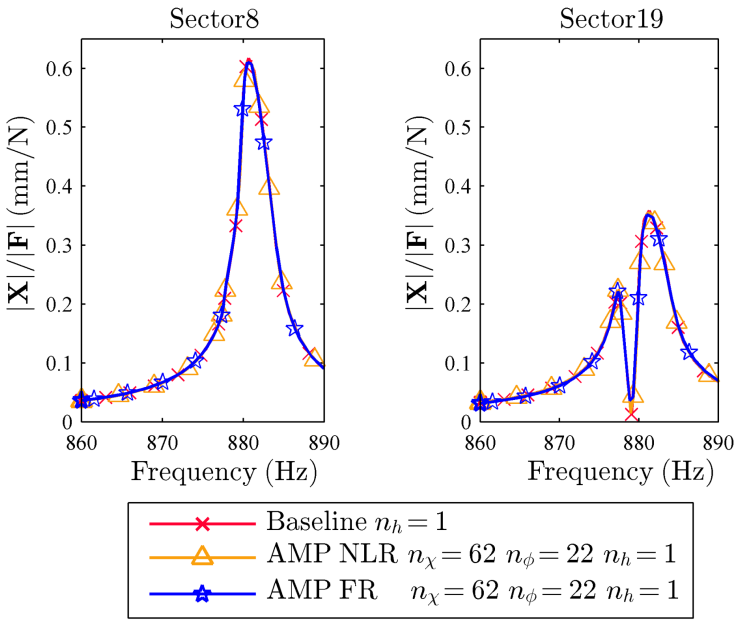

Figure 2.18. ROM responses of mistuned blisk

2.4 Analysis, applicability and limitations of AMPs

The AMP reduction relies on the existence of dominant spatial correlations in the nonlinear dynamics of the baseline system. If the number of these spatial correlations is comparable to the size of the baseline system, neither the AMPs, nor any other reduced basis based method will be able to offer any significant reduction. To generate the boundary conditions needed for the AMPs, modes which represent the dominant motion of the system in the frequency range of interest are used. Motion along these generating modes must dominate (e.g., they can contain most of the energy of the whole system dynamics) in the frequency and amplitude range of interest for the AMPs to be effective in that range. In this work, the dominating stuck mode were adopted as the generating shape because the analysis is limited to microslip near the full-stick region. That is the region of practical interest to most designers, and in this region the stuck modes do dominate the response. However, other generating modes may be used to obtain the AMPs for other ranges if they dominate the motion in the frequency and amplitude of interest, such as the gross-slip modes

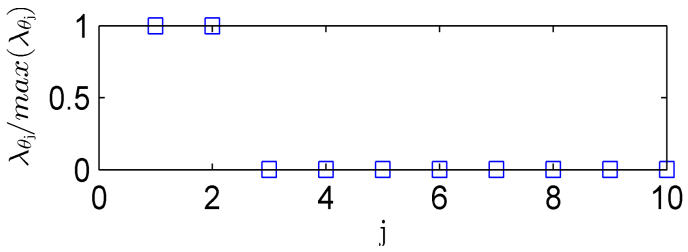

Figure 2.19. Eigenvalues of POMs for EO1 response, $\mu|\mathbf{F0}|/|\mathbf{F}| = 1.35 \times 10^4$

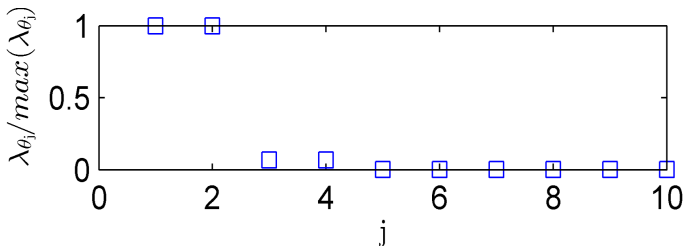

Figure 2.20. Eigenvalues of POMs for EO 12 response, $\mu|\mathbf{F0}|/|\mathbf{F}| = 2.70 \times 10^3$

near the corresponding gross-slip amplitudes and frequencies.

The generating modes themselves are also included in the AMP basis. Since they dominate the dynamics, they capture the larger portion of the displacement. However, the nonlinear forces due to small (subtle) displacements at the contact can have a significant effect on the dynamics especially because they affect friction-induced damping. To accurately capture the dynamics, a reduction basis must not only span the space of the displacements of the system, but also span the space of these nonlinear forces. Thus, convergence of the ROM response with the number of AMPs depends on how accurately the span of the AMPs captures both the force and the displacement spaces. The AMP basis consists of modes which represent motion along the linear modes for special boundary conditions. The accuracy with which the space of nonlinear forces is captured by the AMP basis shows how accurately the boundary conditions are predicted. Another assumption is that the kinematics of the generating modes can capture the boundary conditions accurately enough. If this assumption is violated, the ROM will not be able to predict the response accurately, even if the displacement is spanned by the AMPs.

To analyze the spatial correlations in the response, proper orthogonal decomposition (POD) [62] is applied to the baseline system. The dynamic response of the baseline system at all DoFs is converted from the frequency to the time domain. The time response at different frequencies are collated into a single matrix $\mathbf{Q}$. The proper orthogonal modes (POMs) $\mathbf{\Theta} = [\theta_1 \theta_2 \cdots \theta_{n_\theta}]$ may then be obtained by an eigenanalysis of $\mathbf{Q}\mathbf{Q}^{\mathrm{T}}$ [62]. The POMs represent the spatial correlations observed in the baseline response arranged in the decreasing order of their contribution to the response. The relative dominance of the POMs in the response is indicated by the corresponding eigenvalue λ_θ. The POD analysis was performed for the highest microslip level baseline responses for the frequency ranges shown in Figs. 2.8 and 2.9. The POM eigenvalues normalized by the maximum are shown in Figs. 2.19 and 2.20. These results show that the EO 1 response is dominated by 2 POMs while the EO 12 response contains 4 POMs with non-negligible contributions. These results show the presence of spatial correlations in nonlinear response, which indicates the possibility to reduce the model.

Next, an error metric is introduced to characterize how well an AMP basis captures these correlations. The error e_{θ_j} in capturing a particular correlation represented by a POM θ_j by an AMP basis is defined as the error between the POM and its projection on the AMP basis, namely:

$$e_{\theta_\mathrm{j}} = \frac{||\theta_\mathrm{j} - \mathbf{\Phi}_{n_\chi} \mathbf{\Phi}^{\dagger}_{n_\chi} \theta_\mathrm{j}||_2}{||\theta_\mathrm{j}||_2} \tag{2.39}$$

where n_χ is the number of AMP modes in an unconditioned basis. The POM θ_j is captured perfectly when e_{θ_j} is zero. For a conditioned basis, n_χ may be replaced by n_ϕ, the number of conditioned AMP modes. If an unconditioned AMP basis is used, it is arranged such that the first modes in the basis represent the generating stuck modes, and subsequent AMPs are derived by applying increasing values of $\hat{\mathrm{p}}$. A conditioned basis is arranged in the decreasing order of singular values in the diagonal of $\mathbf{S}_{\mathbf{\Phi}}$ in Eqn. (2.37).

Figures 2.21 and 2.22 show the change of the error metric for different POMs for AMP modes

chosen from the bases used for reduction. For the EO 1 case shown in Fig. 2.21, only unconditioned AMPs were used for the reduction. In this case, the first 2 dominant POMs account for most of the response and have large projections (small residual error) on the first 2 AMPs in the basis (which are the same as two of the tuned stuck modes). This validates the assumption that stuck modes dominate the response and may be used for AMP generation in this case. Since the EO 12 case in Fig. 2.22 consists of response contributions from two families, it is seen that this range requires 4 conditioned AMP modes to capture the 4 most dominant POMs which contribute significantly to the response in this case. However, since the basis is conditioned, the first 4 AMPs in the basis might not exactly represent tuned stuck modes. The errors in the projection of the first 4 POMs on all 4 stuck tuned modes from the two families under consideration for EO 12 response are presented in Table 2.3. Again the residual is very low, which shows that the dominant motion of the system is along the stuck modes. Another fact which supports this argument is that in the frequency region of analysis, the resonant frequency in microslip does not shift significantly from the stuck response frequency. This implies that the elastic energy in the contact is dominated by the elastic energy in the rest of the system. The projections of the POMs for the EO 12 case on the unconditioned AMP mode bases generated from the 1^{st} and 2^{nd} family exclusively are shown in Figs. 2.23 and 2.24. The error residuals for the AMP modes from the 2^{nd}family modes are smaller. This is expected because the response near the frequency region of the 2^{nd}family is higher and thus it contributes more to the POMs.

Table 2.3. $e_{\theta_{\text{j}}}$ for stuck modes from 1^{st} and 2^{nd} families, EO 12 response, $\mu|\mathbf{F0}|/|\mathbf{F}| = 2.70 \times 10^3$

j	1	2	3	4
$e_{\theta_{\text{j}}}$	0.0014	0.0014	0.0017	0.0017

It may be seen in Figs. 2.21 and 2.22 that the AMP bases do not capture the PODs which have small contributions to the response (3-4 for the EO 1 case, and 5-8 for the EO 12 case). Although the contribution of these PODs to the response is small, their contribution to the dynamics might

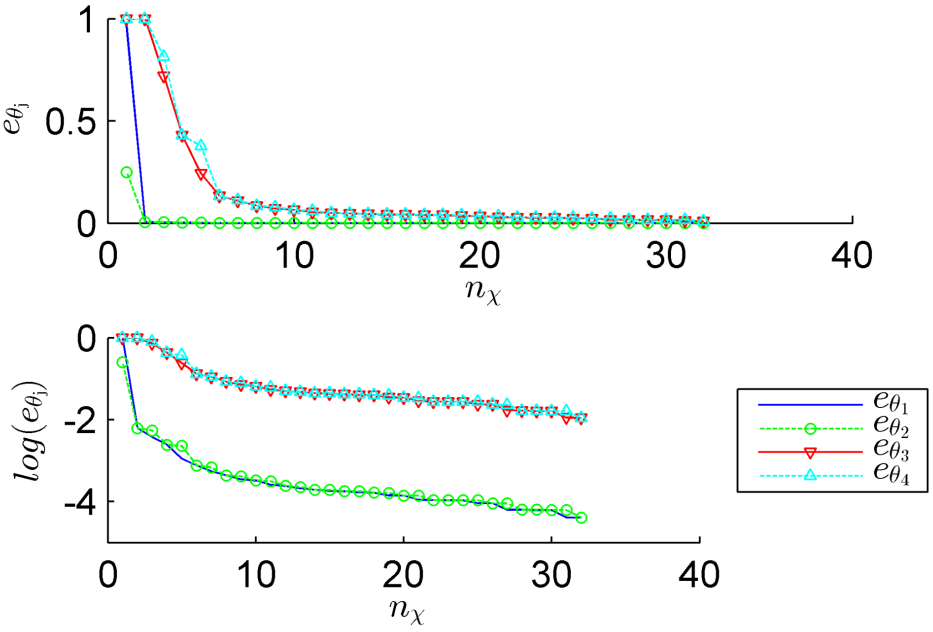

Figure 2.21. e_{θ_j} for unconditioned AMPs, EO1 response, $\mu|\mathbf{F0}|/|\mathbf{F}| = 1.35 \times 10^4$

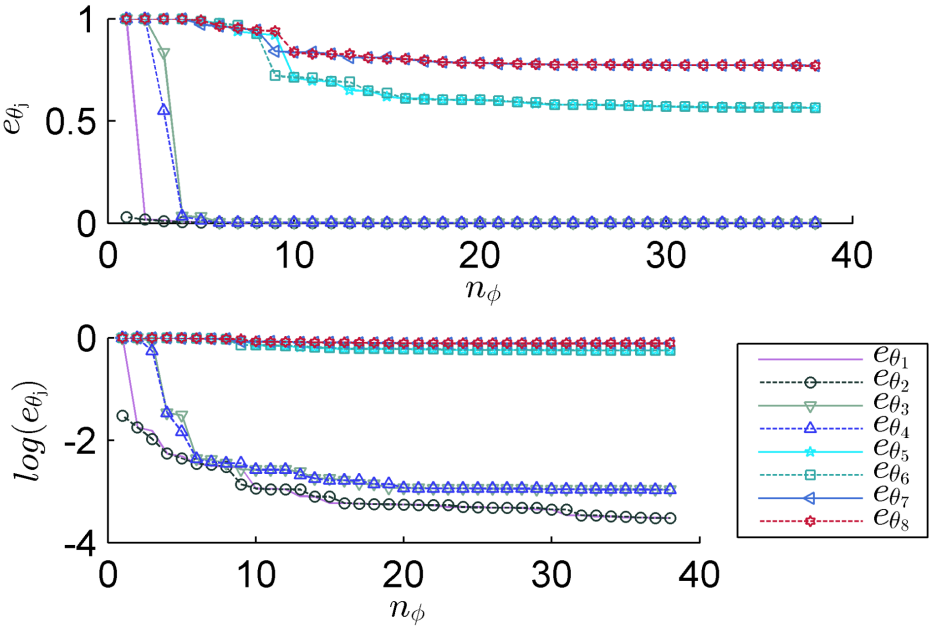

Figure 2.22. e_{θ_j} for conditioned AMPs, EO12 response , $\mu|\mathbf{F0}|/|\mathbf{F}| = 2.70 \times 10^3$

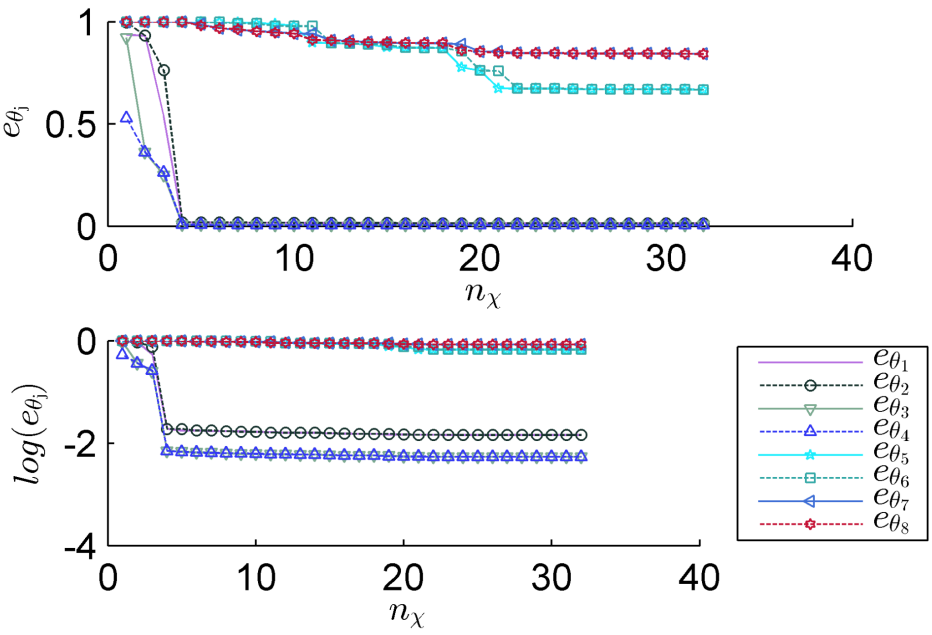

Figure 2.23. e_{θ_j} for unconditioned AMPs generated from 1^{st} family stuck modes, EO12 response, $\mu|\mathbf{F0}|/|\mathbf{F}| = 2.70 \times 10^3$

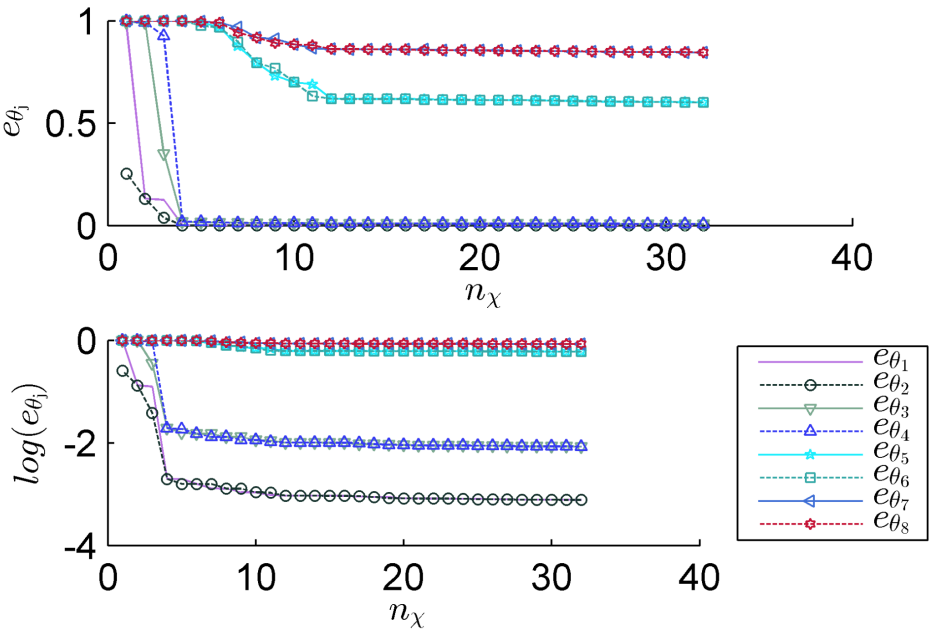

Figure 2.24. e_{θ_j} for unconditioned AMPs generated from 2^{nd} family stuck modes, EO12 response, $\mu|\mathbf{F0}|/|\mathbf{F}| = 2.70 \times 10^3$

be significant. POMs can be used as a reduction basis in the same manner as the AMPs to check the convergence versus the number of POMs. This is shown in Figs. 2.25 for the EO 1 and EO 12 cases. It may be seen that although the ROMs with 2 and 4 dominant POMs as reduction modes, predict the response frequency accurately for EO 1 and EO 12 cases respectively, the less dominant POMs are required to predict the damping and converge to the response of the baseline. This shows that merely spanning the response with the reduction modes may not be sufficient for accurate response prediction with a ROM. Nonlinear contact forces must be captured also. To see how the ROM bases capture the nonlinear contact forces an error metric which calculates the residual between the baseline nonlinear contact force (along a particular direction) at a particular frequency ω and its projection on the reduction basis is defined:

$$\varepsilon_{\mathrm{x}}(\omega) = \frac{\max_h ||\bar{\mathbf{f}}_{C,\mathrm{x},\omega,h} - \mathbf{\Phi}_{n_\chi,C,\mathrm{x}} \mathbf{\Phi}^{\dagger}_{n_\chi,C,\mathrm{x}} \bar{\mathbf{f}}_{C,\mathrm{x},\omega,h}||_2}{\max_h ||\bar{\mathbf{f}}_{C,\mathrm{x},\omega,h}||_2} \tag{2.40}$$

where $\bar{\mathbf{f}}_{C,\mathrm{x},\omega,h}$ is a vector representing the real or imaginary part of the complex dynamic force for the harmonics included in the analysis at frequency ω. $\varepsilon_{\mathrm{x}}(\omega)$ represents the maximum of the errors across all harmonics $h = 1$ to n_h. Similar formulae hold for y and z directions. $\mathbf{\Phi}_{n_\chi,C,\mathrm{x}}$ in Eqn. (2.40) is replaced with $\mathbf{\Phi}_{n_\phi,C,\mathrm{x}}$ or $\mathbf{\Theta}_{n_\theta,C,\mathrm{x}}$ for conditioned AMP or POM ROMs respectively.

The force errors at resonance frequency for the EO 1 and EO 12 cases with different number of POMs retained in the reduction basis are shown in Figs. 2.27 and 2.28. The values of the ε metrics for the AMP modes are shown in Figs. 2.29 and 2.30. Figs. 2.31 and 2.32 show how unconditioned AMP modes of the EO 12 modes span the force space. These figures show why more reduction modes are required to capture the nonlinear forces and damping. More modes have a non-negligible effect on the ε values than they do on the response indicated by the e values.

It must be noted that the error metric ε measures the collective error in forcing at all contact DoFs. The dynamic receptance (which determines the relationship between these forces and displacements), might not ascribe equal importance to all the contact forces. Hence, the error in

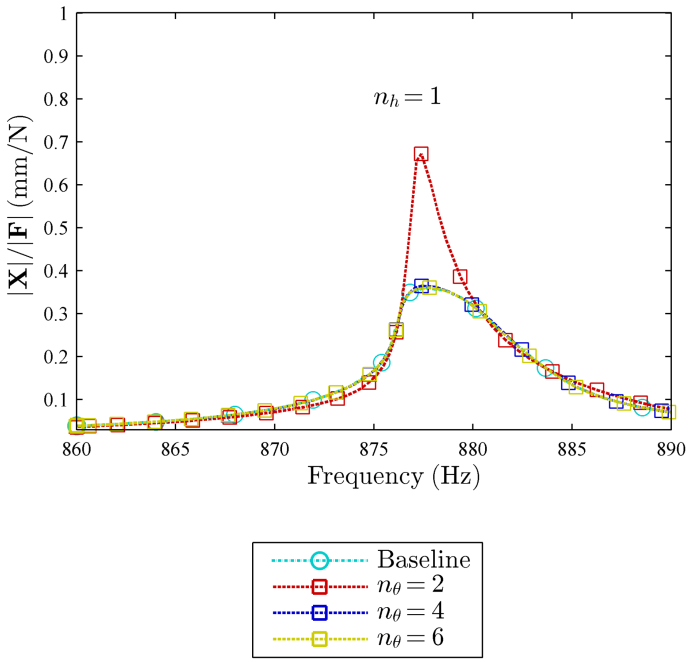

Figure 2.25. Engine order 1 POM ROM responses, $\mu|\mathbf{F0}|/|\mathbf{F}| = 1.35 \times 10^4$

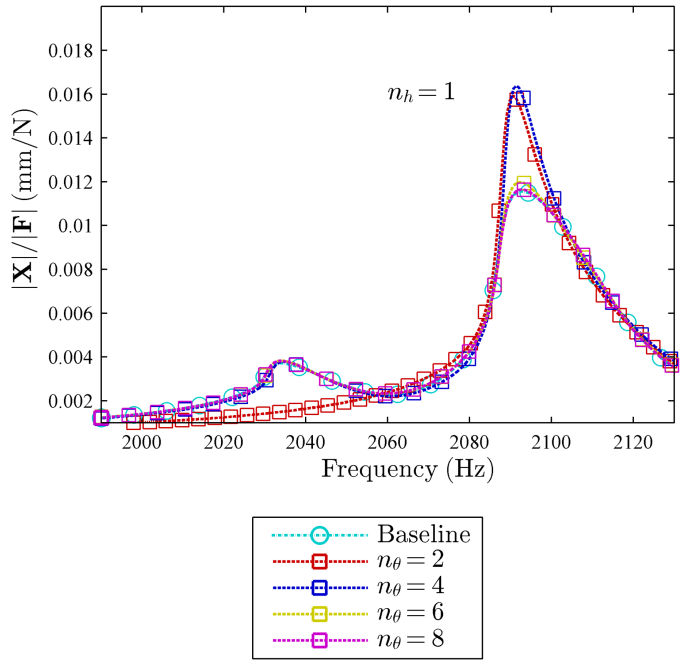

Figure 2.26. Engine order 12 POM ROM responses, $\mu|\mathbf{F0}|/|\mathbf{F}| = 2.70 \times 10^3$

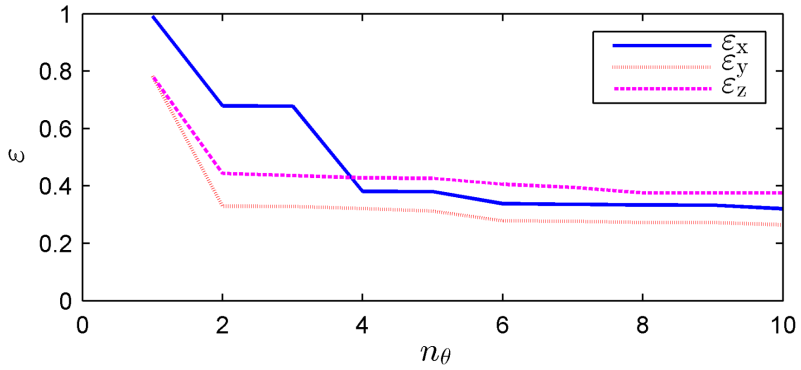

Figure 2.27. ε for POMs, EO 1 response, $\mu|\mathbf{F0}|/|\mathbf{F}| = 1.35 \times 10^4$ at resonance (877.6 Hz)

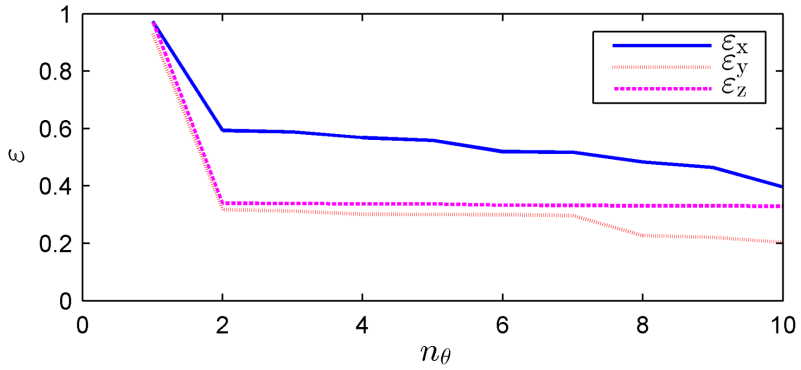

Figure 2.28. ε for POMs, EO 12 response, $\mu|\mathbf{F0}|/|\mathbf{F}| = 2.70 \times 10^3$ at resonance (2,093.2 Hz)

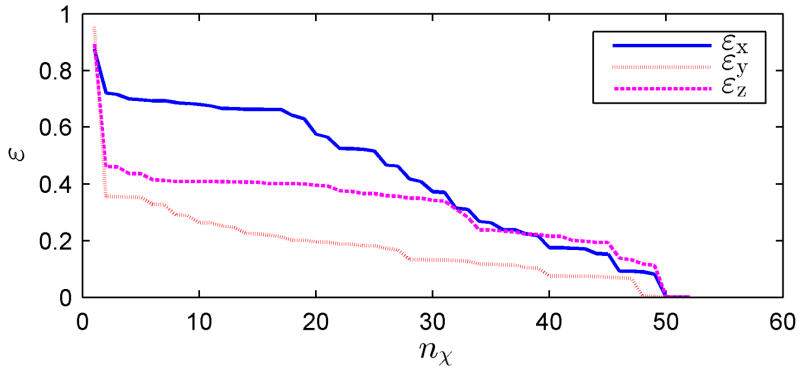

Figure 2.29. ε for AMPs, EO 1 response, $\mu|\mathbf{F0}|/|\mathbf{F}| = 1.35 \times 10^4$ at resonance (877.6 Hz)

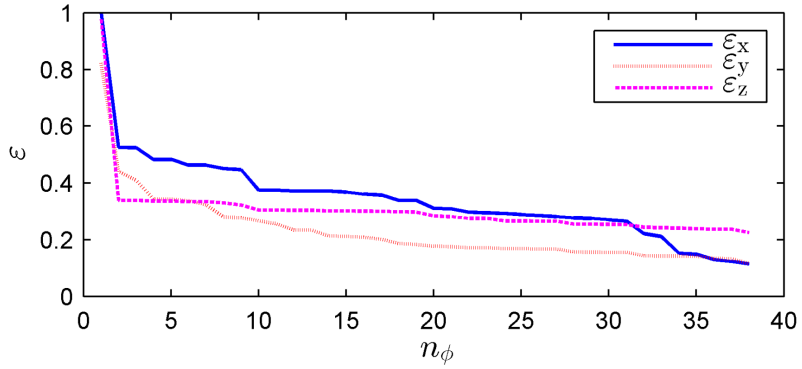

Figure 2.30. ε for conditioned AMPs, EO 12 response, $\mu|\mathbf{F0}|/|\mathbf{F}| = 2.70 \times 10^3$ at resonance (2,093.2 Hz)

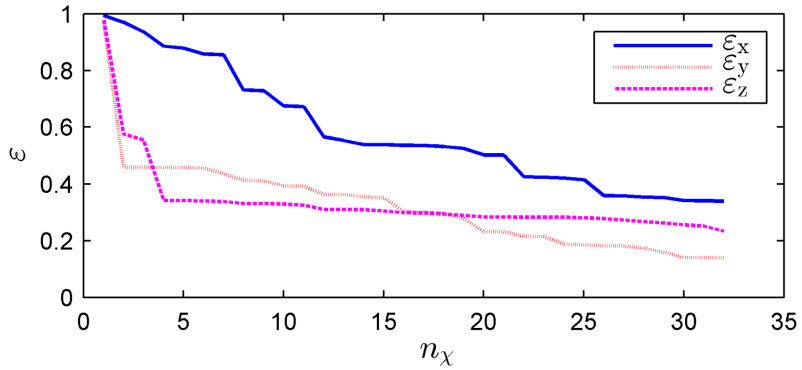

Figure 2.31. ε for unconditioned AMPs generated from 1^{st} family stuck modes, EO 12 response, $\mu|\mathbf{F0}|/|\mathbf{F}| = 2.70 \times 10^3$ at resonance (2,093.2 Hz)

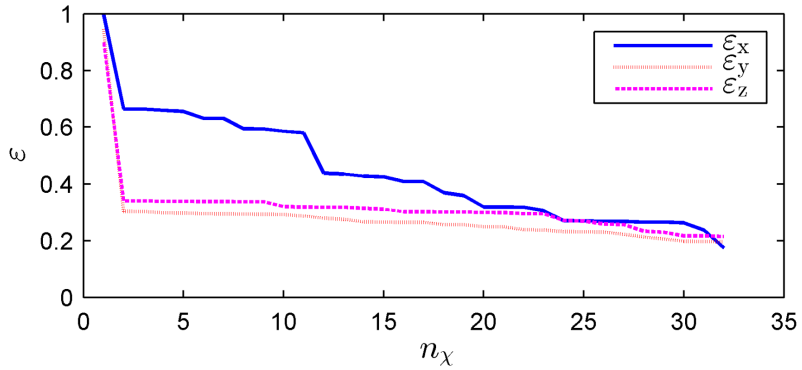

Figure 2.32. ε for unconditioned AMPs generated from 2^{nd} family stuck modes, EO 12 response, $\mu|\mathbf{F0}|/|\mathbf{F}| = 2.70 \times 10^3$ at resonance (2,093.2 Hz)

displacements predicted by the ROM and this error metric cannot be compared directly. Figs. 2.25 to 2.28 show that predicting the correct displacement at the blade-tip with a ROM might not require a reduction basis which spans the entire space of nonlinear forces. The correlation between the degree of accuracy required in capturing the force space and the accuracy of the displacement response cannot be established a-priori without solving the nonlinear equations. As noted earlier, convergence studies (for increasing ROM sizes) are the suggested method to determine the required number of reduction modes.

The ROM converges in terms of number of modes when both error metrics for displacements and forces flatline. As the span of the reduction modes grows (with increasing number of modes to capture the contact displacements more accurately), the predicted contact forces are more accurate, and that affects the accuracy of the calculated displacements. The question of accuracy in determination of the nonlinear forces depends on the ability of the AMP procedure to predict instantaneous contact conditions through the AMP boundary conditions. The method herein of using estimated modal amplitudes to predict these boundary is one of many possible methods. For instance, one may use an iterative scheme where AMP modes at a particular $\hat{\mathrm{p}}$ value are used first to predict the boundary conditions. These are then used to generate the next iteration of AMP modes and predict again the boundary conditions, and so on. The use of the generating mode used in this study may be seen as the first iteration of this scheme. It is found that the basis obtained from this first iteration (i.e., the one based on stuck modes) is sufficient to capture the response. However, such an iterative scheme could be employed in future developments of the AMP method for cases where the dominant mode changes with response amplitude levels.

2.5 Conclusions

A novel method to obtain ROMs for shrouded blisks in the microslip regime using an AMP reduction basis was proposed. The ROM was validated against a full order CB-CMS model for cases with and without small stiffness mistuning in the blades, for single and multiple harmonics.

Two separate methods of reduction, FR and NLR using the same reduction basis are proposed. It is seen that NLR is more accurate but slower. Alternative reduction techniques which reduce the linear and nonlinear DoFs separately and avoid matrix inversion might also be feasible. However, such techniques have not been explored in this study and remain ripe for future investigation. It is seen that the ROMs are able to capture the overall response characteristics of the blisk model accurately. The AMP reduction method itself, is based on simple linear analyses and masking procedures, making the process highly efficient. The procedure is user-friendly and requires relatively few inputs. The accuracy of the ROMs also increases monotonically with the number of AMPs included in the reduction till convergence, making it an attractive candidate for convergence studies to predict model dynamics where the full order model is too cumbersome to solve for validation. AMPs have been used in this study in conjunction with HBM and CB-CMS to facilitate analysis and method development. However, the reduction procedure is independent of these methods and can be used with other nonlinear differential equation solving techniques either in the time or frequency domain. AMPs may also be applied directly to FE models or other reduced models based on those FE models. The contact conditions must be applied separately as these are integral to the procedure for AMP determination, but there is some flexibility in the range of friction models that might be chosen as long as they enforce node to node contact. Although AMPs were developed in this study for shrouded blisks, they may possibly be adapted for reducing other systems with frictional contacts, but the accuracy and effectiveness of the AMP method will need to be evaluated separately.

CHAPTER III

Experimental Contact Parameter Estimation and AMP Validation

A reduced order model (ROM) for systems with frictional nonlinearities called adaptive microslip projection (AMP) was presented and validated using simulations in chapter II. There are also several practical considerations associated with the application of such ROMs to estimate dynamic responses for real systems. One of these challenges, which is independent of dynamic reduction, is proper modeling of friction nonlinearities. This involves choosing suitable contact models and estimating associated contact parameters accurately. Experimental measurements can also be used to verify the AMP procedure by using measured data to confirm the underlying assumptions associated with AMPs. Spatial correlations in the observed nonlinear response may be verified. The idea of estimating contact conditions for the AMPs by varying amplitudes of linear modes of the system can also be validated.

For this study, an experimental rig was developed. The rig consisted of a blade-like beam cantilevered at one end and a large (non-point) floating contact under a normal load at the other end. Frequency responses and linear modes of this structure were measured experimentally. Finite element (FE) models of the structure were adjusted to match the linear modes and obtain the mass and initial stiffness matrices. These were used in conjunction with node to node contact models to simulate nonlinear responses with HBM. It was observed that in addition to the aforementioned

parameters, in the case of a large contact such as in the experiment, the static normal load distribution plays a major role in the nonlinear response. No well-known experimental techniques exist to directly measure this distribution without affecting the system response itself. Only the total applied normal load was known. Hence, the normal load distribution was also parameterized as a spatial function of quantities which expressed the relative distribution at certain spatial locations at the contact. These locations were identified through FE simulations. All parameters were then identified using an optimization routine whose objective was to minimize the error between the experimental and simulated frequency responses at multiple excitation levels. AMP modes were estimated based on measured relative displacements at the contact. These estimated AMP modes were then compared to proper orthogonal modes (POMs) obtained from measured beam responses to investigate how well they capture the nonlinear spatial correlations in the actual response. It was found that the estimated AMP basis was able to capture not only the dominant response, but also the less dominant POMs which may be important for capturing the nonlinear dynamics [97]. The final validation of the efficacy of of the AMPs in capturing the dynamics is obtained by comparing simulated responses of the full order system and reduced order model (ROM) using the contact parameters estimated from experimental responses.

3.1 Experimental rig

3.1.1 Rig design

Experiments to validate the AMP procedure were conducted at the Aeromechanics (AERMEC) laboratory at Politecnico di Torino, Italy. The rig design was conducted with the objective of studying the dynamics of a blade-like structure which would consist of a frictional contact attached to a flexible structure. The final design of the rig is shown in Figs. 3.1 and 3.2. It consists of the dynamic assembly shown in Fig. 3.3, which is the main moving part, and contains the main beam attached to the winglet. One of the surfaces of the winglet is the contact surface. The other (target)

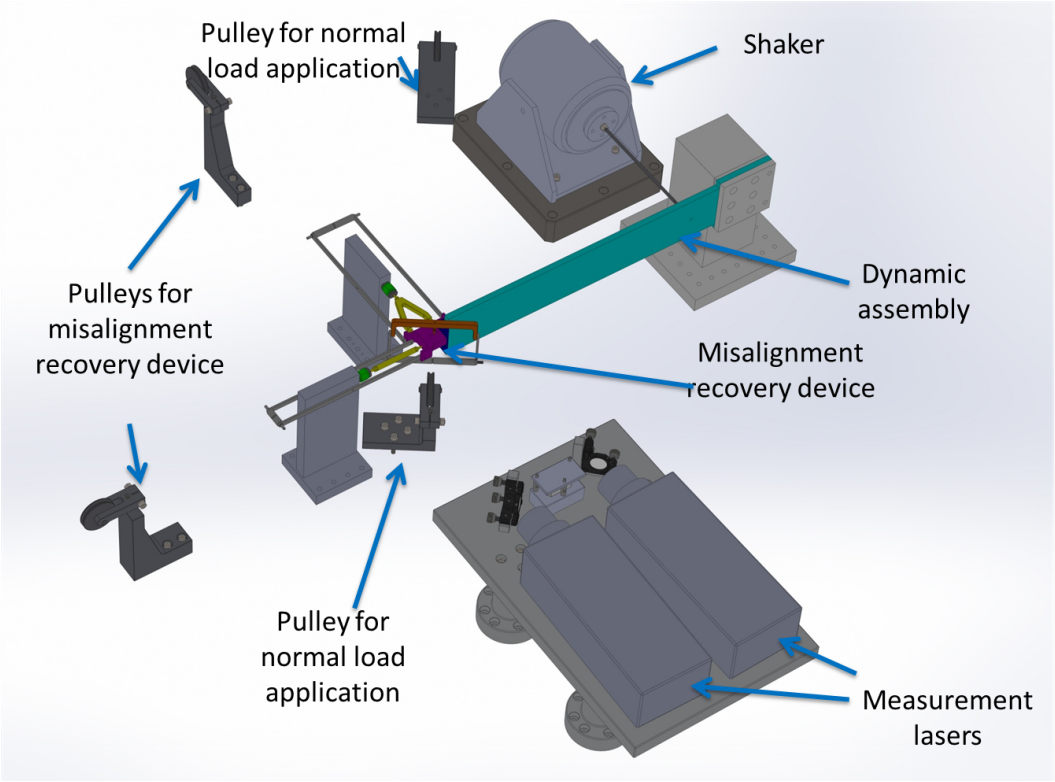

Figure 3.1. Final rig design: solid model

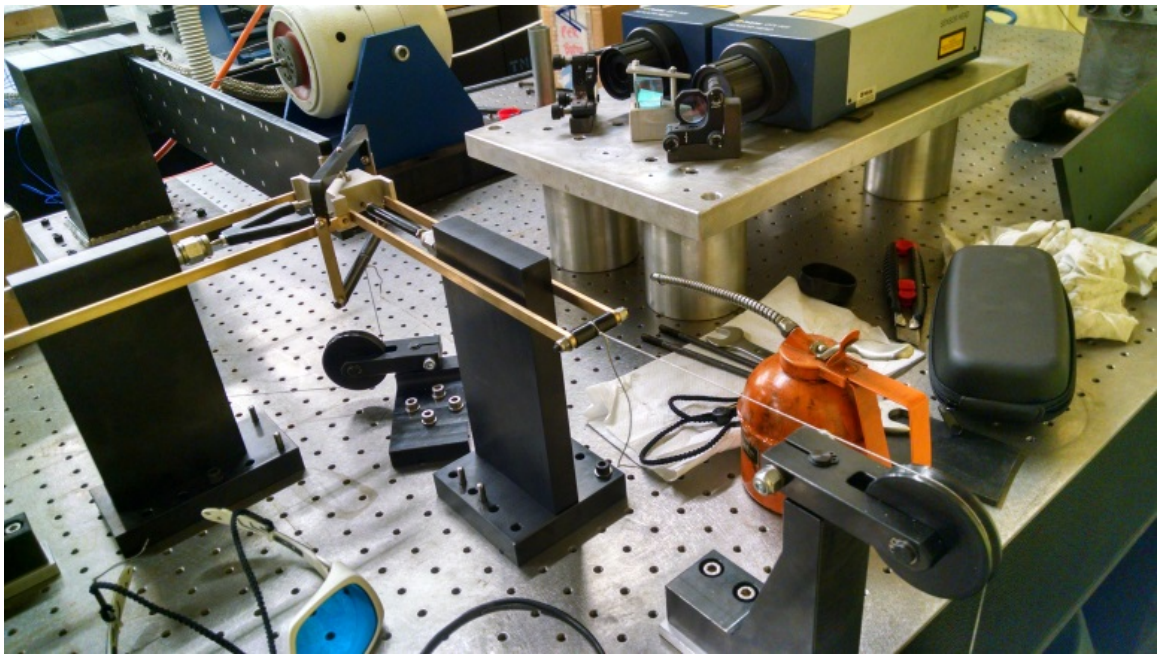

Figure 3.2. Final rig design: experimental apparatus

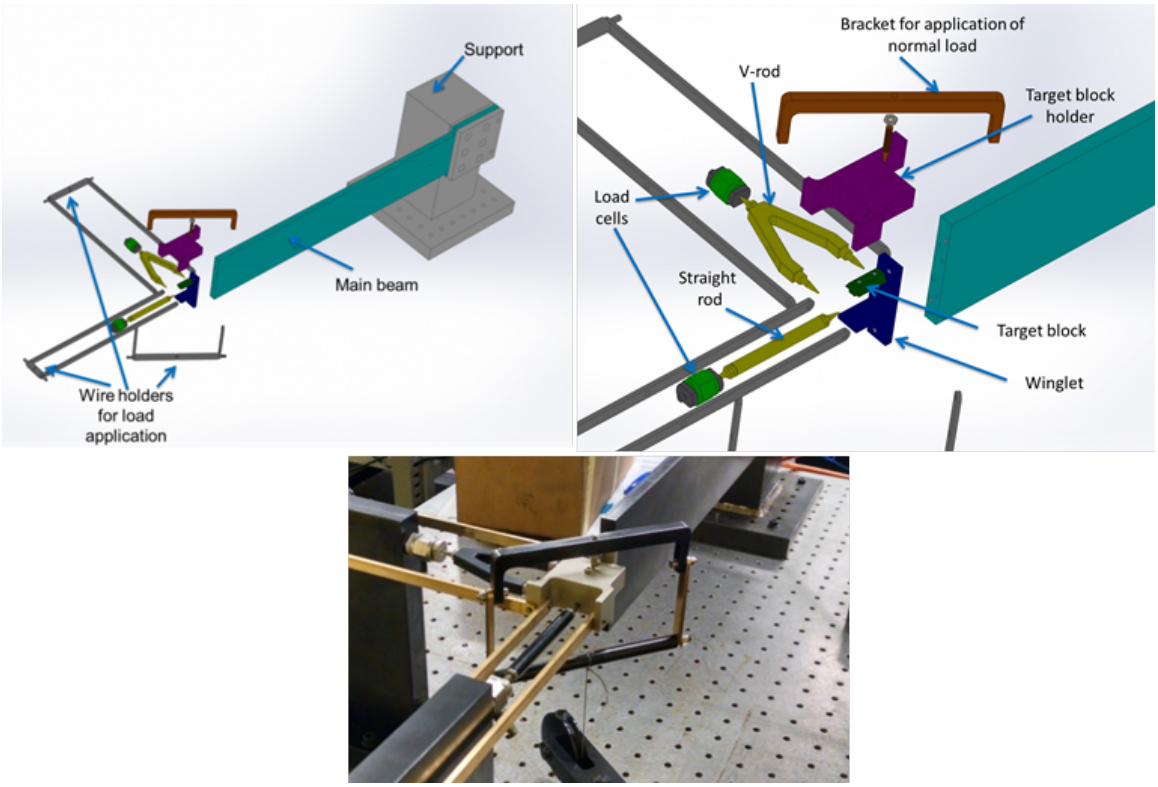

Figure 3.3. Dynamic assembly and misalignment recovery device

surface is on the target block which is attached to the target block holder by screws. The contact area between the two components has the dimensions 22mm x 4mm. The wedge shape of the target block ensures a no slip contact between itself and the target holder. A normal load is applied via a pulley mechanism to the top of the target holder through a bracket. The target holder is held in a misalignment recovery device which consists of the V-rod and straight rod. This provides stiffness in the direction of measurement of tangential forces, but allows small rotations of the plane of the target surface along the axes of the rods to allow for dynamic misalignment recovery and thus prevents separation and ensures that the normal load is applied uniformly at the contact. A shaker is used to provide dynamic excitation to the beam through a stinger.

Modal frequencies of the dynamic assembly at gross slip and full stick, calculated using simulations of baseline FE models in ANSYS®, are shown in Fig. 3.4. It may be seen that the mode of interest (1Fx) does not cross any other modes during microslip (which occurs between the two

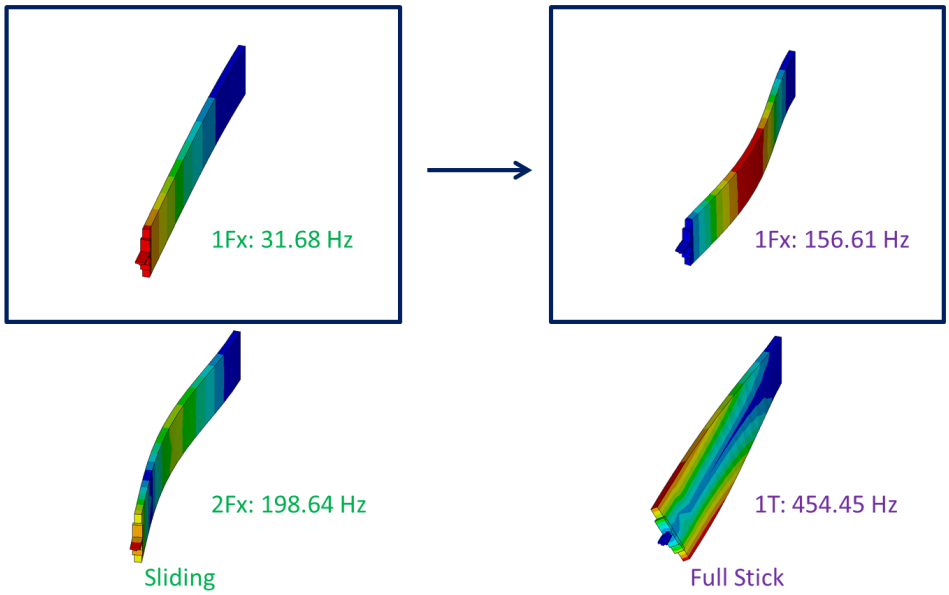

Figure 3.4. Modal frequencies of the dynamic assembly

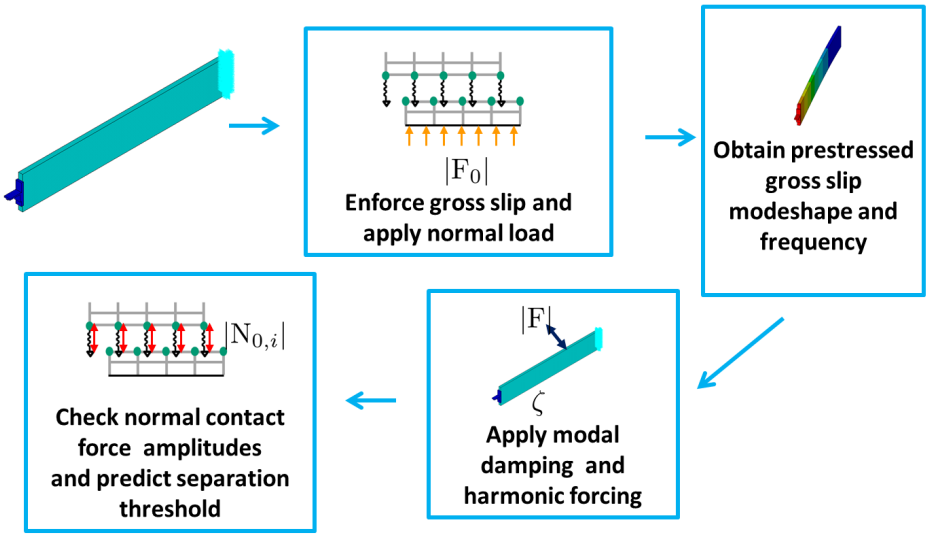

Figure 3.5. Analysis procedure for rig design

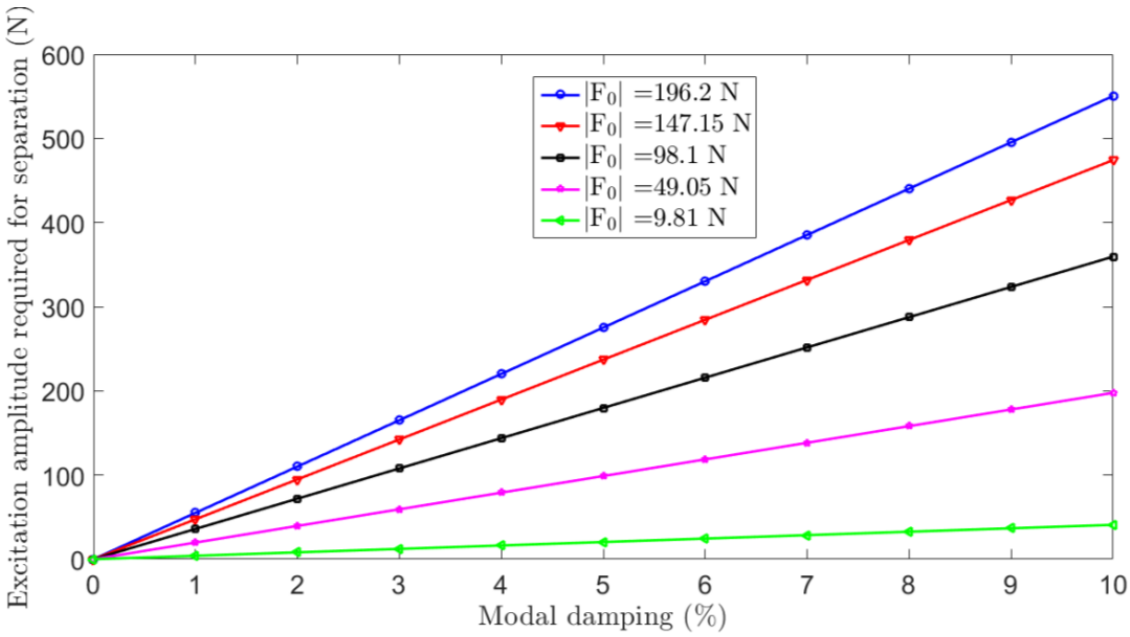

Figure 3.6. Separation thresholds with applied normal load

limiting linear situations shown). This is desirable as having frequency crossings would imply nonlinear spatial correlations in the microslip response arising from multiple modes, which would complicate the AMP validation procedure without any benefit to the research objective. Figure 3.5 shows the procedure adopted for analyzing the separation thresholds for the rig under various situations. First, normal load is applied with gross slip conditions enforced at the contact nodes of the dynamic assembly FE model. Under this pre-stressed condition, a modal analysis is conducted and the gross slip mode is obtained. Next, modal damping is applied, and a harmonic force is applied to the beam to replicate the excitation from the shaker. Following a harmonic analysis, the dynamic normal contact force amplitudes are evaluated at the contact nodes. The amplitude of excitation for which one of these contact force amplitudes first exceeds the static applied normal load determines the dynamic separation threshold.

The thresholds are plotted in Fig. 3.6 for various values of modal damping and static applied normal load. It may be seen that at for reasonable values of normal load and a modest (2 %) modal damping, very high excitation forces are required to achieve separation. Figure 3.7 shows

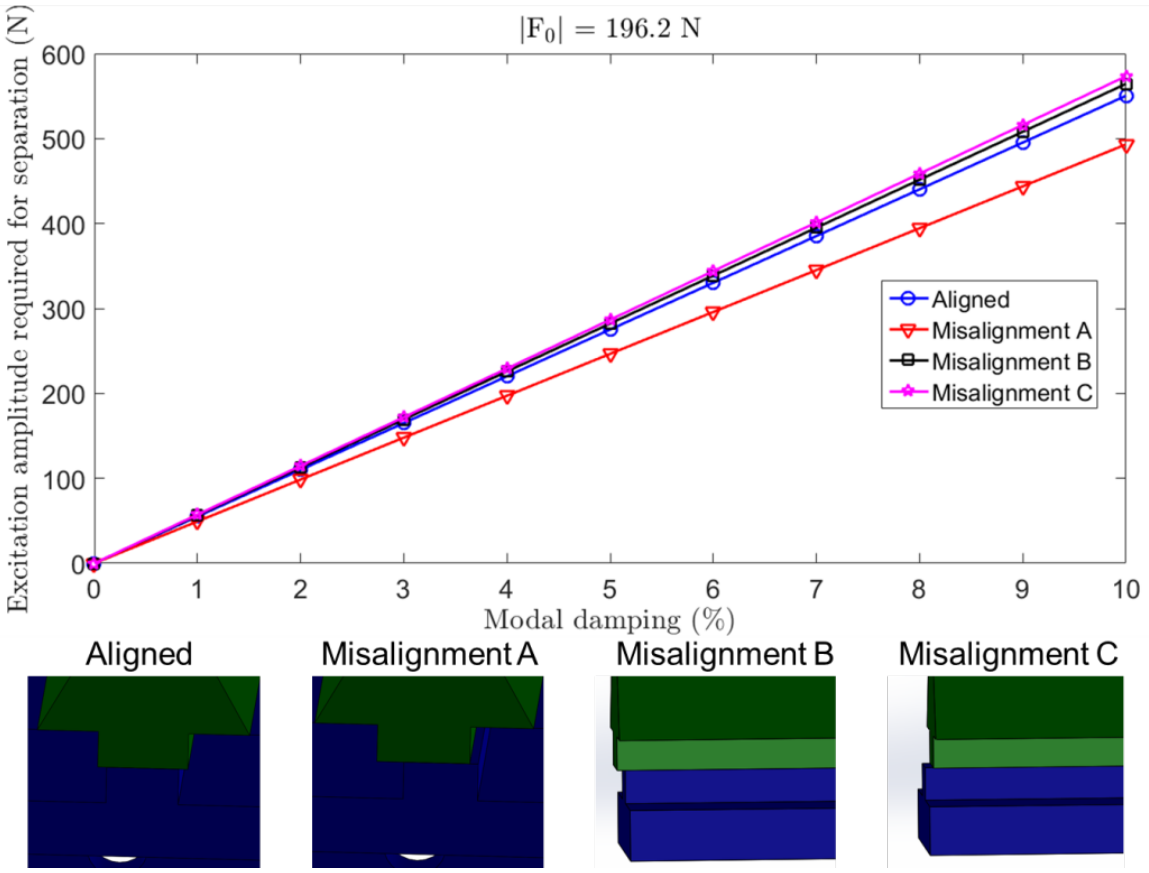

Figure 3.7. Separation thresholds with misalignments

the separation thresholds under different kinds of static misalignments and various values of modal damping. It is seen that the misalignments between the target and contact surfaces (of about 0.5 mm) do not affect the thresholds very much, and hence the operation of the rig without separation can be ensured even under these conditions.

The hysteresis cycle of the rig near gross slip frequencies are obtained by enforcing gross slip displacements to the rig and calculating the friction forces. The hysteresis cycle is plotted in Fig. 3.8 with the microslip regions shown in yellow. The contact conditions at the contact nodes at various stages of the microslip are shown in Fig. 3.8 also. Of particular interest are the contact conditions at nodes on the outside edge of the contact region, where the dynamic velocities can be measured with a laser beam.

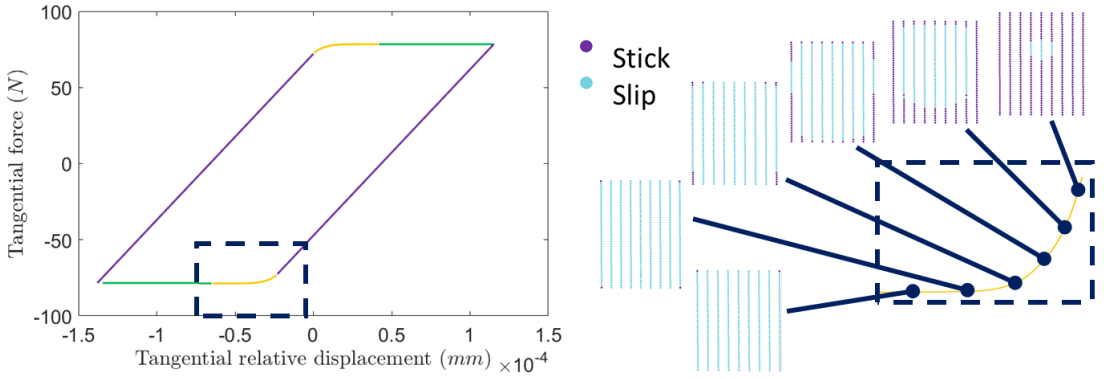

Figure 3.8. Different spatial coherences during microslip at contact in rig simulation (displacement along gross slip mode)

3.1.2 Experimental data collection setup

The experimental setup is shown in Fig. 3.9. Velocities are measured at different locations on the main beam of the test rig using a Polytec scanning laser vibrometer. Velocities near the contacting surfaces of the winglet and the target block are measured by Polytec differential lasers. The beam velocities may be processed either by a PC with proprietary Polytec software which has the capability of calculating linear modes directly, or by a laptop running a LabVIEW based software (developed in-house in Politecnico di Torino) which can synchronize and collect data from 4 different input channels as well as send a output voltage signal for the applied force using a National Instruments (NI) data acquisition (DAQ) system. The contact velocities from the two differential lasers as well as the measured tangential contact forces may be collected by the laptop in addition to the beam velocities. Different measurement points used for the laser vibrometers on both the beam (Bpos) and the contact (Cpos) are shown in Fig. 3.10. The velocities measured by the vibrometers are post-processed to obtain displacements. The experimental test matrix consists of 4 possible input variables, which may be varied to change the outcome of the experiment as shown in Fig. 3.11. The forcing amplitude may be changed for $\mathrm{n_F}$ different experiments. A frequency response function may be obtained by changing the excitation and measurement frequency $\mathrm{n_w}$. The

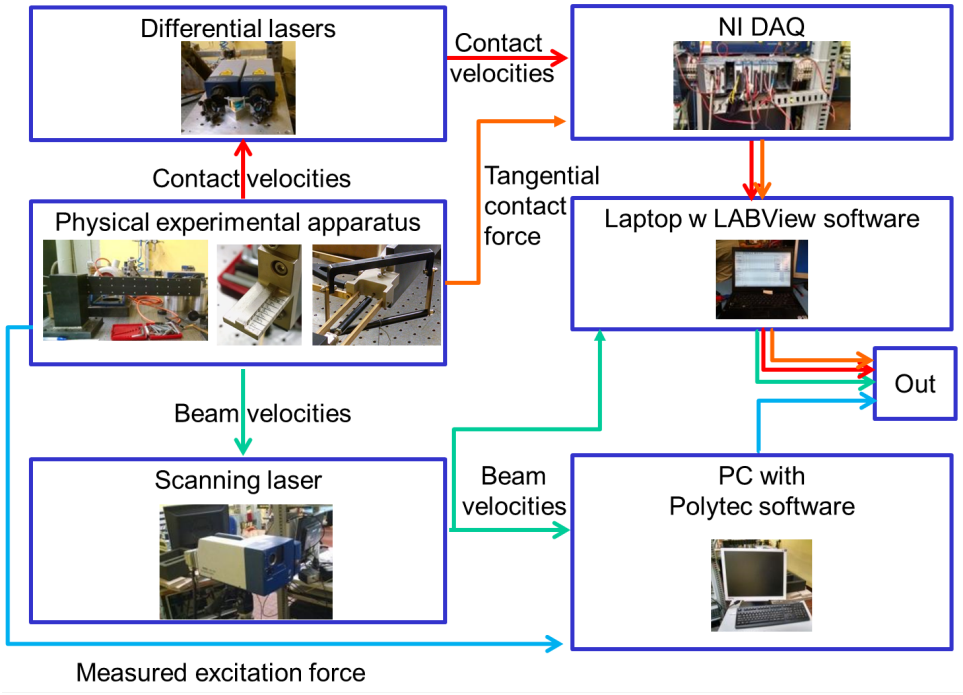

Figure 3.9. Experimental data collection setup

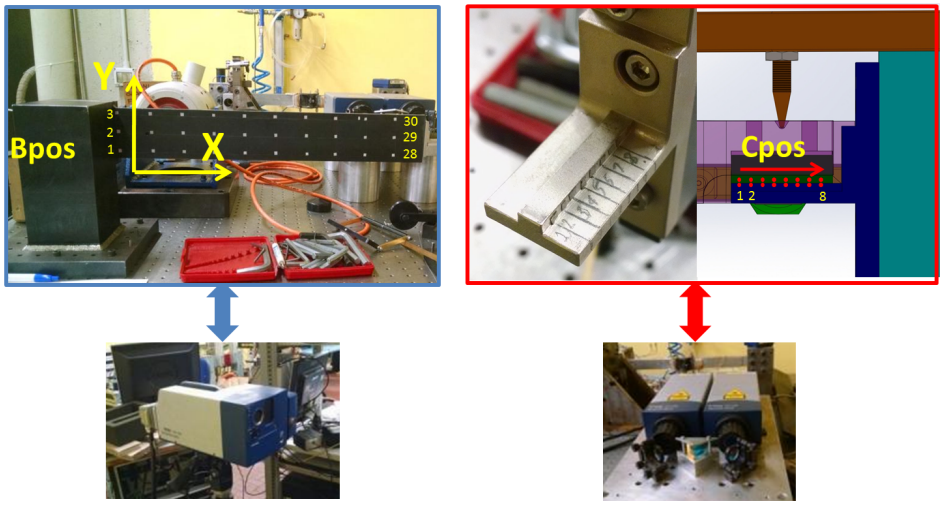

Figure 3.10. Measurement positions on beam (Bpos) and contact (Cpos)

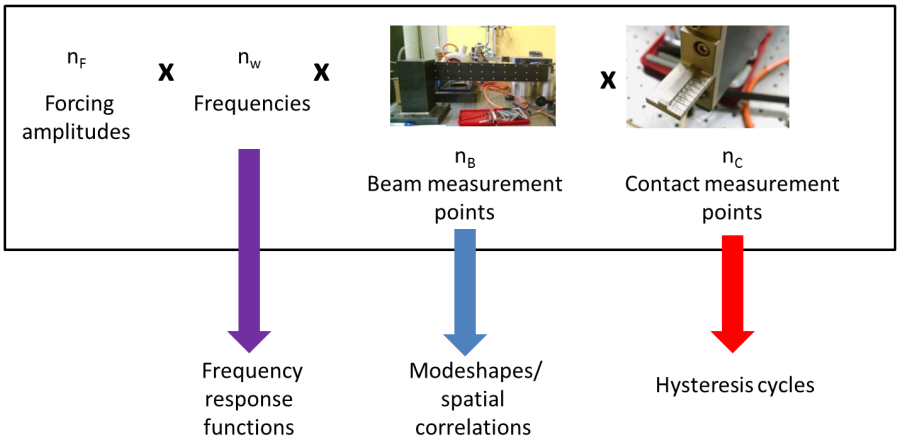

Figure 3.11. Test matrix variables

response may be measured at different beam positions at n_B different points, with other variables and test conditions being held constant to obtain modes under a linear operating condition or the spatial correlations under a nonlinear condition. Responses may be measured at n_C different points across the contact to gather relative displacements at those points, which may be used along with the measured tangential contact force to plot hysteresis cycles.

3.2 Experimental results and analysis

3.2.1 Experimentally observed modes and responses

The first free mode at different forcing amplitudes and the fully stuck mode of the beam, captured using the scanning laser vibrometer are shown in Figs. 3.12 and 3.13 respectively. The normalized free beam modes at different amplitudes are essentially the same. Also, as expected, the first mode is in bending for both the free and stuck cases and the variance of displacement along the Y-direction (as described in Fig. 3.10) of the beam is minimal. For further experimentation, only velocities along the centerline of the beam were measured, as they were sufficient to characterize the motion of the entire beam under the experimental conditions in the frequency ranges of interest.

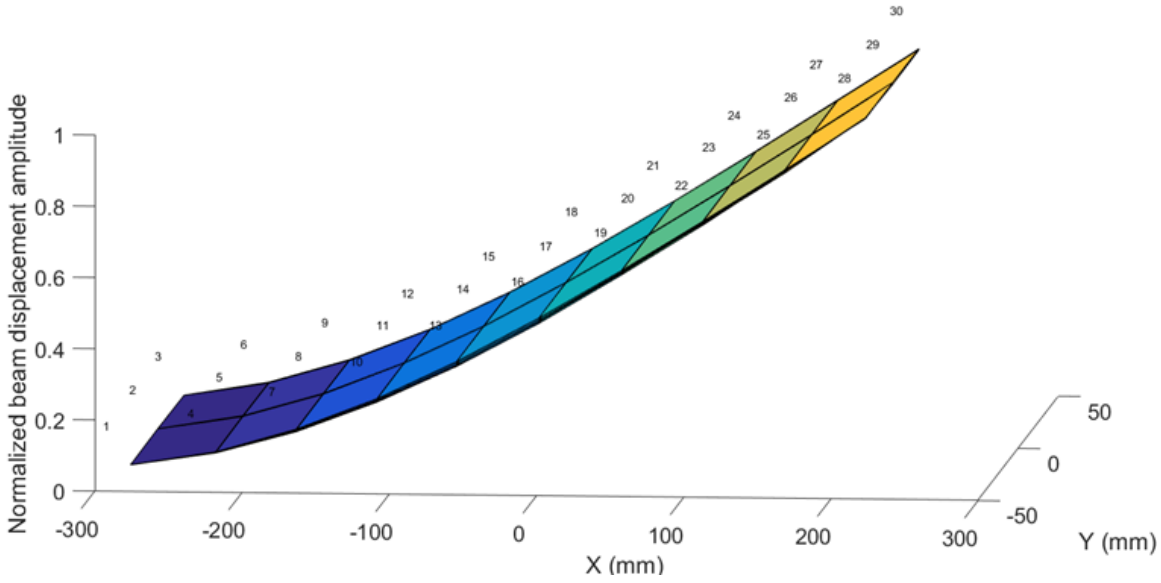

Figure 3.12. Free modes measured using scanning laser vibrometer

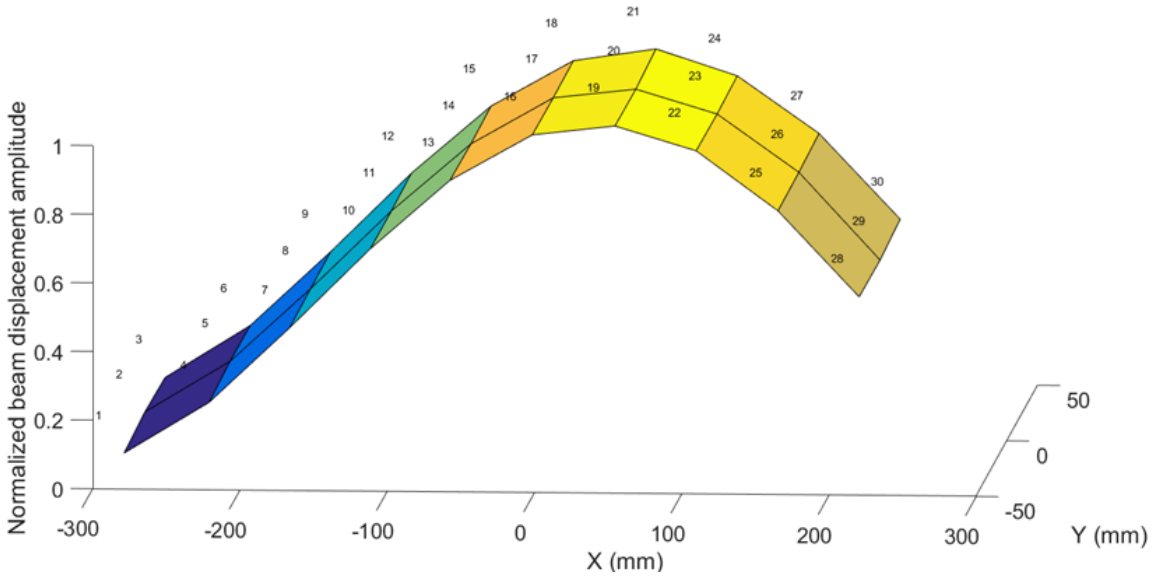

Figure 3.13. Stuck modes measured using scanning laser vibrometer

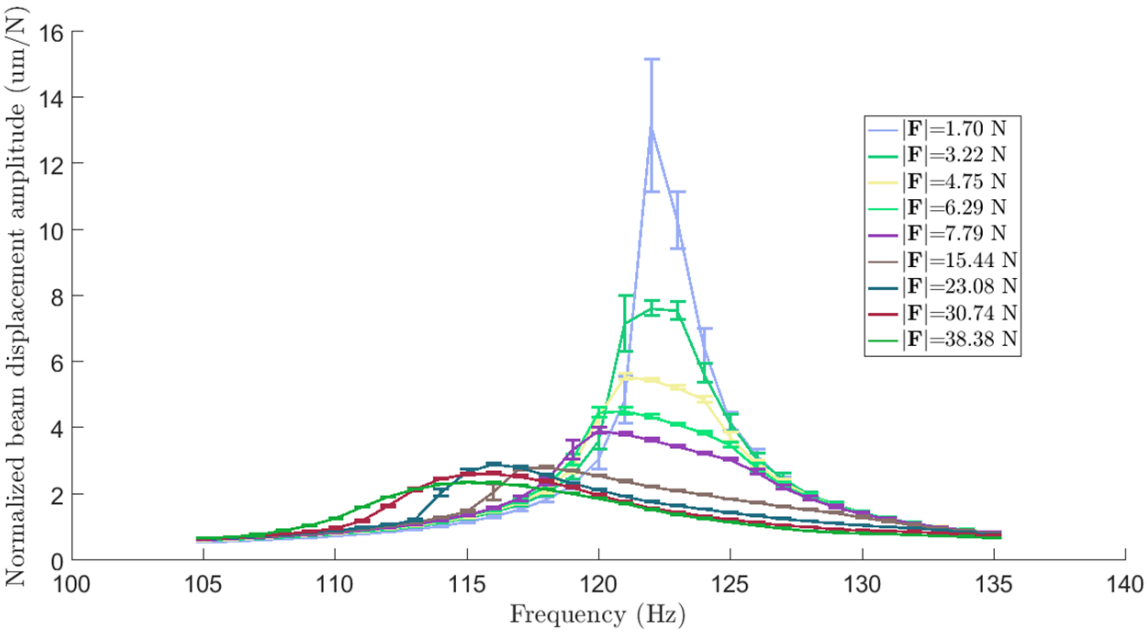

Figure 3.14. Frequency sweeps for free beam and beam with contact

The normalized frequency responses of the beam with contact enforced at different forcing amplitudes are shown in Fig. 3.14 for a point near the middle of the beam (Bpos 17). This response clearly exhibits nonlinear behavior and microslip with a marked decrease in resonant amplitude and frequency with increased forcing magnitude. The overall stiffness of the beam with the contact established is also much higher and the first bending mode frequency is consequently much higher. The resonant frequencies are also close to the simulated values mentioned before.

3.2.2 Estimation of contact parameters from experimental results

To identify the contact parameters from experimental results, first the material properties and constraint conditions near the beam root in baseline FE model were adjusted such that the fully stuck modes and modal frequencies of the fully stuck beam from the model matched those measured experimentally. Craig-Bampton component mode synthesis (CB-CMS) [8] was then used to obtain reduced free mass and stiffness matrices M_f and M_f from the FE model of the assembly, where the active degrees of freedom (DoFs) which are retained unchanged from the FE model

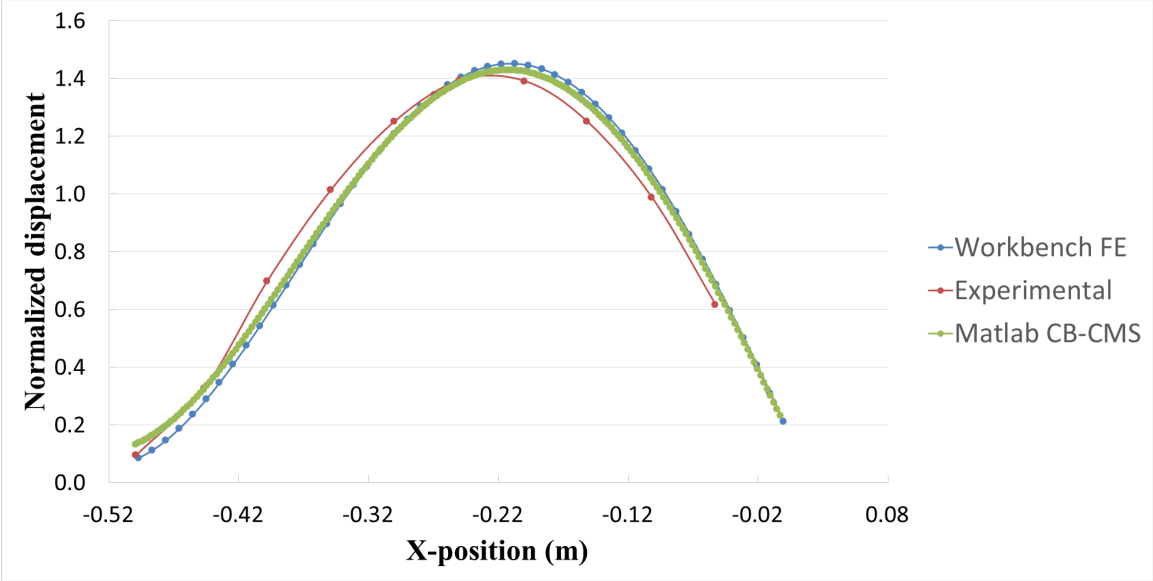

Figure 3.15. Comparison of first stuck mode obtained from experiment and simulations

include the nonlinear contact DoFs and the nodal DoFs corresponding to the locations where the excitation is applied and where displacements are calculated. The normalized first stuck mode from the experimental measurements, baseline FE model and CB-CMS are compared in Fig. 3.15 and are found to be a good match. The CB-CMS system matrices are used to formulate the equation of motion corresponding to the model in the frequency domain obtained using the harmonic balance method (HBM) [34, 35]:

$$\left[-(h.\omega)^2\mathbf{M}_f + (ih\omega m_\beta\beta + 1)m_{\mathbf{K}_f}\mathbf{K}_f\right]\bar{\mathbf{q}}^h = \bar{\mathbf{f}}_E^h + \bar{\mathbf{f}}_C^h \tag{3.1}$$

where h is the harmonic index, ω is the excitation frequency, β is linear proportional damping parameter, $\bar{\mathbf{q}}^h$ is the complex displacement vector corresponding to harmonic h, $\mathbf{f}_E^h$ and $\mathbf{f}_C^h$ are the complex excitation and contact force vectors corresponding to harmonic h. $\mathbf{f}_C^h$ has non-zero values only at DoFs corresponding to contact nodes corresponding to the tangential and normal frictional forces calculated at each node-pair as a function of the local relative displacement [31, 32, 35]. Parameters affecting the nonlinear dynamics are pre-multiplied by multipliers m with subscripts

representing the modified quantities. In addition to the multipliers shown in Eqn. (3.1), we have multipliers for contact parameters which influence the contact force $\mathbf{f}_C^h$, namely $\mathrm{k_x}$ and $\mathrm{k_z}$ for tangential and normal contact stiffness and μ for coefficient of friction respectively, which are implemented directly in the contact model. The multipliers form a part of the parameter space that is identified to determine the contact characteristics. The rest of the quantities which are identified determine the normal load distribution at contact. Initial FE simulations showed that the normal load distribution is fairly uniform perpendicular to the beam axis and varies primarily along the beam axis. Hence, the distribution was parametrized by specifying the relative magnitudes of normal load at 5 points along the contact surface such that the distribution over the surface could be obtained by interpolating linearly between the points and constraining the sum of load values over the entire contact surface to the known total load value measured during experiments. The 5 multipliers and 5 normal load parameters were then identified by treating them as optimization variables in a problem where the objective was to minimize the norm of the error between the experimentally observed and simulated responses at various selected frequencies and excitation levels. Eqn. (3.1) was solved using trust-region nonlinear algebraic equation solvers and the alternating frequency-time technique [36], at every step of the optimization procedure for identifying the multipliers, which itself also uses a gradient based optimization technique.

Figures 3.16-3.19 compare the optimized simulated responses with the experimentally measured responses. As shown in Fig. 3.16, the optimization case where only peak responses at every excitation level is used to calculate the error for optimization cost is not very effective with the optimized simulated responses varying significantly from the experimental results, both in terms of peak response and peak frequency. From these simulations, it was gleaned that the problem was not very sensitive to $m_{\mathrm{k_z}}$ which was dropped for subsequent simulations. In Fig. 3.17, where 3 points near the peak are used for error calculation better results are obtained at higher excitation levels, but the peaks of simulated optimum are far off from the experimental case for lower excitation levels. An attempt was made to enforce the m_β value estimated at the highest excitation

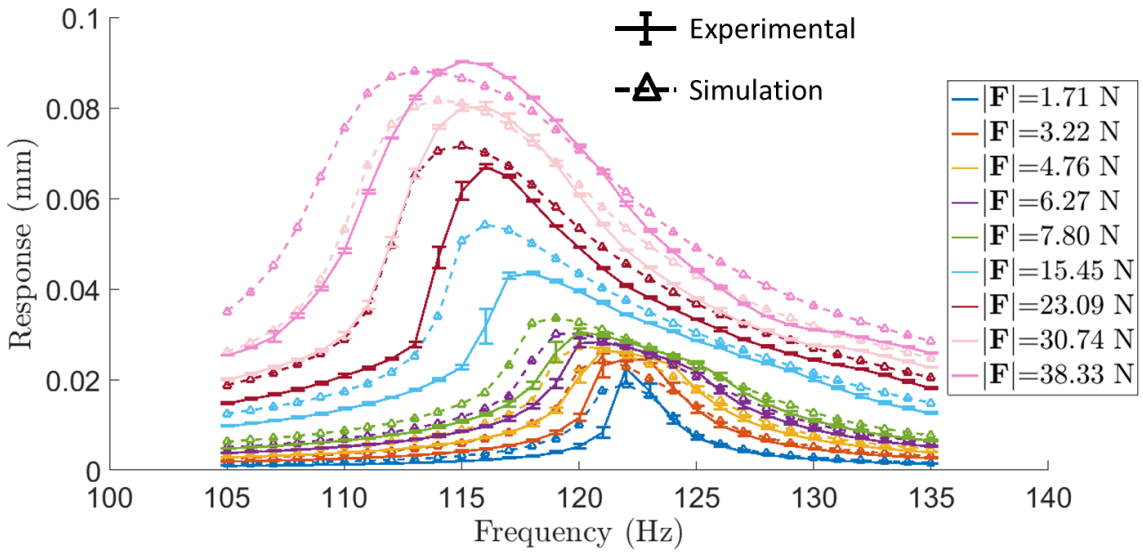

Figure 3.16. Optimized simulated responses using errors at single peak frequency vs experimental responses for beam

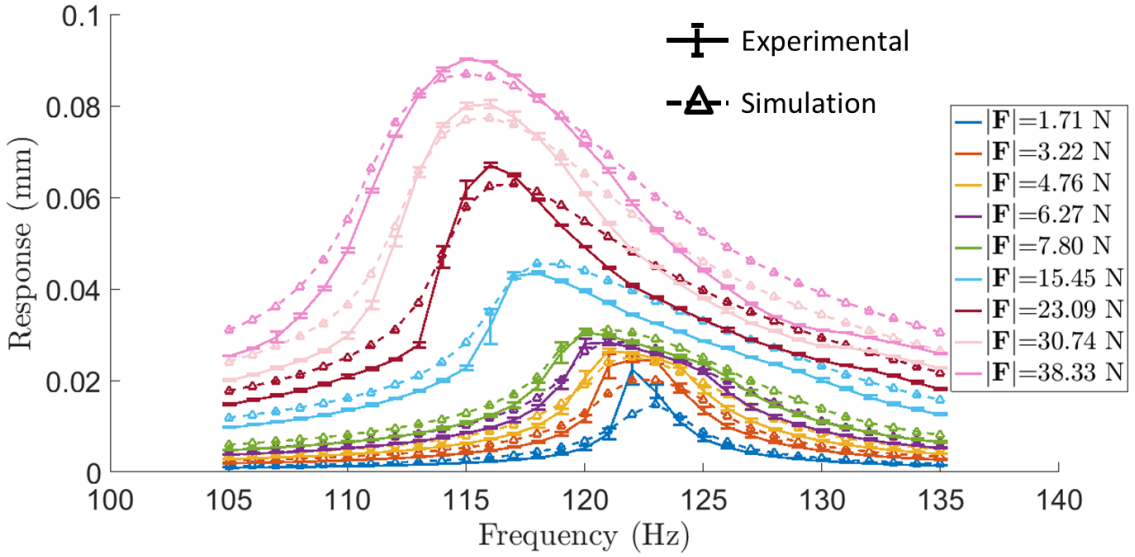

Figure 3.17. Optimized simulated responses using errors at 3 frequency points near peak vs experimental responses for beam

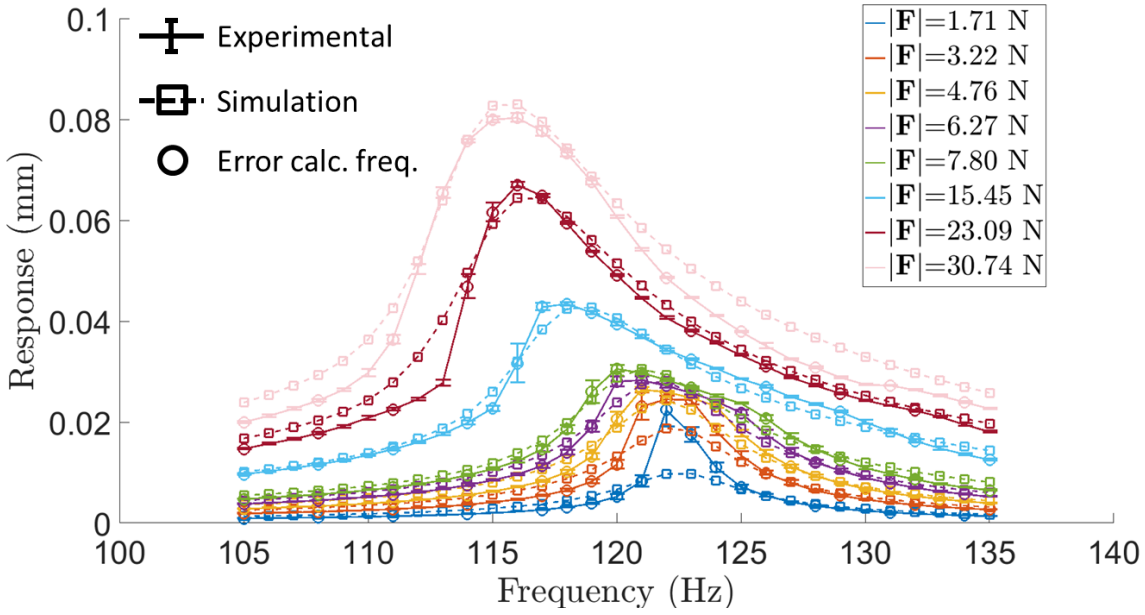

Figure 3.18. Individually optimized simulated responses at each excitation level vs experimental responses for beam

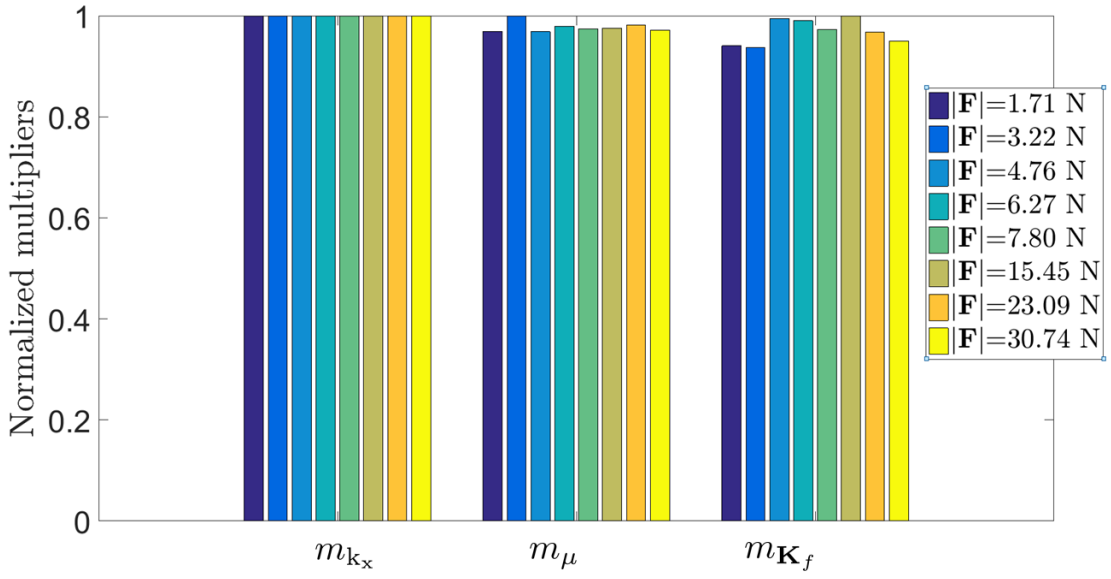

Figure 3.19. Comparison of normalized values of estimated multipliers obtained by individual optimization at each excitation level

level and optimize the rest of the parameters at individual excitation levels with error calculated at multiple frequencies as shown in Fig. 3.18. The simulated frequency responses matched well with experiments in this case. However, as seen in Fig. 3.19, the optimized values of m_f varied with the excitation level. The optimized static normal load distributions were also found to be significantly different at low and high excitation amplitude cases. Hence, the identified parameters from Fig. 3.17 are used for further analysis in this study. For this model, higher percentage errors may be observed at both the resonance of the lowest excitation amplitude case and the off-resonance amplitudes of the high excitation amplitude cases where the response amplitudes are low. Although the identified model fits the data poorly for lower magnitude responses, it captures the peak amplitudes in microslip well, which is the primary region of interest in this study. These errors may be due to unmodeled effects such as the contact of the main beam with the support and variance of response at low amplitudes, which was proportionally much higher for the low amplitude cases in comparison to the high amplitude cases.

3.2.3 Verification of AMP procedure

In one of the experiments, the response of both the beam and the contact was measured at steady state with the contact at microslip near resonance at 112 Hz. The 5 most dominant POMs calculated from the time responses of the beam are denoted as θ_{j} $(j = 1, 2, \cdots, 5)$ are shown in Fig. 3.20. A measure of the relative dominance of the POMs in the response are the corresponding eigenvalues λ_{POM} associated with them, which are plotted in Fig. 3.21, with the corresponding bar colors representing the POMs in Fig. 3.20.

Figure 3.22 shows the nodes on the contact patch in the FE model, where contact conditions are applied. Nodes of different colors represent different groups of nodes based on their proximity to the nearest contact displacement measurement point in the experiments. Since, measurements were made at only discrete points along the edge of the contact patch the true contact conditions could not be determined without uncertainty. Instead, estimates of the contact conditions were obtained

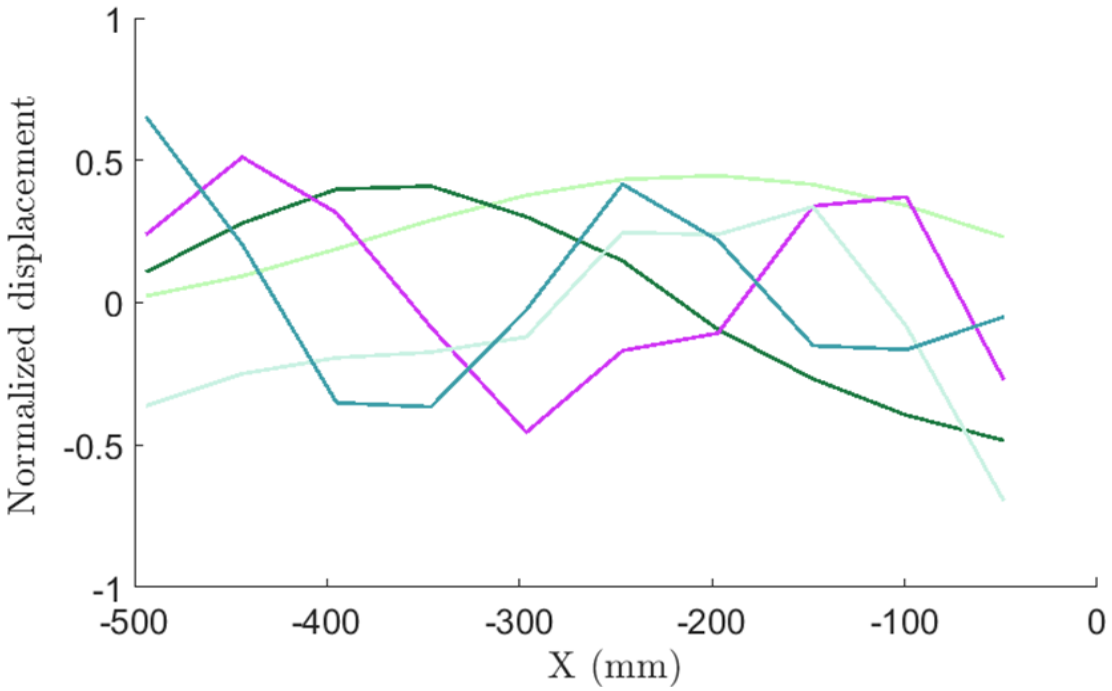

Figure 3.20. POMs obtained from experimental responses near resonance at microslip

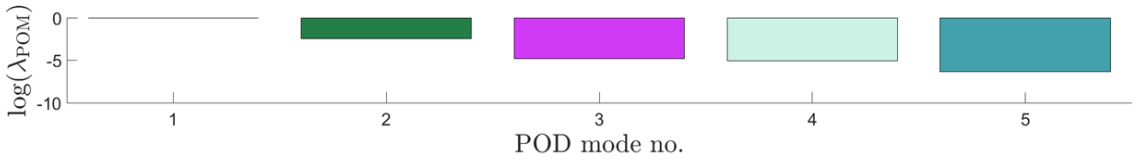

Figure 3.21. Eigenvalues of POMs

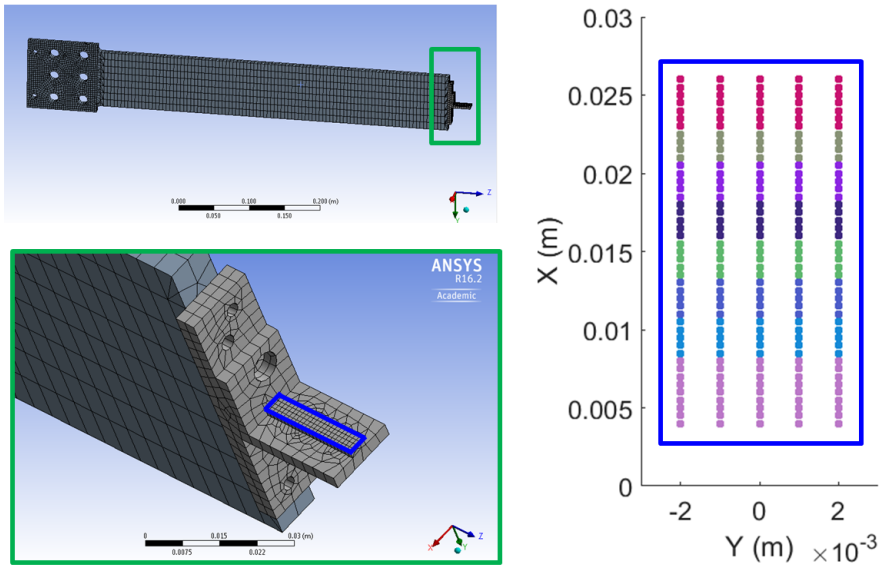

Figure 3.22. FE model of experimental rig

by applying a threshold value on experimentally measured displacements near the contact patch. If the relative displacements were close to zero for a particular measurement, the group of contact nodes near that measurement point was assumed to be stuck at that point in time. If the relative displacement was above the threshold, the corresponding contact nodes were assumed to be in slip. These estimated boundary conditions (BCs) were calculated for the entire period of oscillations from measured experiments and were arranged in order from stick to gross slip. Then AMP modes were calculated from the first 5 BCs closest to stick. Both the experimentally measured stuck mode and estimated AMP basis were compared to POMs using error metrics. e_{st} captures the percentage error between a POM and its corresponding projection on the stuck mode and is defined as follows:

$$e_{st} = \frac{||\theta_{\mathrm{j}} - \psi\psi^{\dagger}\theta_{\mathrm{j}}||_2 \times 100}{||\theta_{\mathrm{j}}||_2} \tag{3.2}$$

where θ_{j} is the POD mode being considered, ψ is the first stuck mode, $\dagger$ represents the pseudo-inverse of a matrix or vector and $||.||_2$ is trhe 2-norm a vector. e_{AMP} is a similar metric which

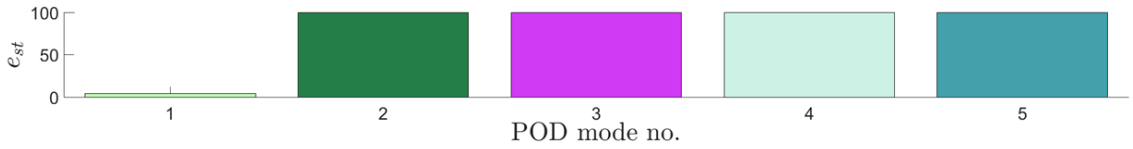

Figure 3.23. Projection error of POMs on experimentally measured stuck mode

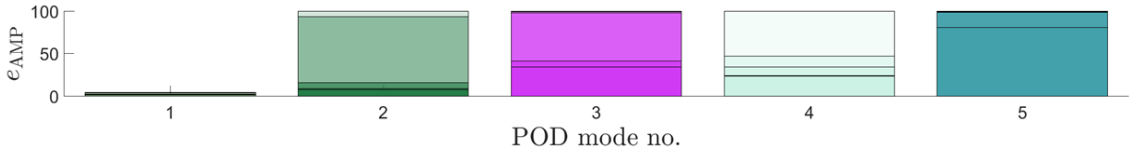

Figure 3.24. Projection error of POMs on estimated AMPs

captures the percentage error between a POM and its corresponding projection on an AMP basis and may be calculated as:

$$e_{\mathrm{AMP}} = \frac{||\theta_{\mathrm{j}} - \mathbf{\Phi}_{n_\chi}\mathbf{\Phi}^{\dagger}_{n_\chi}\theta_{\mathrm{j}}||_2 \times 100}{||\theta_{\mathrm{j}}||_2} \tag{3.3}$$

where $\mathbf{\Phi}_{n_\chi}$ is a matrix whose columns are composed of n_χ AMP reduction basis vectors.

Figures 3.23 plots e_{st} for all the POMs. It may be seen that while, the stuck mode captures the dominant POM well, the other POMs are completely orthogonal to it. It was shown in chapter II that the less dominant POMs might contribute to the dynamics due to important effects at contact surfaces where the displacements are small. Figure 3.24 shows the projection error of POM on AMPs. Each POM is projected onto AMP bases increasing size formed by progressively appending the bases with the 5 estimated AMP modes. The correspondingly decreasing projection errors e_{AMP} as n_χ varies from 1 to 5 for each POM are shown as bars of increasing opacity in Figure 3.24, with the bar color representing the POD mode being projected. It is seen that the AMP basis is able to capture a significant portion of the first 2 POMs. While, this analysis establishes that the AMPs do capture some of the spatial coherences seen in the nonlinear response, this is not sufficient to prove that they can also capture the dynamics.

To prove that the dynamics may be reproduced in a reduced space by projection on the AMPs,

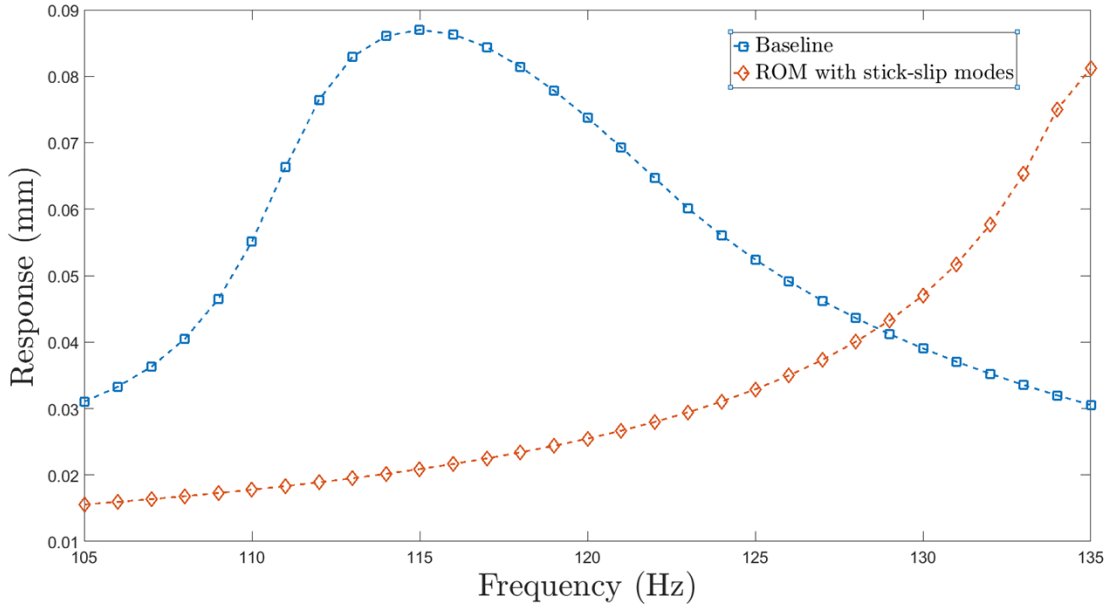

Figure 3.25. Response of ROM created using full stick and gross slip modes for |**F**|=38.33 N vs baseline

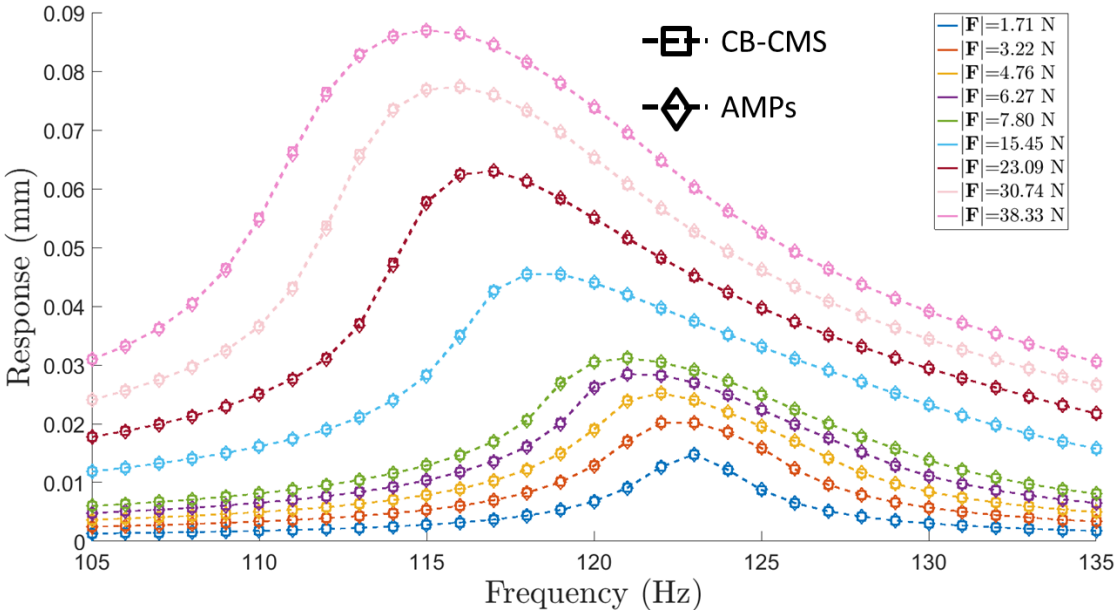

Figure 3.26. Response of AMP ROMs vs baseline

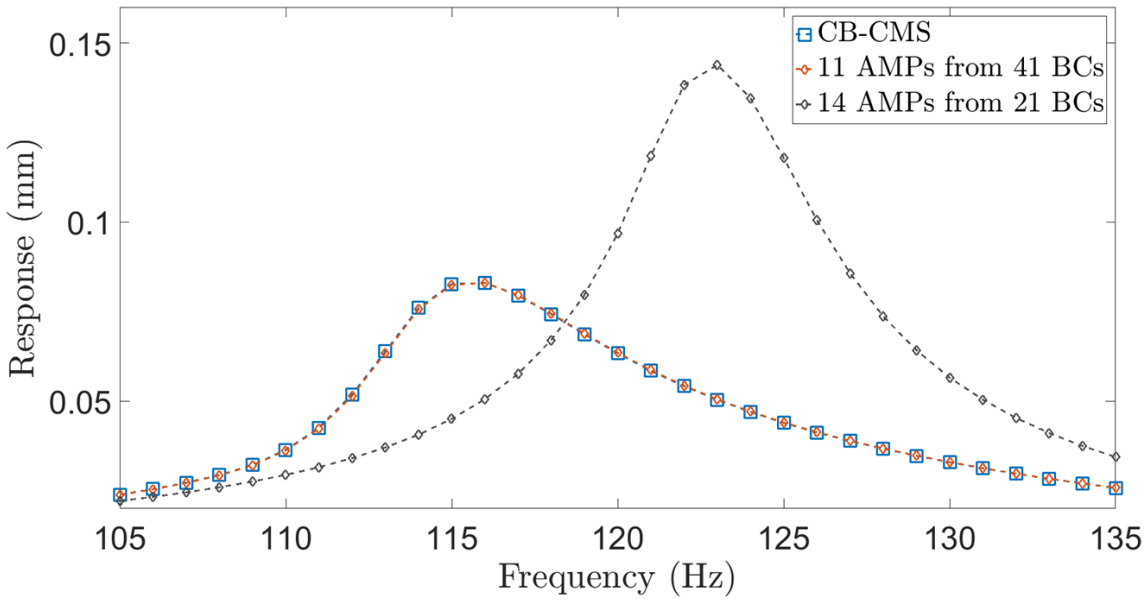

Figure 3.27. Responses of AMP ROMs created using different contact conditions for $|\mathbf{F}|$=30.74 N

full dynamic simulations were carried out using realistic contact parameters estimated in section 3.2.2. Baseline responses of the CB-CMS model augmented with contact models at all the contact nodes were obtained. Then a ROMs were developed by projecting these dynamics onto a basis consisting of only the stick and slip modes. Figure 3.25 shows that at a high excitation amplitude of $|\mathbf{F}|$=38.33 N the ROM using stick-slip modes only fails to capture the nonlinear response of the baseline, proving that the reduction problem is not trivial and that the nonlinear dynamics cannot be estimated simply by using the limiting linear conditions. Another ROM was developed by projection onto the AMP basis consisting of 11 AMPs calculated from 41 BCs. Figure 3.26 shows that the responses obtained from this AMP ROM with far fewer DoFs than the baseline, almost perfectly approximates the baseline response at all excitation levels. Figure 3.27 shows that another AMP ROM created using only 21 BCs but containing more basis vectors (14) is unable to capture the baseline microslip response for an excitation of magnitude $|\mathbf{F}|$=30.74 N. This result validates the assumption that the BCs arising out of the spatial coherences in the nonlinear interactions at the contact interface play a significant role in the dynamics and must be estimated

accurately for model order reduction.

3.3 Conclusions

An experimental rig with a non-point contact designed to operate in microslip, was used to conduct experiments to estimate contact parameters and validate the AMP method. An optimization method was used to minimize errors between simulated and experimentally measured responses. It was possible to successfully identify common contact parameters which could capture the maximum frequency response amplitudes across a range of excitation levels and consequently capture nonlinear damping effects. The predicted responses using estimated parameters were compared to experimentally measured values. Some poor fits were observed at regions of low response amplitudes, which may be due to higher uncertainties and measurement errors in these regions. However, the responses matched the measurements well near resonance peaks at higher excitation amplitudes where the microslip phenomenon being investigated was dominant. Experimentally measured responses were used to calculate POMs of the system, which were then compared to AMP basis vectors generated using contact conditions estimated from experimental measurements. The AMP vectors were found to not only capture the dominant POMs, but also a significant portion of the less dominant POMs which may be necessary to capture not only the bulk response but also the nonlinear dynamics of the system. AMP ROM responses simulated using realistic estimated contact parameters were found to match the baseline responses, validating the procedure for practical applications. ROMs based on projection on stick and slip modes as well as on an AMP basis generated from insufficient number of boundary conditions, were found to not capture the dynamics or predict the response accurately. Hence, the underlying assumptions of the AMPs, namely the existence of spatial correlations in nonlinear response, the boundary condition based reduction basis formulation were validated using experimental measurements.

CHAPTER IV

Effects of Contact Mistuning on Shrouded Blisk Dynamics

The effect of small and large variations of design parameters or material properties in different blades or sectors of a nominally cyclically symmetric tuned structure such as a bladed disk (blisk) has been a popular topic of research in turbomachinery in the past few decades. Even small inter-blade variations or mistuning can radically modify the dynamic response of blisks in certain regimes of operation [5, 75, 98]. Thus, quantifying the effect of such a variation, which often arises out of unavoidable natural uncertainties in material properties and manufacturing processes, is of significant interest to designers. Presently, the widely accepted method for obtaining a comprehensive understanding of the effect of these uncertainties, is to conduct a large number of simulations with different systems generated from the nominal tuned system by altering a mistuning parameter such as material stiffness or density in each sector of the blisk either randomly or deterministically [1, 4].

To reduce the prohibitive simulation times that would be involved in generating finite element models of blisks and then simulating them, different reduction techniques exist depending on the nature of mistuning parameter. Reduction using a subset of nominal system modes (SNM) is a popular method for small mass and stiffness mistuning [14]. Component mode mistuning (CMM) has been used to study stiffness and damping mistuning [16]. However, these SNM and CMM methods were developed for model reduction of blisks with linear degrees of freedom (DoFs) only. Turbine

blisks are often designed with mechanisms such as under-platform dampers (UPDs) or shrouds which provide dynamic damping through a nonlinear Coulomb friction mechanism at a certain interface. In addition to mistuning in the blade parameters which render the linear system matrices non-cyclic, it is also possible to introduce a variation in the parameters defining the localized contacts at the interfaces. The nonlinear ordinary differential equations (ODEs) which represent a structure with contacts may be solved using techniques such as harmonic balance method (HBM) [34, 35, 38, 42, 43] which reduce temporal complexity of such problems but do not reduce the number of nonlinearities. The development of a method to reduce the spatial nonlinear degrees of freedom called adaptive microslip projection (AMPs) is detailed in chapter II of this work. However, the results shown there assume tuned localized contacts throughout the blisk. Research to understand the effects of mistuning in both the blades and contact parameters of the interfaces have been conducted in the past [22, 40, 49]. However, only lumped or single-node contact models were used for modeling friction interfaces in these studies. Also, most existing studies focus on the mistuning of damping characteristics in UPDs. It is known that the distribution of linear resonant frequencies of shrouded blisks with stuck interfaces for different nodal diameters of excitation differs characteristically from those for UPDs. There is a significant difference between modal frequencies of the same family even at higher engine order in the case of shrouded blisks [97]. Therefore, it is of significant interest to research in this field, to analyze how the mistuning of contact parameters in shrouds will influence the system response in microslip.

In this chapter, the effect of mistuning in the stiffness parameters of localized contacts at the shrouds of an otherwise tuned blisk is studied, thus separating the effect of contact mistuning from that of mistuning due to inter-blade variability. The same nominal shrouded blisk as that used in chapter II is used for this study. It has 27 blades with 25 pairs of node to node contacts at each shroud interface. A Craig-Bampton component mode synthesis (CB-CMS) [8–10, 12] method is applied to the finite element model to reduce the linear degrees of freedom in the model. The nonlinear contact DoFs are retained as master nodes without any reductions during the CB-

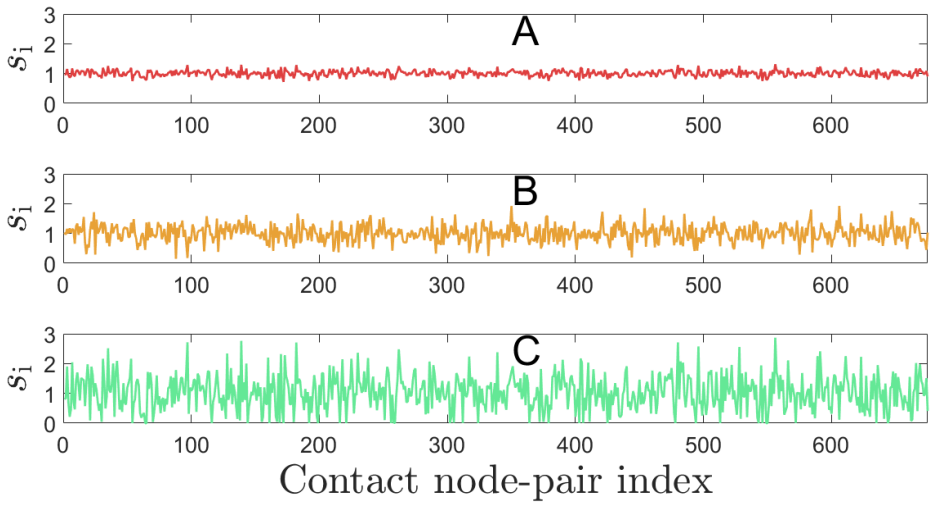

Figure 4.1. Mistuning patterns:
A ($\sigma = 0.1$),B ($\sigma = 0.3$), C ($\sigma = 0.6$)

CMS procedure. Localized contact is simulated by using contact models at each of these DoFs. HBM is used to simulate the nonlinear model and obtain the frequency response of the structure to a traveling wave excitation. The contact stiffness parameters are varied randomly both across and within sectors. The effect of the parameter variations on maximum response amplitude and frequency are analyzed. Probabilistic analyses are carried out by fitting a Weibull function to probabilistic distributions of amplification factors obtained from Monte Carlo simulations of linear and nonlinear forced responses. The study provides a better understanding of the role of mistuning due to local and global variations of friction damping parameters in dictating the response of a blisk structure.

4.1 Forced response simulations

4.1.1 Contact mistuning

For the tuned blisk, all the contact surfaces of the blisk are assumed to have the same total normal and tangential stiffness. However, this total stiffness is not distributed uniformly among

the local contact stiffnesses used in the contact models between different node-pairs on that surface. Stiffnesses used in contact models between node-pairs on the corners of contacting surfaces and nodes on the edges are 0.25 and 0.5 times those used on interior node-pairs respectively. In this way, the local contact stiffness at a node is proportional to the area of contact surrounding that node. This distribution is the same at all contact surfaces for the tuned blisk. For a mistuned contact case each tuned nodal contact stiffness (indexed by i) is multiplied by a scaling factor s_{i} to obtain the mistuned stiffness. Normal and tangential contact stiffnesses are assumed not to vary independently of each other and therefore, the same scaling factor is applied both stiffnesses at each node. Thus, for a randomly generated mistuning pattern, at each contact, an independent random variable s_{i}, generated from a Gaussian distribution with a mean of 1 and standard deviation σ which determines the level of mistuning is used. s_{i} is bounded to be non-negative since the contact stiffness cannot be negative. This bound means that the actual distribution of s_{i} is slightly different from that of a Gaussian random variable with a spike in its probability density function at 0. For reference, numerically calculated values of the mean and standard deviation of the actual distribution for corresponding values of standard deviation σ of the generating distribution are presented in Table 4.1.

Table 4.1. Mean and standard deviation of actual distribution of s_{i} calculated using 10^8 samples

σ	Actual mean	Actual std. dev.
0.1	1.0000	0.1000
0.2	1.0000	0.2000
0.3	1.0001	0.2999
0.4	1.0008	0.3978
0.5	1.0043	0.4900
0.6	1.0119	0.5751
0.7	1.0241	0.6541
0.8	1.0404	0.7281

For low values of variance (of the generating Gaussian distribution), zero values of s_{i} are very

rare. Thus, the mean and standard deviation of the distribution of s_{i} do not differ significantly from those of the generating variable for low values of σ. For higher values of σ, the mean is slightly higher than 1 and the variance slightly lower than that of the generating function. However, the trends observed in blisk response with the level of mistuning are the same. In this study, the mean and standard deviation of the generating Gaussian distribution are used when referring to the s_{i} random variable. Three such mistuning patterns A,B and C, picked from sets with different levels of mistuning standard deviation, are shown in Fig. 4.1. Case C has some s_{i} at 0, which indicates a separation at those nodes. The coefficient of friction μ is the same at all locations and all surfaces for both the tuned and mistuned case. Even though the mistuning is introduced in the contact stiffness, due to the nature of the microslip the values of the contact stiffness actually affect the damping of the blisk more significantly than the response frequency [35, 97]. Hence, the range of values of mistuning standard deviation at which significant effect is observed on the response statistics is of the order of the standard deviations of standard deviations of damping mistuning in linear blisks [17].

4.1.2 Microslip responses

To simulate the contact pre-stresses due to factors such as thermal effects and design interferences, constant equal and opposite normal forces are applied to each contact node-pair. The normalized responses are calculated for different levels of microslip indicated by the dimensionless parameter $\mu|\mathbf{F0}|/|\mathbf{F}|$ using the same procedure as described in section 2.3.1.

The frequency versus nodal diameter plots for the tuned blisk in full stick and gross slip cases are shown in Figs. 4.2 and 4.3. Examples of the response of the tuned and mistuned systems with the contact mistuning patterns in Fig. 4.1 are shown for three different combinations of forcing scenario, frequency range and microslip conditions in Figs. 4.4, 4.5 and 4.6. Figure 4.4 shows the EO 1 excitation response with $\mu|\mathbf{F0}|/|\mathbf{F}| = 13500$, near the ND 1 stuck mode belonging to the first family (see circle with solid line in Fig. 4.2). Figures 4.5 and 4.6 show the EO 12

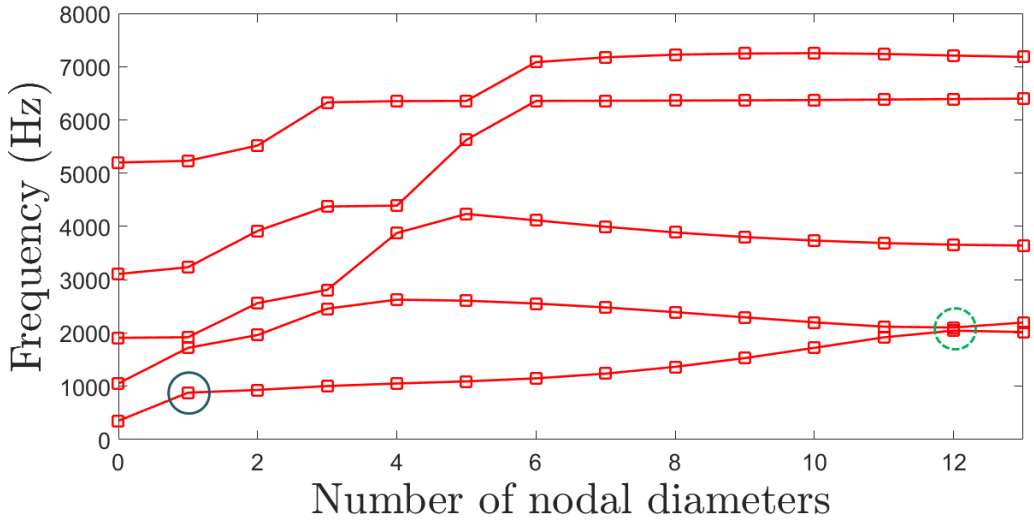

Figure 4.2. Frequency vs no. of nodal diameters for tuned blisk in full stick

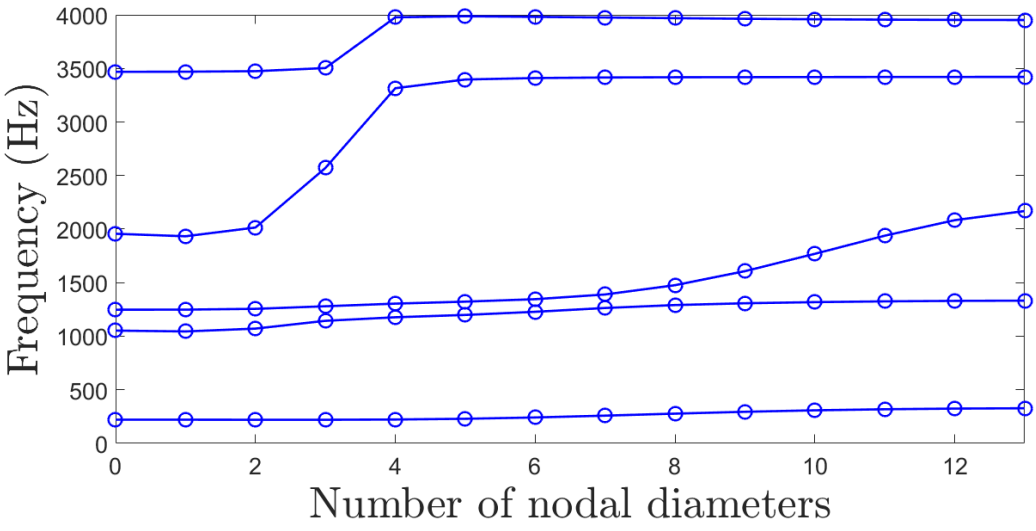

Figure 4.3. Frequency vs no. of nodal diameters for tuned blisk in gross slip

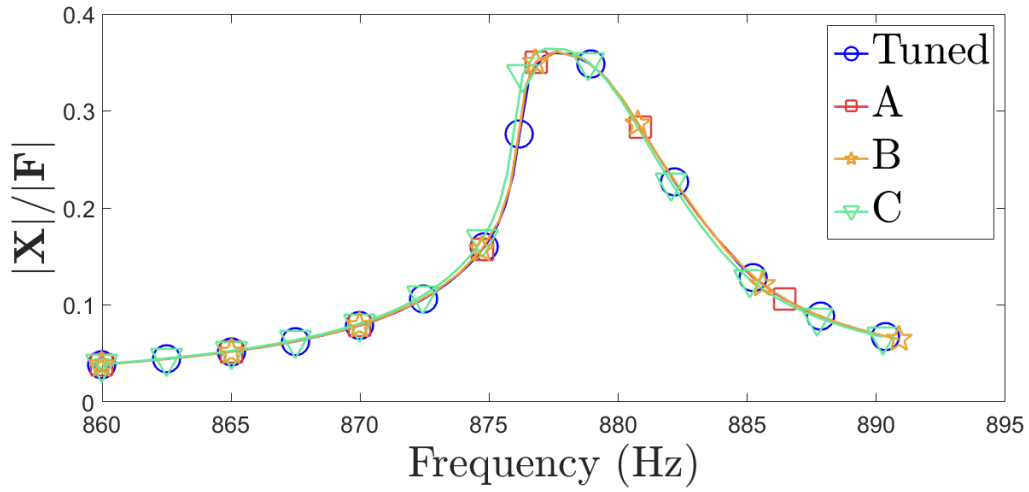

Figure 4.4. Response to EO1 excitation $\mu|\mathbf{F0}|/|\mathbf{F}| = 13500$

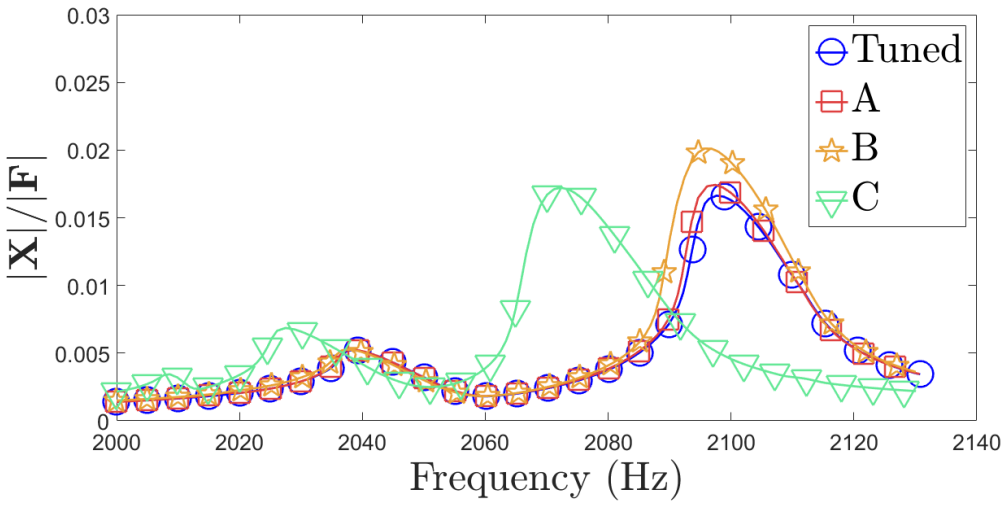

Figure 4.5. Response to EO12 excitation $\mu|\mathbf{F0}|/|\mathbf{F}| = 5400$

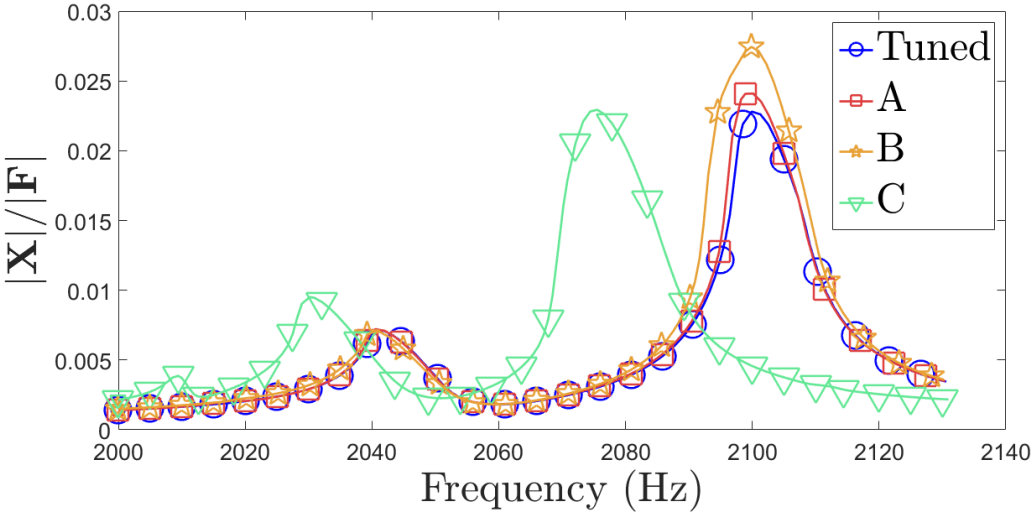

Figure 4.6. Response to EO12 excitation $\mu|\mathbf{F0}|/|\mathbf{F}| = 9450$

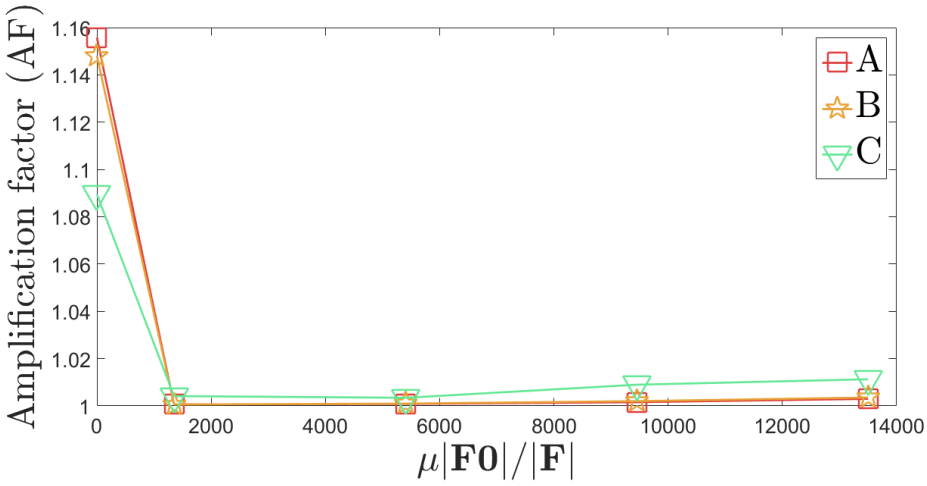

Figure 4.7. AF vs $\mu|\mathbf{F0}|/|\mathbf{F}|$ for EO 1 excitation (one simulation per point)

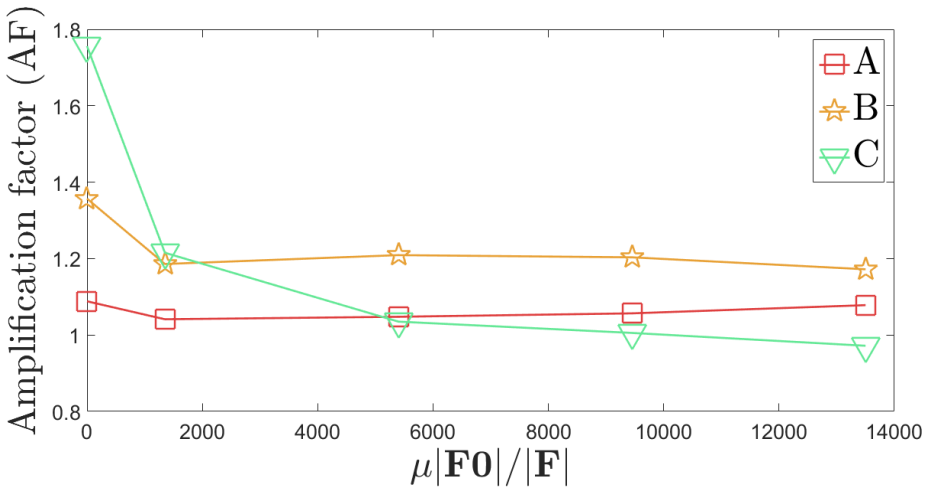

Figure 4.8. AF vs $\mu|\mathbf{F0}|/|\mathbf{F}|$ for EO 12 excitation (one simulation per point)

excitation response for $\mu|\mathbf{F0}|/|\mathbf{F}| = 5400$ and $\mu|\mathbf{F0}|/|\mathbf{F}| = 9450$ in a frequency region where ND 12 stuck modes from both the first and second families contribute to the response (see circle with dashed line in Fig. 4.2). In Figs. 4.4 - 4.6 the markers do not represent the actual frequency resolution but are simply aids to distinguish between the lines which are composed of small straight segments connecting the solution points. The maximum is picked from these solution points. The specified minimum frequency resolution was 1 Hz for EO 1 cases and 3 Hz for EO 12 cases. In practice, the actual frequency resolution is much higher near the peaks when the response is not well damped. The amplification factor (AF) is defined as the ratio of the maximum normalized mistuned response to the maximum normalized tuned response in the frequency region of interest and may be calculated from the responses. The AFs calculated from single simulations of systems with mistuning patterns shown in Fig. 4.1, at different levels of microslip, are displayed in Figs. 4.7 and 4.8. Values at $\mu|\mathbf{F0}|/|\mathbf{F}| = 0$ correspond to the gross slip condition. This shows that the AF obtained is dependent on the response frequency region and the EO of excitation. It may be seen that even at higher σ no significant amplification is seen for EO 1 responses. EO 12 responses show significant AFs compared to the EO1 case. For unshrouded blisks it is generally agreed in the literature [17, 76] that regions of high modal density containing modes from multiple families, also

known as veering regions, are regions of mixed disk and blade motion allowing for higher energy transfer between the blades and disk and higher amplification factors. In the shrouded blisks, the energy transfer between the blades can occur not only through the disk but also through the shrouds and these veering regions can be found at higher nodal diameters as well. The EO 12 region of high modal density is one such case and a similar argument can be used to explain the high amplification factors observed in this region. Also the nature of the variation versus the level of microslip ($\mu|\mathbf{F0}|/|\mathbf{F}|$), changes with mistuning pattern A to C (increase in σ). For case A EO 12 response, the AF decreases from stick as microslip level increases ($\mu|\mathbf{F0}|/|\mathbf{F}|$ decreases). However, for cases B and C the AF increases from stick as level of microslip increases. The nonlinear simulations carried out, include only the first harmonic in the dynamics in the HBM procedure (n_h=1). This is done in the interests of saving computational time, especially since a large number of analyses need to be performed. Even with a single harmonic solution of a single case, such as the one shown in Figs. 4.5 and 4.6 requires 3-10 hours based on factors such as CPU speed and frequency resolution. However, this is a reasonable assumption since it has been shown that for systems with weak nonlinearities such as Coulomb friction the first harmonic dominates the response [96, 97]. For the levels of mistuning and microslip investigated in this study only a few nodes at any surface may be in separation. The friction and normal forces estimated at these nodes might not be very accurate due to single harmonic retained in the HBM. However, most of the nodes on a surface are in contact and hence, the node in separation is affected by the elastic forces exerted on it by its neighbors preventing separation of the entire surface. At any given time, the calculation of the energy dissipated at contact and its effect on the damping which affects the response at the blade-tip is not expected to be affected significantly. The contribution of higher harmonics are likely to increase at high values of mistuning, values high enough to induce separation at multiple neighboring nodes at the same interface and for high levels of microslip; cases which are not investigated in this study. Also, the constant of proportionality used to determine the linear damping matrix from the stiffness matrix is very small (of the order of 10^{-7}). This is because, the

effect of damping provided by nonlinear forces is the primarily of interest in this analysis.

4.2 Probabilistic simulations

The entire possible range of complex dynamics and response behavior of a blisk with contact mistuning in microslip can only be properly captured through probabilistic analyses. Nonlinear analysis is extremely expensive in computation time and only a few simulations can be carried out. Also, to qualify the limits of nonlinear response behavior, the responses of the two linear systems which define its limiting cases may be used: the linear full stick and gross slip cases. Although popular reduction techniques mentioned earlier such as SNM and CMM [14, 16] exist for simulating linear mistuned blisks fast, they cannot be directly applied to shrouded blisks or do not offer significant reductions in this case. To accurately capture the effects of the mistuning patterns which are applied randomly to all the interfaces at all the sectors, a full wheel analysis in CB-CMS co-ordinates is carried out. However, this is still highly time consuming for a large number of simulations.

4.2.1 Weibull distribution

In general, to obtain the true statistics for the amplification factor of a mistuned blisk a large number of Monte Carlo (MC) simulations are necessary. However, in this case, simulation times are large and a number of different cases must be analyzed (e.g. different levels of microslip and mistuning). It would be impractical to carry out many simulations for each case. It has been shown in [76] by Bladh et al. that since the forced vibration response of mistuned linear blisks are bounded [5, 75, 76], the probability distribution of the amplification factors will approach a 3-parameter Weibull distribution. It was also shown that the overall response statistics of a mistuned linear blisk could be derived from a relatively small set (approximately 50 cases) of MC simulations. Hence, to obtain the response statistics of the full stick and full slip systems 100 MC simulations are run for the linear system. The AFs of these simulations are then obtained and fit to

a 3-parameter Weibull distribution whose cumulative distribution function (CDF) which is given in Eqn. (4.1) to the MC CDF.

$$F(x) = e^{(-(\lambda - x)/\delta)^{\beta}} \tag{4.1}$$

where x is a random variable and λ, δ and β are the Weibull distribution parameters to be fitted to the probabilistic data. In this case, x is the AF.

4.2.2 Statistical analysis

The EO 12 response for randomly mistuned blisks in full stick and microslip near the tuned second family stuck ND 12 frequency is analyzed and the AFs in the frequency range of 2,040-2,120 Hz are obtained for several σ. The second family is chosen as opposed to the first family as it is seen from forced responses such as the one in Fig. 4.6 that it responds more than the first family ND 12 mode. To validate if a Weibull fit to a small set of randomly generated cases does give us accurate statistics, 1000 MC simulations are carried out as a baseline by performing a linear analysis on 1,000 blisks with randomly generated s_{i} with $\sigma = 0.1$ and its CDF is obtained. The number of MC cases chosen for validation (1,000) is the same number as in [76]. Then, sets of 100 MC simulations (10 sets numbered 1 through 10) are taken from this superset and a Weibull distribution is fitted to each set using the method described in [76] to obtain one Weibull fit CDF for each set. Figure 4.9 shows the fits obtained from the different sets compared to the empirical CDF from the 1,000 MC simulations. The 50^{th} and 95^{th} percentile AF values obtained from these different fits are compared to the 1,000 case MC values in Fig. 4.10. It is seen that the Weibull fit AFs are quite accurate for the estimated percentiles. The accuracy of the 95^{th} percentile values are the most important since the highest values of the AF is the quantity which most concerns designers.

For nonlinear cases involving microslip, only 50 forced response simulations with different randomly generated mistuning patterns could be reasonably carried out for each probabilistic analysis. For the linear response the AF is bounded by the Whitehead limit [5, 75, 76]. No such limit

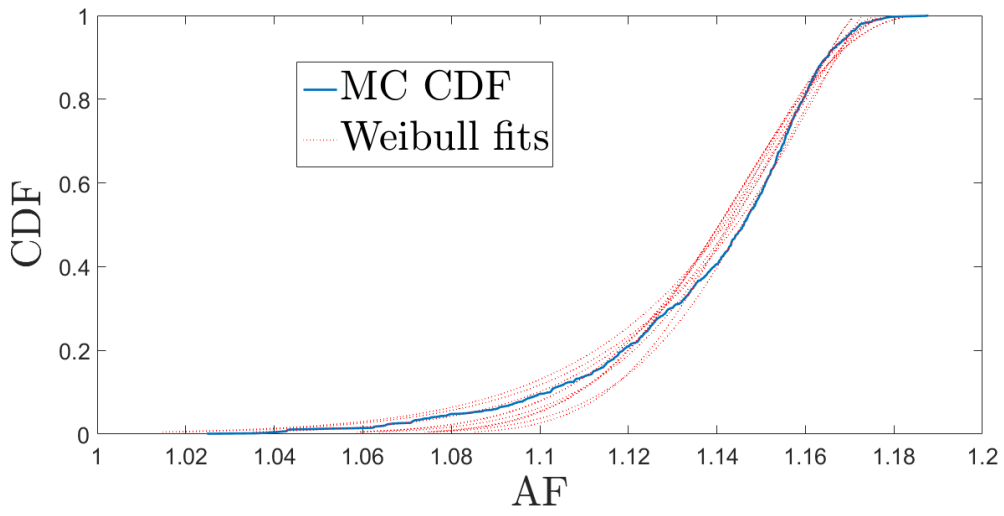

Figure 4.9. Weibull fit to 1,000 case MC CDF using sets of 100 cases for $\sigma = 0.1$

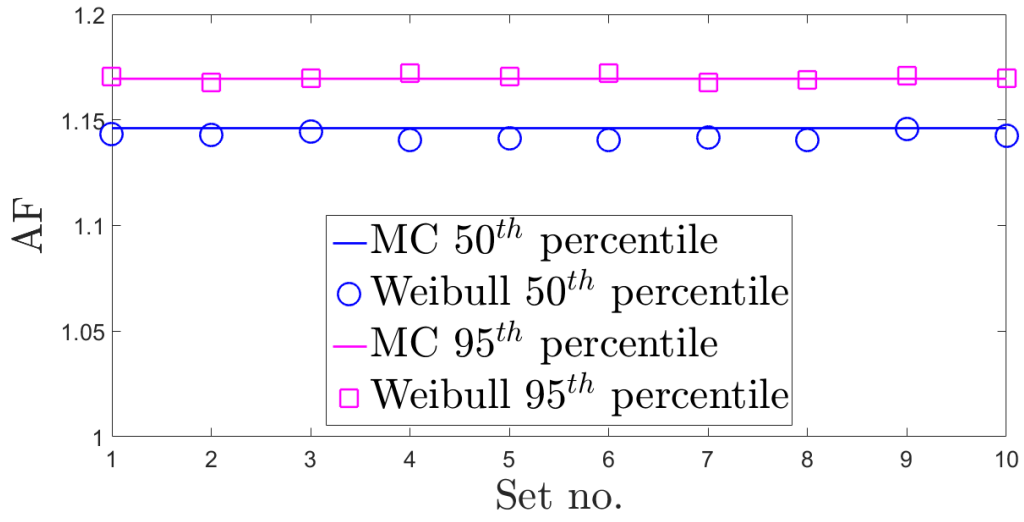

Figure 4.10. Percentiles obtained from Weibull fits using sets of 100 cases

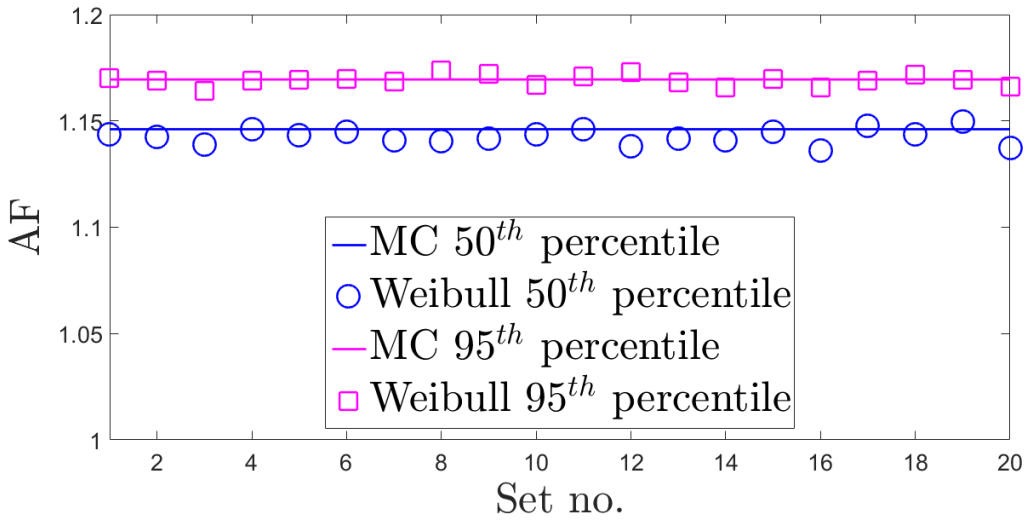

Figure 4.11. Percentiles obtained from Weibull fits using sets of 50 cases

has been established for nonlinear AFs. Without the criteria of bounded response it is not possible to state conclusively that the AFs for the nonlinear cases will follow a Weibull distribution [76] and that a fit obtained with few cases conclusively estimates the statistics. In this study, it was assumed that nonlinear response AFs follow a Weibull distribution and the statistics obtained from fitting the data were analyzed. It is also not possible to conclusively determine the number of MC cases that would be required to obtain accurate fits of a distribution for the microslip cases. This number can be obtained through a convergence study which requires very large amounts of computational time. However, since the microslip region investigated in this study are closer to the full stick linear case than the gross slip situation as mentioned before, it is assumed that the errors in the Weibull fit will not change significantly between full stick and the microslip cases studied here. Hence, one may observe how the accuracy of the Weibull fit varies if only sets of 50 cases (as used in microslip simulations) are used for the full stick case. As seen in Fig. 4.11, using 50 cases instead of 100 does not significantly affect the accuracy of the percentile estimates for the linear case. To investigate and validate the true distribution of AFs for blisks in microslip, it would be necessary to develop ROMs for contact mistuning, as it would be impractically time consuming to perform enough MC simulations otherwise. This offers an interesting subject for future research

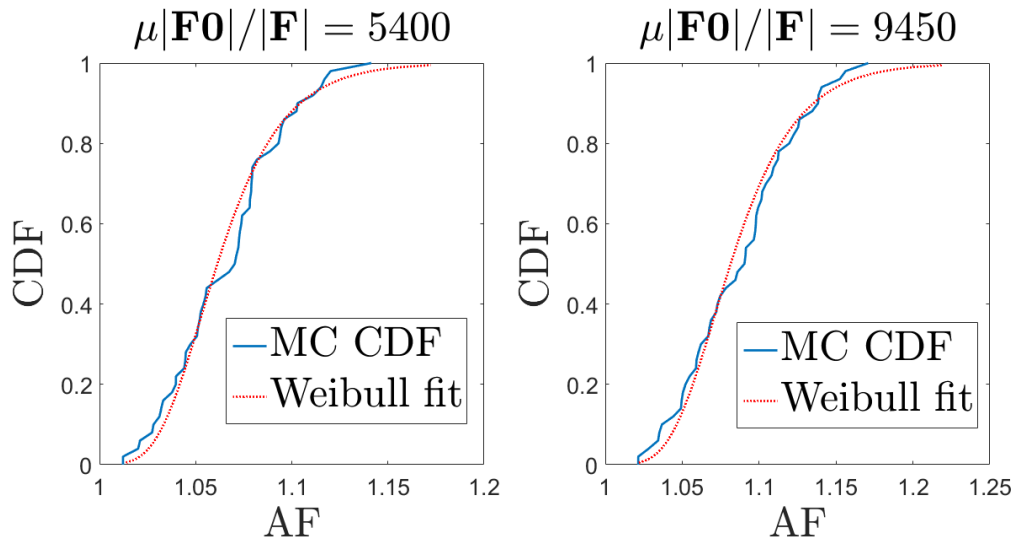

Figure 4.12. Weibull fits for nonlinear response AFs for $\sigma = 0.1$

in this area.

Figure 4.12 shows the Weibull CDF fits for the AF distributions for two different levels of microslip. Figure 4.13 shows AF percentiles for different levels of random mistuning calculated using the procedure described above. In addition to the stuck blisk response statistics represented by the lines without markers, statistics for the blisk in microslip are shown by lines with markers for different values of $\mu|\mathbf{F0}|/|\mathbf{F}|$ and σ. The 50^{th} and 95^{th} percentile values at each σ are obtained from Weibull fits to AFs of a set of mistuned response simulations. The stuck system is a limiting response scenario for a blisk in microslip with very high $\mu|\mathbf{F0}|/|\mathbf{F}|$. It may be seen that for low levels of contact mistuning ($\sigma = 0.1$), as microslip level increases ($\mu|\mathbf{F0}|/|\mathbf{F}|$ decreases) there is a decrease in percentile values of AFs, in the range of microslips simulated. It may also be seen that at $\sigma = 0.1$ the percentile AFs are lower than the corresponding values of the stuck case. However, it is also seen that at a higher mistuning level ($\sigma = 0.4$) the trend is reversed and in microslip the 95^{th} percentile AFs are higher than in the stick case and also increase as microslip increases. Therefore, the level of microslip where 95^{th} percentile AF is minimum, is lower for $\sigma = 0.4$ than for $\sigma = 0.1$. Cases with the same mistuning pattern were used to calculate the statistics for

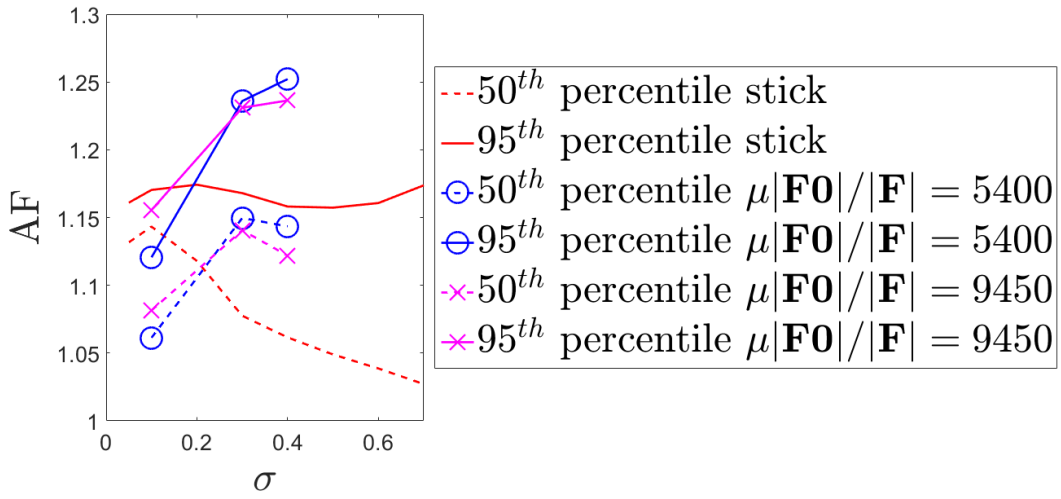

Figure 4.13. AF percentiles for mistuned blisks in full stick and microlsip vs σ

different microslip levels at a given σ. This clearly shows that although the stick cases might be a bound for the damped nonlinear responses, it is not a bound for the AFs especially at higher levels of mistuning.

To obtain a better understanding of these trends, the procedures mentioned for the stuck blisk are repeated to also generate the AF percentile plots for the mistuned systems in gross slip near the frequency range close to the tuned second family ND 12 gross slip frequency (see Fig. 4.3) in the range 1285-1340 Hz in Fig. 4.14. It may be seen that the percentile values for the slip AFs are much higher than that for the stuck case for higher σ. This is expected, because the second modal family of the tuned blisk case shown in Fig. 4.3 is much flatter, with greater modal density than the stick case. Hence, a mistuned blisk in slip is likely to have more tuned modes contributing to the mistuned mode which responds the most, and ultimately yield higher AFs [19] than the stick case. It is clear that at some level of mistuning the maximum AF will vary from the stick to the slip case as the level of microslip increases. However, how the maximum AF varies between these two limits changes with the level of microslip. Of interest to designers is the point where the minimum value of percentile AFs is observed along this path. The maximum value of percentile AFs is likely not limited by these linear cases. But due to the limited number of nonlinear simulations available,

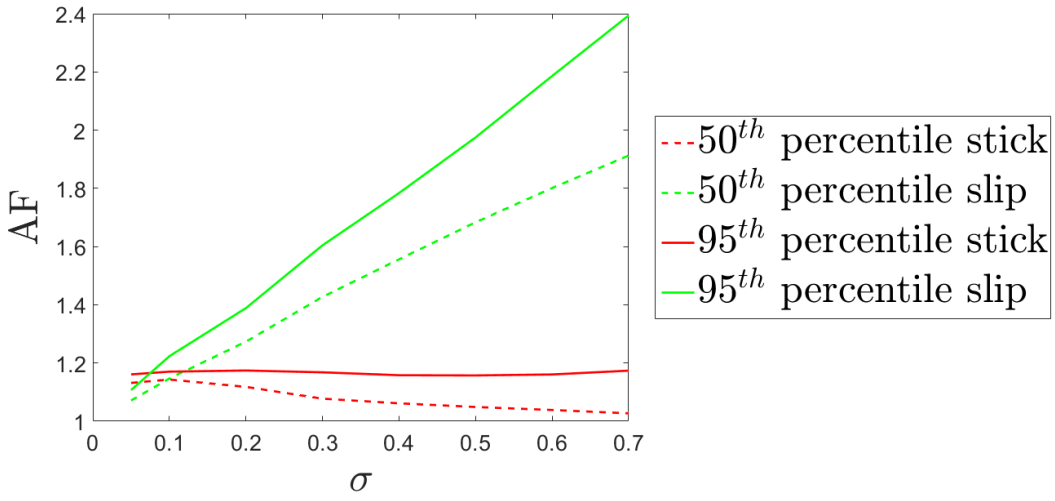

Figure 4.14. AF percentiles for mistuned blisks in full stick and and gross slip vs σ

and the range of microslip levels considered, this can be shown only for the stick case.

4.3 Conclusions

A shrouded blisk with mistuned local contact stiffnesses was analyzed in full stick, gross slip and microslip. Probabilistic analyses were carried out and response statistics were determined by fitting Weibull distributions to data from Monte Carlo simulations. The amplification factor is found to be dependent on the engine order of vibration even for microslip cases. Some engine orders show very little amplification even for very high levels of mistuning. It was seen that both the level of microslip and mistuning determine the amplification factor. Although the response of a blisk in microslip is known to be bounded by the linear cases, it is shown that this is not necessarily true of amplification factors. Even though the microslip cases analyzed were close to the full stick case in terms of resonant frequency, it was seen that at a higher level of mistuning the amplification factor exceeded that of the stick case. The optimum value of amplification factor in microslip varies with the level of mistuning. When designing damping for blades it would be beneficial for designers to use this as an additional criteria along with the optimal damped response. In other words,

the designed level of microslip in the operating region should try to trade-off between the tuned damped response and the highest amplification factors expected due to uncertainty in the contact parameters in that region. To ensure reasonable simulation times in this study, assumptions were made regarding the number of harmonics included in the simulation, and the nonlinear response amplification factor was assumed to follow a Weibull distribution. Also, mistuning is considered only to be at the friction interfaces only. In practice, this interface mistuning will always be accompanied by other effects such as stiffness and damping mistuning in the blade material. This study focuses on the effects of friction parameter mistuning at the interfaces only, with the goal of establishing trends. The simulation results obtained herein might be of use to designers to interpret experimental results. As discussed, the friction mistuning studied herein has a similar effect to that of damping variability in the blades, for near-stuck conditions. A well designed experiment should characterize mistuned blisk response both at fully stuck conditions where the effect of variability in blade materials will dominate the effects of mistuning at the interface, and also at microslip conditions where the interface mistuning can play a greater role.

CHAPTER V

Reduced Order Modeling of Blisks with Nonlinear Coatings

The bladed disks (blisks) found in compressor and turbine stages of turbomachines are nominally designed as cyclic symmetric structures. Although they are designed to be nominally identical, in practice, different sectors of a blisk have small differences due to manufacturing tolerances and material non-uniformities, primarily in the blade segments. Collectively termed as mistuning, this breaking of perfect cyclic symmetry has been studied extensively in the literature. It is known that a mistuned blisk may exhibit significantly higher resonant forced responses, even for small mistuning, when compared to the nominally tuned case [3, 76, 98]. Since mistuning values cannot be predicted before manufacture of the blisk, designers usually account for this fundamental uncertainty by performing probabilistic simulations with different mistuning patterns applied to the nominal design [7, 76, 77]. The number of simulations and associated computational costs required for reasonable probabilistic analyses renders simulation of complex high fidelity models such as finite element (FE) models intractable for this purpose. Thus, the necessity for reduced order models (ROMs) arises.

Various model order reduction methods have been employed for linear blisks with mistuning. These include modifications of general linear reduction methods such as component mode synthesis (CMS) [8–12], as well as more specialized techniques developed especially for blisks such as subset of normal modes (SNM) [14], fundamental model of mistuning (FMM) [15], compo-

nent mode mistuning (CMM) [16–18] and asymptotic model of mistuning (AMM) [19]. However, not all blisks are designed to be linear. In fact, nonlinearities are often introduced into blisk design to lower resonant responses and stresses. Traditionally, friction interfaces on shrouds or under-platform dampers have been employed to provide additional damping. Model reduction and simulation techniques for these structures have also been developed. Some techniques involve employing spatial reduction for the linear degrees of freedom in the model while retaining the non-reduced nonlinear degrees of freedom [35, 40, 49, 50]. There also exist methods which reduce both linear and nonlinear spatial degrees of freedom, for example by projecting the dynamics onto a basis [97] or finding equivalent linear representations [73]. Another possible nonlinear mechanism, which has gained interest from the industry and academia recently, is the use of damping coatings adhered to the blades of the blisk. The nonlinearity in the coating is strain dependent and less localized than frictional damping. Studies have been conducted to determine material properties of these coatings [79, 82] and to analyze the dynamic behavior for a single coated blade or beam [81, 83]. It was found that at the individual blade level, these coatings behave nonlinearly, with their damping and stiffness (and consequently the resonant frequencies) changing based on excitation amplitudes [81, 83]. In this chapter, models and simulation paradigms for a structure with nonlinear coatings are developed. Furthermore, model order reduction for mistuned blisks with nonlinear coatings based on the known amplitude dependent behavior of the coatings for individual blades is investigated.

An academic finite element model of a coated blisk is developed. Linear system matrices are extracted from this model and nonlinearities are enforced at the elemental level for each coating element as a function of local strain values. Dynamic simulations of individual coated blades as well as the coated blisk are performed in the frequency domain using harmonic balance method (HBM) [34, 35] and alternating frequency time (AFT) techniques [36, 37]. These are validated by comparison to time-marching solutions at certain frequencies. From these simulations it is observed that the amplitude dependent behavior of the coated blades causes additional mistuning

in stiffness and damping in the blades due to the different dynamic response of each blade. Thus, the overall effect of the nonlinearity is a mistuning pattern which is amplitude dependent. This fact is leveraged to develop a ROM. The mistuned blisk dynamics are projected onto a set of tuned system modes which allows the dynamics of the reduced system to be expressed in terms of quantities representing the tuned system and parameters representing underlying linear mistuning as well as additional nonlinear stiffness mistuning and damping. The nonlinear parameters are determined as a function of individual blade response amplitudes. This ROM not only reduces spatial degrees of freedom, but also bypasses the expensive element level calculations performed during AFT. The ROM is found to be very accurate when compared to baseline simulations and is suitable for use in probabilistic analyses.

5.1 Modeling a structure with nonlinear coatings

5.1.1 Dynamic equation

The dynamic equation corresponding to a the FE model of a system with nonlinear coating in the time domain with structural damping may be represented as:

$$\mathbf{M}_L\ddot{\mathbf{q}} + \frac{1}{\omega}[\mathbf{C}_L + \mathbf{C}_N]\dot{\mathbf{q}} + [\mathbf{K}_L + \mathbf{K}_N]\mathbf{q} = \mathbf{f}_E \tag{5.1}$$

where $\mathbf{M}$, $\mathbf{C}$ and $\mathbf{K}$ represent system mass, damping and stiffness matrices respectively. $\mathbf{q}$ and $\mathbf{f}$ represent the displacement and excitation force vectors. Subscripts L and N represent linear and nonlinear components of the matrices. The nonlinear components have non-zero value only at the coating degrees of freedom (DoFs). ω is the frequency of excitation. This equation can be used to used to analyze either an individual blade or a full wheel blisk FE model. Alternatively, Eqn. (5.1) may be written as:

$$\mathbf{M}_L\ddot{\mathbf{q}} + \frac{1}{\omega}\mathbf{C}_L\dot{\mathbf{q}} + \mathbf{K}_L\mathbf{q} = \mathbf{f}_E + \mathbf{f}_N \tag{5.2}$$

where the nonlinear force in the system is given by:

$$\mathbf{f}_N = -\frac{1}{\omega}\mathbf{C}_N\dot{\mathbf{q}} - \mathbf{K}_N\mathbf{q} \tag{5.3}$$

The corresponding equations of motion in the frequency domain for harmonic h are given by:

$$\left[-\mathbf{M}_L h^2\omega^2 + jh\mathbf{C}_L + \mathbf{K}_L\right]\tilde{\mathbf{q}}^h = \tilde{\mathbf{f}}_E^h + \tilde{\mathbf{f}}_N^h \tag{5.4}$$

In addition to the conversion to frequency domain in Eqn. (5.4) the solution is carried out in modal co-ordinates $\mathbf{p}$ such that $\tilde{\mathbf{q}}^h = \mathbf{\Phi}\tilde{\mathbf{p}}^h$, where $\mathbf{\Phi}$ is a model reduction matrix composed of linear modes which are retained in the solution. For a baseline model, this reduction is applied to reject some high frequency modes which make convergence slower although they do not contribute significantly to the response in the frequency region of interest, by retaining sufficient modes whose natural frequencies lie near the solution frequencies. In a reduced order model the modes in $\mathbf{\Phi}$ simply represent the reduction modes. Thus, Eqn. (5.4) is reduced to:

$$\left[-\boldsymbol{\rho}_L h^2\omega^2 + jh\boldsymbol{\beta}_L + \boldsymbol{\kappa}_L\right]\tilde{\mathbf{p}}^h = \tilde{\mathbf{g}}_E^h + \tilde{\mathbf{g}}_N^h \tag{5.5}$$

where the reduced system linear matrices and excitation and nonlinear forces are given by:

$$\begin{aligned}
\boldsymbol{\rho}_L &= \mathbf{\Phi}^{\mathrm{T}}\mathbf{M}_L\mathbf{\Phi} \\
\boldsymbol{\kappa}_L &= \mathbf{\Phi}^{\mathrm{T}}\mathbf{K}_L\mathbf{\Phi} \\
\boldsymbol{\beta}_L &= \mathbf{\Phi}^{\mathrm{T}}\mathbf{C}_L\mathbf{\Phi} \\
\tilde{\mathbf{g}}_E^h &= \mathbf{\Phi}^{\mathrm{T}}\tilde{\mathbf{f}}_E^h \\
\tilde{\mathbf{g}}_N^h &= \mathbf{\Phi}^{\mathrm{T}}\tilde{\mathbf{f}}_N^h
\end{aligned} \tag{5.6}$$

5.1.2 Coating matrices

The linear damping of the entire system, which is the sum of the damping in the coating portion of the system and the rest of the system is given by:

$$\begin{aligned}\mathbf{C}_L &= \gamma_{L,b}\mathbf{K}_{L,b} + \gamma_{L,c}\mathbf{K}_{L,c} \\ &= \gamma_{L,b}(\mathbf{K}_{L,b} + \mathbf{K}_{L,c}) + (\gamma_{L,c} - \gamma_{L,b})\mathbf{K}_{L,c} \\ &= \gamma_{L,b}\mathbf{K}_L + (\gamma_{L,c} - \gamma_{L,b})\mathbf{K}_{L,c}\end{aligned} \tag{5.7}$$

where γ_L represents linear structural damping coefficient and additional subscripts c and b represent the coating and non-coating portions of the system respectively. To formulate the nonlinear matrices for the coating stiffness and damping the formulation described in [81] is used. Each element of the coating has a complex-valued Young's modulus with real and imaginary parts $E_{R,el}$ and $E_{I,el}$ which are a polynomial functions of the equivalent elemental strain ϵ_{el} as follows:

$$E_{R,el} = E_{el,R,0} + \sum_{k=1}^{n_k} E_{el,R,k}(\epsilon_{el})^k \tag{5.8}$$

where the subscript el refers to elemental quantities. The imaginary part of the Young's modulus may be obtained by replacing the subscript R with I in Eqn. (5.8). $E_{el,R,0}$ and $E_{el,I,0}$ are the linear or strain-independent components of the real and imaginary parts of the of the coating modulus. Hence, the coating structural damping coefficient is given by $\gamma_{L,c} = E_{el,I,0}/E_{el,R,0}$. The nonlinear stiffness and damping matrices of the system $\mathbf{K}_N$ and $\mathbf{C}_N$ are comprised of (finite) elemental stiffness and damping matrices $\mathbf{K}_{N,el}$ and $\mathbf{C}_{N,el}$, which are functions of the linear elemental coating matrices and the elemental strain as follows:

$$\mathbf{K}_{N,el} = \frac{\mathbf{K}_{L,el}}{E_{el,R,0}} \sum_{k=1}^{n_k} E_{el,R,k}(\epsilon_{el})^k \tag{5.9}$$

$$\mathbf{C}_{N,el} = \frac{\mathbf{K}_{L,el}}{E_{el,R,0}} \sum_{k=1}^{n_k} E_{el,I,k} (\epsilon_{el})^k \tag{5.10}$$

At any instant of time the elemental strain is given by [81]:

$$\epsilon_{el} = \sqrt{\mathbf{q}_{el}^{\mathrm{T}} \frac{\mathbf{K}_{L,el}}{E_{el,R,0} V_{el}} \mathbf{q}_{el}} \tag{5.11}$$

where $\mathbf{q}_{el}$ is the vector of nodal displacements for the element, $\mathbf{K}_{L,el}$ is the corresponding elemental linear stiffness matrix and V_{el} is the elemental volume at zero strain.

5.1.3 Solution of dynamic equation

The forced frequency response of the system is obtained by solving Eqn. (5.5) which were obtained by employing HBM [35]. Multiple harmonics of Eqn. (5.5) ($h = 0, 1, 2, \ldots, n_h$) are retained in the solution. A trust-region based algorithm (TRA) is used to find $\tilde{\mathbf{p}}^h(\omega)$ by solving the optimization problem in which the residual of Eqn. (5.5) becomes zero at the frequency of calculation ω. The optimization routine uses only real valued variables and hence the real and imaginary values of displacement and forces are used instead of a single complex value. To find the nonlinear forces at every iteration of the solver, the AFT [36] method is used where the modal displacements in the frequency domain are converted to physical displacements in the time domain by using fast fourier transforms (FFT) and used to calculate the physical nonlinear forces which are converted back to modal forces in the frequency domain through an inverse fast fourier transform (IFFT) and modal projection. The optimization algorithm used for solution does not require analytical Jacobians to be supplied by the user as estimates of the Jacobian can be calculated by using finite difference. However, in practice, the time required to calculate the finite difference based Jacobians can be prohibitive in terms of computation time. In this study, the analytical Jacobians were provided to the solver. To do so, the derivatives of the nonlinear force with respect to the the real and complex parts of the Fourier coefficients of the nodal displacements are derived at the

elemental level as functions of time from Eqns. (5.3) as:

$$\begin{aligned}\frac{d\mathbf{f}_{N,el}}{d\tilde{\mathbf{q}}^h_{R,el}} &= -\mathbf{K}_{N,el}cos(h\omega t) - \frac{d\mathbf{K}_{N,el}}{d\mathbf{q}_{el}}\mathbf{q}_{el}cos(h\omega t) \\ &+h\frac{d\mathbf{C}_{N,el}}{d\mathbf{q}_{el}}\dot{\mathbf{q}}_{el}sin(h\omega t) + h\mathbf{C}_{N,el}sin(h\omega t)\end{aligned} \tag{5.12}$$

$$\begin{aligned}\frac{d\mathbf{f}_{N,el}}{d\tilde{\mathbf{q}}^h_{I,el}} &= \mathbf{K}_{N,el}sin(h\omega t) + \frac{d\mathbf{K}_{N,el}}{d\mathbf{q}_{el}}\mathbf{q}_{el}sin(h\omega t) \\ &+h\frac{d\mathbf{C}_{N,el}}{d\mathbf{q}_{el}}\dot{\mathbf{q}}_{el}cos(h\omega t) + h\mathbf{C}_{N,el}cos(h\omega t)\end{aligned} \tag{5.13}$$

where t represents a vector of time instances over a period of vibration. The unknown quantities in Eqns. (5.12)-(5.13) may be derived from Eqns. (5.9)-(5.11) and are given by:

$$\frac{d\mathbf{K}_{N,el}}{d\mathbf{q}_{el}}\mathbf{q}_{el} = \frac{\mathbf{K}_{L,el}}{E_{el,R,0}}\sum_{k=1}^{n_k} E_{el,R,k}k(\epsilon_{el})^{k-2}\frac{\mathbf{q}_{el}^{\mathrm{T}}\mathbf{K}_{L,el}\mathbf{q}_{el}}{E_{el,R,0}V_{el}} \tag{5.14}$$

$$\frac{d\mathbf{C}_{N,el}}{d\mathbf{q}_{el}}\dot{\mathbf{q}}_{el} = \frac{\mathbf{K}_{L,el}}{E_{el,R,0}}\sum_{k=1}^{n_k} E_{el,I,k}k(\epsilon_{el})^{k-2}\frac{\mathbf{q}_{el}^{\mathrm{T}}\mathbf{K}_{L,el}\dot{\mathbf{q}}_{el}}{E_{el,R,0}V_{el}} \tag{5.15}$$

Eqns. (5.12)-(5.15) are used during the AFT procedure. Taking IFFT of the quantities in Eqns. (5.12)-(5.13) the derivatives of the fourier coefficients of the physical nonlinear forces with respect to nonlinear physical displacements are obtained at the elemental level. These derivatives are then assembled into global matrices and a modal projection is applied to obtain the derivative of the fourier coefficients of the nonlinear modal forces with respect to nonlinear modal displacements, which can then be used to easily formulate the anaytical Jacobian of the residual of Eqns. (5.3).

5.2 Reduced order modeling for coated blisks

5.2.1 Projection onto tuned modes

A reduction method for the nonlinear blisk is presented with different linear components of Young's modulus $E_{R,0}$ at each blade, also commonly known as small stiffness mistuning. The first step in the reduction is the assumption that the nonlinear dynamics of the mistuned blisk can be captured by projecting them onto the linear modes of the tuned system $\mathbf{\Phi}_o$ in the frequency region of interest. Such a projection, which has been successfully employed for linear blisks in the past [14] is based on the fact that the mistuned modes of a linear blisk with small stiffness mistuning, can be approximated by a linear combination of the tuned modes. In the case of blisks with coatings which entail nonlinearity, there is the additional implicit assumption that the nature of the nonlinearity is weak, such that it does not affect the modes of the responding blisk significantly. If the reduction modes employed to obtain the dynamic equation Eqn. (5.5) are the tuned modes of the blisk in the frequency region of interest $\mathbf{\Phi} = \mathbf{\Phi}_o$, then the reduced order dynamic equation for a coated blisk can be alternatively expressed as:

$$\left[-\boldsymbol{\rho}_{L,r}h^2\omega^2 + jh\boldsymbol{\beta}_{L,r} + \boldsymbol{\kappa}_{L,r} + jh\boldsymbol{\beta}^h_{N,r} + \boldsymbol{\kappa}^h_{N,r}\right]\tilde{\mathbf{p}}^h_r = \tilde{\mathbf{g}}^h_{E,r} \tag{5.16}$$

where $\boldsymbol{\rho}_{L,r}$, $\boldsymbol{\beta}_{L,r}$ and $\boldsymbol{\kappa}_{L,r}$ are the reduced linear system matrices obtained by projection onto the tuned modes in the frequency region of interest. $\boldsymbol{\kappa}^h_{N,r}$ and $\boldsymbol{\beta}^h_{N,r}$ are the reduced additional stiffness and damping matrices due to nonlinearity for harmonic h. $\tilde{\mathbf{p}}^h_r$ and $\tilde{\mathbf{g}}^h_{E,r}$ are the displacements and excitation forces in tuned modal co-ordinates.

5.2.2 Amplitude dependent nonlinearity

Even though the dimensionality of the system of nonlinear equations might be reduced in Eqn. (5.16), the nonlinear stiffness and damping effects and correspondingly the nonlinear forces must be calculated in the physical domain (at each coating node) at each step of the solution iter-

ation, which is higher dimensional than the reduced domain. Hence, a significant portion of the computational effort for solving Eqn. (5.16) using traditional techniques will be spent during the AFT procedure. To avoid this, one may use the fact that the nonlinear coating parameters and consequently the additional nonlinear stiffness and damping $\boldsymbol{\kappa}^h_{N,r}$ and $\boldsymbol{\beta}^h_{N,r}$ are dependent on the response amplitudes at each blade. It is assumed that the effect of the nonlinearity equivalent to a change in linear stiffness or damping at each harmonic which is functionally dependent on the nonlinear blade amplitude. Hence for a blisk with mistuning in the linear stiffness and damping, whose blades have non-identical responses, this amplitude dependency of the nonlinear terms manifests itself as a an additional mistuning and damping parameter whose values are dependent on the response amplitudes at the individual blades.

$$\boldsymbol{\beta}^h_{N,r} = \boldsymbol{\beta}^h_{N,r}(A_{N,s}); \boldsymbol{\kappa}^h_{N,r} = \boldsymbol{\kappa}^h_{N,r}(A_{N,s}) \tag{5.17}$$

where $A_{N,s}$ are the nonlinear blade amplitudes at sectors $s = 1, 2, \ldots, n_s$, n_s representing the number of sectors. $A_{N,s}$ is a single amplitude value determined at one point or node on each blade which can be calculated from the multiharmonic response. For this study, it is assumed that a single dominant blade mode is responsible for blade motion, which implies that a single family of blisk modes can capture the nonlinear blisk response. As the nonlinearity in all blades are assumed to be identical for analysis, the functional dependencies of nonlinear stiffness and damping on blade amplitudes are identical for all blades. Hence, using Eqn. (5.17) in conjunction with Eqn. (5.16) one may avoid AFT and reduce the computational cost of the nonlinear solution.

5.2.3 Nonlinearity as amplitude dependent mistuning

It has been shown in previous studies that the response of a blade with nonlinear coating can be accurately captured by the first harmonic [81]. If this is assumed to be the case for all the blades of the blisk, the representation of the dynamics in Eqn. (5.16) can be simplified greatly. Henceforth,

only the first harmonic of every relevant quantity is calculated and the harmonic index h is dropped for brevity. From, Eqns. (5.16) and (5.17) it follows that:

$$[-\boldsymbol{\rho}_{L,r}\omega^2 + j\boldsymbol{\beta}_{L,r} + \boldsymbol{\kappa}_{L,r} + j\boldsymbol{\beta}_{N,r}(A_{N,s}) + \boldsymbol{\kappa}_{N,r}(A_{N,s})]\tilde{\mathbf{p}}_r = \tilde{\mathbf{g}}_{E,r} \tag{5.18}$$

The restrictions imposed by dropping higher harmonics for the externally applied excitation force $\tilde{\mathbf{g}}_{E,r}$ does not reduce the usability of the model for design studies as the engine order excitations prescribed by designers to study blisk responses can be perfectly expressed as a first harmonic excitation [3, 10, 97]. If the functional dependencies of $\boldsymbol{\beta}_{N,r}$ and $\boldsymbol{\kappa}_{N,r}$ on $A_{N,s}$ were ignored in Eqn. (5.18) it would represent the dynamics of a linear mistuned blisk model. Hence, the nonlinear coated blisk may be thought of as a linear blisk with additional amplitude dependent stiffness and damping mistuning. In light of this realization, the equations may be recast by introducing linear stiffness mistuning parameter and additional nonlinear stiffness mistuning and damping parameters. For a blisk with small stiffness mistuning the mistuned linear stiffness matrix in reduced coordinates may be calculated as:

$$\boldsymbol{\kappa}_{L,r} = \boldsymbol{\Phi}_o^{\mathrm{T}}\mathbf{K}_L\boldsymbol{\Phi}_o = \boldsymbol{\kappa}_{L,r,o} + \sum_{s=1}^{n_s} m_{L,s}\boldsymbol{\kappa}_{L,r,m,s} \tag{5.19}$$

where the tuned component $\boldsymbol{\kappa}_{L,r,o}$ is given by:

$$\boldsymbol{\kappa}_{L,r,o} = \boldsymbol{\Phi}_o^{\mathrm{T}}\mathbf{K}_{L,o}\boldsymbol{\Phi}_o \tag{5.20}$$

and the mistuned component at sector s due to unit stiffness mistuning, $\boldsymbol{\kappa}_{L,r,m,s}$ is calculated as:

$$\boldsymbol{\kappa}_{L,r,m,s} = \boldsymbol{\Phi}_{o,s}^{\mathrm{T}}\bar{\mathbf{K}}_{L,s}\boldsymbol{\Phi}_{o,s} \tag{5.21}$$

$m_{L,s}$ is the linear stiffness mistuning at each sector s. $\mathbf{K}_{L,o}$ is the linear tuned blisk matrix. $\boldsymbol{\Phi}_{o,s}$ is the partition of tuned modes at sector s. $\bar{\mathbf{K}}_{L,s}$ is the change in linear stiffness at sector s from the

tuned case due to a unit stiffness mistuning at that sector. Note that, this might not be proportional to the tuned linear stiffness value for that sector, as usually the blades are mistuned more than the disk portions of the sectors. For the purposes of this study, mistuning has only been considered in the blade and coating portions of the blisk. Using Eqns. (5.7) and (5.19) it may be shown that:

$$\boldsymbol{\beta}_{L,r} = \boldsymbol{\Phi}_o^{\mathrm{T}} \mathbf{C}_L \boldsymbol{\Phi}_o = \boldsymbol{\Phi}_o^{\mathrm{T}} (\gamma_{L,b} \mathbf{K}_L + (\gamma_{L,c} - \gamma_{L,b}) \mathbf{K}_{L,c}) \boldsymbol{\Phi}_o = \gamma_{L,b} \boldsymbol{\kappa}_{L,r} + (\gamma_{L,c} - \gamma_{L,b}) \sum_{s=1}^{n_s} (1 + m_{L,s}) \boldsymbol{\kappa}_{L,r,o,c,s} \tag{5.22}$$

where

$$\boldsymbol{\kappa}_{L,r,o,c,s} = \boldsymbol{\Phi}_{o,s}^{\mathrm{T}} \bar{\mathbf{K}}_{L,o,c,s} \boldsymbol{\Phi}_{o,s} \tag{5.23}$$

where $\bar{\mathbf{K}}_{L,o,c,s}$ is the tuned linear stiffness of the coating portion of sector s. The additional amplitude dependent stiffness due to nonlinearity in reduced coordinates $\boldsymbol{\kappa}_{N,r}$ at any particular response configuration of the blades may be expressed as:

$$\boldsymbol{\kappa}_{N,r} \approx \sum_{s=1}^{n_s} g_m(A_{N,s}) \boldsymbol{\kappa}_{L,r,m,s} = \sum_{s=1}^{n_s} m_{N,s} \boldsymbol{\kappa}_{L,r,m,s} \tag{5.24}$$

where the effective additional stiffness mistuning due to nonlinearity at each blade is determined as a function g_m of nonlinear blade amplitude $A_{N,s}$ and has the value $m_{N,s}$ at sector s. The additional damping matrix due to nonlinearity in modal co-ordinates $\boldsymbol{\beta}_{N,r}$ may be obtained by summing up the additional damping nonlinearity at each sector which is proportional to the linear damping at that sector as follows:

$$\boldsymbol{\beta}_{N,r} \approx \sum_{s=1}^{n_s} f_m(A_{N,s}) \boldsymbol{\beta}_{L,r,s} = \sum_{s=1}^{n_s} \alpha_{N,s} \boldsymbol{\beta}_{L,r,s} \tag{5.25}$$

where the effective additional damping parameter is also expressed as a function f_m of parameter $A_{N,s}$ and has the value $\alpha_{N,s}$ at sector s. $\boldsymbol{\beta}_{L,r,s}$ is calculated as follows:

$$\boldsymbol{\beta}_{L,r,s} = \boldsymbol{\Phi}_{o,s}^{\mathrm{T}} \mathbf{C}_{L,s} \boldsymbol{\Phi}_{o,s} = \gamma_{L,b} \boldsymbol{\kappa}_{L,r,s} + (\gamma_{L,c} - \gamma_{L,b})(1 + m_{L,s}) \boldsymbol{\kappa}_{L,r,o,c,s} \tag{5.26}$$

where $\mathbf{C}_{L,s}$ is the linear damping matrix at sector s. $\boldsymbol{\kappa}_{L,r,s}$ is the reduced stiffness matrix at sector s obtained as follows:

$$\boldsymbol{\kappa}_{L,r,s} = {\boldsymbol{\Phi}_{o,s}}^{\mathrm{T}} \mathbf{K}_{L,s} \boldsymbol{\Phi}_{o,s} = \boldsymbol{\kappa}_{L,o,s} + m_{L,s} \boldsymbol{\kappa}_{L,r,m,s} \tag{5.27}$$

where

$$\boldsymbol{\kappa}_{L,o,s} = \boldsymbol{\Phi}_{o,s}^{\mathrm{T}} \mathbf{K}_{L,o,s} \boldsymbol{\Phi}_{o,s} \tag{5.28}$$

where $\mathbf{K}_{L,o,s}$ is the tuned linear stiffness matrix at sector s. Substituting Eqns. (5.19)-(5.28) in Eqn. (5.18) a set of nonlinear equations may be obtained in reduced coordinates where the nonlinearity is expressed solely in terms of blade amplitudes $A_{N,s}$ and is captured through additional damping and stiffness mistuning parameters represented by $\alpha_{N,s}$ and $m_{N,s}$.

$$\begin{aligned}[-\boldsymbol{\rho}_{L,r}\omega^2 + (j\gamma_{L,b}+1)(\boldsymbol{\kappa}_{L,r,o} + \sum_{s=1}^{n_s} m_{L,s}\boldsymbol{\kappa}_{L,r,m,s}) + j(\gamma_{L,c}-\gamma_{L,b}) \sum_{s=1}^{n_s} (1+\alpha_{N,s})(1+m_{L,s})\boldsymbol{\kappa}_{L,r,o,c,s} + \ldots \\ j\gamma_{L,b} \sum_{s=1}^{n_s} \alpha_{N,s}\boldsymbol{\kappa}_{L,o,s} + \sum_{s=1}^{n_s} (j\gamma_{L,b}\alpha_{N,s}m_{L,s} + m_{N,s})\boldsymbol{\kappa}_{L,r,m,s}]\tilde{\mathbf{p}}_r = \tilde{\mathbf{g}}_{E,r}\end{aligned} \tag{5.29}$$

Eqn. (5.29) can be solved by using TRA. A single iteration step of this model will be much faster as it will avoid the AFT procedure and any involved calculations in higher order co-ordinates such as the physical domain during iteration. The nonlinear parameters in this formulation can be calculated from the amplitude directly in reduced co-ordinates. This also clarifies the choice of the tuned modes as the reduction basis. The objective was to avoid calculations of new reduced order matrices with new mistuning patterns. As shown in Eqns. (5.19)-(5.28) it is only necessary that the requisite reduced order matrices ($\boldsymbol{\kappa}_{L,r,o}, \boldsymbol{\kappa}_{L,r,m,s}, \boldsymbol{\kappa}_{L,r,o,c,s}, \boldsymbol{\kappa}_{L,o,s}$) be generated once for any tuned blisk and the corresponding nonlinear equations for the any linear mistuning pattern can then be generated directly in the reduced co-ordinates. As an alternative to TRA, use of fixed point iterations (FPI) at each frequency may also be employed. FPI iterations will involve re-substituting the solution of the previous iteration into the current iteration and repeating until convergence.

5.2.4 Functional dependencies on amplitude

The functions f_m and g_m which establish the dependency of additional nonlinear damping $\alpha_{N,s}$ and stiffness mistuning $m_{N,s}$ on the nonlinear cantilevered blade response $A_{N,s}$ at blade s may be obtained analytically, from simulations or from experiments. In this study, it is obtained using the simulated nonlinear responses of a cantilevered blade at different excitations. Since these functions are assumed to be identical for all blades, the may be determined for a single nominal blade and its amplitudes $A_{N,o}$. Any small linear stiffness mistuning which modifies the elastic modulus of the blades, will not affect these functions as it will affect the linear and nonlinear amplitudes and frequencies consistently for any blade and the functions are dependent only on the relative measures between the two. Hence, these functions are estimated from the nominal cantilevered blade responses may applied to the mistuned blades in simulations. Specifically, $m_{N,o}$ which represents the additional stiffness due to the nonlinearity for a nominal blade can be estimated using resonant frequencies of the linear and nonlinear simulations (squared resonant frequency is proportional to stiffness) as follows:

$$m_{N,o} \approx \frac{\omega_N^2 - \omega_L^2}{\omega_L^2} \tag{5.30}$$

where ω_N and ω_L are the nonlinear and linear resonant frequencies of the cantilevered blade in the frequency region of interest. $\alpha_{N,o}$ which represents the additional damping for a nominal blade can be determined using the ratio linear and nonlinear normalized responses as follows:

$$\alpha_{N,o} \approx \frac{A_{L,o,max}/|\mathbf{F}|_L}{A_{N,o,max}/|\mathbf{F}|_N} - 1 \tag{5.31}$$

where $A_{N,o,max}$ and $A_{L,o,max}$ are the nonlinear and linear resonant response amplitudes. $|\mathbf{F}|_L$ and $|\mathbf{F}|_N$ are the amplitudes of the excitation forces used in the linear and nonlinear cases respectively. $m_{N,o}$ and $\alpha_{N,o}$ are obtained for different $A_{N,o}$ for different excitation levels and a polynomial least

squares fit is performed to obtain f_m and g_m. It may be shown that the order of these polynomials will be the same as the highest power of equivalent strain in the expression for storage and loss moduli of Eqn. (5.11). Substituting Eqn. (5.11) in Eqn. (5.9) for a single coating element:

$$\mathbf{K}_{N,el} = \frac{\mathbf{K}_{L,el}}{E_{el,R,0}} \sum_{k=1}^{n_k} E_{el,R,k} \left(\sqrt{\mathbf{q}_{el}^{\mathrm{T}} \frac{\mathbf{K}_{L,el}}{E_{el,R,0} V_{el}} \mathbf{q}_{el}} \right)^k \tag{5.32}$$

Assuming motion at blade s to be along single blade mode with amplitude $\mathrm{p}_{b,s}$ such that $\mathbf{q}_{el} = \mathbf{\Phi}_{b,s,el} \mathrm{p}_{b,s}$ from Eqn. (5.32) one may obtain:

$$\mathbf{K}_{N,el} = \frac{\mathbf{K}_{L,el}}{E_{el,R,0}} \sum_{k=1}^{n_k} E_{el,R,k} \left(\sqrt{\frac{\boldsymbol{\kappa}_{L,el}}{E_{el,R,0} V_{el}}} \right)^k \mathrm{p}_{b,s}^k = \sum_{k=1}^{n_k} \mathbf{K}_{N,k,el} \mathrm{p}_{b,s}^k \tag{5.33}$$

where $\boldsymbol{\kappa}_{L,el} = \mathbf{\Phi}_{b,s,el}^{\mathrm{T}} \mathbf{K}_{L,el} \mathbf{\Phi}_{b,s,el}$. Since the nonlinearity has been separated in terms of powers of $\mathrm{p}_{b,s}$, the elemental matrices $\mathbf{K}_{N,k,el}$ may be assembled to form blade level matrices $\mathbf{K}_{N,s,k}$. Consequently, blade matrices $\mathbf{K}_{N,s}$ may be formulated as a matrix polynomial of $\mathrm{p}_{b,s}$ representing additional stiffness matrix at blade s due to the nonlinearity as:

$$\mathbf{K}_{N,s} = \sum_{k=1}^{n_k} \mathbf{K}_{N,s,k} \mathrm{p}_{b,s}^k \tag{5.34}$$

Subsequent projection onto the tuned blisk modes partition $\mathbf{\Phi}_{o,b,s}$ at the blade s will yield:

$$\boldsymbol{\kappa}_{N,r,s} = \mathbf{\Phi}_{o,b,s}^{\mathrm{T}} \mathbf{K}_{N,s} \mathbf{\Phi}_{o,b,s} = \sum_{k=1}^{n_k} \boldsymbol{\kappa}_{N,r,s,k} \mathrm{p}_{b,s}^k \tag{5.35}$$

where $\boldsymbol{\kappa}_{N,r,s,k} = \mathbf{\Phi}_{o,b,s}^{\mathrm{T}} \mathbf{K}_{N,s,k} \mathbf{\Phi}_{o,b,s}$. Since it is assumed that the nonlinear effect can be approximated as additional linear mistuning, in the reduced space the relationship $\boldsymbol{\kappa}_{N,r,s,k} \propto \boldsymbol{\kappa}_{L,r,m,s}$ holds true. Also, $A_{N,s} \propto \mathrm{p}_{b,s}$ as the physical blade amplitude at any point will be proportional to the

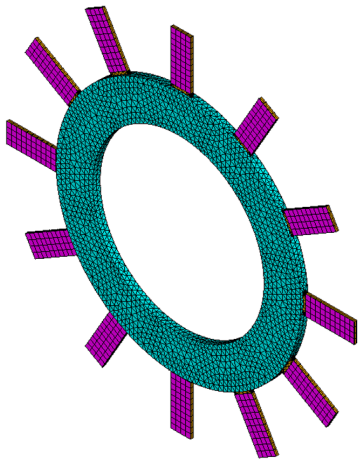

Figure 5.1. Coated blisk

modal amplitude. Hence, using Eqn. (5.24) and (5.35) it follows that:

$$\boldsymbol{\kappa}_{N,r,s} \approx \left(\sum_{k=1}^{n_k} \eta_{s,k} A_{N,s}^{k} \right) \boldsymbol{\kappa}_{L,r,m,s} = m_{N,s} \boldsymbol{\kappa}_{L,r,m,s} \tag{5.36}$$

where $\eta_{s,k}$ are proportionality constants and coefficients of the polynomial. Thus, the additional mistuning may be approximated by a polynomial in blade amplitude $A_{N,s}$ of the order n_k which is the same as the order of the dependence of storage and loss moduli on strain at the elemental level. A similar argument can be applied for additional nonlinear damping.

5.3 Results and analysis

5.3.1 Finite element models

For the purposes of this study an academic FE blisk model of blisk with 12 blades as shown in Fig. 5.1 was developed in ANSYS®. As shown in Fig. 5.2 each blade has the same material as the disk and with total height 42 mm, a width of 16 mm and a thickness of 2 mm. Comparatively the coating is much thinner with a thickness of 0.2 mm. Solid brick finite elements were used to model both the body of the blisk and the coating. Values of important nominal properties

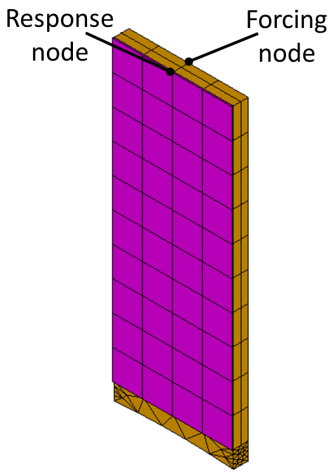

Figure 5.2. Coated blade

Table 5.1. Nominal material properties

Property	Value	Units
$\gamma_{L,b}$	0.0001	dimensionless
E_b	200	GPa
$E_{R,0,c}$	109.8	GPa
$E_{R,1,c}$	-0.011	GPa m/μm
$E_{I,0,c}$	1.525	GPa
$E_{I,1,c}$	0.003125	GPa m/μm

used for the materials are listed in table 5.1. Properties of structural steel were used for the blisk body. The material properties of the coating are those used in [81], which were validated with experimental data. Storage and loss moduli of the coating, as described in Eqn. (5.8) are linear functions of equivalent strain. The negative value of $E_{R,1,c}$ indicates the softening behavior of coating (decrease in stiffness with increase in strain). As shown in Fig. 5.2, two nodes are chosen at opposite sides of each blade at the tip for applying the excitation force and for calculating the response along the axial direction normal to the face of the blade. All the requisite elemental linear (zero strain) blade and full blisk matrices are extracted from these FE models and are then used for simulations in MATLAB® where nonlinearities are enforced as per the equations of motions

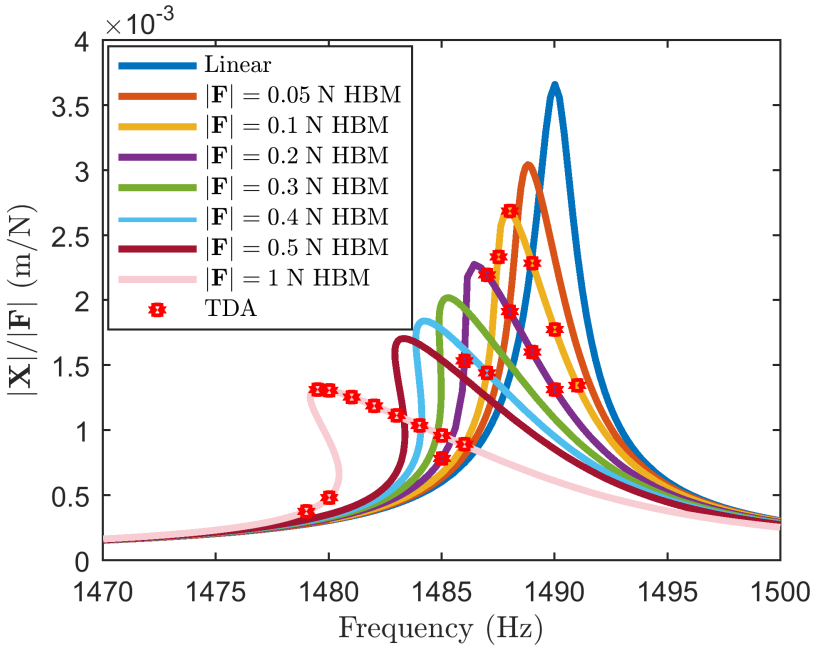

Figure 5.3. Normalized responses of cantilevered blade

mentioned previously in sections 5.1 and 5.2.

5.3.2 Baseline response simulations

Figure 5.3 shows the simulated maximum response amplitudes $|\mathbf{X}|$ of a nominal coated cantilever blade normalized by the excitation amplitude $|\mathbf{F}|$ at various excitation levels in the neigborhood of its first bending mode frequency. The first 100 linear modes of the blade were retained for this analysis. In these baseline cases single harmonic ($n_h = 1$) HBM was employed to obtain frequency responses with a specified minimum resolution of 0.1 Hz. In addition, a transient dynamic analysis (TDA) was also carried out to obtain response amplitudes at selected frequencies for $|\mathbf{F}|$ = 0.1, 0.2 and 1 N excitation cases. In TDA, the equations of motion are simulated in the time domain using a Runge-Kutta time marching method for differential equations and obtain the amplitude after convergence [73]. TDA is computationally very expensive and intractable for design purposes, but is more accurate in general as it does not involve truncating harmonics as in HBM.

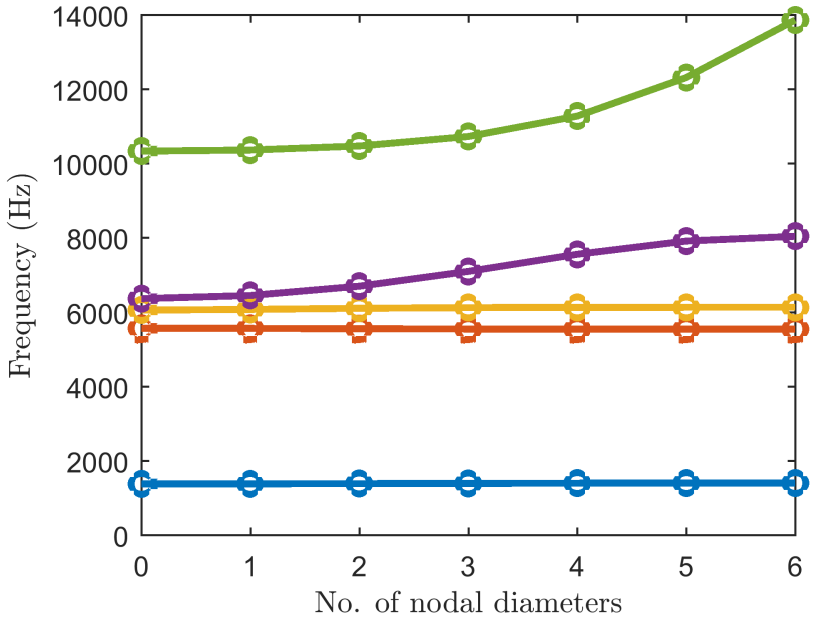

Figure 5.4. Frequency vs No. of nodal diameters

All HBM solutions herein were obtained using TRA unless specifically noted otherwise. Using TDA results for verification, one may observe in Fig. 5.3 that a $n_h = 1$ HBM solution captures the dynamics and predicts the response very accurately, even for the higher excitation cases where the contribution of nonlinearity to the dynamics is greater. It may also be observed that as the excitation amplitude increases, the blade exhibits higher damping (lower normalized response) and a softening behavior (lower resonant frequency) which is consistent with the behavior of coated blades [81]. At the higher excitation levels, it is also observed that the system has multiple solutions for amplitude at some frequencies near the peak which indicates a bifurcation phenomenon. It must be noted that while HBM is able to capture both the stable and unstable branches of such a curve, TDA only converges to points on a stable branch.

Figure 5.4 shows the natural frequencies of the tuned zero strain linear coated blisk plotted against the number of nodal diameters (ND) exhibited by the corresponding modes $\mathbf{\Phi}_o$'s. For such a system, there exist two modes with identical natural frequencies (called a mode-pair) with the

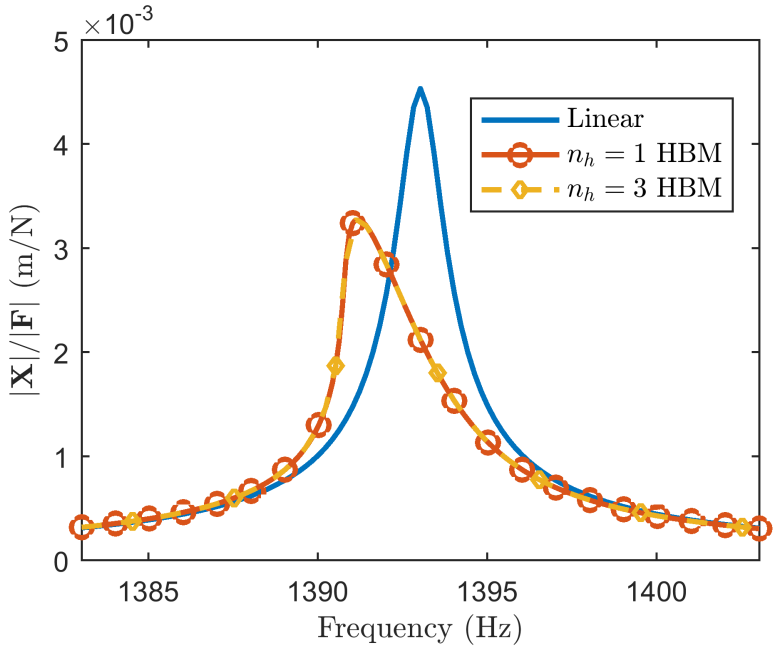

Figure 5.5. Normalized response of tuned blisk:: $|\mathbf{F}| = 0.1$ N, EO 2 excitation

same ND associated with it [3, 97]. Since, the ND patterns exhibited by these tuned linear system mode-pair have a specific spatial harmonic associated with them, they can be excited by a travelling wave excitation of a specific shapes with similar spatial harmonic content, also known as an engine order (EO) excitation which may be expressed in the time-domain as:

$$\mathbf{f}_E(t,\theta) = |\mathbf{F}| cos(\frac{2\pi \mathrm{EO}}{n_s} t + \theta) \tag{5.37}$$

where t is the time index, θ is the circumferential angle on the blisk, $|\mathbf{F}|$ is the excitation amplitude and EO is the non-negative integral engine order of excitation. Any mode-pair will excited by a forcing with the same EO as its ND and by higher EO$=$ k$n_s\pm$ND where k is any integer. Each line in Fig. 5.4 connecting mode-pair frequencies of all NDs represents what is colloquially termed a family of modes with the lowest one being the first family, the next one the second family and so on.

Figure 5.5 shows the maximum response across all blades $|\mathbf{X}|$ of the tuned linear and nonlinear

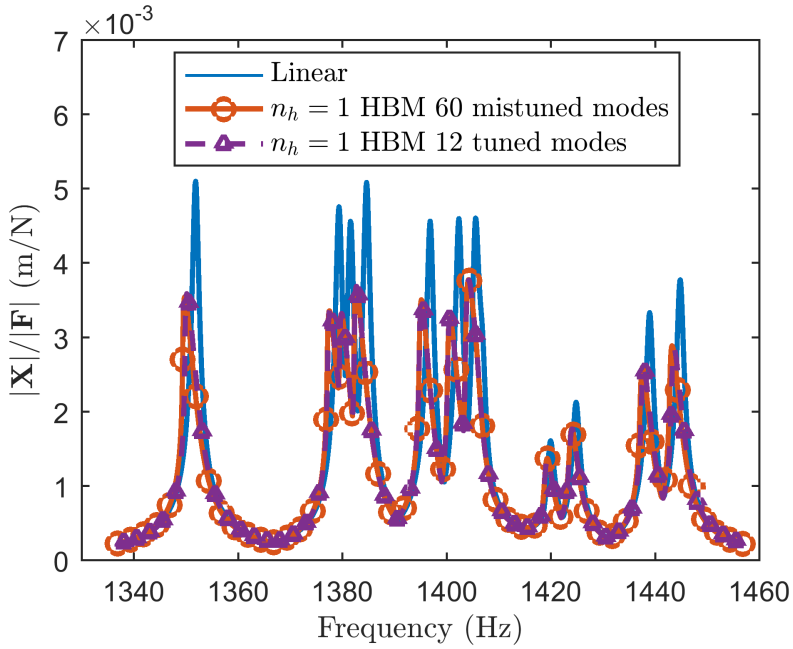

Figure 5.6. Normalized response of mistuned blisk: $|\mathbf{F}| = 0.1$ N, EO 2 excitation, $\sigma = 4\%$

blisks normalized by the amplitude $|\mathbf{F}|$ of an externally applied EO 2 excitation near the frequency of ND 2 mode-pair of the first family. 60 linear modes corresponding to the first five families of the blisk were retained for this simulation. A specified minimum resolution of 0.3 Hz is used for all blisk HBM simulations in this section. It is seen that including the third harmonic in the nonlinear HBM case does not change the simulated response significantly and the first harmonic is deemed sufficient for accuracy. Then, blisks with small linear stiffness mistuning in the blades are investigated. Figures. 5.6 and 5.7 show a case with a single mistuning pattern picked from a set of randomly generated patterns with 4% standard deviation (σ) in the stiffness of the blades. The same excitation is used as in the tuned case. Due to mistuning the modes no longer have perfect nodal diameter patterns and do not exist as perfect mode-pairs. Hence, more than two mistuned modes respond to the EO 2 excitation as is observed from the multiple resonant peaks for the linear and nonlinear cases in Fig. 5.6. In addition to the nonlinear baseline case where 60 mistuned modes are retained in solution, Fig. 5.6 also shows HBM responses for the case where

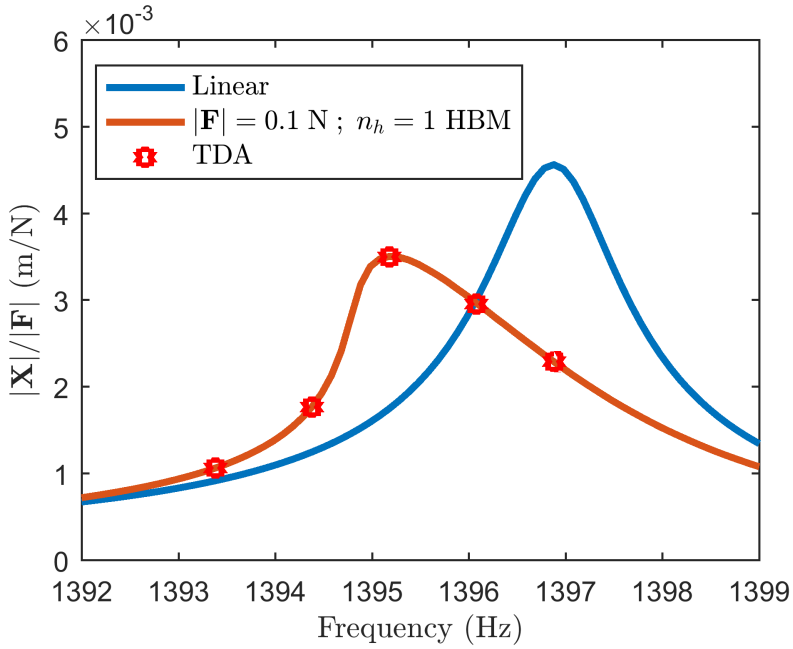

Figure 5.7. HBM vs TDA for single mistuning pattern: $|\mathbf{F}| = 0.1$ N, EO 2 excitation, $\sigma = 1\%$

the dynamics are projected onto the 12 tuned modes of the first family whose accuracy is validated by the close match between the two curves. The $n_h = 1$ nonlinear mistuned baseline in Fig. 5.6 was also validated against the TDA simulations at selected frequencies as shown in Fig. 5.7. The nonlinear damping and softening effects for the mistuned responses are also more clearly observed in Fig. 5.7.

5.3.3 Linear probabilistic analysis

The small linear stiffness mistuning value of $\sigma = 4\%$ used in section 5.3.2 is picked somewhat arbitrarily from the 1-5$\%$ range where maximum mistuned response is generally observed for linear blisks [76, 97]. Usually designers are interested in σ's which have the potential of yielding the highest amplification of the response of a mistuned blisk when compared to the response of the corresponding tuned blisk [7, 76, 77]. This measure is quantified by the ratio of the maximum response of the mistuned blisk to that of the tuned blisk in the frequency region of interest and

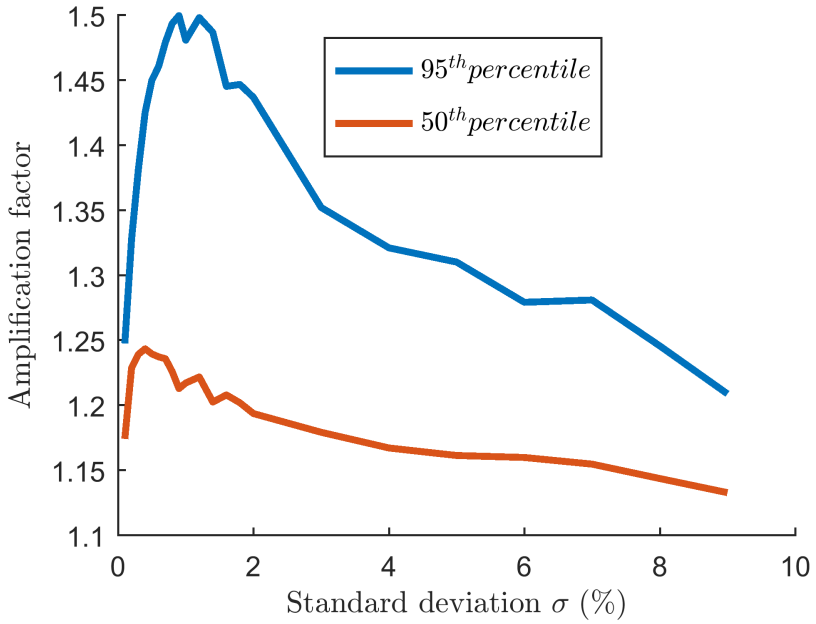

Figure 5.8. Percentile linear amplification factors

is termed amplification factor (AF). A probabilistic analysis for the linear blisk was carried out by simulating different blisks with randomly generated stiffness mistuning patterns with different values of σ. 1000 randomly generated patterns were used for each value of σ. Figure 5.8 shows the 95^{th} and 50^{th} percentile AFs for this data set when simulated in response to an EO 2 excitation in a frequency region spanning natural frequencies of the first family. It is observed that the 95^{th} percentile AF curve, peaks near $\sigma = 1\%$, which is used henceforth in simulations as it has the greatest potential for yielding the extreme cases with highest AFs. The projection onto tuned modes is also validated for different nonlinear cases by simulating the mistuned blisks found to have the 50 highest linear AFs from the set of 1000 simulated for $\sigma = 1\%$. This comparison is shown in Fig. 5.9. It may be seen that the nonlinear AFs for the cases with projection onto 12 tuned modes match very with the nonlinear baseline where 60 mistuned modes were retained, validating the accuracy of the projection.

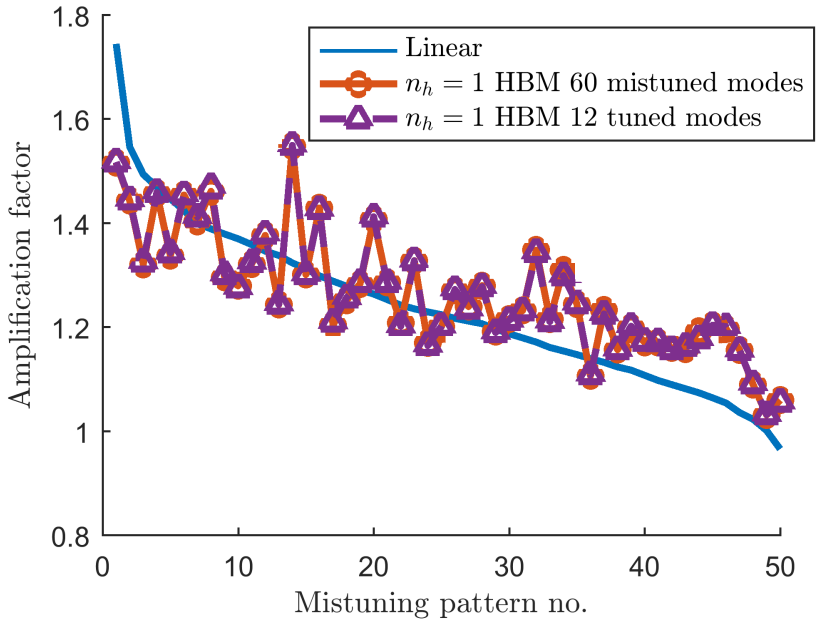

Figure 5.9. AFs for different mistuning patterns: $|\mathbf{F}| = 0.1$ N, EO 2 excitation, $\sigma = 1\%$

5.3.4 Determining explicit amplitude dependency for mistuning parameters

It is observe that since the that the projection of mistuned blisk dynamics on a basis of tuned modes is accurate and first harmonic is dominant, the reduced order model described by Eqn. (5.29) may be used. However, the functions f_m and g_m which establish the dependency of additional nonlinear damping on the nonlinear cantilevered blade response $A_{N,s}$ must be determined first. Using Eqns. (5.30) and (5.31), the additional stiffness mistuning and and damping ($m_{N,o}$ and $\alpha_{N,o}$) may be calculated for various excitation levels and plotted against tuned cantilevered blade nonlinear amplitude $A_{N,o}$ as shown in Figs. 5.10 and 5.11. $A_{L,o,max}$ and $A_{N,o,max}$ in Eqn. (5.31) may be obtained from the response $|\mathbf{X}|$ at peak frequency for the corresponding curve in Fig. 5.3. For the linear case $A_{N,o}$ is considered to be 0 and the corresponding damping and stiffness mistuning parameters are 0 by definition. As the dependency of storage and loss moduli of the coating on strain is linear, it is seen that the values calculated for the parameters from the simulations exhibit a linear dependency on the response amplitude. Hence, a linear least squares fit is employed to

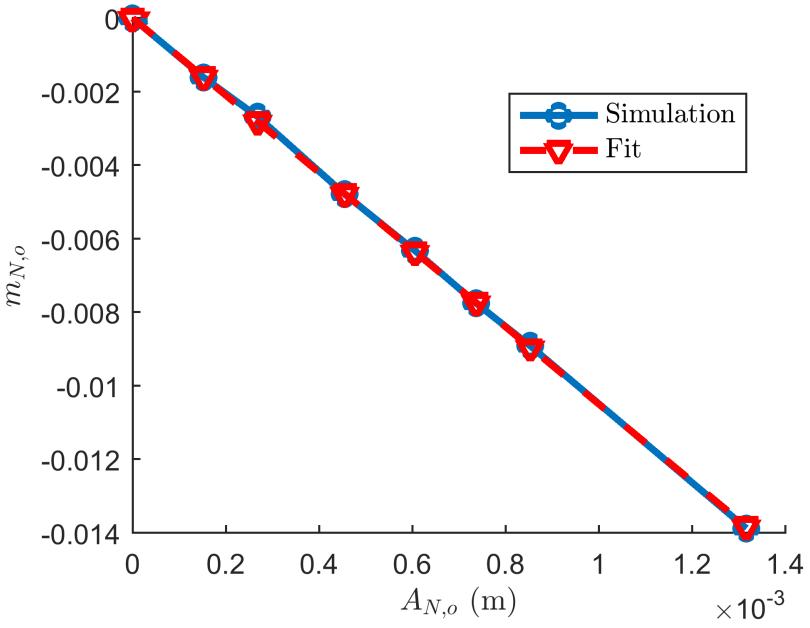

Figure 5.10. Additional stiffness mistuning due to coating

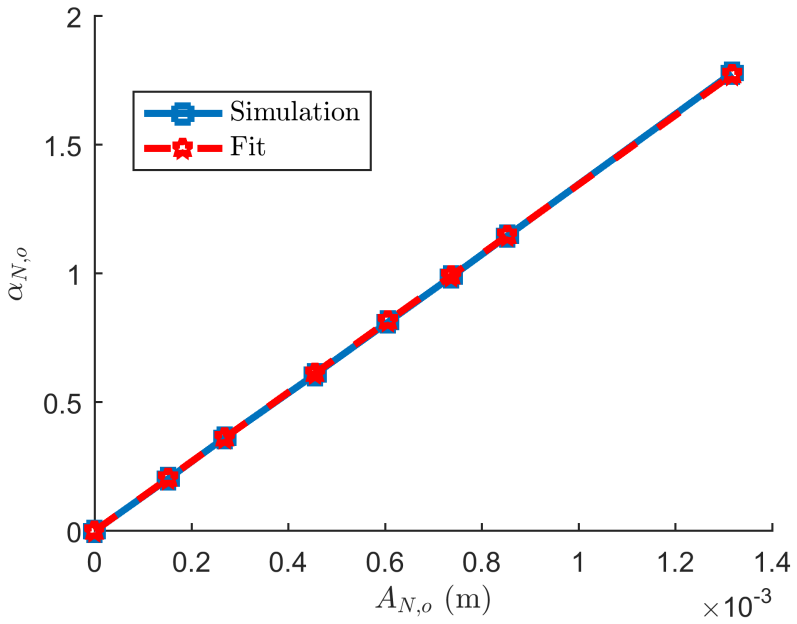

Figure 5.11. Additional damping due to coating

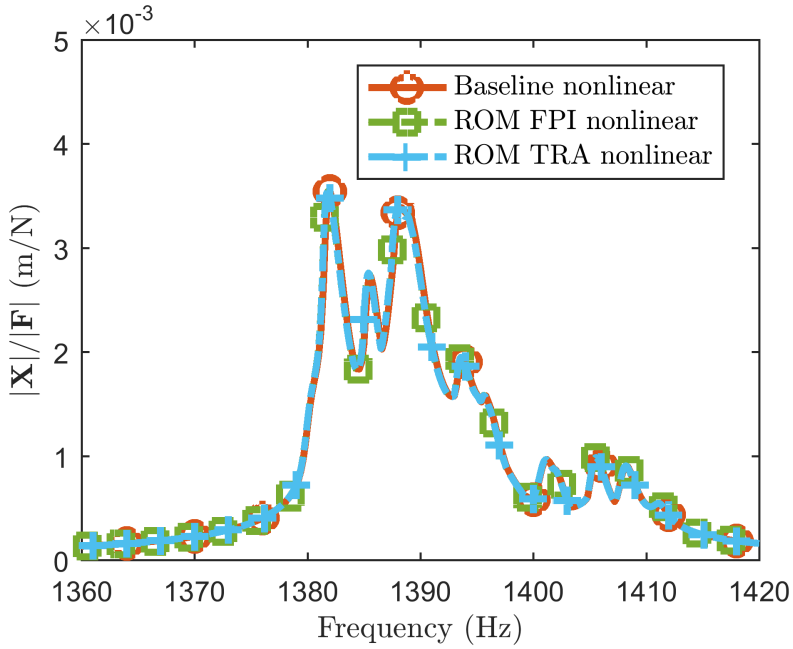

Figure 5.12. ROM vs Baseline: $|\mathbf{F}| = 0.1$ N, EO 2 excitation, $\sigma = 1\%$

calculate the slopes of these linear curves (1345.63 m^{-1} for $\alpha_{N,o}$ and -10.49 m^{-1} for $m_{N,o}$), which completely determine f_m and g_m as the curves pass through the origin. The entire AFT procedure can now be replaced by this simple algebraic relationship to determine the nonlinear parameters from amplitudes in the ROM.

5.3.5 Reduced order model with amplitude dependent nonlinearities

In addition to simulating the ROM using TRA, the accuracy of the FPI method described in section 5.2.3 is also tested. Figures 5.12-5.14 show the comparison of the ROM to the baseline model in response to and EO 2 excitation with amplitudes $|\mathbf{F}| = 0.1$, 0.4 and 1 N near first family natural frequencies. The dynamics of the blisk with 60 mistuned modes retained in simulation is used as the baseline. A specified minimum resolution of 0.1 Hz and a maximum of 200 iterations per frequency is used for all ROM simulations. It may be seen that the ROM simulated using TRA is able to predict the response very accurately for all cases including the highest excitation case

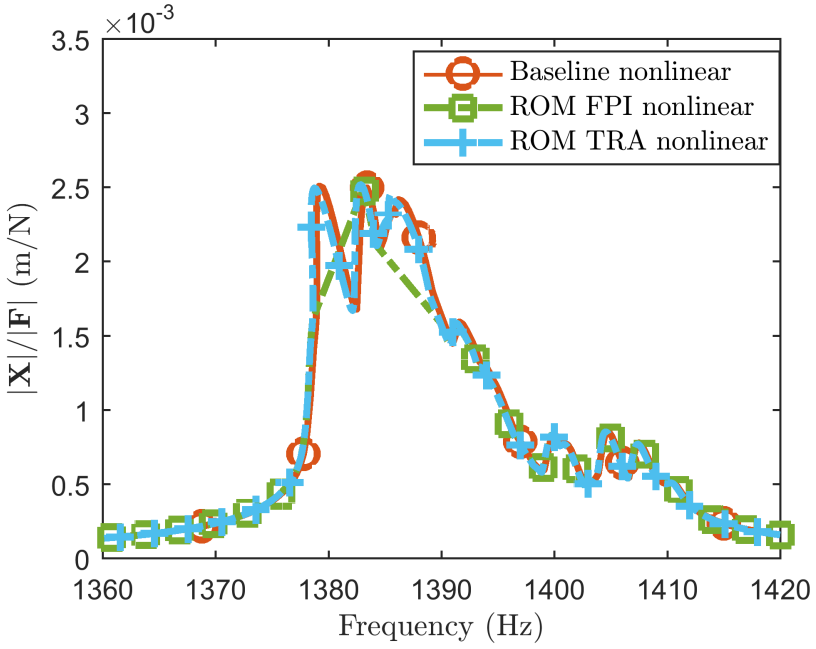

Figure 5.13. ROM vs Baseline: $|\mathbf{F}| = 0.4$ N, EO 2 excitation, $\sigma = 1\%$

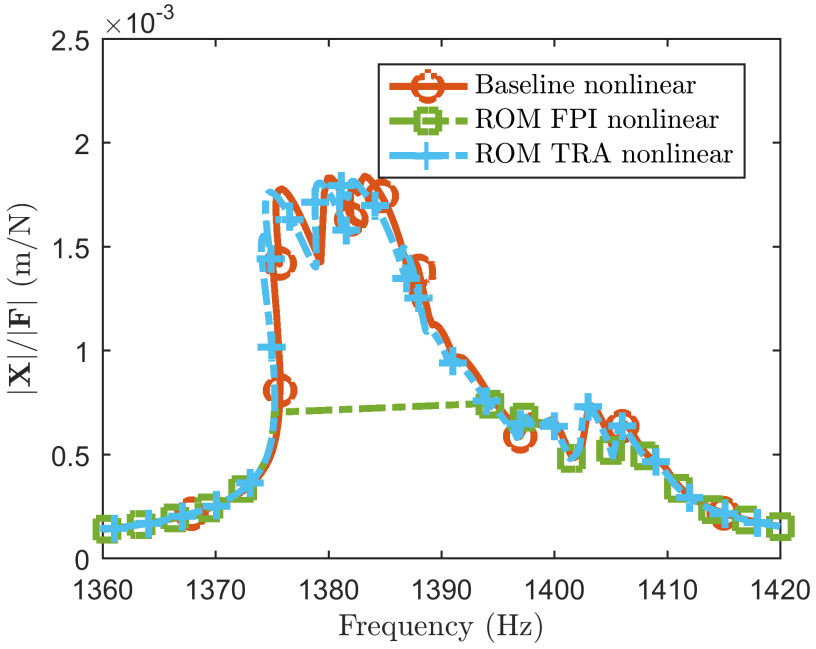

Figure 5.14. ROM vs Baseline: $|\mathbf{F}| = 1$ N, EO 2 excitation, $\sigma = 1\%$

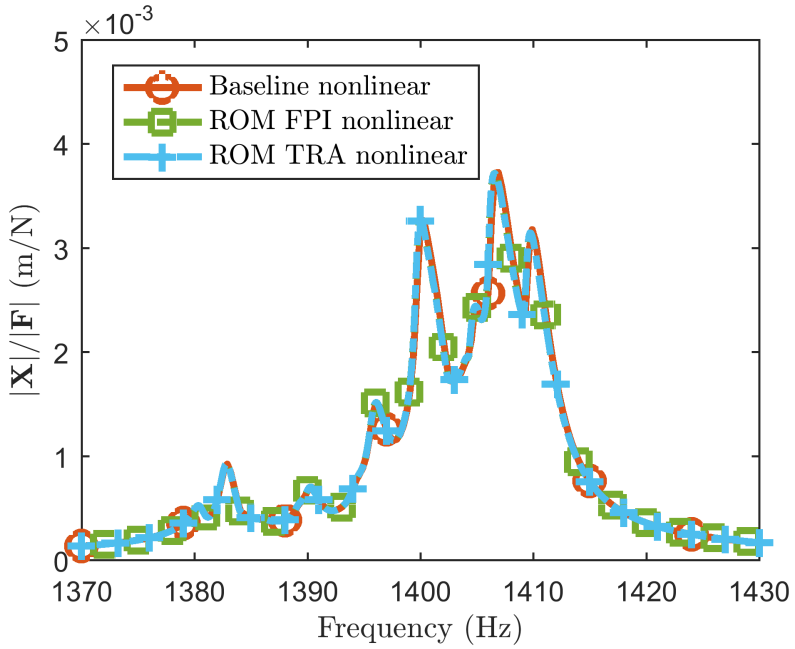

Figure 5.15. ROM vs Baseline: $|\mathbf{F}| = 0.1$ N, EO 5 excitation, $\sigma = 1\%$

where the effect of nonlinearities is most dominant. Only the fully converged points are plotted in the figures. It is seen that for the particular mistuning case shown in Figs. 5.12-5.14, FPI is able to predict the response well for $|\mathbf{F}| = 0.1$ N case. However, convergence is not reached for all frequencies at higher excitation levels and FPI is unable to predict the highest response accurately. It is plausible that increasing the number of maximum iterations or decreasing the frequency resolution will yield better convergence for FPI. However, the results clearly establish the superiority of TRA in terms of accuracy for identical parameters. Figure 5.12 shows the response of the same mistuned case to an EO 5 excitation, validating the accuracy of the ROM in response a different excitation pattern.

5.3.6 Simulation times

Simulation times will vary widely with the computational hardware used, the physical dynamic system being simulated and simulation parameters such as frequency resolution and maximum it-

eration limits and the level of nonlinearity which varies with excitation amplitude. The simulations in this study were conducted on different but comparable machines with desktop CPUs. Only ball-park figures are mentioned for the different simulation types based on empirical observation, as a detailed analysis of CPU times will be rendered invalid for the end user by factors mentioned above. The TDA simulations are very expensive and require simulation times on the order of 2-5 days to converge for a single frequency point. HBM simulations solved using TRA without projection on tuned modes (60 modes) require 2-3.5 hours for a simulation with a frequency range of approximately 100 Hz and 0.3 Hz resolution. A similar HBM simulation with projection (12 modes) requires 1-2 hours. ROMs with TRA and FPI are comparatively much faster requiring only 30-90 seconds for similar frequency ranges and resolutions. Note that although, the baseline simulation times will change based on the number of nonlinear elements in the system being simulated, the ROM size and consequently the simulation time depends only on the number of blades or sectors of the system.

5.4 Discussion

5.4.1 Amplitude dependent mistuning

The primary assumption that enabled the development of the ROM presented in this study is that the strain dependent nonlinearity of the coatings acts to modify the underlying mistuning pattern of the corresponding linear blisk. In the linear case this response is determined by the linear combinations of contributions from various mistuned modes. Each blade responds differently at different frequencies for a mistuned blisk. Figures 5.16 and 5.17 show how the nonlinear effects vary the stiffness at each blade based on their individual amplitudes at different frequencies. Thus, the mistuning pattern itself becomes a function of amplitude and as a consequence also varies with excitation frequency. The negative values of the additional nonlinear mistuning $m_{N,s}$ for the blades in Figs. 5.16 and 5.17 are due to the softening effect (reduction in stiffness) of the nonlinearity. At

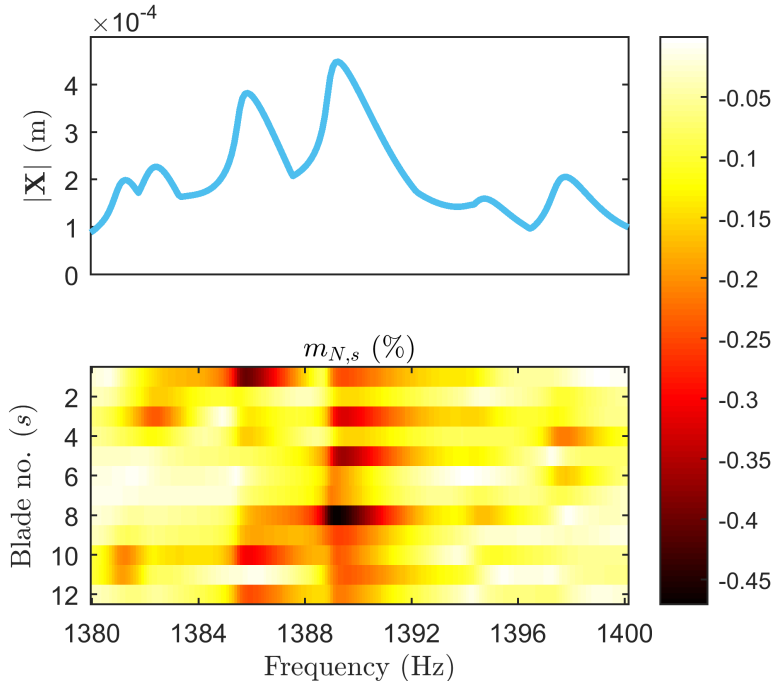

Figure 5.16. Amplitude dependent mistuning: $|\mathbf{F}| = 0.1$ N, EO 2 excitation, $\sigma = 1\%$

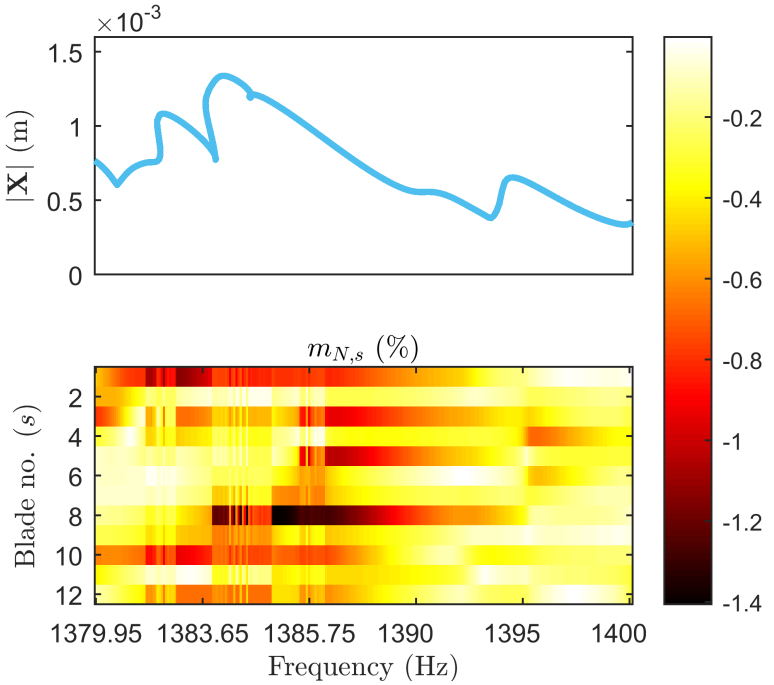

Figure 5.17. Amplitude dependent mistuning: $|\mathbf{F}| = 0.4$ N, EO 2 excitation, $\sigma = 1\%$

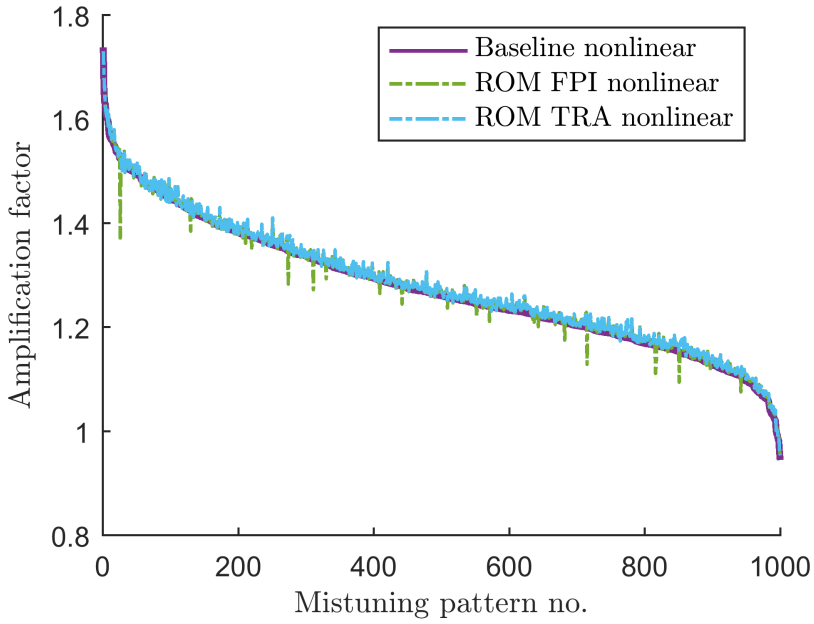

Figure 5.18. ROM vs Baseline AFs for multiple mistuning patterns: $|\mathbf{F}| = 0.1$ N, EO 2 excitation, $\sigma = 1\%$

its maximum value of approximately -0.45%, this additional mistuning value is significant when compared to the underlying linear mistuning of 1% for an excitation of $|\mathbf{F}| = 0.1$ N in Fig. 5.16. This contribution of the nonlinearity increases at higher excitations where the response amplitudes are higher as shown in Fig. 5.17.

5.4.2 Applicability of ROM for nonlinear simulations of coated blisks

Nonlinear simulations with 1000 different underlying linear mistuning patterns with $\sigma = 1\%$ were conducted for a particular excitation regime as shown in Fig. 5.18. The baseline used in this case is the dynamics projected onto the tuned modes. The different cases are arranged in decreasing order of AF for the baseline and compared to the ROMs. It is seen that the response and hence the AF predictions for the ROM with TRA are very accurate. The ROM simulated with FPI falters in predicting accurate AF values for certain mistuning patterns due to the convergence issues mentioned in section 5.3.5. This analysis provides additional validation of the accuracy of

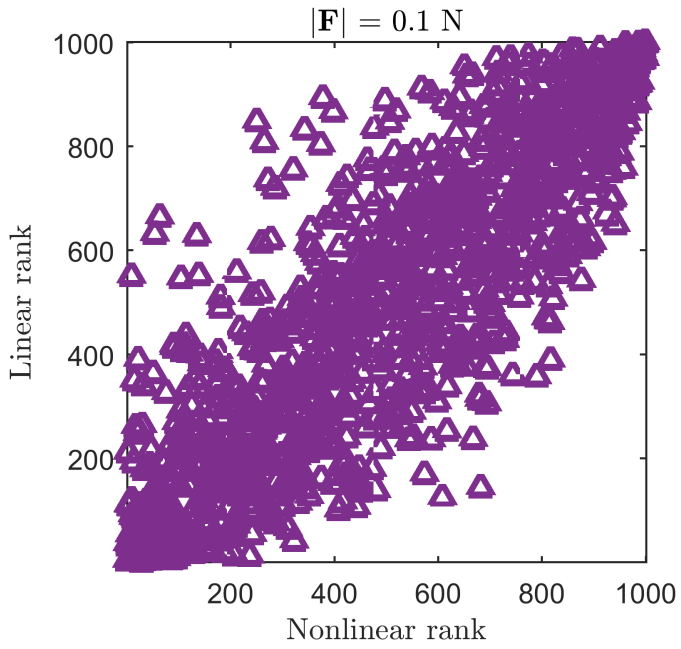

Figure 5.19. Rank comparison of AFs for multiple mistuning patterns: $|\mathbf{F}| = 0.1$ N, EO 2 excitation, $\sigma = 1\%$

the ROM solved using TRA for a coated blisk in different excitation regimes and shows that it can be used to predict nonlinear responses for probabilistic simulations.

However, whether such a simulation might be useful at all is yet to be analyzed. If the AFs for nonlinear blisks do not vary significantly from the linear case, a designer might choose to conduct probabilistic analysis with linear simulations which are by far less expensive than nonlinear ones. To test whether this is the case, the nonlinear AFs are compared to the linear AFs for the same set of linear mistuning patterns. Each pattern is ranked from the highest AF (rank 1) to the lowest (rank 1000) for both the linear and nonlinear cases. The two rankings for all the patterns are then plotted against each other in Fig. 5.19. If the rank and hence the percentile of a particular AF for a particular pattern does not change much with nonlinearity it should lie along the antidiagonal in this plot. It may be seen that several patterns in the plot deviate from this behavior. Hence, it is shown that nonlinearity not only has an effect on the response but also the AFs and it is not possible to predict the mistuning patterns which will exhibit the highest AF in a nonlinear case from linear

simulations. Probabilistic analysis with nonlinear ROMs is an essential tool for designers to predict coated blisk behavior under uncertainty in a nonlinear regime of operation.

5.4.3 Assumptions, possible generalizations and extensions

In this study a single dominant mode was assumed in the blade response. These assumptions will be accurate in frequency regions near isolated flat families. Near veering regions of the frequency versus nodal diameter plot, where multiple blade modes and tuned modal families may be involved [3, 10] the ROM will be less accurate. However, it is well known that in these regions there are significant contributions to the response from disk dominated modes [3, 98] which implies that damping provided by the coated blades will be less effective and the use of the ROM less pertinent. To regain accuracy of the ROM in such a region, the amplitude dependent mistuning and damping would have to be expressed not as function of blade amplitude at a single point, but as a function of the multiple dominant blade modal amplitudes. The use of cantilevered blade responses to approximate the functional dependence of blade nonlinearity on blade amplitudes might also lead to inaccuracies in a veering region where disk-dominant modes contribute to blade motion at the disk-blade interface. Instead it would be advisable to use tuned blisk blade responses or include amplitudes of attachment modes between blades and disk as additional parameters for the functional dependencies. In such a case, it may also be advisable to use other projection bases such as CMM modes whose formulation would be more convenient as the linear CMM ROM already contains mistuning parameters for multiple cantilevered blade modes and uses attachment modes for reduction in its most general formulation [16–18]. Another assumption of the ROM which may be possibly relaxed is the dominance of the first harmonic. In a situation where this is necessary, it is possible that the nonlinear parameters no longer depend directly on physical blade or sector level amplitudes but on the amplitudes of individual harmonics of the modes that comprise it. Accounting for this would require extending the number of additional nonlinear mistuning and damping parameters by a factor of the number of harmonics retained in the simulation, with each

one of these parameters being expressed as a function of all the blade modal harmonic amplitudes. The efficacy of such a ROM may be improved by determining if all these functional dependencies are significant and which harmonic modal amplitudes may me ignored for their calculation.

5.5 Conclusions

In this chapter, simulation techniques were developed for predicting the responses of a blisk containing blades with nonlinear coatings. An academic FE model of a coated blisk is developed. Baseline simulations of both the nominal cyclic symmetric tuned blisk and blisks with linear mistuning in the blades are carried out using the harmonic balance method, which is validated by comparison to time-marching transient dynamic analysis. It is determined that for small stiffness mistuning the nonlinear dynamics of the blisk, can be captured by projection onto the nominal tuned mode family corresponding to the dominant mode of the blade response. It is assumed that there is a dominant blade mode in the response and the strain-dependent nonlinear forces in the coating have the effect of changing the stiffness and damping of a each blade as a function of its amplitude. This effect is verified in simulations of individual cantilevered coated blades. A reduced order model for mistuned coated blisks is developed through the use of the tuned modes projection and additional nonlinear mistuning and damping parameters which capture the dependency of the nonlinearity on nonlinear blade response amplitudes. The reduced order model is compared with the baseline simulations in different regimes of excitation and found to be accurate, while reducing the simulation cost significantly. The amplification of coated blisk responses due to mistuning in the blades is studied for both the linear and nonlinear cases. It is found that the mistuning patterns which exhibit the highest amplifications for a linear case, might not necessarily do so for a nonlinear case, necessitating the use of probabilistic analysis with reduced order models such as the one developed herein to quantify and design for uncertainties. Hence, the representation of strain dependent nonlinearities in a nominally cyclic symmetric structure as additional mistuning and the consequent benefits for model reduction are established for coated blisk simulations,

while providing the requisite mathematical abstraction for possible application to similar nonlinear structures.

CHAPTER VI

Conclusions and Summary of Contributions

In this work, various novel methods for analysis and simulation of turbine bladed disk (blisk) models were developed. These methods primarily address the challenges of characterizing the dynamics in blisks due to the nominal cyclic nature of such systems and the inherent uncertainties in their design and manufacture. Commonly referred to as mistuning, these uncertainties lead to non-uniformity in dynamic parameters such as stiffnesses and damping across the cyclic sectors of these structures, which are also often nonlinearly dependent on blade displacements. These effects act in tandem to engender the complex vibratory behavior observed in these structures. The nonlinearities can be caused due to various distinct mechanisms such as friction, intermittent contacts or coatings and may be intentional or non-intentional. The physics underlying these dynamics may thus be very different and require specialized strategies for modeling. High-fidelity modeling based on first principles is of limited practical use for design because the computational complexity involved in simulating such models renders them infeasible for carrying out probabilistic analyses required to account for uncertainties and mistuning. Hence, the focus of this work has been the development of reduced order models (ROMs) for these structures which are orders of magnitude faster than corresponding high-fidelity models and yet capture the responses and stresses in blisks accurately.

A structure whose dynamics is particularly challenging to analyze and reduce is the shrouded

blisk. The frictional contacts at the shrouds near the blade tip play a major role in the dynamics of such systems. The localized stick-slip conditions and associated nonlinear frictional forces at the interfaces give rise to a microslip regime which refers to any combination of localized contact conditions between two linear extremes: full stick where all contacts are stuck at all times and gross slip where all contacts are slipping beyond the friction limit at all times. The modes of the structure change with excitation amplitude and frequency in the microslip regime making model order reduction a challenging task. In this study, ROMs were obtained for shrouded blisks in the microslip using an adaptive microslip projection (AMP) reduction basis which captures the spatial correlations in the nonlinear blisk response at steady-state across a range of excitation frequencies. The AMP basis vectors are linear modes of intermediate linear systems corresponding to special boundary-conditions at the contact interfaces derived by approximating the effect of the structural response at varying amplitude levels on localized contact conditions at those interfaces. The AMP ROM was validated in simulations by comparing its forced responses against a full order baseline model for various cases of mistuning in different excitation regimes. A convergence study of the ROMs was performed to analyze the number of AMP reduction basis vectors required for accurate dynamic reduction by comparing them to the proper orthogonal modes (POMs) describing the dominant spatial coherences in the response. The AMP reduction procedure avoids explicit calculations of full-order nonlinear responses while performing spatial reduction for both linear and nonlinear degrees of freedom (DoFs) of the model. This makes it highly computationally efficient compared to other commonly used techniques which require nonlinear calculations (eg. POMs) or reduce only linear DoFs (eg. Craig-Bampton component mode synthesis (CB-CMS)). Other advantages include user-friendliness and monotonically decreasing errors with the size of the reduction basis. Although AMP was developed in this study for shrouded blisks, they may possibly be adapted for reducing other systems with frictional contacts in microslip.

Experimental verification was also sought to confirm the presence of spatial coherences in a nonlinear system with contact and validate the AMP procedure. Another experimental objective,

in view of practical application of the developed ROMs, was estimating the contact parameters such as contact stiffnesses, coefficient of friction and normal load distributions which are used to model nonlinear Coulomb friction in both full and reduced order models, but cannot be readily measured directly. An experimental rig consisting of a blade-like cantilevered beam with a large flat-on-flat frictional contact was designed and constructed. Experiments were conducted to measure linear stuck beam modes and to obtain frequency responses of the beam with the contact in microslip. Responses were measured both on the beam face and close to the contact. Finite element (FE) modeling and CB-CMS were used to obtain a linear model of the free beam. This model was augmented with localized contact models and optimization techniques were used to estimate the contact parameters by minimizing the error in simulation responses with respect to experimentally measured values. The identified parameters were then used to create AMP ROMs which were compared with the CB-CMS baseline model for verification and found to accurately predict responses at multiple excitation levels. An AMP basis was also estimated by applying specific boundary conditions to the linear model based on experimentally observed displacements near the contact. This AMP basis was compared to the POMs obtained directly from the experimental response and the two subspaces were found to be a good match, providing further verification for the AMP reduction procedure.

Another aspect of microslip in blisks that was not well-researched in the past, is the effect of variances in contact parameters within a single contact interface and across different interfaces of such a nominally cyclic structure. In this study, contact mistuning in a shrouded blisk with mistuned local contact stiffnesses was analyzed at different contact conditions including linear (all interfaces in full stick or gross slip) and nonlinear (different levels of microslip) operational regimes. Monte Carlo simulations were used to generate probabilistic data of mistuned blisk response amplification compared to tuned blisk response, which is also colloquially referred to as amplification factor (AF) and is a metric commonly used to ascertain the effects of a mistuning. The AF is found to be dependent on the spatial harmonic or engine order (EO) associated with the

traveling-wave forced excitation commonly used for these studies. It was seen that both the level of microslip and mistuning determine the AF. Although the response of a blisk in microslip is known to be bounded by the linear cases of full stick and gross slip, it was seen that this is not necessarily true of AFs. The optimum value of microslip at which the amplification is minimum was found to vary with the level of mistuning. It was concluded that the designed level of microslip in the operating region should try to trade-off between the tuned damped response and the highest AFs expected due to uncertainty in the contact parameters in that region.

A nonlinear damping mechanism, which is increasingly more common in modern blisks and was made possible due to advances in materials and manufacturing technology, is nonlinear damping coatings applied onto blades of blisks. The nonlinear forces due to these coatings are not localized at a few interfaces like in shrouded blisks. Hence, the number of nonlinear DoFs in the models for coated blisks are comparatively higher. However, the silver lining for model order reduction of the dynamics is that the modes of the blades are not affected significantly by the distributed coating nonlinearities and the dynamics can be captured by a set of linearized modes. This work builds upon previous work on modeling coated blades and beams and extends such analyses to tuned and mistuned coated blisks. Modeling methods were developed for obtaining frequency responses of high-fidelity nonlinear FE based models of coated blisks with small linear stiffness mistuning in the blades. It was observed that the nonlinear dynamics of such a mistuned blisk can be captured by projection onto the nominal modes of the corresponding tuned blisk irrespective of the mistuning pattern. It was further shown, that the damping and stiffness at each blade could in general be expressed as polynomial functions of the blade amplitude. This is equivalent to a mistuning in stiffness and damping of the blades which is amplitude dependent. This allowed the development of an extremely fast ROM, where the nonlinearity in the dynamics could be captured directly in the reduced order space by using amplitude-dependent mistuning parameters. ROMs responses were calculated for several different mistuning patterns and operational regimes and validated against full-order model responses. Probabilistic analyses were also carried out using blisks

with randomly generated mistuning patterns. It was found that the mistuning patterns which exhibit the highest AFs for blisks where the coating is assumed to be linear, might not necessarily do so for a nonlinear case. This highlights the indispensability of the developed ROMs, particularly to design for uncertainties.

In summary, the specific contributions of the research included in this thesis to the field of turbomachinery and mechanical engineering in general may be stated as follows:

- The nonlinear vibration response of complex rotating systems that contain Coulomb friction due to shroud-to-shroud dampers was modeled.
- A reduced order modeling tool, namely the adaptive microslip projection (AMP) method was developed for such shrouded blisks and verified in simulation.
- An experimental rig was designed and manufactured to study the effects of nonlinear damping in microslip regime.
- Contact parameters were identified and the AMP method was validated using experimental data obtained from measuring vibratory responses of the experimental rig.
- The effect of variation in contact parameters both within a contact interface and across various interfaces on a nominally cyclic symmetric system was studied using probabilistic analyses with shrouded blisk models.
- An modeling tool was created for capturing the effects of nonlinear damping coatings on the vibration of complex rotating systems.
- The inherent amplitude-dependent stiffness and damping mistuning introduced into the system by these coatings was utilized to create an efficient reduced order modeling technique. The efficacy and accuracy of these models were verified using probabilistic analyses.

In the future, various possible extensions for this work may be envisioned. One possibility for obtaining further reductions in simulation times for AMP ROMs is to forego the alternating-frequency time procedure for all nonlinear DoFs during solution. Methods may be developed to instead estimate nonlinear forces from displacements directly in the frequency domain. One possibility is the use of sampling at certain DoFs, similar to hyper-reduction methods. Although, the inclusion of multiple harmonics were discussed in this work, alternate methods may be developed to obtain AMPs for the coupled multi-harmonic system equations directly, which can then be used for reduction. Application to AMPs other systems with microslip and using more advanced contact models is a possibility. Inspiration may also be gained from the underlying tenets of the AMPs. Particularly, trying to capture spatial correlations in the response and predicting boundary conditions may be good first steps toward developing other ROMs for problems with different physical phenomena.

Damping estimation in systems with contacts remains an industry priority. Both the type and volume of available sensor data from experiments will only increase in the future. It may soon be possible to apply other, more data-hungry, system identification techniques such as those based on auto-regression or neural networks applied with more advanced contact models to get better estimates of nonlinear damping from experimental data. With better estimation of localized contact parameters and greater control over these properties provided by advanced manufacturing techniques, the lessons learned from the study on the effects of contact mistuning may be put to good use.

Advances in materials have also made damping coatings feasible for blisks. The ROM developed and validated for coated blisks in this work may be applied to larger models representing real blisks. More involved studies may be conducted to understand the modifications required to the ROM to account for specific cases such as pre-stress and responses dominated multiple blade families which were not studied in detail here. The idea of reduction based on amplitude dependent mistuning may be also be applied to other similar nonlinear systems with cyclic symmetry.

APPENDIX A

System Matrices of a Cyclic Symmetric Structure

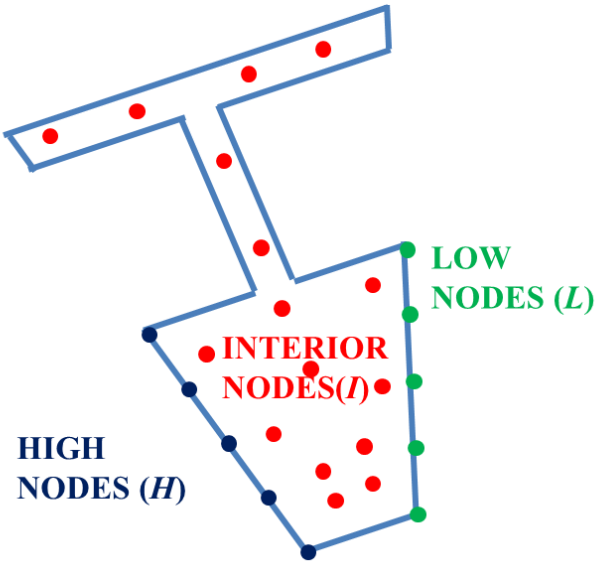

Figure A.1. DoFs for system matrices

The free stiffness matrix $\mathbf{K}^{S_n}$ for a single shrouded blade which comprises sector S_n may be represented as:

$$\mathbf{K}^{S_n} = \begin{bmatrix} \mathbf{K}_{LL}^{S_n} & \mathbf{K}_{LI}^{S_n} & \mathbf{K}_{LH}^{S_n} \\ \mathbf{K}_{IL}^{S_n} & \mathbf{K}_{II}^{S_n} & \mathbf{K}_{IH}^{S_n} \\ \mathbf{K}_{HL}^{S_n} & \mathbf{K}_{HI}^{S_n} & \mathbf{K}_{HH}^{S_n} \end{bmatrix} \tag{A.1}$$

where subscript L refers to degrees of freedom (DoFs) at the Target/Low disk surface, subscript I refers to DoFs in the interior of the blade and subscript H refers to DoFs at the Contact/High disk surface.

Since all the operations applied to the system matrices in this discussion will be similar, only the operations applied to the stiffness matrix are shown. The matrices corresponding to mass and damping will have similar forms.

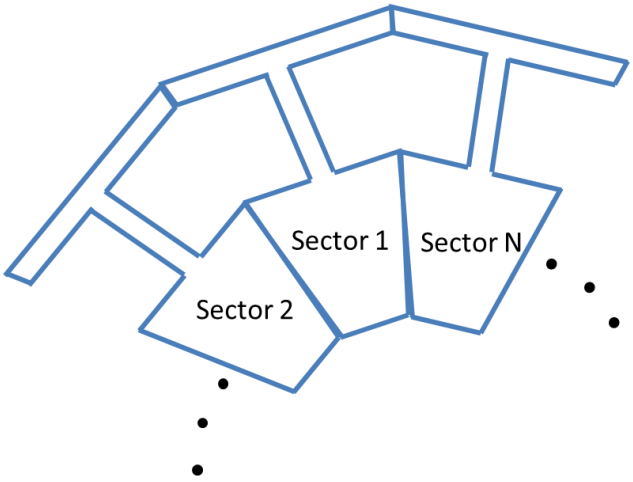

Figure A.2. Full blisk DoFs

The full 360° blisk system matrix which is formed by merging the disk interface DoFs of adjacent sectors as shown in Fig. A.2 is given by:

$$\mathbf{K} = \begin{bmatrix} \mathbf{K}_{II}^{S_1} & \mathbf{K}_{IH}^{S_1} & \mathbf{0} & \mathbf{0} & \mathbf{0} & \cdots & \cdots & \cdots & \mathbf{0} & \mathbf{K}_{IL}^{S_1} \\ \mathbf{K}_{HI}^{S_1} & \mathbf{K}_{HH}^{S_1}+\mathbf{K}_{LL}^{S_2} & \mathbf{K}_{LI}^{S_2} & \mathbf{K}_{LH}^{S_2} & \mathbf{0} & \cdots & \cdots & \cdots & \mathbf{0} & \mathbf{K}_{\mathrm{HL}}^{S_1} \\ \mathbf{0} & \mathbf{K}_{IL}^{S_2} & \mathbf{K}_{II}^{S_2} & \mathbf{K}_{\mathrm{IH}}^{S_2} & \mathbf{0} & \cdots & \cdots & \cdots & \cdots & \mathbf{0} \\ \mathbf{0} & \mathbf{K}_{HL}^{S_2} & \mathbf{K}_{HI}^{S_2} & \mathbf{K}_{HH}^{S_2}+\mathbf{K}_{LL}^{S_3} & \mathbf{K}_{LI}^{S_3} & \mathbf{K}_{LH}^{S_3} & \mathbf{0} & \cdots & \cdots & \vdots \\ \mathbf{0} & \mathbf{0} & \cdots & \cdots & \ddots & & & & & \\ \vdots & \vdots & & & & & & & & \\ \mathbf{0} & \mathbf{0} & \mathbf{0} & \cdots & \cdots & \cdots & \cdots & \cdots & \mathbf{K}_{II}^{S_N} & \mathbf{K}_{IH}^{S_N} \\ \mathbf{K}_{LI}^{S_1} & \mathbf{K}_{LH}^{S_1} & \mathbf{0} & \cdots & \cdots & \cdots & \cdots & \cdots & \mathbf{K}_{HI}^{S_N} & \mathbf{K}_{HH}^{S_N}+\mathbf{K}_{LL}^{S_1} \end{bmatrix} \tag{A.2}$$

where N is the number of sectors/blades. For a tuned system the superscripts S_n $(n = 1, 2, \cdots, N)$ may be dropped and then the generating stiffness matrices [99, 100] of the full blisk system may

be written as:

$$\mathbf{K}_{gen,1} = \begin{bmatrix} \mathbf{K}_{II} & \mathbf{K}_{IH} \\ \mathbf{K}_{HI} & \mathbf{K}_{HH} + \mathbf{K}_{LL} \end{bmatrix} \tag{A.3}$$

$$\mathbf{K}_{gen,2} = \begin{bmatrix} \mathbf{0} & \mathbf{0} \\ \mathbf{K}_{LI} & \mathbf{K}_{LH} \end{bmatrix} \tag{A.4}$$

$$\mathbf{K}_{gen,j} = \begin{bmatrix} \mathbf{0} & \mathbf{0} \\ \mathbf{0} & \mathbf{0} \end{bmatrix} \quad j = 3, 4..., N-1 \tag{A.5}$$

$$\mathbf{K}_{gen,N} = \begin{bmatrix} \mathbf{0} & \mathbf{K}_{IL} \\ \mathbf{0} & \mathbf{K}_{HL} \end{bmatrix} \tag{A.6}$$

The complex stiffness matrix in the cyclic co-ordinates corresponding to the spatial harmonic index h may now be obtained by using the equation [99, 100]:

$$\tilde{\mathbf{K}}^{h}_{\mathbb{C}} = \sum_{n=1}^{N} \mathbf{K}_{gen,j} e^{i(n-1)h\alpha} \tag{A.7}$$

where i is the square root of -1, h is the spatial harmonic index (not the number of harmonics in the harmonic balance method), subscript $\mathbb{C}$ represents the complex nature of the matrix and α is given by:

$$\alpha = 2\pi/N \tag{A.8}$$

$h\alpha$ is commonly referred to as the inter-blade phase angle. Substituting Eqns. A.3- A.6 into Eqn. A.7 one may obtain:

$$\tilde{\mathbf{K}}^{h}_{\mathbb{C}} = \begin{bmatrix} \mathbf{K}_{II} & \mathbf{K}_{IH} + \mathbf{K}_{IL} e^{-ih\alpha} \\ \mathbf{K}_{HI} + \mathbf{K}_{LI} e^{ih\alpha} & \mathbf{K}_{HH} + \mathbf{K}_{LL} + \mathbf{K}_{LH} e^{ih\alpha} + \mathbf{K}_{HL} e^{-ih\alpha} \end{bmatrix} \tag{A.9}$$

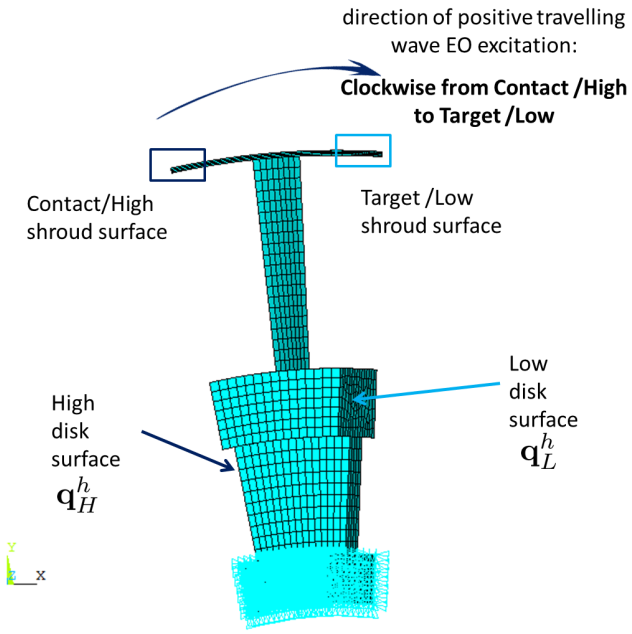

Figure A.3. Cyclic Symmetric CBCMS setup

The stiffness matrix in Eqn. (A.9) may also be obtained by applying constraints between the complex displacements of matching nodes on low and high surfaces of the sector model [41] as shown in Fig. A.3. The constraint equation describing the positive (forward) traveling wave for a blisk free shrouds (with no contact established) may be given by:

$$\tilde{\mathbf{q}}_L^h = \tilde{\mathbf{q}}_H^h e^{-ih\alpha} \tag{A.10}$$

where $\tilde{\mathbf{q}}$ represents a constrained displacement vector. Eqn. (A.10) can be expanded using the complex nature of the quantities as follows:

$$\Re(\tilde{\mathbf{q}}_L^h) + i\Im(\tilde{\mathbf{q}}_L^h) = (\Re(\tilde{\mathbf{q}}_H^h) + i\Im(\tilde{\mathbf{q}}_H^h))(cos(h\alpha) - isin(h\alpha)) \tag{A.11}$$

or

$$\begin{aligned}\Re(\tilde{\mathbf{q}}_L^h) + i\Im(\tilde{\mathbf{q}}_L^h) = (\Re(\tilde{\mathbf{q}}_H^h)cos(h\alpha) + \Im(\tilde{\mathbf{q}}_H^h)sin(h\alpha)) \\ +i(\Im(\tilde{\mathbf{q}}_H^h)cos(h\alpha) - \Re(\tilde{\mathbf{q}}_H^h)sin(h\alpha))\end{aligned} \tag{A.12}$$

Equating real and imaginary parts of Eqn. (A.12) then yields:

$$\Re(\tilde{\mathbf{q}}_L^h) = \Re(\tilde{\mathbf{q}}_H^h)cos(h\alpha) + \Im(\tilde{\mathbf{q}}_H^h)sin(h\alpha) \tag{A.13}$$

and

$$\Im(\tilde{\mathbf{q}}_L^h) = \Im(\tilde{\mathbf{q}}_H^h)cos(h\alpha) - \Re(\tilde{\mathbf{q}}_H^h)sin(h\alpha) \tag{A.14}$$

The complex free blade displacements for any sector of a cyclic symmetric (tuned) blisk corresponding to the stiffness matrix of Eqn. (A.1) may be represented by:

$$\mathbf{q}_{\mathbb{C}}^h = \begin{bmatrix} \mathbf{q}_L^h \\ \mathbf{q}_I^h \\ \mathbf{q}_H^h \end{bmatrix} \tag{A.15}$$

$\mathbf{q}_{\mathbb{C}}^h$ may be transformed into a reduced set of complex co-ordinates $\tilde{\mathbf{q}}_{\mathbb{C}}^h$ which corresponds to the matrix in Eqn. (A.9) given by:

$$\tilde{\mathbf{q}}_{\mathbb{C}}^h = \begin{bmatrix} \tilde{\mathbf{q}}_I^h \\ \tilde{\mathbf{q}}_H^h \end{bmatrix} \tag{A.16}$$

The transformation is represented by the equation:

$$\mathbf{q}_{\mathbb{C}}^h = \mathbf{T}_{\mathbb{C}}^h \tilde{\mathbf{q}}_{\mathbb{C}}^h \tag{A.17}$$

Transformation matrix $\mathbf{T}_{\mathbb{C}}^{h}$ may be defined using Eqn. (A.10) as follows:

$$\mathbf{T}_{\mathbb{C}}^{h} = \begin{bmatrix} \mathbf{0} & \mathbf{I}e^{-ih\alpha} \\ \mathbf{I} & \mathbf{0} \\ \mathbf{0} & \mathbf{I} \end{bmatrix} \tag{A.18}$$

Then the stiffness matrix in cyclic co-ordinates $\tilde{\mathbf{K}}_{\mathbb{C}}^{h}$ of Eqn. (A.9) may be recovered by substituting Eqns. (A.1) and (A.18) in the equation:

$$\tilde{\mathbf{K}}_{\mathbb{C}}^{h} = {\mathbf{T}_{\mathbb{C}}^{h}}^{\mathrm{H}} \mathbf{K}^{S_n} {\mathbf{T}_{\mathbb{C}}}^{h} \tag{A.19}$$

where superscript H represents the Hermitian of a complex matrix. Thus, ignoring the superscripts S_n for a tuned blisk and simplifying Eqn. (A.19) one may obtain:

$$\tilde{\mathbf{K}}_{\mathbb{C}}^{h} = \begin{bmatrix} \mathbf{0} & \mathbf{I} & \mathbf{0} \\ \mathbf{I}e^{ih\alpha} & \mathbf{0} & \mathbf{I} \end{bmatrix} \cdot \begin{bmatrix} \mathbf{K}_{LL} & \mathbf{K}_{LI} & \mathbf{K}_{LH} \\ \mathbf{K}_{IL} & \mathbf{K}_{II} & \mathbf{K}_{IH} \\ \mathbf{K}_{HL} & \mathbf{K}_{HI} & \mathbf{K}_{HH} \end{bmatrix} \cdot \mathbf{T}_{\mathbb{C}}^{h} \tag{A.20}$$

or

$$\tilde{\mathbf{K}}_{\mathbb{C}}^{h} = \begin{bmatrix} \mathbf{K}_{IL} & \mathbf{K}_{II} & \mathbf{K}_{IH} \\ \mathbf{K}_{LL}e^{ih\alpha}+\mathbf{K}_{HL} & \mathbf{K}_{LI}e^{ih\alpha}+\mathbf{K}_{HI} & \mathbf{K}_{LH}e^{ih\alpha}+\mathbf{K}_{HH} \end{bmatrix} \cdot \begin{bmatrix} \mathbf{0} & \mathbf{I}e^{-ih\alpha} \\ \mathbf{I} & \mathbf{0} \\ \mathbf{0} & \mathbf{I} \end{bmatrix} \tag{A.21}$$

or

$$\tilde{\mathbf{K}}_{\mathbb{C}}^{h} = \begin{bmatrix} \mathbf{K}_{II} & \mathbf{K}_{IL}e^{-ih\alpha} + \mathbf{K}_{IH} \\ \mathbf{K}_{LI}e^{ih\alpha} + \mathbf{K}_{HI} & \mathbf{K}_{LL} + \mathbf{K}_{HL}e^{-ih\alpha} + \mathbf{K}_{LH}e^{ih\alpha} + \mathbf{K}_{HH} \end{bmatrix} \tag{A.22}$$

which is the same as Eqn. (A.9).

Often, commercially available software cannot enforce complex constraints. In such a situation the complex constraint described by Eqn. (A.10) may be replaced by the real constraints in the

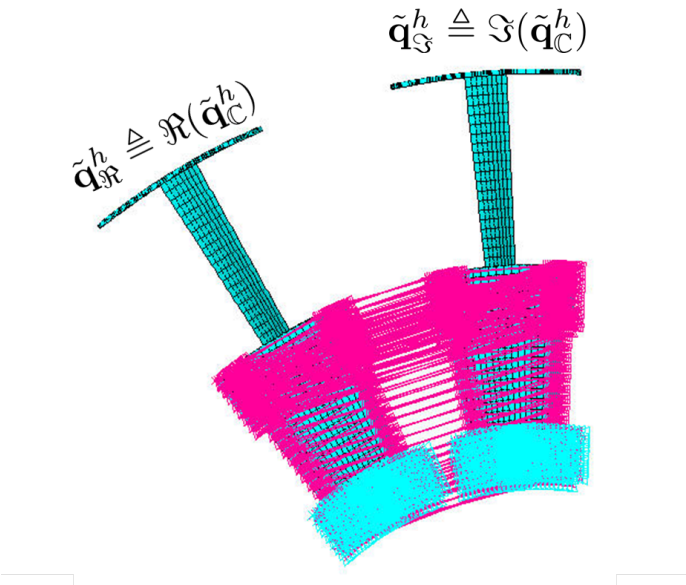

Figure A.4. Constraints on real displacements

Eqns. (A.13) and (A.14). To apply this in practice two identical free sectors of the blisk must be considered, one representing the real part of the free blade displacements and the other the imaginary part as shown in Fig. A.4. The vector of real displacements corresponding to this model is given by:

$$\mathbf{q}^h_{\mathbb{R}} \triangleq \begin{bmatrix} \mathbf{q}^h_{\Re} \\ \mathbf{q}^h_{\Im} \end{bmatrix} \triangleq \begin{bmatrix} \Re(\mathbf{q}^h_{\mathbb{C}}) \\ \Im(\mathbf{q}^h_{\mathbb{C}}) \end{bmatrix} = \begin{bmatrix} \Re(\mathbf{q}^h_L) \\ \Re(\mathbf{q}^h_I) \\ \Re(\mathbf{q}^h_H) \\ \Im(\mathbf{q}^h_L) \\ \Im(\mathbf{q}^h_I) \\ \Im(\mathbf{q}^h_H) \end{bmatrix} \tag{A.23}$$

where subscript $\Re$ represents DoFs belonging to the real sector and subscript $\Im$ represents DoFs belonging to the Imaginary sector.

The corresponding stiffness matrix for this free 2 blade system is given by:

$$\mathbf{K}^{2S} = \begin{bmatrix} \mathbf{K}_{LL} & \mathbf{K}_{LI} & \mathbf{K}_{LH} & \mathbf{0} & \mathbf{0} & \mathbf{0} \\ \mathbf{K}_{IL} & \mathbf{K}_{II} & \mathbf{K}_{IH} & \mathbf{0} & \mathbf{0} & \mathbf{0} \\ \mathbf{K}_{HL} & \mathbf{K}_{HI} & \mathbf{K}_{HH} & \mathbf{0} & \mathbf{0} & \mathbf{0} \\ \mathbf{0} & \mathbf{0} & \mathbf{0} & \mathbf{K}_{LL} & \mathbf{K}_{LI} & \mathbf{K}_{LH} \\ \mathbf{0} & \mathbf{0} & \mathbf{0} & \mathbf{K}_{IL} & \mathbf{K}_{II} & \mathbf{K}_{IH} \\ \mathbf{0} & \mathbf{0} & \mathbf{0} & \mathbf{K}_{HL} & \mathbf{K}_{HI} & \mathbf{K}_{HH} \end{bmatrix} \tag{A.24}$$

The intention is to reduce the system displacements in Eqn. (A.23) to the set of reduced DoFs:

$$\tilde{\mathbf{q}}^h_{\mathbb{R}} \triangleq \begin{bmatrix} \tilde{\mathbf{q}}^h_{\Re} \\ \tilde{\mathbf{q}}^h_{\Im} \end{bmatrix} \triangleq \begin{bmatrix} \Re(\tilde{\mathbf{q}}^h_{\mathbb{C}}) \\ \Im(\tilde{\mathbf{q}}^h_{\mathbb{C}}) \end{bmatrix} = \begin{bmatrix} \Re(\tilde{\mathbf{q}}^h_{I}) \\ \Re(\tilde{\mathbf{q}}^h_{H}) \\ \Im(\tilde{\mathbf{q}}^h_{I}) \\ \Im(\tilde{\mathbf{q}}^h_{H}) \end{bmatrix} \tag{A.25}$$

This may be achieved using the equation:

$$\mathbf{q}^h_{\mathbb{R}} = \mathbf{T}^h_{\mathbb{R}} \tilde{\mathbf{q}}^h_{\mathbb{R}} \tag{A.26}$$

where the transformation matrix $\mathbf{T}^h_{\mathbb{R}}$ may be described using Eqns. (A.13) and (A.14) as:

$$\mathbf{T}^h_{\mathbb{R}} = \begin{bmatrix} \mathbf{0} & \mathbf{I}cos(h\alpha) & \mathbf{0} & \mathbf{I}sin(h\alpha) \\ \mathbf{I} & \mathbf{0} & \mathbf{0} & \mathbf{0} \\ \mathbf{0} & \mathbf{I} & \mathbf{0} & \mathbf{0} \\ \mathbf{0} & -\mathbf{I}sin(h\alpha) & \mathbf{0} & \mathbf{I}cos(h\alpha) \\ \mathbf{0} & \mathbf{0} & \mathbf{I} & \mathbf{0} \\ \mathbf{0} & \mathbf{0} & \mathbf{0} & \mathbf{I} \end{bmatrix} \tag{A.27}$$

By applying this transformation to the the matrix in Eqn. (A.24) one may obtain:

$$\tilde{\mathbf{K}}^h_{\mathbb{R}} = {\mathbf{T}^h_{\mathbb{R}}}^{\mathrm{T}} \mathbf{K}^{2S} \mathbf{T}^h_{\mathbb{R}} \tag{A.28}$$

where superscript T represents the transpose of a matrix.

Expanding Eqn. (A.28):

$$\tilde{\mathbf{K}}^h_{\mathbb{R}} = \begin{bmatrix} \mathbf{0} & \mathbf{I} & \mathbf{0} & \mathbf{0} & \mathbf{0} & \mathbf{0} \\ \mathbf{I}cos(h\alpha) & \mathbf{0} & \mathbf{I} & -\mathbf{I}sin(h\alpha) & \mathbf{0} & \mathbf{0} \\ \mathbf{0} & \mathbf{0} & \mathbf{0} & \mathbf{0} & \mathbf{I} & \mathbf{0} \\ \mathbf{I}sin(h\alpha) & \mathbf{0} & \mathbf{0} & \mathbf{I}cos(h\alpha) & \mathbf{0} & \mathbf{I} \end{bmatrix} \cdot \begin{bmatrix} \mathbf{K}_{LL} & \mathbf{K}_{LI} & \mathbf{K}_{LH} & \mathbf{0} & \mathbf{0} & \mathbf{0} \\ \mathbf{K}_{IL} & \mathbf{K}_{II} & \mathbf{K}_{IH} & \mathbf{0} & \mathbf{0} & \mathbf{0} \\ \mathbf{K}_{HL} & \mathbf{K}_{HI} & \mathbf{K}_{HH} & \mathbf{0} & \mathbf{0} & \mathbf{0} \\ \mathbf{0} & \mathbf{0} & \mathbf{0} & \mathbf{K}_{LL} & \mathbf{K}_{LI} & \mathbf{K}_{LH} \\ \mathbf{0} & \mathbf{0} & \mathbf{0} & \mathbf{K}_{IL} & \mathbf{K}_{II} & \mathbf{K}_{IH} \\ \mathbf{0} & \mathbf{0} & \mathbf{0} & \mathbf{K}_{HL} & \mathbf{K}_{HI} & \mathbf{K}_{HH} \end{bmatrix} \cdot \mathbf{T}^h_{\mathbb{R}} \tag{A.29}$$

or

$$\tilde{\mathbf{K}}^h_{\mathbb{R}} = \begin{bmatrix} \mathbf{K}_{IL} & \mathbf{K}_{II} & \mathbf{K}_{IH} & \mathbf{0} & \mathbf{0} & \mathbf{0} \\ \mathbf{K}_{LL}cos(h\alpha) \\ +\mathbf{K}_{HL} & \mathbf{K}_{LI}cos(h\alpha) \\ +\mathbf{K}_{HI} & \mathbf{K}_{LH}cos(h\alpha) \\ +\mathbf{K}_{HH} & -\mathbf{K}_{LL}sin(h\alpha) & -\mathbf{K}_{LI}sin(h\alpha) & -\mathbf{K}_{LH}sin(h\alpha) \\ \mathbf{0} & \mathbf{0} & \mathbf{0} & \mathbf{K}_{IL} & \mathbf{K}_{II} & \mathbf{K}_{IH} \\ \mathbf{K}_{LL}sin(h\alpha) & \mathbf{K}_{LI}sin(h\alpha) & \mathbf{K}_{LH}sin(h\alpha) & \mathbf{K}_{LL}cos(h\alpha) \\ & & & +\mathbf{K}_{HL} & \mathbf{K}_{LI}cos(h\alpha) \\ & & & & +\mathbf{K}_{HI} & \mathbf{K}_{LH}cos(h\alpha) \\ & & & & & +\mathbf{K}_{HH} \end{bmatrix} \cdot \begin{bmatrix} \mathbf{0} & \mathbf{I}cos(h\alpha) & \mathbf{0} & \mathbf{I}sin(h\alpha) \\ \mathbf{I} & \mathbf{0} & \mathbf{0} & \mathbf{0} \\ \mathbf{0} & \mathbf{I} & \mathbf{0} & \mathbf{0} \\ \mathbf{0} & -\mathbf{I}sin(h\alpha) & \mathbf{0} & \mathbf{I}cos(h\alpha) \\ \mathbf{0} & \mathbf{0} & \mathbf{I} & \mathbf{0} \\ \mathbf{0} & \mathbf{0} & \mathbf{0} & \mathbf{I} \end{bmatrix} \tag{A.30}$$

or

$$\tilde{\mathbf{K}}^h_{\mathbb{R}} = \begin{bmatrix} \mathbf{K}_{II} & \mathbf{K}_{IL}cos(h\alpha) \\ & +\mathbf{K}_{IH} & \mathbf{0} & \mathbf{K}_{IL}sin(h\alpha) \\ \mathbf{K}_{LI}cos(h\alpha) \\ +\mathbf{K}_{HI} & \mathbf{K}_{LL}cos^2(h\alpha) \\ & +\mathbf{K}_{HL}cos(h\alpha) \\ & +\mathbf{K}_{LH}cos(h\alpha) \\ & +\mathbf{K}_{HH} \\ & +\mathbf{K}_{LL}sin^2(h\alpha) & -\mathbf{K}_{LI}sin(h\alpha) & \mathbf{K}_{LL}cos(h\alpha)sin(h\alpha) \\ & & & +\mathbf{K}_{HL}sin(h\alpha) \\ & & & -\mathbf{K}_{LL}cos(h\alpha)sin(h\alpha) \\ & & & -\mathbf{K}_{LH}sin(h\alpha) \\ \mathbf{0} & -\mathbf{K}_{IL}sin(h\alpha) & \mathbf{K}_{II} & \mathbf{K}_{IL}cos(h\alpha) \\ & & & +\mathbf{K}_{IH} \\ \mathbf{K}_{LI}sin(h\alpha) & \mathbf{K}_{LL}sin(h\alpha)cos(h\alpha) & \mathbf{K}_{LI}cos(h\alpha) & \mathbf{K}_{LL}sin^2(h\alpha) \\ & +\mathbf{K}_{LH}sin(h\alpha) & +\mathbf{K}_{HI} & +\mathbf{K}_{LL}cos^2(h\alpha) \\ & -\mathbf{K}_{LL}cos(h\alpha)sin(h\alpha) & & +\mathbf{K}_{HL}cos(h\alpha) \\ & -\mathbf{K}_{HL}sin(h\alpha) & & +\mathbf{K}_{LH}cos(h\alpha) \\ & & & +\mathbf{K}_{HH} \end{bmatrix} \tag{A.31}$$

or

$$\tilde{\mathbf{K}}^h_{\mathbb{R}} = \begin{bmatrix} \mathbf{K}_{II} & \mathbf{K}_{IL}cos(h\alpha) \\ & +\mathbf{K}_{IH} & \mathbf{0} & \mathbf{K}_{IL}sin(h\alpha) \\ \mathbf{K}_{LI}cos(h\alpha) \\ +\mathbf{K}_{HI} & \mathbf{K}_{LL} \\ & +\mathbf{K}_{HL}cos(h\alpha) & -\mathbf{K}_{LI}sin(h\alpha) & \mathbf{K}_{HL}sin(h\alpha) \\ & +\mathbf{K}_{LH}cos(h\alpha) & & -\mathbf{K}_{LH}sin(h\alpha) \\ & +\mathbf{K}_{HH} \\ \mathbf{0} & -\mathbf{K}_{IL}sin(h\alpha) & \mathbf{K}_{II} & \mathbf{K}_{IL}cos(h\alpha) \\ & & & +\mathbf{K}_{IH} \\ \mathbf{K}_{LI}sin(h\alpha) & \mathbf{K}_{LH}sin(h\alpha) & \mathbf{K}_{LI}cos(h\alpha) & \mathbf{K}_{LL} \\ & -\mathbf{K}_{HL}sin(h\alpha) & +\mathbf{K}_{HI} & \mathbf{K}_{HL}cos(h\alpha) \\ & & & +\mathbf{K}_{LH}cos(h\alpha) \\ & & & +\mathbf{K}_{HH} \end{bmatrix} \tag{A.32}$$

Thus, $\tilde{\mathbf{K}}^h_{\mathbb{R}}$ may be represented as:

$$\tilde{\mathbf{K}}^h_{\mathbb{R}} = \begin{bmatrix} \tilde{\mathbf{K}}_{\Re\Re}(h\alpha) & \tilde{\mathbf{K}}_{\Re\Im}(h\alpha) \\ \tilde{\mathbf{K}}_{\Im\Re}(h\alpha) & \tilde{\mathbf{K}}_{\Im\Im}(h\alpha) \end{bmatrix} \tag{A.33}$$

where

$$\tilde{\mathbf{K}}_{\Re\Re}(h\alpha) = \begin{bmatrix} \mathbf{K}_{II} & \mathbf{K}_{IL}cos(h\alpha)+\mathbf{K}_{IH} \\ \mathbf{K}_{LI}cos(h\alpha)+\mathbf{K}_{HI} & \mathbf{K}_{LL}+\mathbf{K}_{HL}cos(h\alpha)+\mathbf{K}_{LH}cos(h\alpha)+\mathbf{K}_{HH} \end{bmatrix} \tag{A.34}$$

$$\tilde{\mathbf{K}}_{\Re\Im}(h\alpha) = \begin{bmatrix} \mathbf{0} & \mathbf{K}_{IL}sin(h\alpha) \\ -\mathbf{K}_{LI}sin(h\alpha) & \mathbf{K}_{HL}sin(h\alpha)-\mathbf{K}_{LH}sin(h\alpha) \end{bmatrix} \tag{A.35}$$

$$\tilde{\mathbf{K}}_{\Im\Re}(h\alpha) = \begin{bmatrix} \mathbf{0} & -\mathbf{K}_{IL}sin(h\alpha) \\ \mathbf{K}_{LI}sin(h\alpha) & \mathbf{K}_{LH}sin(h\alpha)-\mathbf{K}_{HL}sin(h\alpha) \end{bmatrix} = \tilde{\mathbf{K}}_{\Re\Im}(-h\alpha) \tag{A.36}$$

$$\tilde{\mathbf{K}}_{\Im\Im}(h\alpha) = \begin{bmatrix} \mathbf{K}_{II} & \mathbf{K}_{IL}cos(h\alpha)+\mathbf{K}_{IH} \\ \mathbf{K}_{LI}cos(h\alpha)+\mathbf{K}_{HI} & \mathbf{K}_{LL}+\mathbf{K}_{HL}cos(h\alpha)+\mathbf{K}_{LH}cos(h\alpha)+\mathbf{K}_{HH} \end{bmatrix} = \tilde{\mathbf{K}}_{\Re\Re}(-h\alpha) = \tilde{\mathbf{K}}_{\Re\Re}(h\alpha) \tag{A.37}$$

It may be noted that:

$$\tilde{\mathbf{K}}_{\Re\Re}(h\alpha) - i\tilde{\mathbf{K}}_{\Re\Im}(h\alpha) = \tilde{\mathbf{K}}_{\Re\Re}(h\alpha) + i\tilde{\mathbf{K}}_{\Re\Im}(-h\alpha) = \tilde{\mathbf{K}}_{\Im\Im}(h\alpha) + i\tilde{\mathbf{K}}_{\Im\Re}(h\alpha) \tag{A.38}$$

To recover Eqn. (A.9) or (A.22) which describes the free system matrix corresponding the positive (forward) traveling wave of harmonic index h in cyclic co-ordinates from Eqns. (A.34)- (A.37) one may use:

$$\begin{aligned} &\tilde{\mathbf{K}}_{\Re\Re}(h\alpha) - i\tilde{\mathbf{K}}_{\Re\Im}(h\alpha) \\ &= \begin{bmatrix} \mathbf{K}_{II} & \mathbf{K}_{IL}(cos(h\alpha)-isin(h\alpha))+\mathbf{K}_{IH} \\ \mathbf{K}_{LI}(cos(h\alpha)+isin(h\alpha))+\mathbf{K}_{HI} & \mathbf{K}_{LL}+\mathbf{K}_{HL}(cos(h\alpha)-isin(h\alpha))+\mathbf{K}_{LH}(cos(h\alpha)+isin(h\alpha))+\mathbf{K}_{HH} \end{bmatrix} \\ &= \begin{bmatrix} \mathbf{K}_{II} & \mathbf{K}_{IH}+\mathbf{K}_{IL}e^{-ih\alpha} \\ \mathbf{K}_{HI}+\mathbf{K}_{LI}e^{ih\alpha} & \mathbf{K}_{HH}+\mathbf{K}_{LL}+\mathbf{K}_{LH}e^{ih\alpha}+\mathbf{K}_{HL}e^{-ih\alpha} \end{bmatrix} = \tilde{\mathbf{K}}^h_{\mathbb{C}} \end{aligned} \tag{A.39}$$

Thus,

$$\tilde{\mathbf{K}}^h_{\mathbb{C}} = \tilde{\mathbf{K}}_{\Re\Re}(h\alpha) - i\tilde{\mathbf{K}}_{\Re\Im}(h\alpha) = \tilde{\mathbf{K}}_{\Im\Im}(h\alpha) + i\tilde{\mathbf{K}}_{\Im\Re}(h\alpha) \tag{A.40}$$

Care must be taken while using Eqn. (A.40) as using the incorrect sign for i in the equation will yield the complex conjugate of the system matrix which represents the matrix of the system corresponding to the negative (backward) travelling wave in cyclic co-ordinates as follows:

$$\tilde{\mathbf{K}}_{\Re\Re}(h\alpha) + i\tilde{\mathbf{K}}_{\Re\Im}(h\alpha) = \begin{bmatrix} \mathbf{K}_{II} & \mathbf{K}_{IH}+\mathbf{K}_{IL}e^{ih\alpha} \\ \mathbf{K}_{HI}+\mathbf{K}_{LI}e^{-ih\alpha} & \mathbf{K}_{HH}+\mathbf{K}_{LL}+\mathbf{K}_{LH}e^{-ih\alpha}+\mathbf{K}_{HL}e^{ih\alpha} \end{bmatrix} = \tilde{\mathbf{K}}_{\mathbb{C}}^{-h} \tag{A.41}$$

It may also be noted that the real matrix corresponding to constrained two sector system which represents the cyclic symmetric system $\tilde{\mathbf{K}}_{\mathbb{R}}^{h}$ may also be expressed as:

$$\tilde{\mathbf{K}}_{\mathbb{R}}^{h} = \begin{bmatrix} \Re(\tilde{\mathbf{K}}_{\mathbb{C}}^{h}) & -\Im(\tilde{\mathbf{K}}_{\mathbb{C}}^{h}) \\ \Im(\tilde{\mathbf{K}}_{\mathbb{C}}^{h}) & \Re(\tilde{\mathbf{K}}_{\mathbb{C}}^{h}) \end{bmatrix} \tag{A.42}$$

APPENDIX B

Component Mode Synthesis in Cyclic Symmetric Structures

The CB-CMS of the constrained system in Eqns. (A.9) and (A.22) can be carried out by first partitioning the corresponding complex co-ordinates of Eqn. (A.23) into a set of master and slave DoFs as follows:

$$\tilde{\mathbf{q}}^h_{\mathbb{C}} = \begin{bmatrix} \tilde{\mathbf{q}}^h_{\mathbb{C},M} \\ \tilde{\mathbf{q}}^h_{\mathbb{C},S} \end{bmatrix} = \begin{bmatrix} \tilde{\mathbf{q}}^h_{I,M} \\ \tilde{\mathbf{q}}^h_{H,M} \\ \tilde{\mathbf{q}}^h_{I,S} \\ \tilde{\mathbf{q}}^h_{H,S} \end{bmatrix} \tag{B.1}$$

where subscript M refers to the master DoFs and subscript S refers to the slave DoFs.

The complex cyclically constrained system matrix $\tilde{\mathbf{K}}^h_{\mathbb{C}}$ can be partitioned as:

$$\tilde{\mathbf{K}}^h_{\mathbb{C}} = \begin{bmatrix} \tilde{\mathbf{K}}^h_{\mathbb{C},MM} & \tilde{\mathbf{K}}^h_{\mathbb{C},MS} \\ \tilde{\mathbf{K}}^h_{\mathbb{C},SM} & \tilde{\mathbf{K}}^h_{\mathbb{C},SS} \end{bmatrix} \tag{B.2}$$

where subscripts MM, MS, SM or SS represent a matrix partition based on the master-slave partition of the displacement vector.

In a CB-CMS reduction [8] the master nodes are retained while applying a reduction to the slave DoFs to reduce them to DoFs corresponding to a set of slave modes $\tilde{\tilde{\mathbf{q}}}^h_{\mathbb{C},N}$. The reduction is

represented as follows:

$$\tilde{\tilde{\mathbf{q}}}^h_{\mathbb{C}} \triangleq \begin{bmatrix} \tilde{\tilde{\mathbf{q}}}^h_{\mathbb{C},M} \\ \tilde{\tilde{\mathbf{q}}}^h_{\mathbb{C},N} \end{bmatrix} = \mathbf{\Gamma}^h_{\mathbb{C}} \cdot \begin{bmatrix} \tilde{\mathbf{q}}^h_{\mathbb{C},M} \\ \tilde{\mathbf{q}}^h_{\mathbb{C},S} \end{bmatrix} = \mathbf{\Gamma}^h_{\mathbb{C}} \tilde{\mathbf{q}}^h_{\mathbb{C}} \tag{B.3}$$

where $\tilde{\tilde{\mathbf{q}}}^h_{\mathbb{C}}$ are the set of reduced complex CB-CMS co-ordinates, $\tilde{\tilde{\mathbf{q}}}^h_{\mathbb{C},M}$ are displacements of master DoFs retained in the CB-CMS reduction, $\tilde{\tilde{\mathbf{q}}}^h_{\mathbb{C},N}$ are complex modal co-ordinates corresponding to a set of slave modes and $\mathbf{\Gamma}^h_{\mathbb{C}}$ is the complex CB-CMS reduction matrix represented as:

$$\mathbf{\Gamma}^h_{\mathbb{C}} = \begin{bmatrix} \mathbf{I}_{n_M \times n_M} & \mathbf{0}_{n_M \times n_S} \\ \mathbf{\Psi}^h_{\mathbb{C}} & \mathbf{\Phi}^h_{\mathbb{C}} \end{bmatrix} \tag{B.4}$$

where n_M and n_S are the number of master and slave nodes retained per harmonic in the CB-CMS reduced model. $\mathbf{\Psi}^h_{\mathbb{C}}$ is a $n_S \times n_M$ complex matrix whose columns represent the constraint modes and $\mathbf{\Phi}^h_{\mathbb{C}}$ is a $n_S \times n_S$ complex matrix whose columns represent the normal (slave) modes.

The constraint modes are obtained by applying a unit displacement to the master DoFs individually. Hence, it must satisfy the relation:

$$\begin{bmatrix} \tilde{\mathbf{K}}^h_{\mathbb{C},MM} & \tilde{\mathbf{K}}^h_{\mathbb{C},MS} \\ \tilde{\mathbf{K}}^h_{\mathbb{C},SM} & \tilde{\mathbf{K}}^h_{\mathbb{C},SS} \end{bmatrix} \cdot \begin{bmatrix} \mathbf{I} \\ \mathbf{\Psi}^h_{\mathbb{C}} \end{bmatrix} = \begin{bmatrix} \tilde{\mathbf{f}}^h_{\mathbb{C},M} \\ \mathbf{0} \end{bmatrix} \tag{B.5}$$

where $\tilde{\mathbf{f}}^h_{\mathbb{C},M}$ is the complex force applied at the master DoFs along cyclic co-ordinates to enforce the constraint. Simplifying the second row of the matrix Eqn. (B.5), the constraint modes may be determined using the equation:

$$\mathbf{\Psi}^h_{\mathbb{C}} = -{\tilde{\mathbf{K}}^h_{\mathbb{C},SS}}^{-1} \tilde{\mathbf{K}}^h_{\mathbb{C},SM} \tag{B.6}$$

The normal modes are the linear mode-shapes of the system obtained by completely constraining all the master DoFs and can be determined as the solution to the eigenvalue problem:

$$\tilde{\mathbf{K}}^h_{\mathbb{C},SS} \mathbf{\Phi}^h_{\mathbb{C}} = \tilde{\mathbf{M}}^h_{\mathbb{C},SS} \mathbf{\Phi}^h_{\mathbb{C}} \mathbf{\Lambda}^h_{\mathbb{C},SS} \tag{B.7}$$

where $\mathbf{M}$ represents a mass matrix and $\mathbf{\Lambda}$ represents a diagonal matrix containing eigenvalues of the system.

The reduced order CB-CMS matrices may then be obtained by using the reduction matrix $\mathbf{\Gamma}_{\mathbb{C}}^{h}$ in Eqn. (B.4). The CB-CMS reduced stiffness matrix may given by:

$$\tilde{\tilde{\mathbf{K}}}_{\mathbb{C}}^{h} = {\mathbf{\Gamma}_{\mathbb{C}}^{h}}^{\mathrm{H}} \tilde{\mathbf{K}}_{\mathbb{C}}^{h} \mathbf{\Gamma}_{\mathbb{C}}^{h} = \begin{bmatrix} \tilde{\mathbf{K}}_{\mathbb{C},MM}^{h} + {\mathbf{\Psi}_{\mathbb{C}}^{h}}^{\mathrm{H}} \tilde{\mathbf{K}}_{\mathbb{C},SM}^{h} + \tilde{\mathbf{K}}_{\mathbb{C},MS}^{h} \mathbf{\Psi}_{\mathbb{C}}^{h} + {\mathbf{\Psi}_{\mathbb{C}}^{h}}^{\mathrm{H}} \tilde{\mathbf{K}}_{\mathbb{C},SS}^{h} \mathbf{\Psi}_{\mathbb{C}}^{h} & \tilde{\mathbf{K}}_{\mathbb{C},MS}^{h} \mathbf{\Phi}_{\mathbb{C}}^{h} + {\mathbf{\Psi}_{\mathbb{C}}^{h}}^{\mathrm{H}} \tilde{\mathbf{K}}_{\mathbb{C},SS}^{h} \mathbf{\Phi}_{\mathbb{C}}^{h} \\ {\mathbf{\Phi}_{\mathbb{C}}^{h}}^{\mathrm{H}} \tilde{\mathbf{K}}_{\mathbb{C},SM}^{h} + {\mathbf{\Phi}_{\mathbb{C}}^{h}}^{\mathrm{H}} \tilde{\mathbf{K}}_{\mathbb{C},SS}^{h} \mathbf{\Psi}_{\mathbb{C}}^{h} & {\mathbf{\Phi}_{\mathbb{C}}^{h}}^{\mathrm{H}} \tilde{\mathbf{K}}_{\mathbb{C},SS}^{h} \mathbf{\Phi}_{\mathbb{C}}^{h} \end{bmatrix} \tag{B.8}$$

where $\tilde{\tilde{\mathbf{K}}}^{h}$ represents the reduced CB-CMS stiffness matrix.

The reduced matrix given in Eqn. (B.8) may be simplified further based on Eqns. (B.6) and (B.7). However, this simplification is not applied here to prevent loss of generality. The reduced CB-CMS mass matrix also has a similar form and may be simply obtained by replacing $\mathbf{K}$ with $\mathbf{M}$ in Eqn. (B.8).

A regular CB-CMS sub-structuring analysis [8] might be carried out on the real constrained two sector system. Alternatively to Eqn. (A.25) The DoFs of the cyclic symmetric system may be expressed as:

$$\tilde{\mathbf{q}}_{\mathbb{R}}^{h} = \begin{bmatrix} \tilde{\mathbf{q}}_{\mathbb{R},M}^{h} \\ \tilde{\mathbf{q}}_{\mathbb{R},S}^{h} \end{bmatrix} = \begin{bmatrix} \Re(\tilde{\mathbf{q}}_{I,M}^{h}) \\ \Re(\tilde{\mathbf{q}}_{H,M}^{h}) \\ \Im(\tilde{\mathbf{q}}_{I,M}^{h}) \\ \Im(\tilde{\mathbf{q}}_{H,M}^{h}) \\ \Re(\tilde{\mathbf{q}}_{I,S}^{h}) \\ \Re(\tilde{\mathbf{q}}_{H,S}^{h}) \\ \Im(\tilde{\mathbf{q}}_{I,S}^{h}) \\ \Im(\tilde{\mathbf{q}}_{H,S}^{h}) \end{bmatrix} \tag{B.9}$$

The master and slave DoFs belong to nodes in the FEM model in both the real and imaginary sectors. The real system matrix $\tilde{\mathbf{K}}_{\mathbb{R}}^{h}$ which represents the constrained two sector system can be partitioned as:

$$\tilde{\mathbf{K}}_{\mathbb{R}}^{h} = \begin{bmatrix} \tilde{\mathbf{K}}_{\mathbb{R},MM}^{h} & \tilde{\mathbf{K}}_{\mathbb{R},MS}^{h} \\ \tilde{\mathbf{K}}_{\mathbb{R},SM}^{h} & \tilde{\mathbf{K}}_{\mathbb{R},SS}^{h} \end{bmatrix} \tag{B.10}$$

It follows from Eqn. (A.42) that each of the submatrices in Eqn. (B.10) can in turn be represented

by the real and imaginary parts of the corresponding partition of the complex matrix $\tilde{\mathbf{K}}^h_{\mathbb{C}}$ as follows:

$$\tilde{\mathbf{K}}^h_{\mathbb{R},XX} = \begin{bmatrix} \Re(\tilde{\mathbf{K}}^h_{\mathbb{C},XX}) & -\Im(\tilde{\mathbf{K}}^h_{\mathbb{C},XX}) \\ \Im(\tilde{\mathbf{K}}^h_{\mathbb{C},XX}) & \Re(\tilde{\mathbf{K}}^h_{\mathbb{C},XX}) \end{bmatrix} \tag{B.11}$$

where XX represents a matrix partition such as MM, MS, SM or SS.

The CB-CMS reduction in the real domain is represented as:

$$\tilde{\tilde{\mathbf{q}}}^h_{\mathbb{R}} \triangleq \begin{bmatrix} \tilde{\tilde{\mathbf{q}}}^h_{\mathbb{R},M} \\ \tilde{\tilde{\mathbf{q}}}^h_{\mathbb{R},N} \end{bmatrix} = \mathbf{\Gamma}^h_{\mathbb{R}} \cdot \begin{bmatrix} \tilde{\mathbf{q}}^h_{\mathbb{R},M} \\ \tilde{\mathbf{q}}^h_{\mathbb{R},S} \end{bmatrix} = \mathbf{\Gamma}^h_{\mathbb{R}} \tilde{\mathbf{q}}^h_{\mathbb{R}} \tag{B.12}$$

where $\mathbf{\Gamma}^h_{\mathbb{R}}$ is the real CB-CMS reduction matrix represented as:

$$\mathbf{\Gamma}^h_{\mathbb{R}} = \begin{bmatrix} \mathbf{I}_{2n_M \times 2n_M} & \mathbf{0}_{2n_M \times 2n_S} \\ \mathbf{\Psi}^h_{\mathbb{R}} & \mathbf{\Phi}^h_{\mathbb{R}} \end{bmatrix} \tag{B.13}$$

where $\mathbf{\Psi}^h_{\mathbb{R}}$ is a $2n_S \times 2n_M$ real matrix whose columns represent the constraint modes. $\mathbf{\Phi}^h_{\mathbb{R}}$ is a $2n_S \times 2n_S$ real matrix whose columns represent the normal (slave) modes.

As before, the constraint modes $\mathbf{\Psi}^h_{\mathbb{R}}$ are obtained by applying a unit displacement to the master DoFs individually. Hence, it must satisfy the relation:

$$\begin{bmatrix} \tilde{\mathbf{K}}^h_{\mathbb{R},MM} & \tilde{\mathbf{K}}^h_{\mathbb{R},MS} \\ \tilde{\mathbf{K}}^h_{\mathbb{R},SM} & \tilde{\mathbf{K}}^h_{\mathbb{R},SS} \end{bmatrix} \cdot \begin{bmatrix} \mathbf{I} \\ \mathbf{\Psi}^h_{\mathbb{R}} \end{bmatrix} = \begin{bmatrix} \tilde{\mathbf{f}}^h_{\mathbb{R},M} \\ \mathbf{0} \end{bmatrix} \tag{B.14}$$

where $\tilde{\mathbf{f}}^h_{\mathbb{R},M}$ is the real force applied at the master DoFs along cyclic co-ordinates to enforce the constraint.

The normal modes are the linear mode-shapes of the system obtained by completely constraining all the master DoFs of both the sectors and can be determined as the solution to the eigenvalue

problem:

$$\tilde{\mathbf{K}}^h_{\mathbb{R},SS}\mathbf{\Phi}^h_{\mathbb{R}} = \tilde{\mathbf{M}}^h_{\mathbb{R},SS}\mathbf{\Phi}^h_{\mathbb{R}}\mathbf{\Lambda}^h_{\mathbb{R},SS} \tag{B.15}$$

The diagonal eigenvalue matrix $\mathbf{\Lambda}^h_{\mathbb{R},SS}$ corresponds to a system of two constrained sectors with real displacements and is twice the size of $\mathbf{\Lambda}^h_{\mathbb{C},SS}$ which corresponds to a single constrained sector with complex displacements.

Consider the j^{th} real constraint mode $\boldsymbol{\psi}^h_{\mathbb{R},j}$ and the k^{th} real normal mode $\boldsymbol{\phi}^h_{\mathbb{R},j}$. The can be partitioned into sub-vectors corresponding to the real and imaginary sector as follows:

$$\boldsymbol{\psi}^h_{\mathbb{R},j} = \begin{bmatrix} \boldsymbol{\psi}^h_{\Re,j} \\ \boldsymbol{\psi}^h_{\Im,j} \end{bmatrix} \quad \boldsymbol{\phi}^h_{\mathbb{R},k} = \begin{bmatrix} \boldsymbol{\phi}^h_{\Re,k} \\ \boldsymbol{\phi}^h_{\Im,k} \end{bmatrix} \tag{B.16}$$

Based on Eqns. (B.11), (B.14) and (B.16) the j^{th} real constraint mode must thus satisfy:

$$\begin{bmatrix} \Re(\tilde{\mathbf{K}}^h_{\mathbb{C},MM}) & -\Im(\tilde{\mathbf{K}}^h_{\mathbb{C},MM}) & \Re(\tilde{\mathbf{K}}^h_{\mathbb{C},MS}) & -\Im(\tilde{\mathbf{K}}^h_{\mathbb{C},MS}) \\ \Im(\tilde{\mathbf{K}}^h_{\mathbb{C},MM}) & \Re(\tilde{\mathbf{K}}^h_{\mathbb{C},MM}) & \Im(\tilde{\mathbf{K}}^h_{\mathbb{C},MS}) & \Re(\tilde{\mathbf{K}}^h_{\mathbb{C},MS}) \\ \Re(\tilde{\mathbf{K}}^h_{\mathbb{C},SM}) & -\Im(\tilde{\mathbf{K}}^h_{\mathbb{C},SM}) & \Re(\tilde{\mathbf{K}}^h_{\mathbb{C},SS}) & -\Im(\tilde{\mathbf{K}}^h_{\mathbb{C},SS}) \\ \Im(\tilde{\mathbf{K}}^h_{\mathbb{C},SM}) & \Re(\tilde{\mathbf{K}}^h_{\mathbb{C},SM}) & \Im(\tilde{\mathbf{K}}^h_{\mathbb{C},SS}) & \Re(\tilde{\mathbf{K}}^h_{\mathbb{C},SS}) \end{bmatrix} \cdot \begin{bmatrix} \mathbf{1}_j \\ \mathbf{0} \\ \boldsymbol{\psi}^h_{\Re,j} \\ \boldsymbol{\psi}^h_{\Im,j} \end{bmatrix} = \begin{bmatrix} \tilde{\mathbf{f}}^h_{M,\Re,j} \\ \tilde{\mathbf{f}}^h_{M,\Im,j} \\ \mathbf{0} \\ \mathbf{0} \end{bmatrix} \tag{B.17}$$

where subscripts $\Re$ and $\Im$ represent the DoFs of the real and imaginary sector respectively. $\mathbf{1}_j = [0\ 0\ \cdots 1 \cdots 0]^{\mathrm{T}}$ is vector with 1 at the j^{th} index and 0's everywhere else. If Eqn. (B.17) stands it may be seen that the following will also be true:

$$\begin{bmatrix} \Re(\tilde{\mathbf{K}}^h_{\mathbb{C},MM}) & -\Im(\tilde{\mathbf{K}}^h_{\mathbb{C},MM}) & \Re(\tilde{\mathbf{K}}^h_{\mathbb{C},MS}) & -\Im(\tilde{\mathbf{K}}^h_{\mathbb{C},MS}) \\ \Im(\tilde{\mathbf{K}}^h_{\mathbb{C},MM}) & \Re(\tilde{\mathbf{K}}^h_{\mathbb{C},MM}) & \Im(\tilde{\mathbf{K}}^h_{\mathbb{C},MS}) & \Re(\tilde{\mathbf{K}}^h_{\mathbb{C},MS}) \\ \Re(\tilde{\mathbf{K}}^h_{\mathbb{C},SM}) & -\Im(\tilde{\mathbf{K}}^h_{\mathbb{C},SM}) & \Re(\tilde{\mathbf{K}}^h_{\mathbb{C},SS}) & -\Im(\tilde{\mathbf{K}}^h_{\mathbb{C},SS}) \\ \Im(\tilde{\mathbf{K}}^h_{\mathbb{C},SM}) & \Re(\tilde{\mathbf{K}}^h_{\mathbb{C},SM}) & \Im(\tilde{\mathbf{K}}^h_{\mathbb{C},SS}) & \Re(\tilde{\mathbf{K}}^h_{\mathbb{C},SS}) \end{bmatrix} \cdot \begin{bmatrix} \mathbf{0} \\ \mathbf{1}_j \\ -\boldsymbol{\psi}^h_{\Im,j} \\ \boldsymbol{\psi}^h_{\Re,j} \end{bmatrix} = \begin{bmatrix} -\tilde{\mathbf{f}}^h_{M,\Im,j} \\ \tilde{\mathbf{f}}^h_{M,\Re,j} \\ \mathbf{0} \\ \mathbf{0} \end{bmatrix} \tag{B.18}$$

Thus, if $\boldsymbol{\psi}^h_{\mathbb{R},j} = [\boldsymbol{\psi}^h_{\Re,j} \quad \boldsymbol{\psi}^h_{\Im,j}]^{\mathrm{T}}$ is a real constraint mode so is $\hat{\boldsymbol{\psi}}^h_{\mathbb{R},j} \triangleq [-\boldsymbol{\psi}^h_{\Im,j} \quad \boldsymbol{\psi}^h_{\Re,j}]^{\mathrm{T}}$. Based on

Eqns. (A.42), (B.15) and (B.16) the k^{th} real normal mode must satisfy the equation:

$$\begin{bmatrix} \Re(\tilde{\mathbf{K}}^h_{\mathbb{C},SS}) & -\Im(\tilde{\mathbf{K}}^h_{\mathbb{C},SS}) \\ \Im(\tilde{\mathbf{K}}^h_{\mathbb{C},SS}) & \Re(\tilde{\mathbf{K}}^h_{\mathbb{C},SS}) \end{bmatrix} \cdot \begin{bmatrix} \boldsymbol{\phi}^h_{\Re,k} \\ \boldsymbol{\phi}^h_{\Im,k} \end{bmatrix} = \begin{bmatrix} \Re(\tilde{\mathbf{M}}^h_{\mathbb{C},SS}) & -\Im(\tilde{\mathbf{M}}^h_{\mathbb{C},SS}) \\ \Im(\tilde{\mathbf{M}}^h_{\mathbb{C},SS}) & \Re(\tilde{\mathbf{M}}^h_{\mathbb{C},SS}) \end{bmatrix} \cdot \begin{bmatrix} \boldsymbol{\phi}^h_{\Re,k} \\ \boldsymbol{\phi}^h_{\Im,k} \end{bmatrix} \lambda_k \quad \text{(B.19)}$$

where λ_k is the eigenvalue of the k^{th} normal mode. It follows from Eqn. (B.19) that the following also holds true:

$$\begin{bmatrix} \Re(\tilde{\mathbf{K}}^h_{\mathbb{C},SS}) & -\Im(\tilde{\mathbf{K}}^h_{\mathbb{C},SS}) \\ \Im(\tilde{\mathbf{K}}^h_{\mathbb{C},SS}) & \Re(\tilde{\mathbf{K}}^h_{\mathbb{C},SS}) \end{bmatrix} \cdot \begin{bmatrix} -\boldsymbol{\phi}^h_{\Im,k} \\ \boldsymbol{\phi}^h_{\Re,k} \end{bmatrix} = \begin{bmatrix} \Re(\tilde{\mathbf{M}}^h_{\mathbb{C},SS}) & -\Im(\tilde{\mathbf{M}}^h_{\mathbb{C},SS}) \\ \Im(\tilde{\mathbf{M}}^h_{\mathbb{C},SS}) & \Re(\tilde{\mathbf{M}}^h_{\mathbb{C},SS}) \end{bmatrix} \cdot \begin{bmatrix} -\boldsymbol{\phi}^h_{\Im,k} \\ \boldsymbol{\phi}^h_{\Re,k} \end{bmatrix} \lambda_k \quad \text{(B.20)}$$

Thus, if $\boldsymbol{\phi}^h_{\mathbb{R},j} = [\boldsymbol{\phi}^h_{\Re,j} \quad \boldsymbol{\phi}^h_{\Im,j}]^{\mathrm{T}}$ is a real normal mode so is $\hat{\boldsymbol{\phi}}^h_{\mathbb{R},j} \triangleq [-\boldsymbol{\phi}^h_{\Im,j} \quad \boldsymbol{\phi}^h_{\Re,j}]^{\mathrm{T}}$. If $\boldsymbol{\psi}^h_{\mathbb{C},j} \triangleq \boldsymbol{\psi}^h_{\Re,j} + i\boldsymbol{\psi}^h_{\Im,j}$ is a complex mode which represents the forward traveling constraint mode, then its complementary mode given by $\hat{\boldsymbol{\psi}}^h_{\mathbb{C},j} \triangleq -\boldsymbol{\psi}^h_{\Im,j} + i\boldsymbol{\psi}^h_{\Re,j}$ represents the backward traveling constraint mode. A similar argument also holds true for a forward traveling normal mode $\boldsymbol{\phi}^h_{\mathbb{C},j} \triangleq \boldsymbol{\phi}^h_{\Re,j} + i\boldsymbol{\phi}^h_{\Im,j}$ and its backward traveling companion $\hat{\boldsymbol{\phi}}^h_{\mathbb{C},j} \triangleq -\boldsymbol{\phi}^h_{\Im,j} + i\boldsymbol{\phi}^h_{\Re,j}$. Hence, the set of constraint and normal modes may be represented in the real domain in terms of the complex constraint and normal modes by:

$$\boldsymbol{\Psi}^h_{\mathbb{R}} = \begin{bmatrix} \Re(\boldsymbol{\Psi}^h_{\mathbb{C}}) & -\Im(\boldsymbol{\Psi}^h_{\mathbb{C}}) \\ \Im(\boldsymbol{\Psi}^h_{\mathbb{C}}) & \Re(\boldsymbol{\Psi}^h_{\mathbb{C}}) \end{bmatrix} \quad \boldsymbol{\Phi}^h_{\mathbb{R}} = \begin{bmatrix} \Re(\boldsymbol{\Phi}^h_{\mathbb{C}}) & -\Im(\boldsymbol{\Phi}^h_{\mathbb{C}}) \\ \Im(\boldsymbol{\Phi}^h_{\mathbb{C}}) & \Re(\boldsymbol{\Phi}^h_{\mathbb{C}}) \end{bmatrix} \quad \text{(B.21)}$$

The reduced CB-CMS matrices may now be given in the real domain by:

$$\tilde{\tilde{\mathbf{K}}}^h_{\mathbb{R}} = {\boldsymbol{\Gamma}^h_{\mathbb{R}}}^{\mathrm{T}} \tilde{\mathbf{K}}^h_{\mathbb{R}} \boldsymbol{\Gamma}^h_{\mathbb{R}} = \begin{bmatrix} \tilde{\mathbf{K}}^h_{\mathbb{R},MM} + {\boldsymbol{\Psi}^h_{\mathbb{R}}}^{\mathrm{T}} \tilde{\mathbf{K}}^h_{\mathbb{R},SM} + \tilde{\mathbf{K}}^h_{\mathbb{R},MS} \boldsymbol{\Psi}^h_{\mathbb{R}} + {\boldsymbol{\Psi}^h_{\mathbb{R}}}^{\mathrm{T}} \tilde{\mathbf{K}}^h_{\mathbb{R},SS} \boldsymbol{\Psi}^h_{\mathbb{R}} & \tilde{\mathbf{K}}^h_{\mathbb{R},MS} \boldsymbol{\Phi}^h_{\mathbb{R}} + {\boldsymbol{\Psi}^h_{\mathbb{R}}}^{\mathrm{T}} \tilde{\mathbf{K}}^h_{\mathbb{R},SS} \boldsymbol{\Phi}^h_{\mathbb{R}} \\ {\boldsymbol{\Phi}^h_{\mathbb{R}}}^{\mathrm{T}} \tilde{\mathbf{K}}^h_{\mathbb{R},SM} + {\boldsymbol{\Phi}^h_{\mathbb{R}}}^{\mathrm{T}} \tilde{\mathbf{K}}^h_{\mathbb{R},SS} \boldsymbol{\Psi}^h_{\mathbb{R}} & {\boldsymbol{\Phi}^h_{\mathbb{R}}}^{\mathrm{T}} \tilde{\mathbf{K}}^h_{\mathbb{R},SS} \boldsymbol{\Phi}^h_{\mathbb{R}} \end{bmatrix} \quad \text{(B.22)}$$

Using Eqns. (B.11) and (B.21) one may obtain:

$${\boldsymbol{\Psi}^h_{\mathbb{R}}}^{\mathrm{T}} \tilde{\mathbf{K}}^h_{\mathbb{R},XX} = \begin{bmatrix} \Re({\boldsymbol{\Psi}^h_{\mathbb{C},XX}}^{\mathrm{T}}) & \Im({\boldsymbol{\Psi}^h_{\mathbb{C},XX}}^{\mathrm{T}}) \\ -\Im({\boldsymbol{\Psi}^h_{\mathbb{C},XX}}^{\mathrm{T}}) & \Re({\boldsymbol{\Psi}^h_{\mathbb{C},XX}}^{\mathrm{T}}) \end{bmatrix} \cdot \begin{bmatrix} \Re(\tilde{\mathbf{K}}^h_{\mathbb{C},XX}) & -\Im(\tilde{\mathbf{K}}^h_{\mathbb{C},XX}) \\ \Im(\tilde{\mathbf{K}}^h_{\mathbb{C},XX}) & \Re(\tilde{\mathbf{K}}^h_{\mathbb{C},XX}) \end{bmatrix} \quad \text{(B.23)}$$

or

$$\boldsymbol{\Psi}_{\mathbb{R}}^{h^{\mathrm{T}}}\tilde{\mathbf{K}}_{\mathbb{R},XX}^{h} = \begin{bmatrix} \Re(\boldsymbol{\Psi}_{\mathbb{C},XX}^{h^{\mathrm{T}}})\Re(\tilde{\mathbf{K}}_{\mathbb{C},XX}^{h})+\Im(\boldsymbol{\Psi}_{\mathbb{C},XX}^{h^{\mathrm{T}}})\Im(\tilde{\mathbf{K}}_{\mathbb{C},XX}^{h}) & -\Big(\Re(\boldsymbol{\Psi}_{\mathbb{C},XX}^{h^{\mathrm{T}}})\Im(\tilde{\mathbf{K}}_{\mathbb{C},XX}^{h})-\Im(\boldsymbol{\Psi}_{\mathbb{C},XX}^{h^{\mathrm{T}}})\Re(\tilde{\mathbf{K}}_{\mathbb{C},XX}^{h})\Big) \\ \Re(\boldsymbol{\Psi}_{\mathbb{C},XX}^{h^{\mathrm{T}}})\Im(\tilde{\mathbf{K}}_{\mathbb{C},XX}^{h})-\Im(\boldsymbol{\Psi}_{\mathbb{C},XX}^{h^{\mathrm{T}}})\Re(\tilde{\mathbf{K}}_{\mathbb{C},XX}^{h}) & \Re(\boldsymbol{\Psi}_{\mathbb{C},XX}^{h^{\mathrm{T}}})\Re(\tilde{\mathbf{K}}_{\mathbb{C},XX}^{h})+\Im(\boldsymbol{\Psi}_{\mathbb{C},XX}^{h^{\mathrm{T}}})\Im(\tilde{\mathbf{K}}_{\mathbb{C},XX}^{h}) \end{bmatrix} \tag{B.24}$$

or

$$\boldsymbol{\Psi}_{\mathbb{R}}^{h^{\mathrm{T}}}\tilde{\mathbf{K}}_{\mathbb{R},XX}^{h} = \begin{bmatrix} \Re(\boldsymbol{\Psi}_{\mathbb{C},XX}^{h^{\mathrm{H}}}\tilde{\mathbf{K}}_{\mathbb{C},XX}^{h}) & -\Im(\boldsymbol{\Psi}_{\mathbb{C},XX}^{h^{\mathrm{H}}}\tilde{\mathbf{K}}_{\mathbb{C},XX}^{h}) \\ \Im(\boldsymbol{\Psi}_{\mathbb{C},XX}^{h^{\mathrm{H}}}\tilde{\mathbf{K}}_{\mathbb{C},XX}^{h}) & \Re(\boldsymbol{\Psi}_{\mathbb{C},XX}^{h^{\mathrm{H}}}\tilde{\mathbf{K}}_{\mathbb{C},XX}^{h}) \end{bmatrix} \tag{B.25}$$

Similarly,

$$\tilde{\mathbf{K}}_{\mathbb{R},XX}^{h}\boldsymbol{\Psi}_{\mathbb{R}}^{h} = \begin{bmatrix} \Re(\tilde{\mathbf{K}}_{\mathbb{C},XX}^{h}\boldsymbol{\Psi}_{\mathbb{C},XX}^{h}) & -\Im(\tilde{\mathbf{K}}_{\mathbb{C},XX}^{h}\boldsymbol{\Psi}_{\mathbb{C},XX}^{h}) \\ \Im(\tilde{\mathbf{K}}_{\mathbb{C},XX}^{h}\boldsymbol{\Psi}_{\mathbb{C},XX}^{h}) & \Re(\tilde{\mathbf{K}}_{\mathbb{C},XX}^{h}\boldsymbol{\Psi}_{\mathbb{C},XX}^{h}) \end{bmatrix} \tag{B.26}$$

Replacing $\tilde{\mathbf{K}}_{\mathbb{R},XX}^{h}$ with $\tilde{\mathbf{K}}_{\mathbb{R},XX}^{h}\boldsymbol{\Psi}_{\mathbb{R}}^{h}$ in Eqn. (B.25) results in the following:

$$\boldsymbol{\Psi}_{\mathbb{R}}^{h^{\mathrm{T}}}\tilde{\mathbf{K}}_{\mathbb{R},XX}^{h}\boldsymbol{\Psi}_{\mathbb{R}}^{h} = \begin{bmatrix} \Re(\boldsymbol{\Psi}_{\mathbb{R}}^{h^{\mathrm{H}}}\tilde{\mathbf{K}}_{\mathbb{R},XX}^{h}\boldsymbol{\Psi}_{\mathbb{C},XX}^{h}) & -\Im(\boldsymbol{\Psi}_{\mathbb{R}}^{h^{\mathrm{H}}}\tilde{\mathbf{K}}_{\mathbb{R},XX}^{h}\boldsymbol{\Psi}_{\mathbb{C},XX}^{h}) \\ \Im(\boldsymbol{\Psi}_{\mathbb{R}}^{h^{\mathrm{H}}}\tilde{\mathbf{K}}_{\mathbb{R},XX}^{h}\boldsymbol{\Psi}_{\mathbb{C},XX}^{h}) & \Re(\boldsymbol{\Psi}_{\mathbb{R}}^{h^{\mathrm{H}}}\tilde{\mathbf{K}}_{\mathbb{R},XX}^{h}\boldsymbol{\Psi}_{\mathbb{C},XX}^{h}) \end{bmatrix} \tag{B.27}$$

Similar Eqns. for $\boldsymbol{\Phi}_{\mathbb{R}}^{h}$ can be obtained by substituting $\boldsymbol{\Psi}_{\mathbb{R}}^{h}$ in Eqns. (B.25)- (B.27). It may be seen that after substituting these Eqns. together into Eqn. (B.22), simplifying and rearranging the rows and columns one may get:

$$\tilde{\tilde{\mathbf{K}}}_{\mathbb{R}}^{h} = \begin{bmatrix} \Re(\tilde{\tilde{\mathbf{K}}}_{\mathbb{C}}^{h}) & -\Im(\tilde{\tilde{\mathbf{K}}}_{\mathbb{C}}^{h}) \\ \Im(\tilde{\tilde{\mathbf{K}}}_{\mathbb{C}}^{h}) & \Re(\tilde{\tilde{\mathbf{K}}}_{\mathbb{C}}^{h}) \end{bmatrix} = \left[\begin{array}{cc|cc} \Re(\tilde{\tilde{\mathbf{K}}}_{\mathbb{C},MM}^{h}) & -\Im(\tilde{\tilde{\mathbf{K}}}_{\mathbb{C},MM}^{h}) & \Re(\tilde{\tilde{\mathbf{K}}}_{\mathbb{C},MS}^{h}) & -\Im(\tilde{\tilde{\mathbf{K}}}_{\mathbb{C},MS}^{h}) \\ \Im(\tilde{\tilde{\mathbf{K}}}_{\mathbb{C},MM}^{h}) & \Re(\tilde{\tilde{\mathbf{K}}}_{\mathbb{C},MM}^{h}) & \Im(\tilde{\tilde{\mathbf{K}}}_{\mathbb{C},MS}^{h}) & \Re(\tilde{\tilde{\mathbf{K}}}_{\mathbb{C},MS}^{h}) \\ \hline \Re(\tilde{\tilde{\mathbf{K}}}_{\mathbb{C},SM}^{h}) & -\Im(\tilde{\tilde{\mathbf{K}}}_{\mathbb{C},SM}^{h}) & \Re(\tilde{\tilde{\mathbf{K}}}_{\mathbb{C},SS}^{h}) & -\Im(\tilde{\tilde{\mathbf{K}}}_{\mathbb{C},SS}^{h}) \\ \Im(\tilde{\tilde{\mathbf{K}}}_{\mathbb{C},SM}^{h}) & \Re(\tilde{\tilde{\mathbf{K}}}_{\mathbb{C},SM}^{h}) & \Im(\tilde{\tilde{\mathbf{K}}}_{\mathbb{C},SS}^{h}) & \Re(\tilde{\tilde{\mathbf{K}}}_{\mathbb{C},SS}^{h}) \end{array}\right] \tag{B.28}$$

Thus, using Eqn. (B.28) one may obtain the cyclic symmetric CB-CMS matrices in real co-

ordinates from a representation in complex co-ordinates and vice-versa. This also proves, that CB-CMS conserves cyclic symmetry when it is performed in the fashion shown here. The real domain matrices derived from the original two sector model contains information regarding both the forward and backward traveling waves. A detailed descriptions of the forward and backward

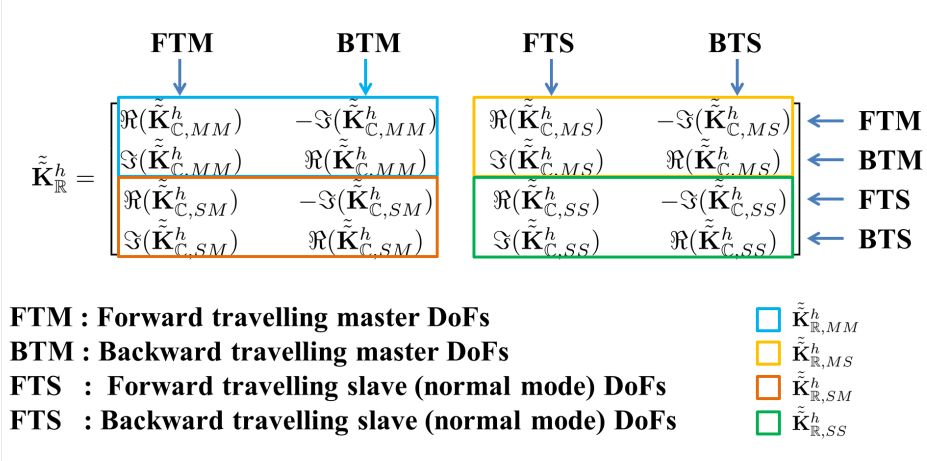

Figure B.1. CB-CMS matrix DoFs

traveling DoFs of the final cyclic symmetric system matrix is shown in Fig. B.1. This is a general formulation which represents both the mass and stiffness matrices. $\tilde{\tilde{\mathbf{K}}}^h_{\mathbb{R},SS}$ and $\tilde{\tilde{\mathbf{M}}}^h_{\mathbb{R},SS}$ are diagonal matrices. Generally, for real systems which have symmetric stiffness matrices in physical DoFs, $\tilde{\tilde{\mathbf{K}}}^h_{\mathbb{R},MS}$ and $\tilde{\tilde{\mathbf{K}}}^h_{\mathbb{R},SM}$ are empty matrices. However, $\tilde{\tilde{\mathbf{M}}}^h_{\mathbb{R},MS}$ and $\tilde{\tilde{\mathbf{M}}}^h_{\mathbb{R},SM}$ are usually full matrices.

Often, one uses a commercially available software to obtain $\tilde{\tilde{\mathbf{K}}}^h_{\mathbb{R}}$ but might require $\tilde{\tilde{\mathbf{K}}}^h_{\mathbb{C}}$ for use in further analysis. Generally, when softwares are used to perform CB-CMS sub-structuring analysis the matrices they yield will not have the rows and columns in the same order as shown in Eqn. (B.28) and must be rearranged. It is straightforward to keep track of master DoFs belonging to the real and imaginary sector and their corresponding indices in $\tilde{\tilde{\mathbf{K}}}^h_{\mathbb{R},MM}$. The slave modes do not have such corresponding physical DoFs and their indices might not be in the correct order. A pair of slave modes which correspond to the forward and backward travelling waves will have the same unique eigenvalue as shown in Eqns. (B.19) and (B.20). These eigenvalues will be proportional to the diagonal elements of the matrix $\tilde{\tilde{\mathbf{K}}}^h_{\mathbb{R},SS}$ and can thus be used to separate the indices which

belong to a particular slave mode-pair. Let these indices be l_k and $\hat{l}_k$ for the forward and backward traveling k^{th} slave mode. However, which of the two indices corresponds to the forward traveling one remains to determined. To do so, one may check the sign of the product of the 1^{st} entry of the l_k^{th} column and $(n_M+1)^{th}$ entry of the $\hat{l}_k^{th}$ columns of $\tilde{\tilde{\mathbf{M}}}^h_{\mathbb{R},MS}$ (the corresponding entries for the stiffness matrix will be a zero matrix). From Eqn. (B.28) it follows:

$$\left[\tilde{\tilde{\mathbf{M}}}^h_{\mathbb{R},MS}\right]_{1,l_k}\left[\tilde{\tilde{\mathbf{M}}}^h_{\mathbb{R},MS}\right]_{n_m+1,\hat{l}_k} = \begin{cases} \left(\Re\left(\left[\tilde{\tilde{\mathbf{M}}}^h_{\mathbb{C},MS}\right]_{1,l_k}\right)\right)^2 > 0 & \implies l_k^{th}\text{mode is forward traveling} \\ -\left(\Im\left(\left[\tilde{\tilde{\mathbf{M}}}^h_{\mathbb{C},MS}\right]_{1,l_k}\right)\right)^2 < 0 & \implies \hat{l}_k^{th}\text{mode is forward traveling} \end{cases} \tag{B.29}$$

where $[\mathbf{A}]_{j,k}$ represents the element at the j^{th} row and k^{th} column of matrix $\mathbf{A}$.

BIBLIOGRAPHY

[1] Srinivasan, A. V., 1997. "Flutter and resonant vibration characteristics of engine blades". *Journal of Engineering for Gas Turbines and Power-Transactions of the ASME,* ***119***(4), pp. 742–775.

[2] Ewins, D. J., 2010. "Control of vibration and resonance in aero engines and rotating machinery - An overview". *International Journal of Pressure Vessels and Piping,* ***87***(9), pp. 504–510.

[3] Castanier, M., and Pierre, C., 2006. "Modeling and analysis of mistuned bladed disk vibration: Current status and emerging directions.". *Journal of Propulsion and Power,* ***22***(2), pp. 384–396.

[4] Castanier, M. P., and Pierre, C., 2002. "Using intentional mistuning in the design of turbomachinery rotors". *AIAA Journal,* ***40***(10), pp. 2077–2086.

[5] Whitehead, D. S., 1998. "The maximum factor by which forced vibration of blades can increase due to mistuning". *Journal of Engineering for Gas Turbines and Power-Transactions of the ASME,* ***120***(1), pp. 115–119.

[6] Kielb, R. E., Hall, K. C., Hong, E., and Pai, S. S., 2006. "Probabilistic flutter analysis of a mistuned bladed disk". *Proceedings of the ASME Turbo Expo 2006, Vol 5, Pts A and B*, pp. 1145–1150.

[7] Beck, J. A., Brown, J. M., Slater, J. C., and Cross, C. J., 2013. "Probabilistic mistuning assessment using nominal and geometry based mistuning methods". *Journal of Turbomachinery,* ***135***(5), pp. 051004–051004–9.

[8] Craig, R. R., and Bampton, M. C. C., 1968. "Coupling of substructures for dynamic analyses". *AIAA Journal,* ***6***(7), pp. 1313–1319.

[9] Hurty, W. C., 1965. "Dynamic analysis of structural systems using component modes". *AIAA Journal,* ***3***(4), pp. 678–685.

[10] Bladh, R., Castanier, M. P., and Pierre, C., 2001. "Component-mode-based reduced order modeling techniques for mistuned bladed disks - Part I: Theoretical models". *Journal of Engineering for Gas Turbines and Power-Transactions of the ASME,* ***123***(1), Jan, pp. 89–99.

[11] Bladh, R., Castanier, M. P., and Pierre, C., 2001. "Component-mode-based reduced order modeling techniques for mistuned bladed disks - Part II: Application". *Journal of Engineering for Gas Turbines and Power-Transactions of the ASME,* ***123***(1), Jan, pp. 100–108.

[12] Bonney, M. S., Kammer, D. C., and Brake, M. R. W., 2015. "Fully parameterized reduced order models using hyper-dual numbers and component mode synthesis". p. V008T13A021.

[13] Beck, J. A., Brown, J. M., Cross, C. J., and Slater, J. C., 2014. "Component-mode reduced-order models for geometric mistuning of integrally bladed rotors". *AIAA Journal,* ***52***(7), pp. 1345–1356.

[14] Yang, M. T., and Griffin, J. H., 2001. "A reduced-order model of mistuning using a subset of nominal system modes". *Journal of Engineering for Gas Turbines and Power-Transactions of the ASME,* ***123***(4), pp. 893–900.

[15] Feiner, D. M., and Griffin, J. H., 2002. "A fundamental model of mistuning for a single family of modes". *Journal of Turbomachinery,* ***124***(4), pp. 597–605.

[16] Lim, S. H., Bladh, R., Castanier, M. P., and Pierre, C., 2007. "Compact, generalized component mode mistuning representation for modeling bladed disk vibration". *AIAA Journal,* ***45***(9), pp. 2285–2298.

[17] Joshi, A. G. S., and Epureanu, B. I., 2012. "Reduced order models for blade-to-blade damping variability in mistuned blisks". *Journal of Vibration and Acoustics-Transactions of the ASME,* ***134***(5).

[18] Nyssen, F., and Golinval, J. C., 2016. "Identification of mistuning and model updating of an academic blisk based on geometry and vibration measurements". *Mechanical Systems and Signal Processing,* ***68-69***, pp. 252–264.

[19] Martel, C., and Corral, R., 2008. "Asymptotic description of maximum mistuning amplification of bladed disk forced response". *Journal of Engineering for Gas Turbines and Power,* ***131***(2), pp. 022506–022506–10.

[20] Khemiri, O., Martel, C., and Corral, R., 2014. "Forced response of mistuned bladed disks: Quantitative validation of the asymptotic description". *Journal of Propulsion and Power,* ***30***(2), pp. 397–406.

[21] Khemiri, O., Martel, C., and Corral, R., 2013. "Asymptotic description of damping mistuning effects on the forced response of turbomachinery bladed disks". *Journal of Sound and Vibration,* ***332***(20), pp. 4998–5013.

[22] Griffin, J. H., and Sinha, A., 1985. "The interaction between mistuning and friction in the forced response of bladed disk assemblies". *Journal of Engineering for Gas Turbines and Power,* ***107***(1), pp. 205–211.

[23] Sinha, A., and Griffin, J. H., 1985. "Effects of friction dampers on aerodynamically unstable rotor stages". *AIAA Journal,* ***23***(2), pp. 262–270.

[24] Menq, C., Bielak, J., and Griffin, J., 1986. "The influence of microslip on vibratory response, part i: A new microslip model". *Journal of Sound and Vibration,* ***107***(2), pp. 279 – 293.

[25] Menq, C., Griffin, J., and Bielak, J., 1986. "The influence of microslip on vibratory response, part ii: A comparison with experimental results". *Journal of Sound and Vibration,* ***107***(2), pp. 295 – 307.

[26] Iwan, W. D., 1966. "A distributed-element model for hysteresis and its steady-state dynamic response". *Journal of Applied Mechanics,* ***33***(4), pp. 893–900. 10.1115/1.3625199.

[27] Segalman, D. J., and Starr, M. J., 2012. "Iwan models and their provenance". pp. 441–449.

[28] Bonney, M. S., Robertson, B. A., Mignolet, M., Schempp, F., and Brake, M. R., 2016. *Experimental Determination of Frictional Interface Models*. Springer International Publishing, pp. 473–490.

[29] Koh, K. H., Griffin, J. H., Filippi, S., and Akay, A., 2005. "Characterization of turbine blade friction dampers". *Journal of Engineering for Gas Turbines and Power-Transactions of the ASME,* ***127***(4), pp. 856–862.

[30] Yang, B. D., and Menq, C. H., 1998. "Characterization of 3D contact kinematics and prediction of resonant response of structures having 3D frictional constraint". *Journal of Sound and Vibration,* ***217***(5), pp. 909–925.

[31] Yang, B. D., and Menq, C. H., 1998. "Characterization of contact kinematics and application to the design of wedge dampers in turbomachinery blading: Part 1 - Stick-slip contact kinematics". *Journal of Engineering for Gas Turbines and Power-Transactions of the ASME,* ***120***(2), pp. 410–417.

[32] Yang, B. D., and Menq, C. H., 1998. "Characterization of contact kinematics and application to the design of wedge dampers in turbomachinery blading: Part 2 - Prediction of forced response and experimental verification". *Journal of Engineering for Gas Turbines and Power-Transactions of the ASME,* ***120***(2), pp. 418–423.

[33] Cigeroglu, E., An, N., and Menq, C. H., 2007. "A microslip friction model with normal load variation induced by normal motion". *Nonlinear Dynamics,* ***50***(3), pp. 609–626.

[34] Cardona, A., Coune, T., Lerusse, A., and Geradin, M., 1994. "A multiharmonic method for nonlinear vibration analysis". *International Journal for Numerical Methods in Engineering,* ***37***(9), pp. 1593–1608.

[35] Firrone, C. M., and Zucca, S., 2011. *Modelling Friction Contacts in Structural Dynamics and its Application to Turbine Bladed Disks, Numerical Analysis - Theory and Application, Prof. Jan Awrejcewicz (Ed.)*. INTECH, Rijeka, ch. 14, pp. 301–334.

[36] Cameron, T. M., and Griffin, J. H., 1989. "An alternating frequency/time domain method for calculating the steady-state response of nonlinear dynamic systems". *Journal of Applied Mechanics-Transactions of the ASME,* ***56***(1), pp. 149–154.

[37] Poudou, O., and Pierre, C., 2003. "Hybrid frequency-time domain methods for the analysis of complex structural systems with dry friction damping". In 44th Structures, Structural Dynamics and Materials Conference, Vol. 1, pp. 111–124.

[38] Siewert, C., Panning, L., Wallaschek, J., and Richter, C., 2010. "Multiharmonic forced response analysis of a turbine blading coupled by nonlinear contact forces". *Journal of Engineering for Gas Turbines and Power-Transactions of the ASME,* ***132***(8).

[39] Zucca, S., and Firrone, C. M., 2014. "Nonlinear dynamics of mechanical systems with friction contacts: Coupled static and dynamic multi-harmonic balance method and multiple solutions". *Journal of Sound and Vibration,* ***333***(3), pp. 916 – 926.

[40] Petrov, E. P., and Ewins, D. J., 2005. "Method for analysis of nonlinear multiharmonic vibrations of mistuned bladed disks with scatter of contact interface characteristics". *Journal of Turbomachinery,* ***127***(1), pp. 128–136.

[41] Petrov, E. P., 2004. "A method for use of cyclic symmetry properties on analysis of nonlinear multiharmonic vibrations of bladed disks". *Journal of Turbomachinery-Transactions of the ASME,* ***126***(1), pp. 175–183.

[42] Frey, C., Ashcroft, G., Kersken, H. P., and Voigt, C. "A harmonic balance technique for multistage turbomachinery applications". In ASME Turbo Expo 2014: Turbine Technical Conference and Exposition, American Society of Mechanical Engineers, pp. V02BT39A005–V02BT39A005.

[43] Forster, A., and Krack, M., 2016. "An efficient method for approximating resonance curves of weakly-damped nonlinear mechanical systems". *Computers and Structures,* ***169***, pp. 81–90.

[44] Cigeroglu, E., An, N., and Menq, C. H., 2007. "Wedge damper modeling and forced response prediction of frictionally constrained blades". *Proceedings of the ASME Turbo Expo 2007, Vol 5*, pp. 519–528.

[45] Cigeroglu, E., An, N., and Menq, C. H., 2009. "Forced response prediction of constrained and unconstrained structures coupled through frictional contacts". *Journal of Engineering for Gas Turbines and Power-Transactions of the ASME,* ***131***(2).

[46] Cigeroglu, E., and Ozguven, H. N., 2006. "Nonlinear vibration analysis of bladed disks with dry friction dampers". *Journal of Sound and Vibration,* ***295***(3-5), pp. 1028–1043.

[47] Grolet, A., and Thouverez, F., 2012. "On a new harmonic selection technique for harmonic balance method". *Mechanical Systems and Signal Processing,* ***30***, pp. 43–60.

[48] Grolet, A., and Thouverez, F., 2015. "Computing multiple periodic solutions of nonlinear vibration problems using the harmonic balance method and groebner bases". *Mechanical Systems and Signal Processing,* ***52-53***, pp. 529–547.

[49] Petrov, E., and Ewins, D., 2005. "Effects of mistuning on the forced response of bladed discs with friction dampers". In Evaluation, Control and Prevention of High Cycle Fatigue in Gas Turbine Engines for Land, Sea and Air Vehicles, Meeting Proceedings RTO-MP-AVT-121, Neuilly-sur-Seine, France: RTO, pp. 1–16.

[50] Tang, W., Baek, S., and Epureanu, B., 2017. "Reduced-order models for blisks with small and large mistuning and friction dampers". *Journal of Engineering for Gas Turbines and Power,* ***139***(1), 1.

[51] Rosenberg, R. M., 1962. "The normal modes of nonlinear n-degree-of-freedom systems". *Journal of Applied Mechanics,* ***29***(1), pp. 7–14.

[52] Grolet, A., and Thouverez, F., 2012. "Free and forced vibration analysis of a nonlinear system with cyclic symmetry: Application to a simplified model". *Journal of Sound and Vibration,* ***331***(12), pp. 2911 – 2928.

[53] Shaw, S., and Pierre, C., 1993. "Normal modes for non-linear vibratory systems". *Journal of Sound and Vibration,* ***164***(1), pp. 85 – 124.

[54] Vakakis, A., 1997. "Non-linear normal modes (nnms) and their applications in vibration theory: An overview". *Mechanical Systems and Signal Processing,* ***11***(1), pp. 3 – 22.

[55] Laxalde, D., Thouverez, F., Sinou, J., and Lombard, J., 2007. "Qualitative analysis of forced response of blisks with friction ring dampers". *European Journal of Mechanics - A/Solids,* ***26***(4), pp. 676–687.

[56] Joannin, C., Chouvion, B., Thouverez, F., Mbaye, M., and Ousty, J. P., 2016. "Nonlinear modal analysis of mistuned periodic structures subjected to dry friction". *Journal of Engineering for Gas Turbines and Power-Transactions of the Asme,* ***138***(7).

[57] Pesheck, E., Pierre, C., and Shaw, S., 2002. "a New Galerkin-Based Approach for Accurate Non-Linear Normal Modes Through Invariant Manifolds". *Journal of Sound Vibration,* ***249***, Jan., pp. 971–993.

[58] Jiang, D., Pierre, C., and Shaw, S., 2005. "Nonlinear normal modes for vibratory systems under harmonic excitation". *Journal of Sound and Vibration,* ***288***(4), pp. 791 – 812.

[59] Shaw, S., and Pierre, C., 1991. "Non-linear normal modes and invariant manifolds". *Journal of Sound and Vibration,* ***150***(1), pp. 170–173.

[60] Pierre, C., Jiang, D., and Shaw, S., 2006. "Nonlinear normal modes and their application in structural dynamics". *Mathematical Problems in Engineering,* ***2006***.

[61] Krack, M., Panning-von Scheidt, L., Wallaschek, J., Siewert, C., and Hartung, A., 2013. "Reduced order modeling based on complex nonlinear modal analysis and its application to bladed disks with shroud contact". *Journal of Engineering for Gas Turbines and Power,* ***135***(10), pp. 102502–102502–8.

[62] Kerschen, G., Golinval, J. C., Vakakis, A. F., and Bergman, L. A., 2005. "The method of proper orthogonal decomposition for dynamical characterization and order reduction of mechanical systems: An overview". *Nonlinear Dynamics,* ***41***(1-3), pp. 147–169.

[63] Amsallem, D., Zahr, M. J., and Farhat, C., 2012. "Nonlinear model order reduction based on local reduced-order bases". *International Journal for Numerical Methods in Engineering,* ***92***(10), pp. 891–916.

[64] Carlberg, K., Farhat, C., Cortial, J., and Amsallem, D., 2013. "The gnat method for nonlinear model reduction: Effective implementation and application to computational fluid dynamics and turbulent flows". *Journal of Computational Physics,* ***242***, pp. 623–647.

[65] Farhat, C., Avery, P., Chapman, T., and Cortial, J., 2014. "Dimensional reduction of nonlinear finite element dynamic models with finite rotations and energy-based mesh sampling and weighting for computational efficiency". *International Journal for Numerical Methods in Engineering,* ***98***(9), pp. 625–662.

[66] Farhat, C., Chapman, T., and Avery, P., 2015. "Structure-preserving, stability, and accuracy properties of the energy-conserving sampling and weighting method for the hyper reduction of nonlinear finite element dynamic models". *International Journal for Numerical Methods in Engineering,* ***102***(5), pp. 1077–1110.

[67] Ryckelynck, D., 2005. "A priori hyperreduction method: an adaptive approach". *Journal of Computational Physics,* ***202***(1), pp. 346–366.

[68] Chati, M., Rand, R., and Mukherjee, S., 1997. "Modal analysis of a cracked beam". *Journal of Sound and Vibration,* ***207***(2), pp. 249 – 270.

[69] Saito, A., and Epureanu, B. I., 2011. "Bilinear modal representations for reduced-order modeling of localized piecewise-linear oscillators". *Journal of Sound and Vibration,* ***330***(14), pp. 3442 – 3457.

[70] Zucca, S., and Epureanu, B. I., 2014. "Bi-linear reduced-order models of structures with friction intermittent contacts". *Nonlinear Dynamics,* ***77***(3), Aug, pp. 1055–1067.

[71] Jung, C., D'Souza, K., and Epureanu, B., 2012. *Bilinear amplitude approximation for piecewise-linear oscillators*. Structures, Structural Dynamics, and Materials and Co-located Conferences. American Institute of Aeronautics and Astronautics. doi:10.2514/6.2012-1793.

[72] Jung, C., D'Souza, K., and Epureanu, B. I., 2014. "Nonlinear amplitude approximation for bilinear systems". *Journal of Sound and Vibration,* ***333***(13), pp. 2909 – 2919.

[73] Baek, S., and Epureanu, B. I., 2017. "Reduced-order models of blisks with small geometric mistuning". *Journal of Vibration and Acoustics,* ***139***(4), pp. 041003–041003–10. 10.1115/1.4036105.

[74] Botto, D., Lavella, M., and Gola, M. M., 2012. "Measurement of contact parameters of flat on flat contact surfaces at high temperature". In ASME Turbo Expo 2012, Vol. **7**, ASME, pp. 1325–1332.

[75] Whitehead, D. S., 1976. "Effect of mistuning on forced vibration of blades with mechanical coupling". *Journal of Mechanical Engineering Science,* ***18***(6), pp. 306–307.

[76] Bladh, R., Pierre, C., Castanier, M. P., and Kruse, M. J., 2002. "Dynamic response predictions for a mistuned industrial turbomachinery rotor using reduced-order modeling". *Journal of Engineering for Gas Turbines and Power,* ***124***(2), pp. 311–324.

[77] Lee, S. Y., Castanier, M. P., and Pierre, C. "Assessment of probabilistic methods for mistuned bladed disk vibration". In Proceedings of the 46th AIAA/ASME/ASCE/AHS/ASC Structures, Structural dynamics, and Materials Conference, AIAA-2005-1990.

[78] Tan, Y., Zang, C., Zhou, B., Duan, Y., and Petrov, E. P., 2016. "Sensitivity analysis of high-frequency forced response for mistuned bladed discs based on high-fidelity models". p. V07AT32A025.

[79] Patsias, S., Saxton, C., and Shipton, M., 2004. "Hard damping coatings: an experimental procedure for extraction of damping characteristics and modulus of elasticity". *Materials Science and Engineering: A,* ***370***(1), pp. 412–416.

[80] Patsias, S., Tassini, N., and Lambrinou, K., 2006. "Ceramic coatings: Effect of deposition method on damping and modulus of elasticity for yttria-stabilized zirconia". *Materials Science and Engineering: A,* ***442***(1), pp. 504–508.

[81] Filippi, S., and Torvik, P., 2011. "A methodology for predicting the response of blades with nonlinear coatings". *Journal of Engineering for Gas Turbines and Power,* ***133***(4).

[82] Torvik, P. J., and Hansel, J., 2009. "Mechanical properties of a ceramic coating with vem infiltration". *Journal of Engineering Materials and Technology,* ***131***(3), p. 031003.

[83] Tassini, N., Lambrinou, K., Mircea, I., Bartsch, M., Patsias, S., and Van der Biest, O., 2007. "Study of the amplitude-dependent mechanical behaviour of yttria-stabilised zirconia thermal barrier coatings". *Journal of the European Ceramic Society,* ***27***(2-3), pp. 1487–1491.

[84] Yang, M. T., and Griffin, J. H., 1997. "A reduced order approach for the vibration of mistuned bladed disk assemblies". *Journal of Engineering for Gas Turbines and Power-Transactions of the ASME,* ***119***(1), pp. 161–167.

[85] Marinescu, O., Epureanu, B. I., and Banu, M., 2011. "Reduced order models of mistuned cracked bladed disks". *Journal of Vibration and Acoustics-Transactions of the ASME,* ***133***(5).

[86] Nacivet, S., Pierre, C., Thouverez, F., and Jezequel, L., 2003. "A dynamic lagrangian frequencytime method for the vibration of dry-friction-damped systems". *Journal of Sound and Vibration,* ***265***(1), pp. 201 – 219.

[87] Borrajo, J. M., Zucca, S., and Gola, M. M., 2006. "Analytical formulation of the jacobian matrix for non-linear calculation of the forced response of turbine blade assemblies with wedge friction dampers". *International Journal of Non-Linear Mechanics,* ***41***(10), pp. 1118–1127.

[88] Yang, B. D., Chu, M. L., and Menq, C. H., 1998. "Stick-slip-separation analysis and nonlinear stiffness and damping characterization of friction contacts having variable normal load". *Journal of Sound and Vibration,* ***210***(4), pp. 461–481.

[89] Petrov, E. P., and Ewins, D. J., 2003. "Analytical formulation of friction interface elements for analysis of nonlinear multi-harmonic vibrations of bladed disks". *Journal of Turbomachinery-Transactions of the ASME,* ***125***(2), pp. 364–371.

[90] Menq, C. H., Chidamparam, P., and Griffin, J. H., 1991. "Friction damping of 2-dimensional motion and its application in vibration control". *Journal of Sound and Vibration,* ***144***(3), pp. 427–447.

[91] Menq, C. H., and Yang, B. D., 1998. "Non-linear spring resistance and friction damping of frictional constraint having two-dimensional motion". *Journal of Sound and Vibration,* ***217***(1), pp. 127–143.

[92] Sanliturk, K. Y., and Ewins, D. J., 1996. "Modelling two-dimensional friction contact and its application using harmonic balance method". *Journal of Sound and Vibration,* ***193***(2), pp. 511–523.

[93] Fitzner, C., Epureanu, B. I., and Filippi, S., 2014. "Nodal energy weighted transformation: A mistuning projection and its application to flade (tm) turbines". *Mechanical Systems and Signal Processing,* ***42***(1-2), pp. 167–180.

[94] Hong, S. K., Epureanu, B. I., and Castanier, M. P., 2013. "Next-generation parametric reduced-order models". *Mechanical Systems and Signal Processing,* ***37***(1-2), pp. 403–421.

[95] Madden, A., Epureanu, B. I., and Filippi, S., 2012. "Reduced-order modeling approach for blisks with large mass, stiffness, and geometric mistuning". *AIAA Journal,* ***50***(2), pp. 366–374.

[96] Petrov, E. P., and Ewins, D. J., 2006. "Advanced modeling of underplatform friction dampers for analysis of bladed disk vibration". *Journal of Turbomachinery,* ***129***(1), pp. 143–150.

[97] Mitra, M., Zucca, S., and Epureanu, B. I., 2016. "Adaptive microslip projection for reduction of frictional and contact nonlinearities in shrouded blisks". *Journal of Computational and Nonlinear Dynamics,* ***11***(4), 7.

[98] Ewins, D. J., 1969. "The effects of detuning upon the forced vibrations of bladed disks". *Journal of Sound and Vibration,* ***9***(1), pp. 65 – 79.

[99] Olson, B. J., Shaw, S. W., Shi, C. Z., Pierre, C., and Parker, R. G., 2014. "Circulant matrices and their application to vibration analysis". *Applied Mechanics Reviews,* ***66***(4).

[100] Davis, P. J., 1979. *Circulant Matrices*, 2nd ed. Wiley, New York.